LA-UR-83-737

p 8, 145

Light-Water Reactor Degraded-Core Cooling Program Technical Note

A DAMAGE ASSESSMENT OF TMI-2

by

P. J. Maudlin, E. C. Schwegler, T. L. Wilson,
J. L. Tomkins, A. W. Cronenberg, and J. A. Moore

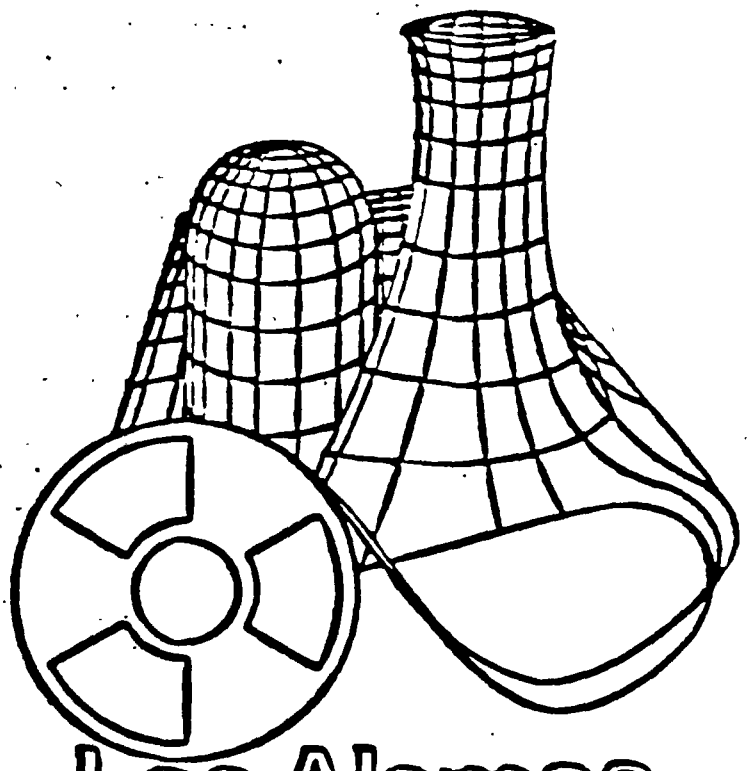

Los Alamos

Los Alamos National Laboratory

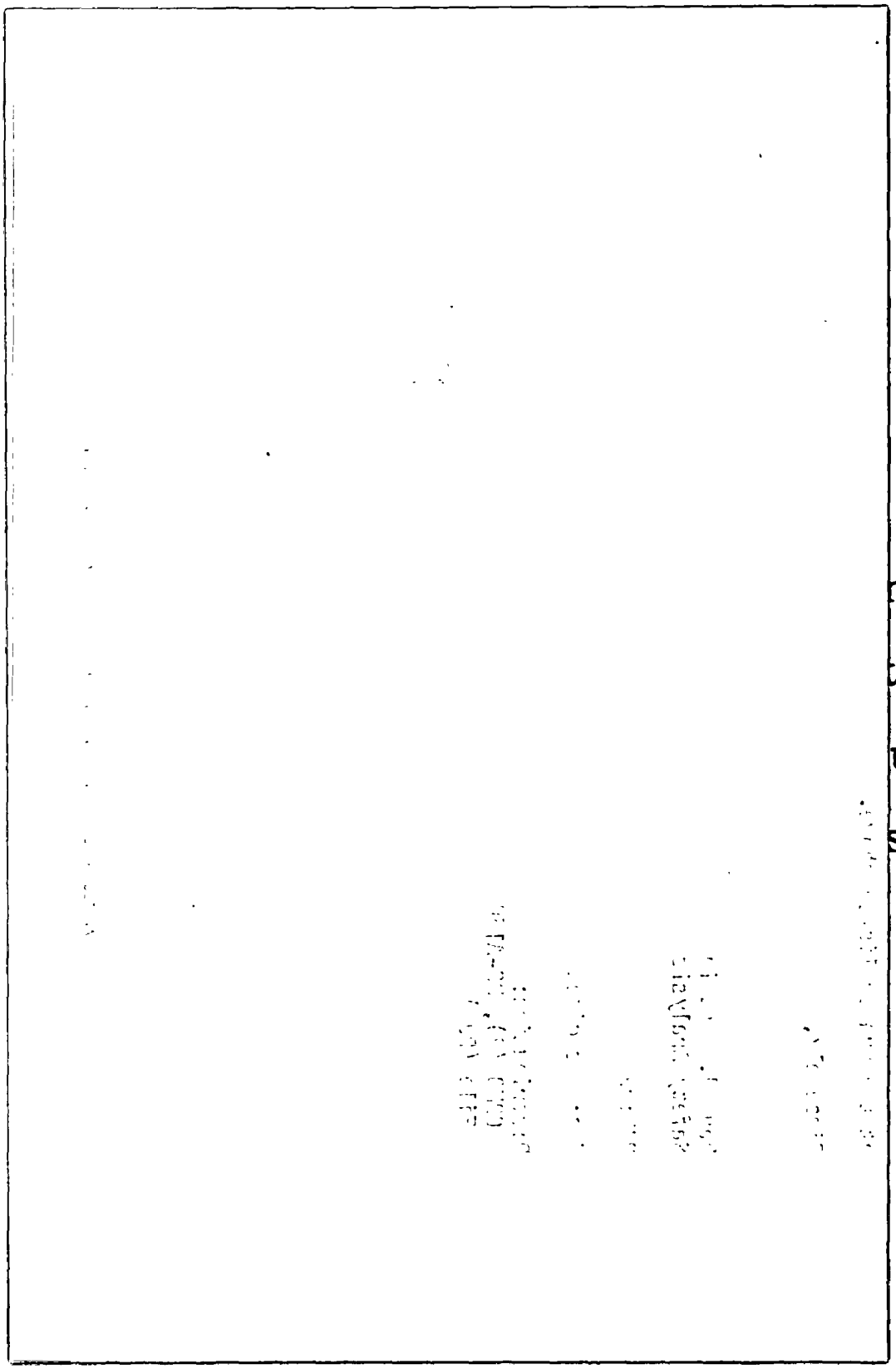

n of

tory

uted

sion.

CONTENTS

LIST OF TABLES

LIST OF FIGURES

(Cont)

(Cont)

(Cont)

(Cont)

(Cont)

A DAMAGE ASSESSMENT OF TMI-2

by

P. J. Maudlin, E. C. Schwegler, T. L. Wilson,
J. L. Tomkins, A. W. Cronenberg, and J. A. Moore

ABSTRACT

The Three Mile Island Unit Two damage configuration sustained during the accident transient on March 28, 1979 is mechanistically calculated using the MIMAS and TRAC-PF1 computer codes. These codes are based on first principles and best-estimate models of the heat transfer and fluid dynamic processes involved. The TMI accident environment is analyzed from the initial loss of mainfeedwater to a point in time just after the 3 hr and 20 min high pressure injection and subsequent core reflood. These calculations show the inconel grid spacers melted first, followed by a melt of the upper 80% of the stainless control rods, and then followed by a fragmentation of the upper 80% of the previously embrittled fuel rods. This debris material relocated to the lower core where a debris bed forms with a packing fraction of 30% between rod stubs and 44% above these stubs. This calculated debris generation and packing fractions, in conjunction with the TMI "quick look" camera observations, indicate that 22% of the fuel rod debris is missing from the core region, and is located out in the ex-core primary system. Total hydrogen production during the accident transient is calculated to be about 400 kg, with the majority of this production (about 75%) being generated during the 3 hr and 20 min core reflood.

I. INTRODUCTION

Since the March 28, 1979 accident at Three Mile Island Unit Two (TMI-2), a large number of analyses have focused on the question of core damage (Ref. 1 - 5). Specifically, this focus is on the nature of the damage (i.e., cladding ballooning, cladding oxidation and embrittlement, fuel liquefaction, fuel rod fragmentation, etc.), and on the spatial distribution of this degraded geometry in the reactor vessel. The sophistication of these analyses range from a back-of-the-envelope calculation to a 30-h calculation using a state-of-art thermal-hydraulics computer code. The results from these calculations form a core damage spectrum that ranges from little damage (ballooning only) to complete fragmentation of the core fuel rods.

The diversity of the calculational results is from uncertainties in such important items as: (1) the makeup and letdown flows that constitute the primary system boundary conditions during the accident, (2) the behavior of degraded core materials, such as the U-Zr-O eutectic, whose properties are not well known, and (3) the use of uncoupled mathematical models to analyze a series of tightly coupled physical processes. This report describes a degraded core analysis of the TMI-2 accident transient that used an integrated system of models, thereby removing the uncertainties associated with item (3).

The primary purpose of this analysis of TMI-2 is to tie together the observed events and sample analysis results with detailed calculations, thereby constructing a consistent picture of the accident progression. This picture will then aid DOE and its contractors in their preparation of equipment and procedures for the cleanup and recovery of TMI-2. A secondary purpose of this work is to help identify important data within the reactor core region that should be collected, and areas of phenomena uncertainty. The collected data will guide future analyses, help verify existing models, and possibly yield

clues for identifying uncertain physical processes that occurred during the accident (for example the "torching" of the fuel assembly upper-end-fittings). We calculated the degraded-core accident transient from time 0 (loss of main-feedwater) through the core reflood that occurred at 3 hr and 18 min. These calculations focused on fuel and control rod damage, and the corresponding generation and transport of molten and/or solid debris, H_2, and fission products within the core region. We used the existing MIMAS (Multified Integrated Meltdown Analysis System) and the (TRAC-PF1)[6] (Transient Reactor Analysis Code) computer codes. The MIMAS code provides an integrated fuel, fluids, radiation heat transfer, and structures analysis based on first principles and best-estimate models of the various physical processes involved in degraded core accidents. The TRAC code provides an integrated thermal-hydraulic, steam-water (two-phase) system analysis for the primary and secondary reactor plant systems. For this work TRAC and MIMAS were run in tandem with TRAC modeling primary system components (piping, pumps, plenums, etc.) external to the core and part of the secondary system, and with MIMAS addressing the in-core physical processes (concentrating on the degraded core phenomena). The linkage between TRAC and MIMAS for this work has the form of TRAC-calculated boundary conditions supplied to MIMAS at the upper- and lower-core support plates.

Section II briefly describes the general programming structure and phenomena modeling contained in the MIMAS code. Similar information for the TRAC code is available in Ref. 6. After reviewing the major accident events that strongly influence the behavior of the primary system, Sec. III then presents calculational results for the TMI-2 accident transient. These results illustrate fuel and control rod behavior, the fluid dynamics of the core coolant and geometry, radiation heat-transfer effects, and adjacent core structure behavior (upper- and lower-core support plates and core baffle). Also included

in Sec. III is sensitivity information for important modeling parameters and various phenomena. Section IV gives a TMI-2 damage assessment summary and conclusions, and identifies important data (from an analyst's point-of-view) that should be collected during the upcoming defueling operations of the reactor vessel. Also identified in this section are several physical processes that are relatively unknown but have a large influence on the overall damage picture of the core. These processes belong to the item (2) uncertainties.

II. MIMAS MODELING AND METHODS REVIEW

The development of MIMAS as a best-estimate degraded-core analysis code is now complete to the extent possible considering the current lack of degraded-core experimental data. MIMAS does not attempt detailed modeling of degraded core phenomena; rather only those aspects that significantly influence gross core and primary system behavior are considered. Currently the degraded-core component includes the following computational modules:

1. two-dimensional modeling of fuel and control rod behavior, including oxidation, embrittlement, melting, and fragmentation;

2. one-dimensional, three-field fluid dynamics for steam, water, debris, H_2, and fission products;

3. two-dimensional radiation heat transfer between fuel pins, fluids, and adjacent core structures;

4. two-dimensional heat-transfer modeling for the adjacent core structures that includes conduction, convection, radiation (thermal and gamma), and melting.

The general structure of the MIMAS code is depicted in Fig. 1. The four computational modules communicate with each other during a calculation via the MIMAS driver. The MIMAS driver handles the input and output, sets up the data structure and array pointers, and transfers control to the appropriate computational module as the calculation proceeds forward in time. Communication of the physical linkages and feedbacks between modules is achieved using specific arrays in the data structure. A more detailed description of each of the four computational modules is given in the following subsections.

II.A. Fuel and Control Rods

II.A.1. General Approach

The choice of significant fuel response models for inclusion in MIMAS was based on judgement and prior experience. The MIMAS code is structured so fuel and control rod models can be added, deleted, or updated as experience and new data warrant. We hope that by comparing the MIMAS model predictions with the results of the TMI-2 core examinations these models can be improved. The extent to which inaccuracies in the fuel rod models affect the TMI-2 analysis results is addressed with sensitivity studies that are described in Sec. III.C.

To analyze degraded core accidents, the MIMAS code divides the core region into a number of axial and radial numerical cells, as diagrammed in Fig. 2. Within each cell, all rod segments have the same average behavior and properties. In analyzing fuel and control rod behavior, both axial and radial core power and burnup distributions are considered. However, axial and radial conduction heat transfer between rod segments is ignored.

The fuel and control rod behavior models in MIMAS are called by the subroutine PINZ, which is the name of the fuel and control rod module depicted in Fig. 1. That module calculates the rod morphological changes and interacts with the fluid fields and thermal radiation. The various fuel and control rod morphological forms that either are or will be considered in the MIMAS code are listed and described in Table I. This list is based on various experimental observations[7,8]. The list can be expanded if warranted by future test results.

A diagram of the first-level subroutines called by PINZ is shown in Fig. 3. As indicated in this figure, each of these first-level subroutines analyzes the behavior of one or more morphological forms of the fuel and control rods, for example intact, candled, etc., and determines when that form will change into another form. The fuel and control rod morphological forms and

changes that occurred during the TMI-2 accident are defined and discussed more completely.

Since the rod segments in each radial and axial core cell are analyzed independently, the programming framework diagrammed in Fig. 3 offers several advantages. For example, the computer run time for fuel rod analysis is approximately the same if the rods throughout the core are intact, or if each core cell contains a different fuel morphological form. Also updating existing fuel and control rod models and/or adding models for additional morphological forms is relatively simple. This point is important, since future testing may reveal important degraded core phenomena not currently modeled in MIMAS.

II.A.2. Model Descriptions

This section describes the principal models used to analyze fuel and control rod behavior in the TMI-2 accident. Only rod models that relate to the TMI-2 accident are presented. The basis for the inclusion of each model is given with the model descriptions.

II.A.2.a. Cladding Rupture and Ballooning Models. For this study, cladding-ballooning initiating conditions and magnitudes are determined from data correlations that bound, as closely as possible, the TMI-2 accident conditions. The following cladding-ballooning correlations, based primarily on single-rod burst data, are considered:

1. The REBEKA correlations,[9] based on data obtained from tests performed by Kernforschungszentrum Karlsruhe, Germany (KfK) in Germany;

2. The MATPRO-11 burst temperature, stress, and strain equations,[7] which incorporate burst temperature/stress data from a variety of sources in the United States. Burst strains are determined from a simplified

first-principles relation between burst stress, temperature, and cladding strength;

3. The ballooning correlations from NUREG-0630,[10] which are based primarily on data from Chung, Garde, and Kassner at Argonne National Laboratory and from Chapman at Oak Ridge National Laboratory (ORNL). Because of its completeness, the ballooning model in NUREG-0630 is considered the best-estimate model for this analysis. The REBEKA and MATPRO models are useful primarily for estimating uncertainties.

These cladding-ballooning correlations consist of two parts: a correlation for burst temperature versus burst stress (or versus rod gas and coolant pressure differential) and a correlation (or equation, in the case of MATPRO) for circumferential burst strain versus temperature. These relationships for the REBEKA and NUREG-0630 correlations are shown in Figs. 4 - 7. These figures also show the temperature ramp-rate sensitivity of the fuel rod ballooning behavior.

As will be discussed more completely, the TMI-2 accident involved cladding heating rates of approximately 1 K/s or less. Thus, this study is concerned primarily with the low heating rate portion of these correlations. For comparison, the burst temperature versus burst pressure relationships for the three correlations at low temperature ramp rates are shown in Fig. 8, whereas the burst strain versus burst temperature relationships for these correlations at low heating rates are shown in Fig. 9. All three correlations in Fig. 8 show a decrease in burst pressure with an increase in temperature; the REBEKA correlation shows an inflection in the burst temperature versus pressure curve in the $\alpha - \beta$ transition region. In Fig. 9, the cladding burst strain initially increases with burst temperature in the α - Zr region, but then decreases as the

$\alpha - \beta$ transition temperature is approached. Above the $\alpha - \beta$ transition temperature the burst strain again initially increases with temperature, and then again decreases as oxidation embrittlement effects dominate.

In the α - Zr region, the predicted MATPRO-11 and REBEKA peak ballooning strains tend to agree, and to lie above the NUREG-0630 strain predictions. In the transition and β - Zr regions, there is considerable disagreement between the three correlations as to the magnitudes of the minimum and maximum ballooning strains, and the temperatures at which they occur. However, as discussed more fully in the following section, these regimes lie outside the temperature range in which rod ballooning is calculated to occur in the TMI-2 core.

Another factor that strongly influences cladding burst strain is the circumferential temperature gradient around the fuel rod. During loss-of-coolant-accident (LOCA) conditions, these gradients can arise from reflood spray effects. As shown in Fig. 10, cladding burst strain decreases with increasing circumferential temperature gradient, with a maximum decrease in burst strain of about 60% for high gradient values.

Although the single-rod burst tests are useful in gathering fundamental burst condition and strain data, they cannot include the effects of rod-rod interaction that would occur for large burst strains in a rod bundle. For example, if all rods in a PWR fuel bundle experienced a circumferential strain of 70%, they would completely fill the coolant channel space and pack the bundle into a square arrray (Fig. 11). Thus, rod-rod contact and possibly temperature gradients, induced by rod-rod interaction in a ballooning fuel rod bundle, limit the rod ballooning strains below the maximum single rod values. The co-planarity of the ballooned sections of the rods also affects the flow blockage in a rod bundle.

A variation of the method described in Ref. 10 is used to transform rod strains predicted by the single-rod burst correlations into rod-bundle flow blockage percentages. Measurements on test bundles showed that on the average, the ratio of the average co-planar rod strain at the maximum flow blockage elevation to the maximum rod burst strain (which would be calculated from the single rod burst correlations) equaled 0.56. In Ref. 10, this ratio is reduced to 0.46 for commercial-sized fuel rod bundles. This lower value was based on the assumption that for large rod bundles, the planar blockage for a given ballooning distribution is less than in smaller bundles because of the random axial positions of the ballooned cladding locations. However, tests on 8 × 8 rod bundles[11,12] revealed that in larger rod bundles, the ballooned portions of the cladding are greater along the rod lengths than in smaller rod bundles. This tends to equalize the flow blockage between the large and small bundles for a given value of maximum cladding ballooning strain. Thus, for this analysis, the value of 0.56 is used for the ratio of the average rod strain at the maximum bundle blockage location to the maximum single rod ballooning strain.

To calculate the best-estimate rod-bundle ballooning blockage for a given temperature-pressure history, the single rod correlations in Figs. 6 and 7 are used to determine the single rod burst temperature and ballooning strains. These ballooning strains are multiplied by 0.56 to determine the average coplanar rod strains at the elevation of maximum flow blockage. Figure 11 data are then used to determine the flow blockage percentages caused by the ballooned rods.

A value of the maximum blockage rod strain-single rod ballooning strain ratio has not been published for the MATPRO and REBEKA correlations. As a rough estimate, the 0.56 factor from NUREG-0630 could be applied to these single rod correlations also. However, based on the single rod strain predictions of

Fig. 9, this would result in the REBEKA and MATPRO correlations predicting much more flow blockages due to rod ballooning than the NUREG-0630 method.

It is further noted in Ref. 10 that the nonballooning components of commercial PWR fuel assemblies (for example guide tubes and instrument tubes) result in about 5% of the original flow area remaining clear even if the ballooned rods shut off 100% of their surrounding areas. Thus, the maximum flow area reduction that can occur in a PWR fuel assembly due to fuel rod ballooning is 95%, assuming that the ballooned rods can totally occupy their flow areas.

II.A.2.b. Zircalloy Oxidation, Hydrogen Generation, and Embrittlement.

Figure 12 shows the modeled cross-section of a fuel rod that has been oxidized in excess steam above 1200 K for a period of time, and that has experienced fuel-cladding contact.[7] At this temperature, the unaffected zirconium (shown in Fig. 12 as the wide center layer) has transformed to the relatively ductile beta-phase. The outermost layer has oxidized to ZrO_2. Immediately adjacent to this layer, another layer exists in which a high oxygen concentration has caused the zirconium lattice to assume the low-temperature alpha-configuration. Oxygen diffuses through both of these outer layers into the beta-zirconium region. Since the beta-zirconium layer is the most ductile of all those shown, this region is assumed to carry all of the cladding load. As the beta-zirconium layer absorbs oxygen by diffusion, it becomes embrittled, eventually breaking up under modest thermal shock loadings. The configuration of the cladding layers adjacent to the fuel is currently open to some question. The inner cladding layer configuration assumed for this study (and shown in Fig. 12) consists of a metallic uranium-zirconium layer sandwiched between two oxygen stabilized alpha-zirconium layers.[7] The oxygen needed to form these layers is assumed to be supplied by the uranium dioxide fuel.

Assuming availability of an excess steam concentration, the growth rates of the ZrO_2 and oxygen-stabilized alpha-zirconium layers follow parabolic kinetics, that is,

$$dL/dt = (A/L) \exp(-B/RT) \quad , \tag{1}$$

where

L = layer thickness

A = constant

B = activation energy

R = gas constant

T = absolute temperature

t = time.

The values of A and B are different for the different layers, and are discussed in detail below.

The growth rate of the ZrO_2 layer is important because it determines the hydrogen production rate according to the chemical equation:

$$2H_2O + Zr = 2H_2 + ZrO_2 + Q \quad , \tag{2}$$

where

Q = heat of reaction = 6.5×10^6 J/kg Zr .

For situations where stoichiometric or excess steam is available, the heat of the steam-zirconium reaction is much greater than the fission product decay heat of the fuel. However, when the steam has a very low flow rate or is stagnant,

the hydrogen produced by the reaction of Eq. (2) can displace the steam adjacent to the cladding, and "starve" the reaction of Eq. (1). Details of this starvation process are discussed more fully in Secs. III.D and III.E. This steam starvation process is quantitatively accounted for by modifying the ZrO_2 layer growth rate equation (Eq. 1) to become

$$dL/dt = (A/L)\, e^{-B/RT}\, x_{H_2O}^2 \quad , \tag{3}$$

where x_{H_2O} is the mole fraction of the steam adjacent to the cladding. As more and more hydrogen is produced by the steam-Zr reaction, x_{H_2O} becomes smaller, and the ZrO_2-layer growth rate (and the accompanying hydrogen production) slows down. The effect of this process on hydrogen production during the TMI-2 accident is discussed in Sec. III.C. Values for A and B in Eqs. (1) and (3) are given in Ref. 7 and are applicable for temperatures up to 1760 K. For temperatures between 1760 K and the Zr melting temperature, the correlation of Urbanic[13] is used in this analysis for the values of A and B in the ZrO_2 layer growth rate equation. A comparison between the steam - Zr reaction rates predicted by the MATPRO and Urbanic correlations are compared in Fig. 13, for excess steam concentrations. Possible reasons for the differences between these two correlations below 1760 K are discussed by Ocken[14], and are briefly described in Sec. III.C.1.d. In this study, the MATPRO correlation is used below 1760 K because it predicts a greater amount of hydrogen produced. Note in Fig. 13 that the Urbanic correlation predicts a jump in the reaction rate above about 1800 K. This is caused by a phase change in the ZrO_2 lattice structure near that temperature.

For completeness, the values for A and B that were used to calculate the various layer growth rates in this study are listed in Table II. While these values for the various oxygen-stabilized alpha-Zr layer growths are strictly applicable only up to 1760 K, they will be used as best-estimate values in the MIMAS code up to the Zr melting temperature until better data are available.

By combining Eqs. (2) and (3), the H_2 production rate from Zircalloy oxidation as a function of temperature is calculated in MIMAS. This H_2 is added to the gas fluid field by a mass transfer function, which is described in Sec. II.B.3.

Since the brittleness of the beta-Zr is correlated with its oxygen content, it is necessary to calculate the rate of oxygen diffusion into the beta-Zr cladding layer. In MIMAS, this is done by numerically solving the Fick's law diffusion equation for the cladding geometry,

$$dC/dt = D\, d^2C/dr^2 \quad . \tag{4}$$

Here, C is the oxygen concentration, D is the diffusion coefficient for oxygen in zirconium, t is time, and r is radial distance into the beta-zirconium layer. The value of D, as well as the exact numerical scheme for solving Eq. (4) are taken from Ref. 7. When fuel-cladding contact occurs, the boundary conditions used in solving Eq. (4) assume high oxygen concentrations on both sides of the beta-Zr layer. Otherwise, oxygen is assumed to diffuse into the beta-Zr only from the outer surface.

The correlations used in this work to describe the relationship between cladding embrittlement, oxygen content, and thermal shock loadings are given in Ref. 7. Briefly, these correlations consider two types of thermal shock loadings that were used in the associated experiments:

1. fast cooling, which is defined as a direct quench of the cladding from a temperature above the alpha-beta Zr phase transition temperature (Cooling rates of 100 K/s occur during this process); and

2. slow cooling, in which the cladding is cooled at 5 K/s to a temperature below the phase transition temperature, followed by a quench.

By carefully correlating analytical results with observed cladding behavior during these cooling rates, a set of criteria was constructed relating beta-Zr oxygen content and temperature history with breakup during cooling. It was found that under fast cooling conditions, the cladding broke up if

1. the cladding temperature ever exceeded 1700 K,

2. oxygen concentration in the beta zirconium exceeded 90% saturation, or if

3. oxygen concentration in the beta zirconium exceeded 65%, by weight.

The cladding was found to shatter under slow cooling conditions if less than 0.3 mm of cladding contained less than one weight percent of oxygen. In the TMI-2 analysis, these criteria and the calculated oxygen content of the beta-Zr cladding layer were used to determine the likelihood of fuel-rod breakup during the core reflood.

II.A.2.c. Fission Product Release Models. An important consequence of the loss of fission products during degraded core accidents is their potential for escape from the reactor containment to the environment and the attendant health hazards associated with such release. To evaluate such a fission product escape potential, a three-stage modeling approach is used in MIMAS; namely,

1. a release model, to predict the release of the radiologically important nuclides from the core fuel rods;

2. a transport model, to predict the mobility of such released nuclides from the core region to the ex-core primary system; and

3. a deposition model, to account for the holdup of various nuclides in the core region due to interactions with structure surfaces.

This section of the report deals with the release model only; fission product transport and deposition are discussed in Sec. II.B.

As discussed in Ref. 15 recent analysis of the consequences of a core meltdown accident indicates that relatively few fission product species are responsible for the radiological health effects associated with such accidents, most notably iodine (I), cesium (Cs), tellurium (Te), and the noble gases xenon (Xe) and krypton (Kr). Iodine is of primary importance since it contributes roughly one-half of the dose resulting in early fatalities. Cesium isotopes have a strong influence on the calculated property damage, but have a smaller, though still important, impact on health effects. In addition, Cs is a carrier for iodine and thus of importance with respect to estimation of iodine release. Te is highly volatile (boiling temperature at 1 atm ≈1285 K) and a precursor of I and Cs. The noble gases Xe and Kr are also of importance because they are gaseous at core temperatures and because they can be expected to be almost entirely released from any fuel debris in a meltdown accident.

Although other chemical species are of radiological, carcinogenic, and toxic importance (e.g., strontium, ruthenium, plutonium, etc.), because of a greater potential for holdup in the fuel debris and primary system, their influence on release evaluation is of lesser importance. Thus, for simplification purposes, only I, Cs, Te, Xe, and Kr are considered in the

present preliminary modeling effort concerning fission product release and transport phenomena. The primary nuclides of each of these chemical species are considered in the present analysis, by lumping into a single effective nuclide.

Essentially five principal mechanisms control the rate of release of fission products from LWR fuel under accident conditions. They are

1. burst release,

2. diffusional release of the pellet-to-cladding gap inventory,

3. grain boundary release (intergranular),

4. diffusion from the UO_2 grains (intragranular), and

5. release from molten material.

Each mechanism becomes dominant at a successively higher temperature. The burst release occurs as a consequence of rod cladding rupture. When the cladding ruptures, the entire amount of noble fission gases previously accumulated in the plenum and in the open voids in the fuel rod can be assumed to be released.

Cesium and iodine are also released when the fuel rod ruptures, but the quantity carried out with the vented gases is considerably less than for the noble fission gases. The burst release of Cs and I depends upon the fuel rod temperature, the total volume of gas vented, and the amount of Cs and I initially in the gap space.

Following the burst release, the amount of Cs and I remaining in the gap space will diffuse out of the rupture opening. This diffusional escape of the gap contents is a slow process and is quantitatively considerably smaller than the burst release.

Beginning at ~1350 C, fission gases, Cs, and I, previously accumulated at the grain boundaries, are released via a grain boundary diffusion mechanism. Higher temperatures are probably required for low burnup fuel in which the concentration of fission products is lower. The mechanism is driven by the formation, swelling, and coalescence of bubbles of fission gases.

At completion of the burst release, diffusional escape of the gap inventory, and release of the grain-boundary inventory, ~60 - 90% of the noble fission gases, Cs, and I remain in the UO_2 grains. Subsequent release then occurs via solid state diffusion from the interior of the UO_2 grains, which increases with the square root of time. Such intragranular release is insignificant at cladding burst temperatures (750-1100 C), but the fractional release rate doubles approximately every 100 C, so that by 2000 C the fraction of remaining inventory released is about 10%/min for fission gas, Cs, and I.

The fifth major release mechanism is escape from molten fuel, which is due to increased bubble or solid inclusion mobility in molten UO_2. The details of the melting process are complex and imperfectly understood, partly because chemical transformations occur simultaneously with the melting process, that altering the melting points of key materials. However, a mechanistic model for fission product release from melting fuel would be based upon (1) the vapor pressure of fission products in their appropriate chemical form and in the appropriate phase (metallic or oxidic), (2) transport effects from the melting surface to bulk of the gas phase, and (3) diffusion to the melt surface.

For whole core meltdown accidents, the release processes are even more complex. Components that can be made airborne during the in-primary-vessel phase of a meltdown accident include fission products, cladding, fuel, structure, and control rods. Cladding, structure, control rods, and fuel can be expected to exist initially as separate immiscible melt phases. However, as

oxidation progresses at higher temperatures, the oxides of the cladding, structure, and control rods can dissolve in fuel, altering the melting temperature and the vaporization rates. Because of the necessary involvement of these considerations, establishment of a single model that can successfully predict fission product release under all situations is difficult.

The original formulation in the Reactor Safety Study (WASH-1400) is still a commonly used method. In this approach, the release rate of a given fission product, x, from the molten fuel is assumed to be a constant. However, as suggested in Ref. 15, the rate of release of fission products and other aerosol materials from heated and melting fuel is modeled more accurately by assuming the release rate to be proportional to the concentration, that is,

$$dM_x/dt = -k_x(T)M_x \quad , \tag{5}$$

where M_x is the mass of species x in the mixture and k_x is a fractional release rate coefficient assumed to be a function of temperature T only. This treatment significantly improves that used in WASH-1400 in that fission product releases from the fuel may now be related to core heat-up time.

Based upon this approach, the explicit model for fission product release from fuel used in the MIMAS code is,

$$dM_x^n/dt = -k_x(T)M_x^{n-1} \quad , \tag{6}$$

where n is a time step designator and dM_x^n/dt is the rate of release of fission products from heated fuel. For calculation, the fractional release coefficients can be approximated by equations of the form

$$k(T) = Ae^{BT} \quad , \tag{7}$$

where the constants, A and B, are different for each element. The appropriate constants for several volatile species are given in Table III. The total fission product release from the disrupted core is then the sum of the releases of the different constituents, from the various finite regions of the core, which for MIMAS are noded based on temperature considerations. Thus, to determine the total fission product mass released, it is necessary to specify only the inventories of each element at the time of accident initiation.

Until the time of rod disintegration, the MIMAS code considers the actual fission product injection into the gas fluid field to occur only at the location of cladding rupture. An option exists in MIMAS to have fission products released from the entire length of the rod (high fission product mobility through the gap) or only from the fuel adjacent to the cladding rupture (zero fission product-gap mobility). For the TMI-2 analysis, the high fission product-gap mobility option was used. The fission-product total mass is added to the gas fluid field by means of a mass transfer function as described in Sec. II.B.3.

After rod disintegration, the resulting debris is assumed to be rapidly quenched so that fission product high-temperature-release from the debris is negligible. If necessary, this assumption will be modified as available data indicates.

II.A.2.d. Control Rod Meltdown Models. The MIMAS code currently contains models for the degraded core behavior of stainless-steel cladding, AgInCd absorber control rods contained in a Zircalloy guide tube. Until recently, these control rods were considered rather passive elements during the core heatup and meltdown phase of a degraded core accident, with their only effect perhaps being the generated heat and hydrogen due to oxidation of the guide tubes. However, experiments conducted at ORNL[16,17] to address aerosol release

and transport of vaporized core components have exhibited interesting control rod disintegration phenomena and interaction of control rod materials with fuel rods. These tests were bench-type experiments, where a centrally-located control rod was surrounded by Zircalloy-clad UO_2 fuel rods. Induction heating was employed to induce control rod melting. A pyrometric view port was used to obtain a temperature signature of the control rod relocation behavior.

In one test, the assembly was heated slowly in a steam environment over a period of 7-1/2 minutes, to a maximum temperature of about 1800 C. Post-test examination revealed a free standing fuel column remaining with essentially all of the metallic components candled to the bottom of the test section. Analysis of the aerosol yield showed that it consisted of about 6.5% of the cadmium and 0.35% of the silver. No other constituents were detected.

In another test, an extended core melt experiment was conducted. Here the test bundle was subjected to an incremental increase in temperature. At a bundle average temperature of 2400 C, the post-test debris indicated complete meltdown of the fuel rods via liquefaction induced by control rod melt attack. The end result was complete fuel rod disintegration, with a solidified fuel-rod debris located at the bottom of the test section. Such results, if extrapolated to the TMI-2 accident, would indicate severe core disintegration if a 2400 C temperature had been reached, and may significantly impact core meltdown phenomena and modeling efforts for reactors which employ AgInCd control rods.

To cause such severe control-material induced damage, the following event sequence is postulated: The AgInCd alloy (which melts at 1070 K) is contained within the stainless steel cladding until the cladding melts at 1700 K. The pressure of the contained Cd vapor then sprays the molten control material out through the cladding break, the perforated guide tube, and over the surrounding fuel rods. The high soluability of Zr in Ag and In at these temperatures[19,20]

causes the Zircalloy cladding to dissolve in the molten control material and drain to the lower portion of the rods.

Whether or not this sequence would occur during an actual LWR degraded core accident is open to question: the ambient pressures, temperatures, and Zircalloy oxidation state in the reactor core may be different from the test conditions. Thus, in MIMAS, a user specified choice of control rod meltdown models is provided, namely:

CRMELT - A Control Rod MELTdown model, with liquefied AgInCd described in terms of melt relocation and resolidification, and where eutectic formation and phase interaction with adjacent fuel rods is ignored; and

CRFRI - A Control Rod/Fuel Rod Interaction model, where material phase interaction between molten AgInCd and adjacent fuel rods is considered in the modeling of molten AgInCd relocation and resolidification.

For both of these options, temperature is considered the dominating parameter for control rod meltdown behavior, so the following thermal conditions govern the modeling approach:

1. Uniform Temperature - The temperature of the AgInCd absorber material, stainless-steel cladding, and Zr guide tube are considered uniform within the

entire core cell and taken as equal to the local steam temperature.

2. Melt Temperatures - The melting points of the various constituents (median value of the solidus- liquidus) are:

T_m (AgInCd) = 1070 K,

T_m (stainless-steel) = 1700 K.

3. Zr Guide Tube - The beta-to-alpha and ZrO_2 oxidation products are modeled in a manner similar to the fuel rod cladding oxidation. However, the effect of reaction heat on AgInCd temperature is ignored; thus, the guide tube temperature is specified by the local steam temperature.

For the assumed condition of uniform temperature, complete melting of the AgInCd absorber material (T_m = 1070 K) is predicted prior to melting of the stainless steel cladding (T_m = 1700 K). However, until cladding rupture occurs via melting, the molten AgInCd is assumed to remain "bottled" within the intact cladding. This assumption is supported by studies of the Ag-Fe system that indicate that Ag and Fe are immiscible in the liquid state and therefore exclude alloyability (see Refs. 19, 20) and low temperature eutectic formation. Cladding rupture via melting can therefore be expected to occur at or near the stainless-steel melt temperature. For the present, the cladding melt criterion is considered the predominant mode of cladding failure. For the core axial cell

where the cladding melting point is first predicted, local cladding failure is assumed, at which time release of the "bottled" molten AgInCd within that cell and above cells (which contain molten AgInCd) occurs. This breach/release mode is one of catastrophic failure, where no resistance to molten AgInCd release is offered by either the cladding or guide tube.

In the CRMELT option, upon control rod cladding failure, the mass of the molten control material, cladding, and guide tube are transferred to the debris field by means of a mass transfer function such as that discussed in Sec. II.B.3. No further interactions of the molten control material with surrounding fuel rods is considered. In the CRFRI option, upon control rod cladding failure the molten AgInCd is assumed to be sprayed efficiently over the fuel rods at the axial location where the failure occurs. At the time of control rod failure complete melting of the fuel rod Zr-cladding is assumed, resulting in a free-standing fuel column stripped of Zr. The resultant Ag-In-Zr eutectic is placed in the debris fluid field (by means of a mass transfer function) for relocation analysis.

Preliminary examination of the TMI-2 core debris (filter samples) has shown no solid evidence of Ag-Zr or In-Zr alloy. Thus, in this analysis of the TMI-2 accident, the CRMELT option was used to describe control rod melt behavior.

II.A.2.e. Fuel-Cladding Liquefication Phenomena. When the material between the ZrO_2 layer and the fuel pellet melts, the molten cladding can dissolve a portion of the UO_2 pellet and form "liquefied fuel". The subsequent behavior of the section of the fuel rod containing liquefied fuel is a function of the prior history of the rod, and is generally known only qualitatively. However, since the behavior of fuel rod sections containing liquefied fuel is important to the overall reactor response to a degraded core accident,

best-estimate models for liquefied fuel phenomena are included in MIMAS, with the understanding that these models will be updated as soon as pertinent data are available.

In the MIMAS models for liquefied fuel phenomena, the oxide layer existing on the cladding outer surface is assumed to contain the molten cladding/liquefied fuel until the dissolution of the UO_2 in the available molten cladding is complete. The solubility of UO_2 in the molten cladding is given by the Zr-UO_2 binary phase diagram shown in Fig. 14, which is based on data by Politis[21]. In this diagram, the variation in the melting point of zirconium with oxygen content is represented by the solid and dashed phase boundaries between zero and 0.05 UO_2 mole fraction and 2100 to 2200 K. In MIMAS, if the fuel and cladding are in contact, the cladding is assumed to contain sufficient oxygen to elevate its melting point to 2200 K. Also, the melting of the U-Zr metallic layer shown in Fig. 12, which occurs far below 2200 K, is not modeled. The liquidus temperature increases with increasing UO_2 mole fraction up to approximately 2670 K, above which two liquid phases are formed. Above this temperature, the melting point of zirconium dioxide is approached, so the initial assumption of a containing ZrO_2 layer is no longer valid.

Heat-of-fusion effects are included in MIMAS for the melting of the non-oxidized cladding, but the heat of solution of UO_2 in molten Zr is not known and is not included at this time. Given a volume of molten Zr in a particular cladding element and the temperature of that element, the data in Fig. 14 are used by MIMAS to calculate the fraction of the pellet radius that would dissolve in the molten cladding at equilibrium. The rate at which the melt front advances into the UO_2 pellet from the original fuel-cladding interface is calculated with the equation

$$\Delta R = [1.634 \times 10^{-26} \exp (1.66 \times 10^{-2} T)\, \Delta t + \Delta R_o]^{1/2} \quad , \qquad (8)$$

where

ΔR = distance traveled by liquefied fuel interface into the fuel pellet during a time step (m),

T = absolute temperature of melt (K),

Δt = time step length (s), and

ΔR_o = liquefied fuel interface distance into fuel pellet at beginning of time step (m).

This equation was formulated by Turk[22], with data for determining the values of the constants provided by Hagen[8]. Thus, by combining the data of Fig. 14 with the melt front velocity Eq. (8) and the temperature and molten cladding volume of the rod segment, the liquefied fuel volume in the cladding segment can be calculated as a function of time.

The behavior of fuel rod segments containing liquefied fuel varies strongly with prior rod history. Experimental observations of Hagen[8] indicate the following scenarios:

1. With rapid fuel rod heatup rates, the ZrO_2 cladding layer is relatively thin when the liquefied fuel forms. The volume expansion of the liquefied fuel apparently breaks up the ZrO_2 layer, followed by downward relocation of the liquefied fuel and ZrO_2 fragments. An atrophied fuel pellet stack may remain behind.

2. With moderate fuel rod heating rates, the ZrO_2 cladding layer is somewhat thicker and stronger during the liquefied fuel formation. The liquefied fuel leaks out and downward through perforations in the oxide layer, leaving behind an intact, but badly damaged, fuel rod structure.

3. With low fuel rod heating rates, the oxide cladding layer becomes thick enough to contain the liquefied fuel, so that the oxidized fuel rod remains intact throughout the transient.

These observations are somewhat more quantitatively expressed in the results of a later series of experiments[23] shown in Fig. 15. This figure shows the cladding temperature histories for four simulated fuel rods, electrically heated in steam at different power levels. In the initial part of the curves, the heating is due to the electrical power input only; above approximately 1600 C, the heat of reaction of the Zr oxidation causes an increase in the cladding temperature ramp rates. Liquefied fuel formed in all four tests; in the test with the two lower initial temperature ramps, the liquefied fuel was contained within the oxide cladding shells. The two more rapidly heated rods broke apart after liquefied fuel formation. The temperature ramp rate (below 1600 C) below which the rods remained intact equals approximately 1 K/s.

One extremely important result of liquefied fuel formation illustrated in Fig. 15 is the sudden decrease in cladding temperature. As shown in Fig. 15, this temperature drop begins when the peak cladding temperature reaches between 1950 C and 2150 C, which is well within the range of liquefied fuel formation. Throughout this cladding temperature drop, the electrical power input to the rod was actually increased, so the cause of the drop had to be a decrease in the cladding oxidation rate. It is presently unknown if this decrease in the cladding oxidation rate at high temperatures is due to the formation of liquefied fuel, or whether the molten cladding simply drained to a cooler section of the rod.

As discussed in Sec. III of this report, the cladding temperature rise rates during the TMI-2 accident were less than 1 K/s. Therefore, it is expected that the oxidized fuel rods in TMI-2 remained intact until reflood, even if some liquefied fuel formation actually occurred. In the MIMAS model for the rod behavior under these conditions, the cladding oxidation rate is decreased exponentially after liquefied fuel begins to form, with a time constant equal to about 10 min. This results in cladding temperature decay profiles similar to those shown in Fig. 15.

II.A.2.f. Fuel Rod Disintegration and Debris Formation. As noted above, the fuel rod heating rates prior to significant oxidation heating in the TMI-2 accident were sufficiently low that the oxidized cladding is estimated to remain intact until reflood. Upon reflood, those cladding sections that met the fast and/or slow cooling embrittlement criteria given in Sec. II.B.2.b were assumed to break up directly into debris.

For the "best estimate" TMI-2 analysis, the breakup of the embrittled rod sections is calculated to occur when the cladding cooling rate equaled either 5 or 100 K/s, depending on the embrittlement level of the cladding. The resulting rod fragments are transferred into the debris field using the time-dependent, mass transfer function described in Sec. II.B.3. This mass transfer function is an exponentially increasing/decreasing function, which for the debris transfer is assumed to have 10 s time constant. The fraction of the debris mass which consists of unoxidized Zircalloy is also calculated.

The size distribution of the debris particles from the disintegrated fuel rods are of great interest in determining debris bed configuration and behavior. This particle size distribution is probably a function of cladding oxygen content, the fuel rod cooling rate, liquefied fuel volume, burnup, and others. Further data on the relation between these factors and debris particle sizes

should be forthcoming from upcoming experiments at Sandia National Laboratory, KfK, and Idaho National Engineering Laboratory.[24,25,26] As a best-estimate particle size distribution for the TMI-2 analysis, data from a series of tests performed at KfK were used.[27] The composite disintegrated fuel particle size distribution from these tests is shown in Fig. 16. This figure shows a significant particle size range between 0.1 and 4 mm, with the maximum fraction of particles having a significant dimension between 2 and 2.5 mm.

II.A.2.g. Fuel Rod Temperature Analysis Model. Subroutine TEMCALC, which is called from subroutine INTACT (see Fig. 3), solves for the temperature field in intact and ballooned fuel rod elements based on a one-dimensional radial finite-difference approximation to the general conduction equation,

$$\frac{1}{r}\left[\frac{\partial}{\partial r}\left(r\,k\,\frac{\partial T}{\partial r}\right)\right] + q''' = \rho c_p \frac{\partial T}{\partial t} \quad . \tag{9}$$

The finite difference equations are solved in a conservative manner, sequencing from left to right, where the left boundary corresponds to the smallest radius.[6] Nodal points are positioned on material interfaces and material properties are evaluated between nodes (see Fig. 17).

For the innermost fuel pellet node (i=1), the finite difference equation is

$$-\left[\frac{r_{3/2}\,k_1}{\Delta r_1} + \frac{1}{2}\left(r_1\,\Delta r_1 + \frac{\Delta r_1^2}{4}\right)\frac{(\rho c_p)_1}{\Delta t}\right] T_1^{n+1} + \frac{r_{3/2}\,k_1}{\Delta r_1}\,T_2^{n+1}$$

$$= -\frac{1}{2}\left(r_1\,\Delta r_1 + \frac{\Delta r_1^2}{4}\right)\left[\frac{(\rho c_p)_1}{\Delta t}\,T_1^n + q_1'''^{n+1}\right] \quad , \tag{10}$$

with the boundary condition

$$- rk \frac{dT}{dr}_{i=1} = 0 \qquad (11)$$

at the pellet inner radius surface. In these equations,

k_i = material thermal conductivity in node i,

$(\rho c_p)_i$ = product of material density and specific heat in node i,

q_i''' = internal heat generation in node i,

Δt = time step size,

n = time step level, i.e., n = present time, n+1 = present time + Δt, and

T_i = temperature of node i.

For interior nodes ($1 < i < NF$) in the fuel pellet, the finite-difference equation is

$$\frac{r_{i-1/2}\, k_{i-1}}{\Delta r_{i-1}} T_{i-1}^{n+1} - \left\{\frac{r_{i-1/2}\, k_{i-1}}{\Delta r_{i-1}} + \frac{r_{i+1/2}\, k_i}{\Delta r_i} + \frac{1}{2\Delta t}\left[\left(r_i\, \Delta r_{i-1} - \frac{\Delta r_{i-1}^2}{4}\right)(\rho c_p)_{i-1} + \left(r_i\, \Delta r_i + \frac{\Delta r_i^2}{4}\right)(\rho c_p)_i\right]\right\} T_i^{n+1} + \frac{r_{i+1/2}\, k_i}{\Delta r_i} T_{i+1}^{n+1}$$

$$= -\frac{1}{2}\left(r_i\, \Delta r_{i-1} - \frac{\Delta r_{i-1}^2}{4}\right)\left[\frac{(\rho c_p)_{i-1}}{\Delta t} T_i^n + q_{i-1}'''^{,n+1}\right] + \left(r_i\, \Delta r_i + \frac{\Delta r_i^2}{4}\right)\left[\frac{(\rho c_p)_i}{\Delta t} T_i^n + q_i'''^{,n+1}\right], \qquad (12)$$

where NF is the number of nodes in the fuel.

The gap that exists between the fuel and the cladding in fuel rods is treated by explicit noding on fuel and clad surfaces and a heat-transfer coefficient between these nodes. Stored energy and internal heat generation in the gap region are neglected. The finite difference equation for the outermost fuel pellet node (i=NF) is

$$\frac{r_{NF-1/2}\ k_{NF-1}}{\Delta r_{NF-1}}\ T_{NF-1}^{n+1} - \left[\ \frac{r_{NF-1/2} k_{NF-1}}{\Delta r_{NF-1}} + r_{NF}\ h_{gap}\right.$$

$$\left. + \frac{1}{2}\left(r_{NF}\ \Delta r_{NF-1} - \frac{\Delta r^2_{NF-1}}{4}\right)\ \frac{(\rho c_p)_{NF-1}}{\Delta t}\right]\ T_{NF}^{n+1} + r_{NF}\ h_{gap}\ T_{NF+1}^{n+1}$$

$$= -\frac{1}{2}\left(r_{NF}\ \Delta r_{NF-1} - \frac{\Delta r^2_{NF-1}}{4}\right)\ \left[\ \frac{(\rho c_p)_{NF-1}}{\Delta t}\ T_{NF}^{n} + q'''^{n+1}_{NF-1}\right]\ , \quad (13)$$

and the boundary condition at the outer pellet surface is

$$-\ k\ \frac{dT}{dr}_{i=NF} = h_{gap}\ (T_{NF} - T_{NF+1})\ . \quad (14)$$

Here, h_{gap} is the conductance of the pellet-cladding gap (or contact surface). The method used for determining the magnitude of h_{gap} is discussed in the next section.

In the cladding region, the internal heat generation rate is redefined to include metal-water reaction and radiation heat transfer when appropriate. For the innermost cladding node (i=NF+1), the finite difference equation is

$$r_{NF+1}\, h_{gap}\, T_{NF}^{n+1} - \left[r_{NF+1}\, h_{gap} + \frac{r_{NF+3/2}\, k_{NF+1}}{\Delta r_{NF+1}} \right.$$

$$\left. + \frac{1}{2} \left(r_{NF+1}\, \Delta r_{NF+1} + \frac{r_{NF+1}^2}{4} \right) \frac{(\rho c_p)_{NF+1}}{\Delta t} \right] T_{NF+1}^{n+1} + \frac{r_{NF+3/2}\, k_{NF+1}}{\Delta r_{NF+1}} T_{NF+2}^{n+1}$$

$$= - \frac{1}{2} \left(r_{NF+1}\, \Delta r_{NF+1} + \frac{\Delta r_{NF+1}^2}{4} \right) \left[\frac{(\rho c_p)_{NF+1}}{\Delta t} T_{NF+1}^{n} + q'''^{n+1}_{NF+1} \right] . \quad (15)$$

Eq. (14) and the finite difference equation for interior cladding nodes (NF+1) < i < N is identical to Eq. (12). For the outermost cladding node (i=N), the finite difference equation is

$$\frac{r_{N-1/2}\, k_{N-1}}{\Delta r_{N-1}} T_{N-1}^{n+1} - \left[\frac{r_{N-1/2}\, k_{N-1}}{\Delta r_{N-1}} \right.$$

$$\left. + \frac{1}{2} \left(r_N\, \Delta r_{N-1} - \frac{\Delta r_{N-1}^2}{4} \right) \frac{(\rho c_p)_{N-1}}{\Delta t} + f_{ss}\, r_N\, (h_\ell + h_g) \right] T_N^{n+1}$$

$$= - \frac{1}{2} \left(r_N\, \Delta r_{N-1} - \frac{\Delta r_{N-1}^2}{4} \right) \left[\frac{(\rho c_p)_{N-1}}{\Delta t} T_N^n + q'''^{n+1}_{N-1} \right]$$

$$+ r_N \left[h_\ell \left(f_t\, T_N^n - T_\ell^{n+1} \right) + h_g \left(f_t\, T_N^n - T_g^{n+1} \right) \right] , \quad (16)$$

with the boundary condition at the outer surface given by

$$- k \left. \frac{dT}{dr} \right|_{i=N} = h_\ell \left(T_N - T_\ell \right) + h_g \left(T_N - T_g \right) , \quad (17)$$

where

h_ℓ = heat transfer coefficient to liquid,

h_g = heat transfer coefficient to gas,

T_ℓ = liquid temperature,

T_g = gas temperature,

f_{ss} = steady-state flag (1 for steady-state calculation, 0 otherwise), and

f_t = transient flag (1 for transient calculation, 0 otherwise).

Note that for a steady-state calculation, $f_{ss} = 1$ and $f_t = 0$ a fully implicit form is used. Under transient conditions, $f_{ss} = 0$ and $f_t = 1$ a semi-implicit form is obtained.

Equations (10), (12), (13), (15), and (16) can be written in the familiar tridiagonal form for the nodal temperatures T_i^{n+1} [28]:

$$\begin{aligned} a_1 T_1^{n+1} + b_1 T_2^{n+1} &= d_1 \\ a_2 T_1^{n+1} + b_2 T_2^{n+1} + c_2 T_3^{n+1} &= d_2 \end{aligned} \tag{18}$$

$$\begin{aligned} a_{N-1} T_{N-1}^{n+1} + b_{N-1} T_{n-1}^{n+1} + c_{N-1} T_N^{n+1} &= d_{N-1} \\ b_N T_{N-1}^{n+1} + c_N T_N^{n+1} &= d_N \end{aligned}$$

The system of equations (18) can be solved for the temperatures T_i^{n+1} by a variety of methods. MIMAS uses a special tridiagonal matrix inversion scheme.

II.A.2.h. Materials Properties, Gap Conductance, and Cladding Stress. This section discusses a number of models whose results are used by various subroutines called from INTACT. Most of the material property models are for thermal properties, and therefore supply values for the finite-difference equations in the TEMCALC routine. Other models for fission gas release,

cladding plenum pressure, and differential fuel-cladding expansion are used to calculate fuel-cladding gap conductance and cladding stress.

Models for the fuel and cladding material thermal properties in MIMAS are from Ref. 7. The models for UO_2 and Zircalloy cover a temperature range extending beyond the material melting points. The thermal conductivity for ZrO_2 as a function of temperature was also taken from Ref. 7; the specific heat and density of ZrO_2 used in MIMAS were derived from data given in Ref. 29. The effects of the heat of fusion of Zircalloy is approximated in the TEMCALC analysis by assigning an artificially high specific heat to the cladding when the melting point is reached. This artificial specific heat equals one tenth of the Zircalloy heat of fusion. When the molten Zircalloy (with the high specific heat) reaches a temperature 10 K above the melting point, the actual molten Zircalloy specific heat value from Ref. 7 is used. Best-estimate values for the thermal properties of liquefied fuel are assumed to equal the median between the corresponding molten zirconium and molten UO_2 values.

To calculate the size of the fuel-cladding gap, the differential fuel-cladding expansion is calculated in MIMAS using the models from Ref. 7 for fuel and cladding thermal expansion and fuel-fission-product swelling as a function of temperature. Once the gap size is calculated, subroutine GAPCON calculates the gap heat-transfer coefficient (h_{gap}) as a function of three components: gap gas conductance, fuel-clad interfacial contact, and fuel-clad thermal radiation. The equation used is

$$h_{gap} = h_{gas} + h_{radiation} \quad , \qquad (19)$$

where

$$h_{gas} = k_{gas}/(r_{gap} + \delta) \quad , \tag{20}$$

$$h_{radiation} = \frac{\sigma F \left(T_f^4 - T_c^4\right)}{(T_f - T_c)} \quad , \tag{21}$$

and

$$F = 1/[\ 1/\varepsilon_f + (R_f/R_c)(1/\varepsilon_c - 1)] \quad . \tag{22}$$

Subscripts f and c refer to fuel and clad, respectively, σ is the Stefan-Boltzman constant, and the quantity F is the inner to outer cylinder view factor. A value of 4.4×10^{-6} m is used for δ, which includes the mean surface roughness of the fuel and clad and the temperature distances. The values for k_{gas} are calculated from the GTHCON model in Ref. 7.

The amount of fission product gas released from the fuel is calculated with the FGASRL model of Ref. 7. To calculate the total gas pressure in the fuel rod, the MIMAS code adds this released fission gas to the initial rod fill gas, which ranges in pressure at room temperature from 25 to 42 atm.[3] The fuel - rod gas pressure is calculated as a function of time calculated with the perfect gas law. The cladding stress is calculated with the thin cylinder formula

$$s = \frac{Pd}{2t} \quad , \tag{23}$$

Where, s is the cladding stress, P is the difference between the rod internal gas pressure and the coolant pressure, d is the mean rod diameter, and t is the beta-zirconium layer thickness. Cladding stress caused by fuel-cladding contact is not considered in MIMAS at present. Whenever the fuel outer diameter is

calculated to be greater than the cladding inner diameter, the cladding is assumed to be pushed out by the fuel.

II.B. Fluid Dynamics

The fluid dynamic modeling and methods described in this section are based upon those of the TRAC-PF1[6] computer code development effort. The form of the conservation equations and the solution techniques used in MIMAS are straightforward extensions of those in TRAC that have undergone many man-years of evolution. Although this section will briefly describe the fluid dynamics used in MIMAS, the interested reader is referred to Ref. 6 for more detail.

II.B.1. Conservation Equations

The fluid-dynamic conservation equations currently being solved in the MIMAS code are a one-dimensional version of the following general form

$$\frac{\partial(\alpha\rho)}{\partial t} + \nabla\cdot(\alpha\rho\vec{v}) = \sum \Gamma_j \quad , \tag{24a}$$

$$\alpha\rho\left[\frac{\partial\vec{v}}{\partial t} + \vec{v}\nabla\vec{v}\right] = -\alpha\nabla P - \sum\vec{f}_j - \alpha\rho g \quad , \text{ and} \tag{24b}$$

$$\frac{\partial(\alpha\rho e)}{\partial t} + \nabla\cdot(\alpha\rho e\vec{v}) = -P\left[\frac{\partial\alpha}{\partial t} + \nabla\cdot(\alpha\vec{v})\right] + \sum[q + \Gamma h]_j \quad . \tag{24c}$$

Eqs. (24a) through (24c) conserve mass, momentum, and internal energy, respectively. In these equations the symbols are defined as follows:

α = volume fraction,

ρ = material density,

$\vec{v}$ = velocity vector,

t = time,

$\nabla\cdot$ = divergence operator,

∇ = gradient operator,

g = gravitational acceleration,

Γ_j = mass source or sink function j,

P = total static pressure,

$\vec{f}_j$ = friction force vector j,

e = material internal energy,

q_j = heat transfer j,

h_j = material enthalpy j, and

$\sum$ = summation symbol over index j.

Table IV itemizes the materials that are conserved in the fluid-dynamics solution; that is, a continuity equation of the form of Eq. (24a) is solved for each of the twelve materials listed in Table IV. The third column of this table indicates the field of motion of each material and the fourth column indicates the energy field associated with each material. Currently, a motion equation of the form of Eq. (24b) is solved for each of the three fields: gas, water, and corium. Also an energy equation of the form of Eq. (24c) is solved for each of the same three fields. In other words, materials 1 - 7 are combined to form the gas field, for which motion and energy conservation is performed. For the same purpose, material 8 forms the water field, and materials 9 - 12 are combined to form the corium field.

The dependent variables being solved for within the MIMAS fluid-dynamics are: three volume fractions (α_{gas}, α_{water}, α_{corium}), three velocities (v_{gas}, v_{water}, v_{corium}), three temperatures (T_{gas}, T_{water}, T_{corium}), a total pressure (P), a hydrogen partial pressure (P_H), five fission-product densities (ρ_I, ρ_{Cs}, ρ_{Kr}, ρ_{Xe}, ρ_{Te}), and four fuel-rod/structure densities (ρ_{UO_2}, ρ_{Zr}, ρ_{ZrO_2}, ρ_{steel}). This is a total of twenty unknowns that are solved for using eighteen

conservation equations, appropriate equations of state, phase-change relationships, constitutive equations for friction and heat-transfer coefficients, and the following constraints on volume fractions and partial pressures:

$$1 = \alpha_{gas} + \alpha_{water} + \alpha_{corium}; \text{ and} \tag{25a}$$

$$P = P_{steam} + P_H + \sum P_{FP_j} \quad . \tag{25b}$$

Equation (25a) conserves total volume, and Eq. (25b) sums all the partial pressures to form the total pressure.

II.B.2. Constitutive Equations

For the solution of Eqs. (24), relationships for the friction forces ($\vec{f}_j$) and heat fluxes (q_j) that exist between the various fluid materials and structures are needed. In particular, resistance and heat-transfer coefficients are needed for the six fluid-structure combinations;

1. gas and water,
2. gas and structure,
3. water and structure,
4. water and corium,
5. gas and corium, and
6. corium and structure.

The actual values of these coefficients are of course geometry and flow regime dependent.

The friction force is defined in MIMAS as

$$\vec{f} = F_{geom}\ \alpha\rho\ C_f\ \Delta V\ |\Delta V|\ \hat{k}, \tag{26}$$

where F_{geom} is a geometry factor (for example, F_{geom} is $\frac{1}{2D_H}$ for internal-flow wall friction, where D_H is a hydraulic diameter), $\alpha\rho$ is a macroscopic density, C_f is a friction factor or drag coefficient, ΔV is a relative velocity, and $\hat{k}$ is a unit vector pointing in the axial direction. The main difficulty is obtaining the resistance coefficients, C_f, for the six combinations.

The procedure and software for determining the resistance coefficients for the first three combinations have been extracted directly from the TRAC-PF1 code. The interested reader is referred to Ref. 6 for the details. The resistance coefficient for the fourth combination is determined using drag coefficient correlations for a sphere moving in an infinite medium of water[30]; this assumes the corium field consists mainly of solid particles or molten droplets. The resistance coefficient for the fifth combination is assumed to be zero, thus neglecting the friction of solid particles and molten material falling through a gas environment. The resistance coefficient for the sixth combination is assumed to be zero when the corium field consists mainly of solid particles, or is determined by a correlation for boundary layer flow on a vertical flat plate[30] when the corium field consists mainly of molten material draining down the sides of fuel rods or other structure surfaces.

The heat fluxes are defined in MIMAS with the familiar form:

$$q = Ah\Delta T, \tag{27}$$

where A is the heat-transfer area, h is the heat-transfer coefficient, and ΔT is a temperature difference. Again, the main difficulty is obtaining heat-transfer coefficients for the six fluid-structure combinations. Predictably, this process is similar to the above determination of resistance coefficients.

The procedure and software for determining heat-transfer coefficients for the first three combinations is again extracted directly from the TRAC-PF1 code (see Refs. 6 and 31 for details). The heat-transfer coefficient for the fourth combination is determined using a correlation for a sphere moving in an infinite medium of water[32]. This correlation assumes the corium field to consist of solid particles or molten droplets. The heat-transfer coefficient for the fifth combination is determined in a similar fashion to the fourth combination; a sphere falling in an infinite medium of gas[32]. The heat-transfer coefficient for the sixth combination is assumed to be zero when the corium field consists mainly of solid particles, or determined by a correlation for boundary layer flow on a vertical flat plate[32] when the corium field consists mainly of molten material draining down the sides of fuel rods or other structure surfaces.

II.B.3. Mass-Transfer Functions

Before the conservation Eqs. (24) can be solved, mass-transfer functions (Γ_j) are needed to describe the loss and gain of mass that occurs during phase change, chemical reactions, or material fragmentation. For example, there is an injection of hydrogen into the gas field during the process of cladding oxidation, and a corresponding loss of water vapor from the steam component of the gas field. This H_2 gain and H_2O loss is accounted for in the conservation equations by the mass-transfer functions Γ_j.

At the present time there are a total of eleven mass-transfer functions existing in the MIMAS conservation equations. These are:

1. H_2O vaporization and condensation,

2. H_2 generation due to metal oxidation,

3. H_2O vapor loss due to metal oxidation,

4. debris generation due to fuel rod fragmentation,

5. control rod melting and freezing,

6. fission product release from the fuel,

7. fission-product deposition on structure surfaces,

8. inconel grid-spacer melting and freezing,

9. stainless-steel melting and freezing,

10. zirconium melting, freezing and oxidation, and

11. oxide (UO_2 and ZrO_2) melting and freezing.

The mathematical form for each of these mass-transfers (Γ_j) is described next.

The form of the mass transfer function that models H_2O vaporization and condensation is discussed in detail in Ref. 6 and will not be repeated here. The parameters which determine the H_2, H_2O, and Zr mass transfers associated with the metal-oxidation reaction, and the fission-product release from failed fuel rods are both discussed in Sec. II.A. The fission-product deposition of CsI and I on structure surfaces has the form[33]

$$\Gamma_i = Av_{di}\rho_i \ , \tag{28}$$

where i = Cs or I, A is the structure surface area exposed to Cs and I, V_{di} is

the diffusion velocity of Cs or I toward the structure surface, and ρ_I is the density of Cs or I in the gas field of the fluid dynamics.

The remaining mass transfers that deal with fragmentation or melting/freezing all have the form

$$\Gamma = 2\mu m_o e^{-\mu\tau} (1-e^{-\mu\tau}), \tag{29}$$

where μ is a time constant that determines the rate at which the mass transfer takes place, m_o is the quanity of mass in a two-dimensional mesh cell that is involved in the mass transfer, and τ is the time elasped since the mass transfer was initiated and is also cell-dependent. For example, when the control rod mass m_o melts (at $\tau = 0$) in a particular numerical cell in the reactor core, Eq. (29) represents the mass transfer of this material into the corium field of the fluid dynamics at a rate determined by the time constant μ (typically μ is about 0.1 s^{-1}). The exponential terms in Eq. (29) represent a smoothing function; integration of Eq. (29) from zero to infinite time yields "m_o" for the right-hand-side integral.

II.B.4. Solution Techniques

The solution of the conservation equations represented by Eqs. (24) is achieved by using the stability enhancing Two-Step numerical method.[34] This method has some similarity to the historic predictor-corrector class of numerical solution techniques, and is designed to propagate the information needed for stability with minimal implicit coupling between spatial cells. The practical advantage of using the Two-Step method is its inherent ability to exceed the material Courant limit by orders of magnitude. The interested reader is directed to Ref. 34 for more detail.

Ten of the eighteen conservation equations discussed in Sec. II.B.1 are solved using the Two-Step method; these are the continuity, motion, and energy equations for the gas, water, and corium fields, and a hydrogen continuity equation. The other continuity equations for the five fission product densities and the structure materials, Zr, ZrO_2 and steel, are solved in either an uncoupled or explicit fashion external to the Two-Step method.

An additional constraint is imposed on the solution of the conservation equations to simulate the formation of debris beds. Once fragmented or molten debris is generated and begins to relocate to some level to form a debris bed, the void fraction of this material (that is, α_{corium}) is partially constrained not to exceed a maximum packing fraction in any given numerical cell. This constraint is imposed by monitoring the corium volume fraction for each cell and, when $\alpha_{corium} > \alpha_{max}$ (typically about 44%), then the appropriate corium velocity, v_{corium}, is forced to zero implying that the cell is full of debris. This action insures that a cell will not overfill, but still allows α_{corium} for the cell to change as the debris cools, melts, or fragments further.

The maximum packing fraction for a cell is determined by assuming a debris size distribution and using a mechanistic debris bed packing model[35]. This model follows the dynamics of non-random packing of fuel and control debris around and above surviving rod segments, and on top of a porous floor (such as a grid-spacer or lower support plate). The irregular shape of the debris particles is also accounted for in this model. The interested reader is referred to Ref. 35 for the details.

II.C. Radiation Heat Transfer

For a thermal-radiation heat-transfer model to be useful in an analysis of the TMI-2 accident or in the analyses of similar postulated LWR accidents in which degraded core conditions exist, the model must be able to treat a wide

variation, both temporal and spatial, of core conditions. Among the specific core conditions that must be modeled are intact geometry, partial disruption, rubble bed, slumped, and various combinations of these. Also, the model must account for absorption and emission of thermal radiation in the water, gas, and core debris that may exist in the core.

To meet these modeling objectives, a thermal-radiation heat-transfer model based on a combination of a net radiation enclosure model[36] and a flux model was developed. Each numerical cell is treated as a net radiation enclosure with internal structures and a homogeneous, non-scattering, absorbing, and emitting medium. The internal structures are modeled as surfaces that are diffuse emitters, absorbers, and reflectors. The medium components are treated as diffuse emitters and absorbers. The numerical cell boundaries are modeled as "black" surfaces that absorb all incident thermal radiation. The thermal radiation absorbed by the numerical cell boundary is treated as a directed flux that enters from the adjoining cell. The cell boundary fluxes are the means by which cell-to-cell thermal radiation heat transfer is accomplished. The model treats each numerical cell as three-dimensional, however, the coupling to adjacent cells may be one-, two-, or three-dimensional.

For an enclosure, the net radiative flux leaving surface k in the wavelength interval between λ and $\lambda + d\lambda$ is

$$dq_{\lambda,k} = dq_{\lambda o,k} - dq_{\lambda i,k} \quad , \tag{30}$$

where $dq_{\lambda o,k}$ = total radiative flux leaving surface k in the wavelength interval between λ and $\lambda + d\lambda$ and

$dq_{\lambda i,k}$ = total radiative flux incident on surface k in the wavelength interval between λ and $\lambda + d\lambda$.

Also, the total radiative flux leaving surface k in the wavelength interval between λ and $\lambda + d\lambda$ is

$$dq_{\lambda o,k} = \varepsilon_{\lambda,k}\, e_{\lambda b,k}\, d\lambda + \rho_{\lambda,k}\, dq_{\lambda i,k} \quad , \tag{31}$$

where $\varepsilon_{\lambda,k}$ = emissivity of surface k at wavelength λ,

$e_{\lambda b,k}$ = black-body emission term for surface k in the wavelength interval between λ and $\lambda + d\lambda$, and

$\rho_{\lambda,k}$ = reflectivity of surface k at wavelength λ.

Equations (30) and (31) can be combined to eliminate the $dq_{\lambda i,k}$ term. The resulting equation is

$$dq_{\lambda,k} = \frac{\varepsilon_{\lambda,k}}{\rho_{\lambda,k}} \left(e_{\lambda b,k}\, d\lambda - \frac{1}{\varepsilon_{\lambda,k}}(1 - \rho_{\lambda,k})\, dq_{\lambda o,k} \right) \quad . \tag{32}$$

If the term $dq_{\lambda i,k}$ in Eq. (30) is expressed in summation form, a second equation for $dq_{\lambda,k}$ as a function of $dq_{\lambda o,k}$ can be written. This equation is

$$dq_{\lambda,k} = dq_{\lambda o,k} - \sum_{j=1}^{N} \left(dq_{\lambda o,k}\, F_{k-j}\, \overline{\tau}_{\lambda,j-k} + e_{\lambda b,g}\, d\lambda\, F_{k-j}\, \overline{\alpha}_{\lambda,j-k} \right) \quad , \tag{33}$$

where F_{k-j} = view factor from surface k to surface j,

$\overline{\tau}_{\lambda,j-k}$ = mean transmission coefficient for medium between surfaces j and k at wavelength λ,

$e_{\lambda b,g}$ = black-body emission for medium between surfaces j and k in the wavelength interval between λ and $\lambda + d\lambda$,

$\bar{\alpha}_{\lambda,j-k}$ = mean absorption coefficient for medium between surfaces j and k at wavelength λ, and

N = number of surfaces in the enclosure.

Combining Eqs. (32) and (33) to eliminate the $dq_{\lambda,k}$ terms results in a set of equations in which the $dq_{\lambda o}$ terms are the dependent variables. This set of equations is given by

$$dq_{\lambda o,k} = \varepsilon_{\lambda,k}\, e_{\lambda b,k}\, d\lambda + \rho_{\lambda,k} \sum_{j=1}^{N} \left(dq_{\lambda o,j}\, F_{k-j}\, \bar{\tau}_{\lambda,j-k} + e_{\lambda b,g}\, d\lambda\, F_{k-j}\, \bar{\alpha}_{\lambda,j-k} \right) , \qquad (34)$$

where k varies from 1 to N. The set of equations defined by Eq. (38) is linear and complete if the source terms $e_{\lambda b,k}$ and $e_{\lambda b,g}$ are known and if the view factors, mean absorption coefficients, mean transmission coefficients, emissivities, and reflectivities are constant. For these assumptions to be valid, the temperatures of the various surfaces within the enclosure must not change significantly during a time step.

In this model, all surfaces are assumed to be diffuse emitters, absorbers, and reflectors and to behave according to Kirchhoff's law. Therefore, the following relationships are valid:

$$A_k F_{k-j} = A_j F_{j-k} , \qquad (35)$$

$$\rho_{\lambda,k} = 1.0 - \varepsilon_{\lambda,k} , \qquad (36)$$

$$\bar{\alpha}_{\lambda,j-k} = \bar{\alpha}_{\lambda,k-j} , \text{ and} \qquad (37)$$

$$\bar{\alpha}_{\lambda,j-k} = 1.0 - \bar{\tau}_{\lambda,j-k} \quad . \tag{38}$$

The calculation of $\bar{\alpha}_{\lambda,j-k}$ and $\bar{\tau}_{\lambda,j-k}$ depends on the intervening medium between surfaces j and k and on the view factor between surfaces j and k. Therefore, for a medium with a macroscopic cross section, a_λ, for thermal radiation at wavelength λ, a transmission coefficient can be defined as

$$\tau_\lambda(s) = e^{-a_\lambda s} \tag{39}$$

where s is the path length. The mean transmission coefficient is then defined to be

$$\bar{\tau}_{\lambda,j-k} = \frac{1}{A_j F_{j-k}} \int_{A_k} \int_{A_j} \frac{\tau_\lambda(s) \cos\beta_k \cos\beta_j}{\pi s^2} dA_j \, dA_k \tag{40}$$

where

$$F_{j-k} = \frac{1}{A_j} \int_{A_k} \int_{A_j} \frac{\cos\beta_k \cos\beta_j}{\pi s^2} dA_j \, dA_k \tag{41}$$

is the view factor between surfaces j and k and A_j and A_k are the areas of surfaces j and k, respectively. The view factors, mean transmission coefficients, and mean absorption coefficients are calculated as a function of time and space.

The numerical cell boundaries are modeled as "black" surfaces, that is they have emissivities of 1.0 and reflectivities of 0.0. Therefore, for the cell boundaries, Eq. (34) can be simplified to

$$dq_{\lambda o,k} = dq_{\lambda b,k} \tag{42}$$

where $dq_{\lambda b,k}$ is the flux entering the enclosure through the cell boundary from an adjoining cell. Application of Eq. (40) results in a reduction in the order of the matrix that must be solved for each cell by the number of cell boundaries. However, because $dq_{\lambda b,k}$ is an unknown, an iterative solution procedure must be used for the boundary fluxes.

Once the values of $dq_{\lambda o}$ have been determined, the net radiation heat transfer from the structure surfaces and from the medium can be determined. For surface k the net radiation heat transfer leaving it is given by

$$Q_k = A_k \int (dq_{\lambda o,k} - dq_{\lambda i,k})\, d\lambda \quad , \tag{43}$$

where A_k = area of surface k, and

$$dq_{\lambda i,k} = \sum_{j=1}^{N} \left(dq_{\lambda o,j}\, F_{k-j}\, \overline{\tau}_{\lambda,j-k} + e_{\lambda b,g}\, d\lambda\, F_{k-j}\, \overline{\alpha}_{\lambda,j-k} \right) \quad . \tag{44}$$

For the medium, the net radiation heat transfer leaving it is determined from the net radiation heat transfer leaving the surfaces. The net radiation heat transfer from the medium is given by

$$Q_g = - \sum_{k=1}^{N} Q_k \quad . \tag{45}$$

This radiation heat-transfer model has been integrated into MIMAS in a two-dimensional (radial and axial direction) form.

This model treats radiation heat transfer between the fuel pins, gas, water, corium, core radial structures, and upper and lower core structures.

View factors among the various core structures are calculated for intact geometry (see Appendix B) and are recalculated during transients to account for changes in geometry. These view factors are calculated for each numerical cell. Also, view factors are calculated between each core structure and each numerical cell boundary.

Material property data, mass absorption coefficients, and emissivities are currently treated as temperature dependent. Also, at this time a single energy group is treated. The mass absorption coefficient data (gas, water, corium) are combined to form a total macroscopic absorption cross section for use in the calculation of mean absorption coefficients and mean transmission coefficients. Mass weighting is used to combine the individual absorption cross sections whereas temperature and mass weighting are used to form the emission term for the medium. A numerical approximation of Eq. (40) is used in the calculation of mean transmission and absorption coefficients. The mean transmission and absorption coefficients are calculated each time step.

Equation (45) is used to calculate the net energy change in the fluids. Distribution of this energy among the medium components (gas, water, and corium) is proportioned according to their individual macroscopic absorption cross sections.

II.D. Structural Heat Transfer

Conduction of heat in the vessel structural components is computed by a pair of one-dimensional finite-difference models taken almost directly from the TRAC-PF1 code. The heat conduction equation for slab structures (plates) and

cylindrical shells (walls) allow a variable degree of explicit or implicit differencing. This is controlled by the variable ϕ, that is,

$\phi = 1$, fully implicit,

$\phi = 1/2$, Crank-Nicolson, and

$\phi = 0$, fully explicit.

For the calculations reported here, a value of $\phi = 0.6$ was used. Temperature dependent material properties are obtained from the subroutine MPROP found in the TRAC-PD2 computer code.[37] Also included in the conduction equations is a simple melting model that accounts for the heat of fusion but does not advect or relocate any molten structural material.

II.D.1. Cylindrical Wall Heat Conduction

The temperature distribution within the walls of cylindrical vessel components is calculated with a one-dimensional heat-conduction equation in cylindrical polar coordinates:

$$r\rho c_p \frac{\partial T}{\partial t} = \frac{\partial}{\partial r}\left(rk \frac{\partial T}{\partial r}\right) + rq''' \quad , \tag{46}$$

where

c_p = specific heat,

k = coefficient of thermal conductivity,

q''' = internal heat generation,

r = radius,

T = temperature,

t = time, and

ρ = material density.

This model is used for the vessel wall, thermal shield, core barrel, and core baffle plates.

The finite-difference form of Eq. (46) is derived by applying an integral approach (see Ref. 38) to the elemental volumes shown in Fig. 18, and is very similar to the scheme given by Eqs. (10) through (18).

The boundary conditions applied to the inner (i = 1) and outer (i = I) surfaces are

$$\text{Convection} = -k\frac{\partial T}{\partial r}_{i=1 \text{ or } I} = \pm \{h_\ell(T_\ell - T_i) + h_v (T_v - T_i)\}, \text{ and} \quad (47)$$

$$\text{Radiation} = q_R \Big|_{i=1 \text{ or } I} . \quad (48)$$

Equation (47) permits the exchange of heat between the structure and the liquid and vapor phases of the flow field. In addition, an adiabatic boundary condition may be specified. The incident thermal radiation, q_R, is computed in the radiation heat transfer module of MIMAS.

Node points in the finite-difference mesh are conveniently placed on material interfaces. Material properties are evaluated between nodes. The resulting set of I linear equations are solved with a tridiagonal equation solver. A lumped parameter solution is also available at the discretion of the user.

II.D.2. Slab Heat Conduction

Heat conduction within flat plate vessel components is calculated with the TRAC-PD2[37] finite-difference derivation to the one-dimensional conduction equation

$$\rho c_p \frac{\partial T}{\partial t} = \frac{\partial}{\partial x}\left(k \frac{\partial T}{\partial x}\right) + q''' \quad , \tag{49}$$

where x denotes the space dimension. Treatment of boundary conditions, material properties, and solution of equations is analogous to the cylindrical case.

II.E. Debris Bed Packing and Oxidation

In this section, preliminary models for two aspects of debris bed behavior are described, namely:

1. a model to calculate the volume of debris that can be contained by a core numerical cell, i.e., the debris packing fraction, and
2. a model for the hydrogen and oxidation heat production of metallic Zircalloy particles in the debris.

Modeling these items was accomplished by making a number of simplifying assumptions in regard to debris particle shape, size, and chemical and thermal behavior. However, all of these assumptions have a basis in physical reality, and produce results that are reasonable. Some of these results can be checked by examining the TMI-2 core remains (see Sec. IV.C).

II.E.1. Debris Bed Packing Model

The model and analysis used to estimate the packing fraction distribution of the debris disintegrated fuel rods are described in detail in Ref. 35. This model utilized the debris particle size distribution shown in Fig. 16, and assumed all debris particles were spheres. Debris resulting from the initial rod breakup were assumed to fall between equally-spaced vertical cylinders to simulate the effects of fuel rod stubs. Debris generated later in the reflood period was assumed to fall on a uniform debris bed surface. Initially, the debris particles were assumed to fall on a porous floor (that is, the

lower-support plate), so that debris particles that contacted the floor and that were smaller than the pore size were eliminated from the debris bed.

The debris particles in the various size ranges were assumed to be randomly released at a point above the contact surface, and to impact that surface with a negligible velocity. The debris particles then stop at their first two-point contact to simulate (to a certain extent) the fact that the debris particles are irregularly shaped rather than smooth spheres.

The actual calculation of the debris packing for TMI-2 conitions was performed with a computer code written by Visscher and Bolsterli[48]. Between the rod stubs the debris packing fraction averaged 0.29, while above the stubs the debris achieved a packing fraction of 0.44. Very few particles were calculated to drop through the porous floor.

The packing fraction of the debris bed is in the same range as the intact fuel assemblies. Thus, when converted to debris, the fuel in the TMI-2 core should nearly fill its own volume. Given the small debris particle sizes, however, a good portion of the debris could have been carried out of the core during the post-accident operation of a reactor coolant pump. This supposition is supported by evidence of considerable radioactive material located throughout the TMI-2 primary system. However, as best estimate values for this analysis, maximum debris packing fractions were set equal to 0.30 between rod stubs and 0.44 elsewhere.

II.E.2. Debris Oxidation Model

The fundamental assumption utilized in this model is that the oxidation behavior of a debris bed (hydrogen generation, heat production) can be based on the behavior of an idealized, average debris particle. For this analysis, this average debris particle was assumed to be spherical, with a diameter of 2 mm, which is about the median size for the distribution of Fig. 16. Since this

diameter is greater than the cladding thickness (0.6 mm, unoxidized) the Zircalloy-containing debris particles were assumed to consist of one-half Zircalloy and one-half some other material, that is, the Zircalloy particle shape was assumed to be hemispherical.

At the beginning of each time step during the MIMAS code execution, the fluid dynamics module calculated the total mass of debris, and the mass of unoxidized Zircalloy debris in each core computational cell (Sec. II.B). Given these masses and a debris particle configuration, the effective oxide layer thickness over the surface of the Zircalloy debris particle was calculated at the beginning of each time step. The growth of this oxide layer during the time step was assumed to follow the same kinetics equation as the intact cladding, Eq. (3). Likewise, the form of the steam starvation function $(x_{H_2O})^n$ was assumed to the be same. However, because of the greater possibility of hydrogen trapping in a debris bed, the exponent, n, for debris steam starvation was assumed to equal 4. Once the oxide layer growth during the time step was calculated, Eq. (2) was used to determine the hydrogen production and heat of oxidation.

In a manner similar to the behavior of the intact fuel rods, when the debris bed temperature in a given cell reaches the Zircalloy melting point, the unoxidized Zircalloy can be expected to form a liquified fuel eutectic with the UO_2 debris particles. This eutectic either ceases to oxidize or drains to a cooler portion of the vessel. In either case, the debris heat of oxidation ceases in a cell where the debris temperature exceeds the Zircalloy melting point. For the current simiplified analysis, this process was modeled by simply terminating the debris oxidation. In more advanced versions of this model, the liquified fuel mass will be tracked to its final location, with its oxidation behavior (if any) fully analyzed along the way.

III. ACCIDENT RESULTS AND SENSITIVITY STUDIES

III.A. TMI-2 Accident Events

The purpose of this section is not to list the long sequence of accident events (available, for example, in Ref. 39), but to review just those events that affect the primary system and the core damage analysis presented here. Therefore, the sequence of events discussed here and listed briefly in Table V, has been extracted from Ref. 39 and is only a small subset of the actual accident sequence of events.

Referring now to Table V, the initiating event (time = 0) for this analysis was selected to be the loss of main feedwater to the steam generators with an abnormal, temporary loss of auxiliary feedwater. This is followed at 6 s by a lifting of the pressurizer electromatic relief valve (ERV) on a high-pressure signal of 156.4 bar, and at 10 s by a reactor scram on a high-pressure signal of 163.3 bar. At 12 s the ERV did not reseat as the pressure dropped below 152.9 bar, but remained fully open. This stuck ERV thus started an effective small-break loss-of-coolant accident having a break area of 6.78×10^{-4} m^2.

At 41 s the high-presure-injection (HPI) pump 1A was manually started to counter the dropping pressurizer level (the letdown flow had been previously stopped) resulting from the steam generator overcooling the primary coolant, and from the ERV mass loss. At 121 s the HPI pump 1C came on automatically on a low pressure signal of 113.7 bar, thus increasing the HPI flow to a maximum rate of 55.0 kg/s. The automatic HPI system was switched over to manual operation at 193 s, allowing the operators to throttle this coolant injection arbitrarily. Isolation valves on the auxiliary feedwater system, which had been closed previously, were opened at 498 s, thus providing coolant to the nearly dry secondary side of the steam generators. At 563 s a letdown flow was started as

part of the effort to control the pressurizer level. Thereafter, the high-pressure-injection makeup and letdown flows were varied by the operators to such an extent that the uncertainty in the magnitude of these flows is probably the most important uncertainty associated with the TMI-2 accident transient.

The next major accident event was the stagnation of the coolant in the primary system loops. The loop B reactor coolant pumps were manually tripped off at 4380 s, followed by a similar action for the loop A pumps at 6037 s. This action transformed the two-phase, forced convection flow situation in the core to a pool boiling situation, which initially uncovered the upper portion of the fuel rods. This pool boiling state endured for roughly 6000 s (1.67 hr).

The block valve downstream of the pressurizer ERV was closed at 8520 s, thus terminating the mass loss from the primary system. At 9600 s the HPI flow was stopped, depriving the reactor vessel of a source of water mass until the core reflood/refill that occurred at 11880 s. One of the reactor-coolant pumps (pump 2B) was toggled on at 10440 s for approximately 1200 s (20 min) but it is doubtful whether this action moved any significant mass of water into the vessel downcomer. Also note that the letdown flow continued between 9600 s to 11880 s.

Finally at 11880 s the HPI flow was again established at its maximum, 55.0 kg/s, and maintained for a complete reflooding of the core region. Most of the fuel rod damage occurred during this injection, and at 12080 s the radiation monitors in the reactor building registered off-scale.

III.B. Numerical Solution Description

III.B.1. A Tandem TRAC/MIMAS Calculation

The calculational strategy for the TMI-2 accident transient used a combination of the TRAC-PF1 and MIMAS codes; TRAC is used to model the primary and part of the secondary system for the purpose of providing boundary conditions to the MIMAS core calculation. As indicated in Fig. 19, a tandem

TRAC and MIMAS calculation is continued until fuel rod ballooning is predicted, at about 9800 s. Then the TRAC calculation is terminated because TRAC cannot account for core-geometry changes. The MIMAS calculation continues through the core-heatup phase and subsequent core reflood at 11880 s. After 9800 s boundary conditions for MIMAS are inferred from plant pressurizer data[3] and best-estimate makeup/letdown flows[4]. The details of these boundary condtitions for the TRAC and MIMAS calculations are given in Sec. III.B.4.

The reason for running TRAC and MIMAS in a tandem operation for the first 9800 s, instead of starting MIMAS as an initial condition problem from TRAC information at 9800 s, is to avoid solution discontinuities that usually occur in the practical solution of the fluid dynamics equations. Also this tandem operation offers the convenience of using only the MIMAS graphics package to illustrate the core region results for the entire transient. The additional computing cost associated with producing identical TRAC and MIMAS core results in the time interval from 0 to 9800 s is very small, because the cost of running MIMAS is very small relative to the cost of running TRAC.

III.B.2. Core Numerical Modeling

We assumed the TMI-2 core region to contain the 177 fuel assemblies, the core baffle plates, and the upper- and lower-core support plates. The upper and lower plenums and downcomer annulus are excluded in this core region definition. The core region is modeled numerically using the two-dimensional (radial and axial) half-core mesh shown in Fig. 2. This mesh scheme divides the core into five axial levels and three radial rings (fifteen numerical cells total), enclosed by a cylindrical-shell baffle wall and upper- and lower-support plates represented by discs. For intact geometry each mesh cell contains and models fuel and control rods, inconel grid spacers, possibly part of a core support

plate, possibly part of a core baffle plate, and of course the steam/water coolant.

For TMI-2, the radial width of a mesh cell is 0.56 m and the axial height is 0.73 m. The radius of the upper- and lower-support plates, and the baffle wall is 1.67 m. The inner, middle, and outer radial rings have 4160, 11856, and 20800 fuel rods respectively, and 160, 416, and 512 control rods respectively. The coolant flow area for the core is 5.94 m^2, which includes the bypass-flow area in the baffle and reflector regions. These dimensions and areas and other geometry descriptions were obtained from Ref. 40.

III.B.3. Primary and Secondary System Numerical Modeling

The primary system and part of the secondary system were modeled using the TRAC-PF1 code. A TRAC component schematic of the primary and secondary systems that were modeled is shown in Fig. 20. This figure splits the component geometry into vessel components, loop-A components, and loop-B components. Each of these components is described in Table VI in terms of how it relates to the actual primary and secondary systems hardware, and according to the number of thermal-hydraulic mesh cells it contains.

Some of the important features of this TRAC model are: (1) This model is completely one-dimensional even in the reactor vessel. (2) The vessel is modeled using a composite of TEEs for the downcomer, plenum volumes, upper head, hot-leg and cold-leg connections, and a five cell reactor core. The physically split cold leg is modeled explicitly for loop A, whereas a combined cold-leg model is used for loop B. (3) The eight vessel vent valves are combined into a single valve having a maximum area equal to the sum of the individual areas. (4) On the secondary side, the steam-generator downcomer and main steam line are explicitly modeled, whereas the turbine is simulated with a pressure boundary

condition, and the main and auxiliary feedwater systems are simulated with mass-flow-rate boundary conditions.

Using this TRAC model, a steady-state calculation simulated normal full-power operation (2711 MW_{th}) before the accident. Results from this calculation are given in Table VII, which compares TRAC predictions of various system responses with plant data obtained from B&W for TMI-2, and from Duke Power for Oconee. In general the predictions compare well with the data; the largest difference is 3% for the core pressure drop. When comparing with Oconee data, it should be noted that Oconee's design power level and main-feedwater to the steam generators are both 5% lower than the corresponding quantities for TMI-2.

III.B.4. Boundary Conditions

The boundary conditions discussed in this section cover both the conditions needed for the TRAC calculation, and those needed for the MIMAS calculation. Referring now to the TRAC component schematic given by Fig. 20, the primary and secondary systems require eleven pressure and mass-flow-rate boundary conditions. These are: (1) the steam-generator back-pressures represented by components 61 and 71, (2) the pressurizer relief valve back-pressure represented by component 26, (3) the main feedwater flow rates represented by components 60 and 70, (4) the auxiliary feedwater flow rates represented by components 62 and 72, (5) the makeup flow or high-pressure injection flow rates represented by components 9, 19, and 39, and (6) the letdown flow rate represented by component 31.

Some of these TRAC primary and secondary boundary conditions are given in detail in Sec. II.C of Ref. 3 and will not be repeated here: these are the steam-generator back-pressures, the pressurizer relief valve back-pressure, the auxiliary feedwater flows, and the makeup and letdown flows for the first 6000 s

of accident time. The makeup and letdown flows after 6000 s were obtained from Ref. 4, which is the current best-estimate of the magnitude of these flows. The main-feedwater flow rates to the steam generators are taken to be zero throughout the accident transient.

Boundary conditions needed for the MIMAS calculation were obtained from the TRAC calculation at the interfaces of components 98, 99 and 88 shown in Fig. 20a. These interfaces physically represent the core upper- and lower-support plates. The conditions needed at the lower-support plate include the steam and water temperatures given by Fig. 21, steam and water volume fractions given by Fig. 22, and steam and water velocities given by Fig. 23. At the upper-support plate only the system pressure is needed and that is given by Fig. 24. The corium velocity and volume fraction are both assumed to zero at the core lower-support plate, along with the hydrogen and fission-product densities. This corium boundary condition implies that molten or solid debris will pile up on the core lower-support plate to form a debris bed.

III.C. Fuel and Control Rod Behavior

In this section, the fuel and control rod responses to the TMI-2 accident are discussed in detail both in regard to the predictions of the models presented in Sec. II.A, and in regard to the uncertainties in these models. In the presentation of the fuel and control rod responses, the direct model predictions are referred to as the "best estimate" results, and are presented first. The effects of uncertainties in some of the more important rod behavior models are evaluated by calculating the core response to parameter variations in the models. The results of these sensitivity studies and their impact on the predictions of the TMI-2 core response to the accident are presented in the latter part of this section.

III.C.1. Best Estimate Analysis Results

III.C.1.a. Fuel and Control Rod Initial Conditions and Temperature History. The fundamental entity which drives the various morphological changes in the fuel rod during the TMI-2 accident analysis is the cladding temperature. The cladding temperature in turn is determined by the fuel decay heat power, the coolant flow, thermal radiation, cladding oxidation, and eutectic formation. In this analysis, the control rods are assumed to be passive elements, so that the average temperatures of the control rod sections is assumed equal to the local coolant temperatures.

The significant core conditions at the beginning of the TMI-2 accident are listed in Table VIII. The core cell numbers correspond to those indicated in Fig. 2. The core power, burnup, neutron fluence, and fission product inventory distributions are based on data from Refs. 40 and 15. The decay power history for the TMI-2 core is given in Table IX, and is from Ref. 41.

The cladding temperature histories for the fuel rod sections in the three core rings during the interval 9000 to 11880 s are shown in Figs. 25 to 27. Prior to 9000 s, the cladding temperatures are either constant or slowly increasing. The effects of a number of the accident events and rod morphological changes on the temperature histories are evident from these plots. The initial gradual cladding temperature rises that occur between 9000 and 11000 s over the various rod axial levels are caused by the water boiloff after stagnation of the primary system. The exponential cladding temperature increases around 11000 s are due to the initiation of cladding oxidation above 1000 C. The extremely rapid cladding temperature increases in levels 3 - 5 caused by the switch from MATPRO to Urbanic kinetics above 1800 K, as described in Sec. II.A.2.6. The cladding temperature downturns that follow these exponential increases are caused by steam starvation or eutectic formation

effects. The temperature perturbations that occur in the fuel rod cladding around 10800 s are due to control rod melting. All of these phenomena are discussed in more detail in the following sections.

III.C.1.b. Cladding Burst, Ballooning and Flow-Blockage. As discussed in Sec. II.A.2.a, the time and magnitude of cladding burst and ballooning depends on the cladding temperature and internal/external cladding pressure differential. Cladding temperature histories for the TMI-2 fuel rod elements are shown in Figs. 25 - 27; the histories of the TMI-2 cladding stresses (which are proportional to the net rod internal pressures from Eq. (23) are shown in Figs. 28 and 29. At the beginning of the transient, the net cladding stress is compressive because the coolant pressure is greater than the rod internal pressure. As the accident progresses, the coolant pressure drops and the rod temperature increases, so that the cladding stresses eventually become tensile.

For this calculation, the cladding burst/ballooning correlations from NUREG-0630 were used to give best estimate results. By applying the temperature/stress histories to the NUREG-0630 correlations presented in Sec. II.A.2.a, the cladding burst times, temperatures, pressures, and single-rod burst strains given in Table X for the three core radial rings were calculated by MIMAS. By multiplying the single rod strains by the 0.56 conversion factor discussed in Sec. II.A.2.a and applying these results to Fig. 11, the corresponding rod-bundle blockage percentages given in Table X were determined. While these flow blockages are relatively high, recent work[9] has shown that blockages of these magnitudes do not significantly affect core reflood.

Uncertainties in the calculated ballooning flow blockage results arise primarily from three sources: uncertainty in the single rod burst and ballooning correlations, uncertainty in the transient core environment, and uncertainty in

the factor that converts the single rod ballooning strain to a percent flow blockage in the fuel rod bundle.

The results in Table X show that for the TMI-2 fuel rods, the ballooning occurred in the α-Zr region. As shown in Fig. 8, the three burst temperature/pressure correlations are in relatively good agreement. However, in the α-Zr region, the MATPRO-11 and REBEKA correlations predict substantially greater single rod ballooning strains than does the NUREG-0630 correlation, which was used to obtain the Table X values. The reasons for this difference may be inferred from the various references in which these correlations are derived, and will not be repeated here. However, the fact that significant differences exist in these correlations produces an uncertainty in the results of all three correlations.

Reference 30 presents a TRAC code primary system analysis of the TMI-2 accident with primary emphasis on coolant flow and behavior. In this study, it was calculated that an ERV closure at ~8500 s causes some water to flow back down the high hot leg of loop A and into the core. This event could result in coolant spraying over the fuel rods, causing large cladding circumferential temperature gradients. From the data of Fig. 10 this spraying could drastically decrease the cladding ballooning strains.

Another source of uncertainty in this analysis is in the average ballooning blockage/maximum ballooning ratio of 0.56. Although this value correlated well with all bundle test data considered in Ref. 10, none of these tests were prototypic in regard to bundle size or TMI-2 cladding heating rate. Test results from a larger rod bundle revealed significant variations in the rod ballooning patterns and flow blockage magnitude with test bundle size and/or boundary structure.

Because of these uncertainties in the TMI-2 fuel rod ballooning magnitudes, and because most of the ballooned rods in the TMI-2 core fragmented during reflood, the sensitivity of the overall TMI-2 core response to the accident to the effects of ballooning blockage variations was studied. This study is described in Sec. III.C.2.a.

III.C.1.c. Fission Product Release. A comparison between the total TMI-2 core fission product inventory for I, Cs, Te, Xe and Kr at the beginning of the transient and the corresponding masses of these elements calculated to remain in the fuel material at the beginning of reflood (11880 s after accident initiation) is given in Table XI. The amounts of these elements that were calculated to leave the core during the TMI-2 accident are discussed in Sec. III.D.

The uncertainty in the values given in Table XI arises from variances both in the initial amounts of the elements in the TMI-2 core at the beginning of the accident, and in the release rate constants presented in Sec. II.B.2.c. The initial fission-product masses in the core were calculated by a method given in Ref. 33. In this method, the total mass of the stable iodine isotopes (half-life of one day or longer) in the TMI-2 core was taken from Ref. 42. The masses of the stable isotopes of Cs, Te, Xe, and Kr were determined from the I mass by multiplying by the appropriate fission product yield ratios from Refs. 43 and 15. Other estimates of the fission product masses in the TMI-2 core are given in Ref. 40.

The uncertainty in the value of the fuel release coefficients for Cs, I, and Te of Table XI is estimated in Ref. 15 to equal approximately one order of magnitude. This uncertainty applies only to the rate of release from the fuel. Thus, the total fission-product mass released from the fuel is not necessarily

uncertain by an order of magnitude. No estimate of the uncertainty in the release of the noble gasses was given in Ref. 15.

Notification has been given that Ref. 15 will be revised in the near future. Thus, the values of the release coefficients of Table III may change. Likewise, an effort is being made to formulate more mechanistic models for fission-product release during severe core accidents. This effort may result in the calculation of fission-product releases different from those in Table XI. Thus, no detailed uncertainty analysis or sensitivity study was performed for fission product release in this work. However, as noted in Ref. 33, the release coefficient method used here should give considerably more accurate results than assuming constant release rates, as was done in WASH-1400.

III.C.1.d. Hydrogen Generation, ZrO_2 Layer Thickness and Heat of Zr-H_2O Reaction. The hydrogen production rate due to the Zr-steam reaction was calculated by the MIMAS code using Eqs. (2) and (3). The resulting total hydrogen produced as a function of time up through core reflood is shown in Fig. 47. This figure includes hydrogen generated by the fuel rods, guide tubes, and the debris. Section III.D.4 discusses various aspects of the debris oxidation results, whereas the following discussion is concerned with intact fuel rods and guide tubes only.

For each cladding section, the oxide layer growth rate was determined by using the values of A and B for ZrO_2 formation from Table II in Eq. (3). The fuel rod oxide layer thicknesses as a function of time for the various core sections are shown in Figs. 30 - 32. In general, these oxide layer thicknesses correlate well with the cladding temperatures of the various sections shown in Figs. 25 - 27.

The rod power contribution due to the Zr-steam reaction is also determined by the heat of reaction indicated by Eq. (2) and the oxygen uptake rate equation. The rod linear heat rates due to ZrO_2 formation as a function of time and core location are shown in Figs. 33 - 35. For times beyond 10500 s, the Zr-steam reaction supplies more power to the core than does the fission product decay heat. The extremely rapid variation of the cladding oxidation heat production with time emphasizes the sensitivity of this response to temperature and steam starvation effects. As shown in Figs. 33-35, level 5 decreases its oxidation rate as level 4 oxidation increases and contributes to steam starvation in level 5. This process proceeds down the rod length: level 3 oxidation contributes to steam starvation and oxidation power decrease of level 4, and level 2 does the same to level 3. Superimposed on this general pattern are fluctuations in the oxidation power production due to self-starvation within a level, temperature fluctuations, and liquefied fuel formation. A flow reversal prior to the beginning of reflood causes fresh steam to contact cladding in level 5, causing a sudden spike in cladding oxidation (see Figs. 33 and 34).

The decrease in the hydrogen generation, ZrO_2 layer growth, and the heat generated by the Zr-steam reaction caused by steam starvation effects, are quantitized by the x_{H_2O} term of Eq. (3). Existing data for the decrease in Zr oxidation as a function of local steam mole fraction and temperature are too sparse for an accurate empirical formulation of this term. We assumed this function to be the square of the local mole fraction of steam. Stream starvation thus influences all phenomena that involve the Zr-steam reaction.

One source of uncertainty in the best estimate results shown in Figs. 30 - 35 is the accuracy of the kinetic constants given in Table II for application in Eq. (3). A number of experiments have studied the kinetics of the high

kinetic constants determined by experiments in which the Zircalloy specimens were internally heated tend to agree, as do the results of experiments in which the specimens were externally heated. However, there appears to be a real difference between the results of internally heated and externally heated tests. This is illustrated in Fig. 12, where the MATPRO results are from externally heated tests, whereas the Urbanic tests were internally heated. Ocken postulates that this difference is caused by temperature gradient effects across the specimen tubing wall thickness: in externally heated tests the oxide layer is hotter than the unreacted metal, whereas in internally heated tests the opposite is true. Which experimental heating method best approximates the TMI-2 accident situation is difficult to determine. The MIMAS calculations indicate that if this heat generation is assumed uniform accross the cladding, then when the cladding heat of oxidation becomes significant, the oxide layer is slightly hotter than the metal.

An even more important uncertainty in the results of Figs. 30 - 35 is the effect of steam starvation. As previously noted, because of the scarcity of data, the fundamental relationship between local temperature, steam mole fraction, and the Zr-steam reaction rates can only be estimated. Because so many factors influence steam starvation effects on Zircalloy oxidation kinetics, and vice versa, the exponent the steam mole fraction function in Eq. (3), was changed from 2 to 1. The results of this sensitivity study are given and discussed in Sec. III.C.2.

III.C.1.e. Control Rod Disintegration. As noted in Sec. II.B.2, the control rods are assumed to disintegrate when the local coolant temperature equals the stainless steel cladding melting temperature. No further interaction between the molten control rod material and the core was considered.

Table XII shows the times at which the control rods disintegrate in each core section. This table shows that by the time the reflood begins, the control rods in the upper 80% of the core have melted.

The thermal time constant for the control rods is given by

$$\theta = \alpha/r^2 \quad , \tag{50}$$

where α is the average thermal diffusivity of the control rod material and r is the effective control rod radius. Neglecting the relatively thin cladding material, θ equals approximately 1.6 s^{-1}, which is approximately twice the core temperature rise rate prior to the control material melting. Thus, the temperature lag between the control rods and coolant should indeed be small, as we assumed.

The heat of oxidation of the Zircalloy control rod guide tube is included in the total core heat production, but is assumed to have direct influence on the control rod material temperature. A comparison of Figs. 25 and 37 shows that the fuel rod cladding temperature is always only a few degrees above the coolant temperature, even though the heat of Zircalloy oxidation is included in the fuel rod temperature calculation. Again, this indicates that before melting, the control rods closely follow the coolant temperature.

The effect of the latent heat of fusion of both the absorber material and the stainless steel cladding is also neglected in this analysis. Assuming the latent heat of fusion for the absorber material to be 1.44 MJ/kg, the total heat absorbed by 80% of the control rod material during melting is 3170 MJ. The core power during the time that the upper 80% of the core is exposed to steam is approximately 27 MW. Thus, the maximum effect of the control rod material heat of fusion would be to delay the time of control rod disintegration by 120 s.

The effects of neglecting possible fuel-rod control material interactions discussed in Sec. II.B.2 are so extensive that they cannot be fully assessed at this time. Obviously, extensive dissolution of the fuel rod cladding by the molten control material would result in core disintegration before to reflood. The effects of such an early core disintegration on coolant temperature, fission-product release, and hydrogen production is unpredictable at this time; the pertinent models do not exist. If fuel-absorber material interaction is important, these models will have to be developed from the results of upcoming degraded fuel tests[24,25].

III.C.1.f. Effects of Liquefied Fuel Formation. Using the model described in Sec. II.B.2, the MIMAS code analysis of the TMI-2 accident predicts that liquefied fuel forms only in core element cell level 4, ring 1 (see Fig. 2) at approximately 11000 s into the accident. In this core section, the maximum melt distance is calculated to equal 1 mm inward from the fuel pellet outer surface. This melt distance is strongly dependent on the rate at which the cladding oxidation reaction is terminated (if indeed it terminates at all) after the onset of fuel liquefaction.

In general, termination of cladding oxidation as indicated by the data of Hagen[23] is probably the most important effect of fuel liquefaction for the case of low heating rates, where the liquefied fuel is contained by the cladding oxide layer. However, because of the relatively small amount of liquefied fuel calculated to form during the TMI-2 accident, uncertainties in the modeling of these phenomena do not greatly affect the overall calculated outcome of the TMI-2 accident. Should the liquefied fuel break out of the cladding oxide layer instead of remaining within, approximately 12% of the core volume would convert to debris at 11000 s.

The effects of uncertainty in the rate at which cladding oxidation is terminated by fuel liquefaction are examined in a sensitivity study described in Sec. III.C.2.c below. For this calculation, the Zircalloy oxidation reaction is assumed to continue unaffected by liquefied fuel formation until either all of the cladding is oxidized, or until the cladding ZrO_2 layer reaches its melting temperature.

III.C.1.g. Fuel Rod Disintegration. At the time the TMI-2 core was reflooded, the MIMAS code predicts that the fuel rod cladding in the upper 80% of the core was embrittled to the point where the thermal stresses induced by a 5 K/s cooling rate would cause rod breakup. Upon core reflood, a pulse of saturated steam is created by the injected water contacting the hot (but not embrittled) lower 20% of the fuel rods. This steam rapidly cools the upper part of the core within a few minutes of the initiation of reflood, causing almost immediate disintegration of the embrittled fuel sections. The exact times at which fuel rod disintegration occurs in the various core cells is shown in Table XIII. These times indicate that the breakup of the fuel in the core is rather incoherent in regard to location, but because the breakup occurs over a short time period, this incoherency is of little practical consequence.

Two important sources of uncertainty in the calculated time and extent of fuel rod breakup are the effect of steam starvation on the rate of oxygen diffusion into the cladding, and local heat transfer effects, which were not analyzed in the MIMAS calculation.

In the calculation of oxygen diffusion into the β-Zr layer, the oxygen concentration at the β-Zr layer boundaries (see Fig. 12) was assumed to at least equal the local saturation concentration. This saturation concentration varies with temperature, but in general is sufficiently small that it is probably maintained at the β-Zr boundaries when excess steam is available on the cladding

outer surface. However, under steam starvation conditions, the oxygen concentration of the β-Zr layer surface may be drastically decreased, thereby slowing down the oxygen diffusion and the β-Zr embrittlement at high core temperatures. This effect is quite complicated, but can probably be quantified by performing Zircalloy embrittlement tests under steam-starvation conditions.

At high core temperatures, radiation heat transfer from the fuel to the surrounding structure becomes an important core temperature regulation mechanism. As described in Sec. III.G., for the relatively coarse noding scheme utilized in this calculation, the surrounding core structures were assumed to be simple plates and cylinders and the radiation heat-transfer view factors from fuel to structures were calculated accordingly. In reality, these structures are more complicated, with local irregularities that may locally affect heat transfer from the fuel. Likewise, local heat conduction paths may exist, which were not considered in this analysis. Thus, sections of the fuel rods at or near the core periphery may not have embrittled to the extent indicated by the MIMAS calculation, and may have survived the reflood more or less intact (but still badly damaged). A thorough inspection of the remains of the TMI-2 core will indicate the importance of these local heat transfers.

III.C.2. Sensitivity Study Results

The purpose of the sensitivity studies to be described next is to investigate the effects of uncertainties in key models on the TMI-2 accident results predicted by MIMAS. The scope of this work is such that no attempt was made to quantify the variation in the TMI-2 accident effects as a function of the uncertain parameter. Rather, the uncertain parameter was changed by a significant amount from the best-estimate value, the TMI-2 accident analysis was redone, and significant changes in the key accident results from the best-estimate case were noted. These chosen "key" results are hydrogen

generation up to the time of reflood, fission product release, number of core cells that embrittled under slow-cooling conditions, and the time range over which embrittlement occurred. Hydrogen generation during reflood was not considered in these sensitivity studies because this process itself is highly uncertain. The model sensitivities that were investigated in the study were for cladding ballooning flow blockage, steam starvation effectiveness, and cladding oxidation termination due to liquefied fuel formation.

III.C.2.a. Ballooning Blockage Variation Study. For this study, the cladding ballooning strain was artificially limited so that the total flow area reduction never exceeded 20%. Table XIV shows the differences between the best estimate key results and the results for the limited ballooning blockage calculation. This table shows that the differences between the two cases are slight. The number of elements experiencing eutectic formation and slow cooling embrittlement are the same for the two cases. Likewise, the time periods over which cladding slow-cooling embrittlement occurs are not significantly different. Slightly less hydrogen is produced for the low ballooning blockage case because the total Zircalloy area exposed to steam is somewhat less. The fission-product release is also somewhat less for the limited ballooning case because the fuel temperatures in the top core elements are lower. During the reflood, the fuel rod breakup showed a different spatial pattern for these two cases, although the times for breakup initiation and the time periods over which fuel breakup occurred were virtually the same for the two cases.

These results show that while knowledge of ballooning blockage in fuel rods during degraded core accidents is important for determining local effects prior to core reflood, the effects of ballooning blockage uncertainties on whole-core responses to TMI-2 type accidents are probably small.

III.C.2.b. Steam Starvation Variation Study. For this study, the exponent on the steam mole fraction in Eq. (3) was changed from 2 to 1. This effectively lowered the steam starvation process during the calculation, and should have increased the Zircalloy oxidation rate. The comparison of the key results for this case with corresponding best-estimate case results given in Table XV shows that this indeed happened. The higher Zircalloy oxidation that occurred in the low-starvation calculation resulted in significantly more hydrogen generated by the fuel than in the best-estimate case. Likewise, higher core temperatures resulted in a greater fission-product release. Also, two elements experienced eutectic formation prior to reflood for the low starvation case. The volume of embrittled fuel at reflood was the same for both cases. Likewise, the time over which cladding embrittlement occurred was approximately the same for the low starvation case and the base case.

These results indicate that knowledge of the overall steam-saturation process is necessary to calculate accurately hydrogen generation, fission product release, and liquefied fuel formation for degraded core accidents.

III.C.2.c. Continuation of Cladding Oxidation After Eutectic Formation. For this analysis, the MIMAS Zircalloy oxidation model was altered so that cladding oxidation continued unaffected by liquefied fuel formation. For the TMI-2 accident, the best-estimate MIMAS analysis predicts that liquefied fuel will form only in core cell level 4, ring 1 (see Fig. 2). The effect of continuing the oxidation of the fuel rods in this element after the formation of liquefied fuel is shown in Table XVI. The increase in hydrogen production over the base-case is expected because of the continuing production by this cell. A greater difference was prevented by steam starvation effects. Somewhat more fission products are released in the liquefied fuel oxidation case because of higher temperatures in the upper core regions. The amount of cladding

embrittlement and the cladding embrittlement times are virtually the same for both cases.

The effects of continuing cladding oxidation past liquefied fuel formation times would have undoubtedly been more significant had more liquefied fuel been present in the core. As in the base case, the liquefied fuel that was calculated to form in the TMI-2 core during reflood existed for such a short time before disintegration that its effects were negligible. However, for a severe core accident sequence where considerable liquefied fuel is created over a long time period, the effect of liquefied fuel on cladding oxidation could significantly influence the overall accident impact.

III.D. Fluid Dynamics of the Core Coolant and Geometry

The time-dependent fluid-dynamic behavior of water, steam, H_2 and fuel rods in the core region during the TMI-2 accident is discussed in this section. A discussion of the TRAC water/steam ex-core behavior out in the primary and secondary systems is not included here, since this discussion would nearly duplicate the work described in Ref. 3. The interested reader is referred to Ref. 3 for a detailed discussion of primary and secondary systems behavior during the accident.

The following four subsections divide the accident transient discussion into the four phases:

1. core two-phase forced convection (0 to 6000 s),
2. pool boiling and core heatup (6000 to 9800 s),
3. fuel and control rod damage (9800 to 11880 s), and
4. core reflood and fuel rod fragmentation (11880 to 14000 s).

Each subsection will discuss the major fluid-dynamic phenomena occurring in the time interval associated with that accident phase.

III.D.1. The Core Two-Phase Forced Convection Phase: 0 to 6000 s

After the loss of main-feedwater to the steam generators (which in this analysis is defined as time zero) and the reactor scram at 10 s, the primary system water is overcooled by the steam generators and begins to depressurize as the water density increases. This depressurization is observed in Fig. 36, which shows primary system pressure versus core level and time. The core level "0" in this figure and in following surface figures corresponds to the lower-support plate and level "5" corresponds to the upper-support plate.

In the time interval from 0 to 1000 s, Fig. 36 shows the pressure decreasing from about 160 bars down to about 70 bars where it levels off temporarily out to about 6000 s. This presssure plateau is formed when the primary-side coolant achieves a near-thermal-equilibrium with the secondary side steam-generator coolant: both sides containing a saturated steam/water mixture at about 70 bars pressure.

During this interval of 0 to 6000 s, the four reactor-system coolant pumps are operating, maintaining the core region in a two-phase forced convection flow situation. The steam and water temperatures in the core are slowly varying and close to saturation during this time interval, as indicated by Figs. 37 and 38. The volume fraction of steam however, presented in Fig. 39, is gradually increasing as water flashes to vapor during the initial depressurization and is further vaporized by the decay heat power of the fuel rods. Figure 39 shows the steam volume fraction increasing from 0% at time 0 to about 60% at 6000 s. The corresponding behavior of the water volume fraction is shown in Fig. 40 (note the time axes for these surfaces have been rotated to provide the best perspective of the surface).

The steam and water velocities are presented in Figs. 41 and 42. In general the steam velocity has the same surface shape as the water velocity but moves somewhat faster due to buoyancy forces. The water velocity is seen to gradually decrease with time as the pump heads degrade with increasing steam volume fraction. At 4380 s, the loop-B pumps are tripped by the operators and the core water velocity is seen in Fig. 42 to drop sharply (by about a factor of 2) as loop B stagnates. At 6037 s the loop-A pumps are tripped by the operators and the core water velocity is dropped to zero (Fig. 42) as loop A and the entire primary system stagnates.

The major fluid-dynamic features of this core two-phase forced convection phase (0 to 6000 s) are summarized as follows:

1. There is a 90-bar pressure drop in the primary system as the steam generators overcool the primary coolant which is heated only by decay heat.

2. For most of this phase, the core pressures and temperatures are near constant at saturation values controlled by steam-generator heat transfer.

3. The steam volume fraction gradually increases as water is vaporized by the initial pressure drop and by the core decay heat.

4. At 4380 s loop B stagnates and at 6037 s the entire primary system stagnates, thus terminating the two-phase forced convection flow situation in the core and its associated good heat transfer characteristics.

III.D.2. The Pool Boiling and Core Heatup Phase: 6000 - 9800 s

After stagnation of the primary system coolant at about 6000 s, the two-phase forced convection flow situation that previously existed in the core collapses into a pool boiling situation. This collapse is observed in the volume fraction surfaces of Figs. 39 and 40 by the discontinuity that occurs soon after 6000 s. Figure 39 for example shows a homogeneous steam volume of about 60% in all core mesh cells at 6000 s. This uniform profile suddenly changes into a pool-boiling profile where the steam volume fraction is zero at all core levels except the top level, where most of the fuel rods are uncovered.

After the formation of pool boiling in the core, the residual decay heat in the fuel rods (about 27 MW) continues to boil coolant water, uncovering more and more of the core. This uncovery is observed in the volume fraction surfaces, Figs. 39 and 40, by the increasing steam fraction and decreasing water fraction, respectively, in between 6200 s and 9800 s. The water fraction in Fig. 40 is decreasing to zero sequentially for the core levels, starting at the core top and moving down. This roughly represents the water level dropping in the core.

During this pool boiling and core uncovery phase, the core pressure shown in Fig. 36 decreases again to a minimum of 40 bars between 6000 s and 8520 s. This additional pressure drop of 30 bars, down from the pressure plateau that existed before 6000 s, results from the stagnation of the primary system and the mass loss out the stuck-open relief valve on the pressurizer. At 8520 s the relief valve is effectively closed by a down-stream block valve, sealing the primary-system boundary. The core pressure then begins to rise as further core boiling repressures the primary system. This temporal primary system depressurization briefly flashes some core water to vapor, further uncovering the core. However, this undesirable situation terminates when the block valve

is closed at 8520 s and the system repressurization condenses some steam and increases the core water level. This flashing and condensing causes the small steam-fraction peak at 8520 s in Fig. 39.

The steam temperature surface in Fig. 37 shows some heatup in the upper core starting at about 7000 s. The fuel rods in this region cannot be cooled sufficiently by the stagnated steam environment to avoid a temperature excursion. This upper-core heatup continues in a rather well behaved linear fashion beyond 9800 s.

The stagnation of the water and steam in the core region can be observed in the velocity surfaces given by Figs. 41 and 42. The steam velocity decreases sharply after 6000 s to a pool-boiling vapor rise rate that ranges from 1 mm/s to 1 cm/s. The water velocity decreases at 6000 s to near zero, but subsequently turns negative when a mesh cell is nearly boiled dry and gravity-driven water droplets fall back to the descending water level. This process explains the depressions in the Fig. 42 velocity surface between 6000 and 12000 s.

The major fluid-dynamic features of this pool boiling and core heatup phase (6000 to 9800 s) are summarized as follows:

1. The coolant in the core region collapses into a pool boiling state after stagnation of the primary system at 6000 s.

2. The upper-core begins a near-linear heatup at 7000 s, as the water level falls and fuel rods are uncovered to convect heat to a dry steam environment.

3. The pressurizer relief valve is effectively closed at 8520 s. This closure terminates a system depressurization and initiates a repressurization that persists until core reflood.

III.D.3. The Fuel and Control Rod Damage Phase: 9800 to 11880s

After 9800 s of accident transient time, the previously intact fuel rod geometry begins to degrade in the high-temperature steam environment (T_{gas} ≈ 1000 K). Fuel rod ballooning occurs in mesh cell 5 (top core cell) in all three radial rings, releasing fission products to the primary system and forming a partial flow-area blockage at the top of the core. This blockage represents an additional flow resistance, and further decreases the steam velocity and thus the fuel rod heat transfer even further. The onset of this resistance is observed in Fig. 43 by the level 4 steam velocity oscillations at 9800 s, where the steam is adjusting to the blockage, and hence decreasing from ~1 cm/s to ~1 mm/s.

The fission products that are released from the ballooned-rod sections form a partial pressure out in the gas volume (see Fig. 44) and move with the gas up and out of the core. The masses of fission products that leave the core region and move into the primary system are shown in Fig. 45. Table XI indicates what percent of the initial fission product inventory was released from the fuel rods, and since the MIMAS calculation predicted negligible deposition on core structure surfaces, Table XI also indicates the ex-core release. Although the release from the fuel rods starts soon after rod ballooning (9800 s), significant amounts of fission products are not transported into the primary system until after 11000 s, as indicated by Fig. 45.

At 10200 s the cladding temperature at level 4 reaches the zirconium oxidation threshold of 1273 K, and a H_2 partial pressure is generated in the gas volume. The density of H_2 from this Zr-steam reaction is shown as a surface in Fig. 46. This surface shows the H_2 buildup at different core levels and how the reaction moves down the fuel rods as cladding at lower levels heats to the oxidation threshold. The total amount of H_2 generated is presented in Fig. 47.

This generation increases exponentially until the partial pressure of H_2 builds up a mole-fraction of 80 to 90%, then steam starvation of the oxidation reaction begins to flatten the curve (see Fig. 47, between 11000 and 11880 s).

Figure 48 shows the history of the hydrogen mass transfer function associated with the cladding oxidation. This figure indicates that level 4 begins oxidizing first, followed by level 5, which spikes up sharply because of its large ballooned surface area but then drops back sharply as the reaction starves for steam. This steam starvation occurs both locally in level 5 and in the upstream source from level 4 since the oxidation in level 4 deprives level 5 of an additional convective source of steam. Level 3 begins oxidizing next, and after about 500 s it starves the level 4 and level 5 reactions until level 2 begins oxidizing at about 11200 s and starves all the downstream reactions. This situation persists until just before reflood at 11880 s, when the gas flow field reverses direction in level 5, supplying the previously starved oxidation reaction in level 5 with ample steam from the upper plenum. This reignites the oxidation in level 5 as shown in Fig. 48. Level 1 never realizes sufficiently high temperatures to initiate the oxidation reaction, as shown in Fig. 48.

Figure 49 shows a cladding temperature surface for ring 1, which is very similar in shape to the gas temperature surface of Fig. 37. Indeed since the core region heatup is very slow and the steam-hydrogen gas is near stagnation, the gas is close to thermal equilibrium with the cladding; the cladding is typically only a few degrees Kelvin above the gas temperature. At 10200 s the surface in Fig. 49 shows the exponential increase in cladding temperature in the upper core caused by the oxidation. This increase flattens out suddenly at about 11000 s as steam starvation begins to throttle the oxidation back to the low rate indicated in Fig. 48.

Figure 50 shows a baffle-wall surface temperature profile for the core region. This profile is again similar in shape to the cladding temperature (Fig. 49) and the gas temperature (Fig. 37). However, during this phase of the accident, the only significant heat-transfer mechanism for the baffle wall (as for the upper-support plate) is thermal radiation, dumping heat from the fuel rods and gas to the baffle-wall heat sink. Indeed, Fig. 51 shows the level 4 temperature drops between the cladding, gas, and baffle wall as heat moves from the fuel rods to the gas and structure. These three temperatures are almost identical at saturation until level 4 boils dry at about 9000 s. Afterwards they rise sharply and closely follow each other until reflood, when the fuel rods disintegrate and the gas begins to cool the baffle wall by convection.

At 10800 s the stainless steel control rods begin to melt ($T_m \cong 1700$ K) and drain to the bottom of the core. The inconel grid-spacers have previously melted ($T_m \cong 1500$ K) and do not present a hindrance to this control rod relocation. As this molten material drains to the bottom of the core, the water remaining in this location is quickly vaporized on contact. This water vaporization is shown in Fig. 52 by the sharp drop in the water volume fraction curve for level 1 (core bottom) at 11000 s. Figure 53 presents a velocity surface of this control rod material that shows a gravity-driven profile as the melt relocates down through the core and then stops (freezes) on top of the lower-support plate. The buildup of this material on the lower-support plate is shown by the corium volume fraction surface in Fig. 54, which indicates a maximum volume fraction of about 9%.

The major fluid-dynamic features of this fuel and control rod damage phase (9800 to 11880 s) are summarized as follows:

1. Cladding ballooning ocurrs at about 9800 s, decreasing the flow area in level 5 by 80%, decreasing the steam rise velocity from 1 cm/s to

1 mm/s, and greatly enlarging the zirconium surface area available for subsequent oxidation.

2. The Zr-steam oxidation reaction begins in level 4 at 10200 s and later spreads to all levels except level 1. The control mechanism that limits this cladding oxidation is the local and upstream steam starvation effects resulting from a large H_2 partial pressure.

3. The control rods begin to melt and relocate to the lower-support plate at 10800 s, building up a corium volume fraction of 9%, and vaporizing the remaining water in the bottom core mesh cell.

III.D.4. The Core Reflood and Fuel Rod Fragmentation Phase: 11880 to 14000 s

An unthrottled, high-pressure injection of coolant water (55.0 kg/s) is initiated by the operators at 11880 s, and is indicated by the step increase in the water velocity boundary condition given in Fig. 23c. The pressure surface in Fig. 36 reflects this reflood by the fall in pressure at 11880 s as core steam condenses on the rising water interface, and the hot gas, which is mostly H_2, is rapidly cooled (shown by the Fig. 55 surface).

The volume fraction of the gas is shown in Fig. 56. This surface shows the decrease of the gas fraction as the water level rises through the core, and indicates that roughly 1400 s (23 min) are required for the core to cool and refill completely with water. Level 5 retains a steam fraction of about 20% as upper-plenum steam falls to condense on the level 5 water interface.

Figure 57 presents a gas velocity surface that shows a steam velocity pulse in level 1 as cold water contacts hot fuel rods and structure. This saturated steam pulse or cloud billows up through the core and thermally shocks the previously embrittled fuel rods in levels 2 through 5 with rod cooling rates in excess of 5.0 K/s. The resulting fuel rod fragmentation showers the lower

core region with hot particles of fuel pellets and cladding, building up the debris bed, as indicated by the corium volume fraction surface in Fig. 58 and more quantitatively by the α_{corium} curves in Fig. 59. The fragmentation of the fuel rods fills the bottom three core mesh cells with debris and partially fills the level 4 cell. This debris bed configuration has incorporated the TMI-2 "quick-look" observations by allowing debris to leak out of the core until the top of the debris bed is roughly 5 feet below the upper-support plate. This "calibrated" bed then contains about 75800 kg (or 77%) of debris, out of a total generation (calculated by MIMAS) of 98500 kg, implying that 22700 kg (or 23%) of the debris is missing from the core region.

Despite this fuel rod damage, the HPI continues to refill the core, cooling the forming debris bed in the process. Figure 60 shows a surface of the debris temperature as it cools because of the increasing water level, the partially filled level 4 cell being the last to cool. Figure 61 shows a similar profile for the baffle-wall surface temperature.

Hydrogen generation during the initial phase of the core reflood is extremely important. As already discussed, at the onset of core reflood when the first pulse of saturated steam billows up through the core, the partial pressure of H_2 (that previously starved the cladding oxidation reaction) is swept out of the core, exposing the hot cladding (~2000 K) to a pure steam environment. This ignites the cladding oxidation reaction, as indicated by the hydrogen source function shown in Fig. 62. In this figure level 2 spikes first because this level is swept first by the steam cloud, followed sequentially by levels 3, 4 and 5, as the steam rises up through the core. The shut-off mechanism on these oxidation bursts is not steam starvation, but rather zirconium melting and relocation, or convective cooling of the zirconium by the saturated steam. Once the zirconium is cooled below the oxidation threshold

temperature of 1273 K, the H_2 concentration in the core (see Fig. 63) is soon reduced to zero because of the sweeping action of the steam. Figure 47, which indicates the total H_2 generated during the accident, shows that more than 75% of this generation occurs during the core reflood phase when the starvation mechanism discussed above is no longer a dominant phenomena.

Figure 64 shows the water volume fraction surface during the reflood phase as the water rises through the core. Note that even at late times the water fraction does not achieve a value of unity. This is because the water must share the available total volume with fuel and control rod debris.

The major fluid-dynamic features of this core reflood and fuel rod fragmentation phase (11880 to 14000 s) are summarized as follows:

1. A full capacity high-pressure injection is initiated that eventually refloods the core with water.
2. The embrittled fuel rods are thermally shocked and fragmented by rising saturated-steam clouds.
3. Small pieces of fuel rods fall into the lower core to form a debris bed that fills core levels 1 - 3 and partially fills level 4.
4. Hydrogen generation during this reflood is large because of the ample supply of steam rising with sufficient velocity to sweep the H_2 out of the core and mitigate the steam-starvation effect.

III.E. Hydrogen Blanketing

Section III.C describes the production of hydrogen gas during the fuel damage phase (9800 - 11880 s). Hydrogen is produced when steam comes in contact with hot fuel rod cladding. Continued production of hydrogen is proportional to the amount of water vapor available to oxidize the zirconium cladding. This raises the question, "Is the local concentration of H_2 near the cladding surface

an important factor in subsequent H_2 production?" In answering this question, the advection of steam through the core and the radial diffusion of H_2 in H_2O in the vicinity of a typical fuel rod is investigated.

During the boiloff phase, the average steam velocity (u) in the core ranges from 1 mm/s to 1 cm/s. Therefore, a reasonable upper bound for u is 1 cm/s. An average transit length (ℓ) during this time period is taken to be 2 m, about half the core depth. Hence, a minimum characteristic core advection time τ_a is

$$\tau_a = \frac{\ell}{u} = 200 \text{ s} \quad . \tag{51}$$

The diffusion of H_2 into H_2O is a function of (1) the diffusion coefficient D_{12} and (2) the geometry of the flow field.

For typical values of temperature and pressure, 1400 K and 1.38×10^7 Pa, $D_{12} = 9 \times 10^{-6}$ m^2/s. This value, calculated using a method given by Chapman and Cowling[44], is given in appendix A.

The axial flow between pins, for purposes of this discussion, is modeled as the flow between two vertical plates. The distance between plates (d) is obtained by preserving the gas volume to cladding surface area ratio,

$$d = \frac{2(p^2 - \pi r_r^2)\Delta z}{2\pi r_r \Delta z} = 6.83 \times 10^{-3} \text{ m} \quad , \tag{52}$$

where

p = rod pitch = 0.0145 m,

r_r = rod radius = 0.00545 m,

Δz = axial distance.

The axial Reynolds number (Re_z) for this flow, with pure steam, is

$$Re_z = \frac{\rho u z}{\mu} = \frac{(21.34)\ (0.01)z}{5.7 \times 10^{-5}} = 3744\ z \quad . \tag{53}$$

From boundary layer theory the laminar flat plate boundary layer thickness (δ) is given approximately as

$$\delta = \frac{5\ z}{\sqrt{Re_z}} \quad . \tag{54}$$

For the vertical plate model, a fully developed flow would occur over a length of 1.75×10^{-3} m. Hence, a fully developed flow exists over the depth of the core throughout this time period.

Finally, the concentration profile adjacent to a fuel pin is examined. A reasonable approximation here is to neglect the vertical advection of mass and consider only the diffusion of hydrogen. For the vertical plate model,

$$\frac{\partial C_{H_2}}{\partial t} = D \frac{\partial^2 C_{H_2}}{\partial r^2} \quad , \tag{55}$$

where

C_{H_2} = concentration of H_2 ($0 < C_{H_2} < 1$),

$C_{H_2}(0,t) = C_{H_2}(d,t) = C_s = 1$,

$C(r,0) = C_i = 0$,

C_i = initial concentration,

C_s = concentration at the surface (selected as a dimensionless 1), and

D = mass diffusion coefficient = 0.09 cm^2/s.

The concentration $C_{H_2}(r,t)$ is given by Chapman[45] as a series expansion:

$$C_{H_2}(r,t) = C_s + (C_i - C_s)\frac{2}{\pi}\sum e^{-(n\pi/d)^2 Dt}\left(\frac{1-(-1)^2}{n}\right)\sin\left(\frac{n\pi r}{d}\right) . \qquad (56)$$

The concentration level at the centerline (r = d/2) is shown in Fig. 65. Initially, no H_2 is present but by t = 2 s the H_2 concentration at the centerline has reached 97% of the surface concentration. Hence, H_2 concentration levels in the core are expected to lag the surface concentration by no more than 2 s. The characteristic advection time τ_a is 200 s - one hundred times the characteristic H_2 diffusion time.

Therefore, the assumption of a uniform spatial mixture of H_2 and H_2O is expected to introduce little error into the zirconium oxidation calculation.

III.F. Adjacent Core Structures Behavior

In this section the modeling of the vessel structures adjacent to the core and the choice of boundary conditions are discussed. The outer radial boundary for these calculations is the outer surface of the thermal shield, that is, the inner surface of the downcomer annulus. During the fuel damage phase (9800 - 11880 s) the thermal response of the structures will be examined for the base case and for the case of an adiabatic boundary condition applied to the outer radial boundary. The resulting effect on other key parameters is also given. Differences between the base case and adiabatic boundary case are seen to be negligibly small.

III.F.1. Wall Model

The baffle plates, core barrel, and thermal shield are modeled (see Fig. 66) as a single cylindrical shell with inner and outer radii of 1.6 m and 1.72 m, respectively. This wall forms the outer boundary of ring three at all axial levels (see Fig. 2). The radial conduction of heat in the wall is then computed, with the wall convecting heat with the gas and water fields, and exchanging radiant energy with adjacent structures, fluids, and fuel pins.

III.F.1.a. Wall Boundary Condition (Base Case). Because the flow in the downcomer is not directly modeled in this study, the following model is used to approximate the heat exchange between the outer wall surface (r = 1.72 m) and the water/gas fields in the downcomer:

1. Downcomer velocities (v) and mass flow rates (m) consistent with those values used as inflow boundary conditions to the core (see Sec. III.B) are obtained.
2. The downcomer pressure (P_b) and fluid temperatures are taken to be the pressure given by Fig. 24 and the corresponding saturation temperature (T_{sat}), respectively.
3. At each axial level the wall outer temperature (T_w) and the values of v, m, P_b, T_{sat} obtained in 1, 2 are used to calculate heat transfer coefficients h_v and h_ℓ.

III.F.1.b. Wall Boundary Condition (Adiabatic Case). An adiabatic boundary condition,

$$k \frac{\partial T}{\partial t}_{i=I} = 0, \tag{57}$$

is obtained by setting the heat transfer coefficients (h_v, h_ℓ) to zero.

III.F.2. Upper and Lower Core Support Plate Models

The support plates are modeled as flat circular slabs with outer radii of 1.6 m. The bottom plate is located at the bottom of level 1 and forms the lower boundary for all three rings. Similarly, the top plate is placed at the top of level 5 and forms the upper boundary in each ring. The axial conduction of heat in the plates is then computed with the plates convecting heat with the gas and liquid fields in the core, and exchanging radiant energy with adjacent structures, fluids, and fuel pins.

An adiabatic convective boundary condition is used for both plates: top of the upper plate and bottom of the lower plate. Radiant energy is exchanged with an equivalent black body at the core inflow or outflow fluid temperature. A summary of modeling parameters, material properties, and boundary conditions for all structural components is given in Table XVII.

III.F.3. Structural Thermal Response (9000 - 11880 s)

During the fuel rod damage phase of the transient (9800-11880 s) the structures heat in response to the hot steam in the core and from thermal radiation emmitted by the fuel rods. In the later stages of this phase ($t > 11000$ s), thermal radiation dominates the problem. The structural surfaces facing the core are seen to experience a rapid rise in temperature (Figs. 67-71, 73-78) as the core boils dry and the fuel rods heat.

The surface temperature rise is especially large in the top three wall levels and in the top plates, where the exposure to hot steam and fuel rods is longest and most severe. Peak surface temperatures in the top three wall cells are about 2000 K, with the highest temperatures being 2016 K in the base case and 2080 K in the adiabatic-boundary-condition case, both at level 4. The temperature history for the wall surface at level 4 is shown in Fig. 70. Several items are noted that apply, generally, to other wall and plate surfaces:

1. The use of an adiabatic boundary condition has very little effect on the surface temperature, even as late as t = 11880 s when reflood begins. This point will be discussed further. Further, the adiabatic boundary condition makes a negligibly small difference in other important core responses considered during this phase (Figs. 79-94).
2. The surface temperature is still rising at the beginning of reflood. This is expected because a finite amount of time is needed for the reflood water and steam to begin cooling the upper core structure.
3. The surface temperature for the top three wall levels (Figs. 69-71) and the upper-core support plate in all three rings (Figs. 73, 75 and 76) exceeds the melting temperature of 1700 K for 304 stainless-steel. The structural heat conduction model includes the heat of fusion (see item 4) but does not advect or relocate molten material. Hence, temperatues above 1700 K should be viewed qualitatively and only as an indication of melting. Figure 72, which shows the temperature profile in the hottest wall (level 4), indicates that the "melt front" penetrated 30% (3.6 cm) of the wall thickness. A shallower melt front was observed elsewhere.

Because the baffle plates, core barrel, and thermal shield were treated as one wall (instead of three) we conclude that actual temperatures would be higher on the inside (that is, in the baffle plates) and cooler toward the outside since the actual gaps between the three plates represent more heat transfer resistance. However, the primary cause of uncertainty in calculating the structural heat transfer is the modeling of radiation view (or shape) factors. The view factor from the fuel pins to the walls is especially critical (see

Sec. III.G). For this reason, the view factors and not the modeling of the structures or the boundary conditions are the principle source of error in computing wall temperatures.

4. For t > 11000 s the wall and top plate temperature profiles advance in a stair step manner. This, for the most part, reflects successive nodes reaching the melting point. Then, after the heat of fusion has been added, the temperature begins rising again.
5. Structures in level 1 (Figs. 67, 74, 76, 78) remain cool (T < 600 K) until t = 11100 s when the core finally boils dry (Fig. 91). Consequently, the surface temperatures are only 800 K at the end of this time period.

Initially, one might think that the radial adiabatic boundary condition would have more effect on increasing the inside wall surface temperatures than is observed (Figs. 67-71); even in the hottest wall, the difference was only 64 K. The explanation is the thickness, and hence heat capacity, of the wall. With a convective heat transfer coefficient, h_g = 100 W/m^2-K, the 12 cm thick wall has a time constant of more than 6000 s, that is, more than 6000 s are required for the average wall temperature to rise (or fall) by 1/e (37%) of its initial value provided the gas temperature and h_g are constant. Therefore, the length of the severe core damage phase (~ 2000 s) is too short for the adiabatic boundary condition to significantly effect maximum wall temperatures.

III.F.4. Cladding Temperatures

Cladding temperatures for rings 1 and 3 for both boundary conditions are shown in Figs. 79-88. The effect of the adiabatic boundary is again negligible. Further, the cladding temperatures show almost no change from ring 1 to 3. The maximum temperature is 2207 K in ring 1, level 4, at t = 11000 s. A complete discussion of fuel cladding behavior is found in Sec. III.C.

III.F.5. Other Flow Field Responses

In Figs. 89-94 the effect of the outer wall boundary condition on six additional important core responses is seen to be small. Hydrogen and Iodine exiting the core, gas, liquid and corium volume fractions in level 1, and gas temperature in level 5 are shown. Significant features here are the 102 kg of H_2 leaving the core before reflood (Fig. 89) and the boiling dry of the core by 11100 s. These features are discussed in detail in Sec. III.D.

III.G. Radiation Heat-Transfer Effects

In Sec. III.F a comparison was made between the base case and the adiabatic radial boundary condition case. Differences caused by the adiabatic condition were insignificant. In this section we will compare the base case and a model where no thermal radiation is allowed. Again this comparison is made during the fuel damage phase (9800 - 11880 s). Maximum surface temperatures for walls and plates are as much as 789 K lower for the no radiation case. Maximum cladding temperatures, by contrast, are as much as 567 K higher.

III.G.1. Structural Thermal Response

The effect of turning off the radiation is to cool the walls and plates. This effect is shown in the surface temperatures (Figs. 95-99, 101-106) and in the wall temperature profile at level 4 (Fig. 100). In the top part of the core (levels 3-5) the temperature difference is noticable as early as 9000 s because of the voiding of that part of the core and the subsequent rise in cladding temperatures. Because the radiation view factor from the wall to the pins (in ring 3) is very close to 1.0, the wall surface temperature is expected to be strongly coupled to the cladding temperatures, especially when radiation drives the problem ($T > 1000$ K). The surface temperature profiles for the base case verify this expectation.

In level 1 the maximum wall surface temperatures with and without radiation, are 798 K and 650 K. Only after t = 11100 s, when this level boils dry, does radiation have a noticeable effect. By contrast, higher levels boil dry sooner leading to elevated cladding temperatures, which in turn expose wall surfaces to significant thermal radiation at an earlier time (t = 10000 s). Figures 97 and 98 show peak temperatures without radiation of 1144 K and 1240 K, fully 789 K and 775 K lower than the base case counterparts. This vividly illustrates the role of radiation in heating the walls during the core damage phase.

Further, the wall temperatures are seen to be very sensitive to the way in which the radiation from the pins is modeled. Consider the wall at level 4 (Fig. 98). The maximum surface temperature at any level occurs here at t = 11880 s and is 2015.9 K. The view factor from the pins to the wall is

$$F_{PO} = 0.01387 \ . \tag{58}$$

A discussion and derivation of viewfactors is given in Appendix B. Changing F_{PO} to 0.01336 resulted in the maximum surface temperature dropping to 2009.5 K - a difference of 6.4 K. Thus a measure of the sensitivity is

$$\frac{1.78 \text{ K}}{1\% \text{ change in } F_{PO}} \ . \tag{59}$$

Using Eq. (59) to extrapolate to the case of no radiation ($F_{PO} = 0$) gives a peak surface temperature of 1838 K (177.9 K less than the base case). However, Fig. 98 shows that the peak temperature for the radiation case is actually 1240 K. Hence, not only is radiation the dominant feature in heating the walls

but the results are very sensitive (in a nonlinear fashion) to the modeling of the radiation view factors.

Upper and lower core-support plate temperatures are shown in Figs. 101-106. For the bottom plates (Figs. 102, 104, 106), radiation accounts for 163 K of the peak surface temperatures of 807 K, again reflecting the effects of water cooling until t = 11100 s. The top plates, like the upper wall levels, are exposed to elevated cladding temperatures (> 1000 K) for a longer time than structures in level 1. This is reflected in the peak plate temperatures of 1860 K, 1886 K, and 1846 K for rings 1, 2, and 3, respectively. The corresponding temperatures without radiation are 1411 K, 1411 K, and 1412 K, about 450 K cooler than the base-case values.

III.G.2. Cladding Temperatures

By prohibiting the transfer of energy by thermal radiation, the axial temperature distribution in the cladding is drastically changed, especially when radiation would normally have been the primary mode of heat transfer (T > 1000 K). Figures 107-116 show this to be the case. Levels 4 and 5 of ring 3, which boil dry first, indicate that if radiation were inhibited peak cladding temperatures would be as much as 567 K and 452 K above the base case values of 2038 K and 1773 K (Figs. 115 and 116), respectively. In the lower part of the core, just the opposite is true. Fuel pins that normally would have received radiation from the hotter pins above, are cooler by about 200 K. This illustrates the equilibration resulting from radiation heat transfer.

III.G.3. Other Flow Field Responses

As in the last section, neglecting radiation heat transfer raised the calculated cladding temperatures in the top part of the core by as much as 567 K. Such a high temperatures would hasten the production of hydrogen (Fig. 117). However, the 107.2 kg produced by t = 11880 s in the no-radiation

case is only 6 kg more than in the base case. Since H_2 production is severely throttled by steam starvation in the later fuel damage period, elevated cladding temperatures would have only this modest effect in additional H_2 production.

The core boils almost completely dry before radiation drives the problem. Hence, the liquid and gas volume fractions (Figs. 119, 121) are only slightly affected by the no-radiation condition case. The gas temperature at the top of the core (Fig. 122) again represents the phenomena discussed in the last subsection - without radiation the level 5 fuel rods would be hotter, thereby heating the gas by convection. The maximum temperatures shown on Fig. 122 are 2195 K and 1835 K, respectively.

IV. DAMAGE ASSESSMENT SUMMARY AND CONCLUSIONS

IV.A. Final Configuration of the Core Region

The best-estimate analysis of the TMI-2 accident described in the previous sections of this report present the following picture of the final damage configuration for the core region (see Fig. 123):

1. The upper 80% of the fuel rods in the core disintegrated during reflood, and therefore this portion of the core region is generally devoid of intact rods. Local effects may result in some exceptions to this assessment, some assembly end fittings with attached fuel rod stubs may remain attached to the upper tie plate. Likewise, because of the uncertainty in the radiation view factors used in this study, a number of the fuel rods around the core periphery may have remained cooler than calculated. Thus, some of these rods may have remained intact, although they would be badly damaged.
2. If contained entirely within the core, the debris from the disintegrated fuel and control rods would fill most of the core volume. However, because the small debris-particle sizes would be easily levitated by the post-accident operation of a reactor coolant pump, an appreciable fraction of the debris (about 23% as discussed in Sec. III.D.4) would be carried out of the core. This results in the voided volume existing in the upper part of the core observed by the TMI-2 "quick-look", with the lower part of the core being filled with debris, and with debris packed between the fuel rod stubs that remain attached to the bottom core support plate (illustrated in Fig. 123). The coolant flow maintained by the reactor coolant pump through the core for an extended time period after the accident may have caused

particle-particle abrasion in the debris bed. This, in turn, could result in smaller particle sizes and hence less debris in the core at the time of the "quick-look" than immediately after the accident.

3. The structural components immediately surrounding the core (upper support plate, lower support plate, baffle plates) have substained some melting, with local perturbations possibly resulting in small regions of greater damage (see Fig. 123). Surface melting probably occurred over central portions of the upper support plate and upper portions of the baffle plates, with a possibility of gross, through-structure melting at some locations. Undamaged structure adjacent to the core includes the lower support plate and lower baffle wall, which remained relatively cool throughout the accident.

The behavior of the debris bed during the reflood phase was modeled only in a preliminary manner. However, the results given above indicate that some metallic Zircalloy melting and Zr-UO_2 eutectic formation may have occurred in the debris bed, followed by draining of this liquid material to cooler portions of the vessel. Thus, some evidence of this process may be found near the bottom of the debris bed or in the lower plenum in the form of a sheet or layer of resolidified Zr-UO_2 eutectic.

IV.B. Uncertain Physical Processes

Based on the results of the best-estimate analyses and sensitivity studies presented above, the uncertainties in the following physical processes were judged to have the greatest potential impact on analytical studies of degraded core accidents of the TMI-2 type.

IV.B.1. Steam Starvation

This process affects both core power production and hydrogen generation during a degraded core accident. The functional relationship between the Zircalloy oxidation rate and ambient oxygen concentration and temperature needs to be determined. Both intact rod geometries and debris bed configurations are of interest. Also, steam-starvation effects on Zircalloy embrittlement rates need to be quantified.

IV.B.2. Eutectic Formation Effects

The formation of liquefied fuel can result in the fragmentation of fuel rods, and perhaps in the mitigation of zirconium oxidation for fuel that does not disintegrate. The conditions under which liquefied fuel ruptures the fuel rod cladding need to be quantified under prototyical degraded core environments. Also, the mechanism by which liquefied fuel formation affects the fuel rod temperatures needs to be investigated.

IV.B.3. Fission Product Release and Transport

The importance of the fission-product source term during a degraded core accident dictates that fission-product release and transport be analyzed by the most accurate and reliable methods available. While the methods employed by the MIMAS code in this analysis have a general experimental basis, more precise mechanistic fission-product release and transport models under development should provide even more accurate assessments in the future.

IV.B.4. Molten Absorber Material-Fuel Interactions

Extensive dissolution of fuel rod cladding by molten AgInCd could result in extensive loss of core geometry and debris formation significantly earlier during a degraded core accident than previously considered. On the positive side, this interaction could also terminate Zircalloy oxidation at an earlier time, resulting in a lower hydrogen production during degraded core accidents. Currently planned experiments should better define these effects.

IV.B.5. Brittle Fuel Rod Fragmentation Due to Thermal Shock and Debris Behavior

The rate and coherence of embrittled fuel rod bundle fragmentation during reflood is of interest for both debris bed formation and debris heat tranfer to the coolant. The debris size distribution is also important for analyzing debris bed behavior. Again, degraded core experiments are currently planned to provide information on these processes. Finally, several uncertain aspects of debris bed behavior of importance, especially in regard to hydrogen production, are oxidation kinetics for debris, steam starvation, and cooling rate.

IV.C. Important Data to be Obtained From TMI-2

This section lists a number of observations and measurements that could be made during the defueling of the TMI-2 core that would aid in better defining some of the uncertain physical processes. This list is not intended to be comprehensive; recommendations for the more obvious observations such as condition of remaining fuel rods, evidence of structural melting and identification of deposited fission products have been made by a number of workers. Rather, this list of TMI-2 observations and measurements is intended to improve specific uncertainties in the MIMAS models that were used in this study.

IV.C.1. Core Samples of the Debris Bed

The need for a measurement of debris-particle size and general composition is obvious. However, particular attention should be paid to the distribution of particle sizes and composition of the debris as a function of depth in the debris bed. Because the lighter debris particles were levitated after the accident, a large number of smaller particles should be at the top of the debris bed. Also, the MIMAS code predicts control rod melting before any fuel rod breakup, so that most of the control rod debris should be located at the bottom of the debris bed. Extensive interaction between the conrol rod material and the fuel rods would result in the control material being more evenly distributed throughout the debris bed. Finally, evidence of a layer (instead of particles) of resolidified Zr-UO_2 eutectic near the bottom of the debris bed would indicate material melting, possibly caused by Zircalloy particle oxidation.

IV.C.2. Oxidation Configuration of Debris

The contribution of the debris particles to the core heat of oxidation and hydrogen production is of great interest. If the debris particles show evidence of significant, uniform surface oxidation, then significant debris oxidation occurred in TMI-2, and hydrogen and heat generation by the debris before cooling would be significant. However, if the debris particles are relatively unoxidized, or show evidence of oxidation on one side only (for example, debris from oxidized cladding), then debris cooling probably occurred too rapidly for significant heat or hydrogen generation. Finally, the thickness of the oxide layer on uniformly oxidized debris could give some insight into the oxidation kinetics of Zr debris beds.

IV.C.3. Elemental Composition of Debris

The MIMAS analysis of the TMI-2 accident predicts that relatively little liquefied fuel formed during the accident, and the liquefied fuel that did form was contained within the fuel rods until reflood. The first prediction can be checked by examining the debris bed for relative amounts of frozen Zr-UO_2 eutectic particles. Evidence of early rod breakup and candling caused by liquefied fuel formation can be found by searching for debris particles consisting of frozen eutectic attached to layers of Zr and ZrO_2. If found, the position of such particles within the debris bed could give information on the time and location of liquefied fuel-induced rod disintegration (see Sec. IV.C.1).

In a similar manner, evidence of fuel rod-control material interaction can be found from debris particle elemental composition. A relatively large number of Zr-In or Zr-Ag debris particles, more or less uniformly distributed throughout the debris bed, would indicate extensive fuel-control material interaction and possible fuel rod breakup before reflood.

REFERENCES

1. W. Bixby, et. al., "Assessment of Core Integrity," NSAC Memo IAG-TA-0004 (April 1979).

2. Babcock and Wilcox Internal Memo, G. A. Meyer (April 1979).

3. J. R. Ireland, P. K. Mast, T. R. Wehner, P. B. Bleiweis, W. L. Kirchner, and M. G. Stevenson, "Preliminary Calculations Related to the Accident at Three Mile Island," Los Alamos National Laboratory report NUREG/CR-1353, LA-8273-MS (March 1980).

4. K. H. Adrian and D. G. Cain, "TMI-2 Accident Core Heat-Up Analysis," NSAC-24 (January 1981).

5. J. R. Ireland, T. R. Wehner, and W. L. Kirchner, "Thermal Hydraulic and Core Damage Analyses of the TMI-2 Accident," Nuclear Safety 22, No. 5, (Sept. - Oct. 1981) pp. 583-593.

6. "TRAC-PF1: An Advanced Best-Estimate Computer Program for Pressurized Water Reactor Analysis," to be published as a Los Alamos Report.

7. "MATPRO-Version 11 (Revision 1), A Handbook of Materials Properties for Use in the Analysis of Light Water Reactor Fuel Rod Behavior," NUREG/CR-0947, TREE-1280, Rev. 1 (1980).

8. F. J. Erbacher, "LWR Fuel Cladding Deformation in a LOCA and Its Interaction With Emergency Core Cooling," Proc. of ANS Topical Meeting on Safety Aspects of Fuel Behavior, Vol. 2, Sun Valley, Idaho (August 1981) pp. 100-113.

9. D. A. Powers and R. O. Meyer," Cladding Swelling and Rupture Models for LOCA Analysis," NUREG-0630 (1980).

10. A. W. Longest, "Multirod Burst Test Program Progress Report for January - June, 1981," NUREG/CR-2366 Vol. 1, ORNL/TM-8058 (December 1981).

11. J. L. Crowley, "Multirod Burst Test Program Progress Report for July - December 1981," NUREG/CR-2366 Vol. 2, ORNL/TM-8190 (March 1982).

12. V. F. Urbanic and T. R. Heidrick, "High Temperature Oxidation of Zircalloy-2 and Zircalloy-4 in Steam," J. of Nuc. Mat. 75 (1978) pp. 251-261.

13. H. Ocken, R. R. Biederman, C. R. Hahn, R. E. Westerman, "Evaluation Models of Zircalloy Oxidation in Light of Recent Experiments," Zirconium in the Nuclear Industry (4th conference), ASTM STP 681, American Society for Testing and Materials (1979) pp. 514-536.

14. U. S. Nuclear Regulatory Commission, "Technical Bases for Estimating Fission Product Behavior during LWR Accidents," NUREG-0772 (1981).

15. G. W. Parker, G. E. Creek, and A. L. Sutton, "Aerosol Release and Transport", ORNL Quarterly Report for July-Sept. 1981.

16. G. W. Parker, G. E. Creek, and A. L. Sutton, "Aerosol Release and Transport", ORNL Quarterly Report for Dec. 1981.

17. D. L. Hagrman, "Materials Properties Models for Severe Core Damage Analysis", EGG-CDD-5801 (May 1982).

18. R. P. Elliott, Constitution of Binary Alloys: 1st Supplement (McGraw-Hill, New York, 1965) p. 7.

19. M. Hanson, Constitution of Binary Alloys (McGraw-Hill, New York, 1958) p. 20.

20. C. Politis, "Untersuchungen in Dreistoffsystem Uran-Zirkon - Sauerstoff," KfK 2167 (1979).

21. Walter Turk, "Design and Verification of Modular Computer Models for Interpreting Rod Melting Experiments," IKE Report 4-94 (February 1980) pp. 50-52.

22. S. Hagan and H. Malauschek, "Bundle Experiments on the Meltdown Behavior of P.W.R. Fuel Rods," Transactions of the American Nuclear Society 33, San Francisco, Calif. (November 11-15, 1979) pp. 505-506.

23. S. Hagen, "Out-of-Pile Experiments on the High Temperature Behavior of Zry-4 Clad Fuel Rods," to be published in the Proceedings of the 6th International Conference on Zirconium in the Nuclear Industry, Vancouver, B. C., Canada (June 28 - July 1, 1982).

24. S. Hagen, "Out-of-pile Bundelexperimente Zur Untersuchung Schwerer Kernschaden - Zielsetzung und Versuchmatrix," KfK Primarbericht, PNS-Nr. 657182 (January 1982).

25. J. M. Broughton, "Severe Core Damage Assessment Program Experiment Requirements," EGG-TFBP-5067 (March 1980).

26. R. W. Garner, G. T. Liv, and B. J. Buescher, "Feasibility Analysis for the Severe Fuel Damage Test Program in the Power Burst Facility," EGG-TFBP-5296 (October 1980).

27. E. H. Karb, L. Sepold, P. Hofmann, C. Peterson, G. Schanz and H. Zimmerman, "KfK in-Pile Tests on LWR Fuel Rod Behavior During the Heatup Phase of a LOCA," KfK Report No. 3028 (October 1980).

28. B. Carnahan, H. A. Luther, J. O. Wilkes, Applied Numerical Methods (John Wiley and Sons, New York, 1969).

29. R. C. Weast and M. J. Astle, eds., CRC Handbook of Chemistry and Physics (CRC Press, Roca Raton, FL., 1979).

30. J. W. Daily and D. R. F. Harleman, Fluid Dynamics (Addison-Wesley Publishing Company, 1966).

31. D. A. Mandell, "The TRAC-PD2 Boiling Curve," Los Alamos National Laboratory report LA-UR-80-3679 (January 1981).

32. R. B. Bird, W. E. Stewart, and E. N. Lightfoot, Transport Phenomena (John Wiley and Sons, 1960).

33. A. Cronenberg, "Fission Product Release/Transport/Deposition Models for MIMAS," Engineering Science and Analysis report ESA/LANL-102 (May 1982).

34. J. H. Mahaffy, "A Stability Enhancing Two-Step Method for One-Dimensional Two-Phase Flow," Los Alamos report LA-7951-MS (1979).

35. J. A. Moore, "A Mechanistic Debris Bed Packing Model," LA-9619-MS (1983).

36. R. Siegel and J. R. Howell, Thermal Radiation Heat Transfer (McGraw-Hill Book Company, 1972) pp. 550-558.

37. TRAC-PD2: An Advanced Best-Estimate Computer program for Pressurized Water Reactor Loss-of-Coolant Accident Analysis," Los Alamos report LA-8709-MS (1981).

38. P. J. Roache, Computational Fluid Dynamics (Hermosa Publishers, Albuquerque, NM, 1972).

39. "Analysis of Three Mile Island - Unit 2 Accident," NSAC-80-1 (March 1980).

40. "TMI-2 Accident Core Heat-Up analysis, A Supplement," NSAC-25 (June 1981).

41. T. R. England and W. B. Wilson, "TMI-2 Decay Power: LASL Fission-Product and Actinide Decay Power Calculations for the President's Commission on the Accident at Three Mile Island," LA-8041-MS (October 1979).

42. C. A. Pelletier, "Iodine-131 Behavior During the TMI-2 Accident," NSAC-30 (Sept. 1981).

43. S. Glasstone and A. Sesonske, Nuclear Reactor Engineering (Van Nostrand Co., Princeton, NJ, 1967) p. 37.

44. S. Chapman and T. G. Cowling, The Mathematical Theory of Non-Uniform Gases, 2nd Ed. (Cambridge University Press, London, 1952).

45. A. J. Chapman, Heat Transfer, 2nd Ed. (Macmillan, New York, 1967).

46. F. M. White, Viscous Fluid Flow (McGraw-Hill, New York, 1974).

47. E. R. Gilliland, Ind. Eng. Chem. 2b (1934) p. 681.

48. W. M. Visscher and M. Bolsterli, "Random Packing of Equal and Unequal Spheres in Two and Three Dimensions," Nature 239, No. 5374 (October 27, 1972) pp. 504-507.

APPENDIX A

DIFFUSION OF HYDROGEN GAS INTO STEAM

For dilute gases, the kinetic theory yields the following expression for the binary-diffusion coefficient D_{12} between species 1 and 2 (H_2 and H_2O in this case)[44]:

$$D_{12} = \frac{0.001858\ T^{3/2}\ [(m_1 + m_2)/m_1m_2]^{1/2}}{P\sigma_{12}^2\Omega_D} \qquad \text{(A-1)}$$

where

D_{12} = binary-diffusion coefficient, cm^2/s,

m_1, m_2 = molecular weights of two gases,

Ω_D = diffusion collision integral,

σ_{12} = effective collision diameter, Å,

T = temperature, K, and

P = pressure, atm.

Eq. (A-1) is used to find D_{12} for H_2 and H_2O. The relevant physical properties are

m_{H_2}	= 2.016	m_{H_2O}	= 18.016,
σ_{H_2}	= 2.827Å	σ_{H_2O}	= 2.641Å,
$T_{\varepsilon_{H_2}}$	= 59.7K	$T_{\varepsilon_{H_2O}}$	= 809.1K, and
T	= 1400 K	P	= $1.38 \times 10_7$ Pa (136 atm).

Now:

$$\sigma_{12} = (\sigma_1 + \sigma_2)/2 = 2.734\text{Å}, \text{ and}$$

$$\Omega_D = T^{*-0.145} + (T^* + 0.5)^{-2} \qquad \text{(see Ref. 46)}$$

where

$$T_{\varepsilon_{12}} = (T_{\varepsilon_1} T_{\varepsilon_2})^{1/2} = 219.8 \text{ K},$$

$$T^* = T/T_{\varepsilon_{12}} = 6.37,$$

and then

$$\Omega_D = 6.37^{-0.145} + (6.37 + 0.5)^{-2} = 0.7857.$$

Substitution of these results into Eq. (A-1) gives

$$D_{12} = 0.0905 \text{ cm}^2/\text{s} \quad .$$

Another method (see Ref. 47) gives a comparable value

$$D_{12} = 0.0405 \text{ cm}^2/\text{s} \quad .$$

APPENDIX B

RADIATION VIEWFACTORS FOR CORE GEOMETRY

For simple geometries, radiation view factors may be found by a straightforward application of the general theory described in Sec. II.C. For more complicated geometries, the mathematical difficulties may become formidable, requiring numerical methods or other approximate techniques.

Despite simple geometric shapes, calculation of view factors in cells containing fuel pins is not simple. Most of the radiation leaving a typical fuel pin will strike a nearby fuel pin. But what about the fraction that leaves the pin array and strikes core structures? The determination of view factors is a critical parameter in predicting the maximum temperatures attained by core structures.

Here, a heuristic approach to determining the view factors within computational cells containing fuel pins is adopted. A view factor, denoted as F_{ij}, is the fraction of radiant energy leaving surface i that strikes surface j. In the development that follows, the following subscripts are used within a computational cell:

B - bottom surface

I - inner radial surface

O - outer radial surface

P - fuel pin surface

T - top surface

The view factor F_{PB}, for example, denotes the viewfactor from the pins to the bottom surface within a given computational cell. In a similar manner, surface areas are denoted as A_I for the area of surface i.

In the development that follows, the viewfactors for a cell in ring 3 will be estimated. The calculation in this outer ring is especially important since the outer surface is a wall (see Sec. III.F for a discussion of adjacent core structures). A similar procedure is used for finding viewfactors in rings 1 and 2.

1. Surface Areas

$A_B = 2.18\ m^2$,

$A_I = 5.14\ m^2$,

$A_0 = 7.16\ m^2$,

$A_P = 521.37\ m^2$, and

$A_T = 2.18\ m^2$,

where A_B and A_T are net areas (axial area minus cross-sectional area of pins).

2. Estimate F_{PI} and F_{PO}

From geometric considerations a reasonable assumption is that the peripheral pin area that faces the inner (outer) cell boundary sees only that boundary. Interior pins will, except for a small fraction, see only other pins. Hence, we expect F_{PI} and F_{PO} to be close to

$$F_{PO} = \frac{A_I}{A_P} = 0.00986 \quad \text{and} \tag{B-1}$$

$$F_{PO} = \frac{A_0}{A_P} = 0.01373 \quad . \tag{B-2}$$

3. Estimate F_{PB} and F_{PT}

Any cell containing pins is essentially full of pins. Therefore, to a first approximation; F_{BO}, F_{BI}, F_{IO}, F_{TI}, and F_{BT} will be very small compared to F_{BP} and F_{TP}. This is readily apparent considering the depth-to-pitch ratio (50.5:1). Thus, to a first approximation

$$F_{BP} = F_{TP} = 1 \quad . \tag{B-3}$$

4. Estimate F_{PB} and F_{PT}

Applying the reciprocity theorem and the results obtained in Eq. (B-3),

$$F_{PB} = F_{BP} \frac{A_B}{A_P} = 0.00418 \quad \text{and} \tag{B-4}$$

$$F_{PT} = F_{PB} = 0.00418 \quad . \tag{B-5}$$

Another estimate for F_{PB} may be obtained by enclosing a single fuel with a hollow cylinder. The hollow cylinder represents, in the mean, all neighboring fuel pins. With this model then, radiation emerging from the bottom of the annulus is F_{PB} and radiation out the top is F_{PT}. From geometric considerations, a reasonable upper bound for the radius of the hollow cylinder (r_c) is 0.015 m. The exact view factor for this geometry is

$$F_{PT} = F_{PB} = 0.00454 \tag{B-6}$$

By comparison, a choice of $r_c = 0.0109$ m in Eq. (B-6) gives

$$F_{PT} = F_{PB} = 0.00267 \tag{B-7}$$

Examining Eqs. (B-5) - (B-7) we estimate F_{PB} and F_{PT} as

$$F_{PB} = F_{PT} = 0.004 \tag{B-8}$$

5. Estimate F_{PP}

Using the enclosure property and the results from items 2-4,

$$F_{PP} = 1 - F_{PI} - F_{PO} - F_{PB} - F_{PT}$$

$$= 1 - .00986 - 0.01373 - 2\ (0.004) = 0.9684 \tag{B-9}$$

This confirms the idea that nearly all of the radiation from the fuel pins strikes other fuel pins.

6. Calculation of Viewfactors

The above set of viewfactors can, in principle be used to assemble a complete viewfactor matrix. In addition to the geometric requirements (addressed in items 1-5) the viewfactors must obey the reciprocity theorem

$$F_{ij}\ A_i = F_{ji}\ A_j \tag{B-10}$$

and the enclosure property

$$\sum_j F_{ij} = 1 \tag{B-11}$$

for each surface i, where n is the total number of surfaces.

The resulting viewfactor matrix from Eq. (B-11) yields n equations. Since the viewfactors from the top and bottom surfaces are identical (by symmetry), the five equations in the present case may be reduced to four. Here, the equation for the top surface is eleminated. Application of Eq. (B-10)

establishes that no more than seven viewfactors will have to be found in order to assemble the complete viewfactor matrix. Three viewfactors are required by cell geometry to be zero:

$$F_{BB} = 0 \quad , \tag{B-12}$$

$$F_{IO} = 0 \quad , \tag{B-13}$$

$$F_{II} = 0 \quad . \tag{B-14}$$

Since the radial distribution of radiation leaving the pin array is of most concern, we require

$$F_{PI} = \frac{A_I}{A_O} F_{PO} \tag{B-15}$$

which simply says that pin radiation striking the inner and outer cell boundaries will be divided up in proportion to area.

The viewfactor F_{OO} is easily computed with an exact formula. This leaves five unknowns: F_{PP}, F_{PO}, F_{PB}, F_{OB}, F_{BI}; F_{PP} may then be assumed or, using the results of Eqs. (B-8) and (B-15), estimated as

$$F_{PP} = 1 - \frac{A_I + A_O}{A_P} - 2\,(0.004) \tag{B-16}$$

The four viewfactor equations now contain four unknowns. Upon rearrangement the equations are,

$$F_{PO} = \frac{A_I + A_0\ (1-F_{00}) + A_P\ (1 - F_{PP})}{2A_B + A_P\ (1 + A_I/A_0)} \tag{B-17}$$

$$F_{PB} = 1/2\ \{1 - F_{PP} - (1 + A_I/A_0)\ F_{PO}\} \tag{B-18}$$

$$F_{0B} = 1/2\ \{1 - F_{00} - (A_P/A_0)\ F_{PO}\} \tag{B-19}$$

$$F_{BI} = (A_I/A_B)\ F_{0B} \tag{B-20}$$

As it turns out, only a narrow range of F_{PP} values yield a physically meaningful solution:

$$0.96 \leq F_{PP} \leq 0.99 \quad . \tag{B-21}$$

This confirms the earlier F_{PP} estimate Eq. (B-9) and is consistent with values given by Eq. (B-16).

The complete viewfactor matrix, for cells in each of the three rings, is given in Table XVIII.

TABLE I.a
FUEL AND CONTROL ROD SECTION MORPHOLOGICAL FORMS

Form	Description	Occurred in TMI-2
Intact (Fuel) and Control	Intact geometry, thermal expansion distortion only.	Yes
Ballooned	Breached cladding, gross cladding expansion away from fuel, possible fuel pellet disruption.	Yes
Eutectic Containing	Liquified fuel contained within ZrO_2 shell.	Yes
Embrittled	β-Zr contains sufficient oxygen that embrittlement criteria of Sec.II.A. are met.	Yes

TABLE I.b
FUEL AND CONTROL ROD SECTION MORPHOLOGICAL FORMS

Form	Description	Occurred in TMI-2
Directly Disintegrating (Fuel and Control)	Embrittled section which is transforming to debris upon cooling or cladding melting.	Yes
Atrophied	Partial pellet stack which remains after liquified fuel and cladding particles drain away.	No
Perforated	Perforated cladding surrounding atrophied pellet stack. May contain or be emitting liquified fuel.	No
Candled	Rod section coated with molten or frozen debris. Insufficient debris to form debris bed.	No

TABLE II
VALUES FOR A AND B FOR CLADDING LAYER GROWTH RATES (Eqs. 1 and 3)

Layer	A	B
ZrO_2 1270K<T<1850K	1.126×10^{-6} $m^2/5$	1.502×10^5 J/mol
T>1850K	2.074×10^{-6} $m^2/5$	1.332×10^5 J/mol
Oxygen Uptake 1270K <T<1850K	16.8 $(Kg/m^2)^2$	1.668×10^5 J/mol
T>1850K	30.9 $(Kg/m^2)^2$	1.381×10^5 J/mol
Outer O_2 Stab. α–Zr	7.615×10^{-5} $m^2/5$	2.05×10^5 J/MOL
Inner O_2 Stab. α–Zr	7.0×10^{-5} $m^2/5$	1.84×10^5 J/mol
O_2 Stab. α–Zr Next to Fuel	3.2×10^{-5} $m^2/5$	2.05×10^5 J/mol

TABLE III
RELEASE COEFFICIENT CONSTANTS A AND B FOR
I, Cs, Te, Xe, and Kr (Eq. 7)

Species	1000C < T ≤ 2200C		T > 2200C	
	A	B	A	B
I	1.65×10^{-7}	.00667	1.89×10^{-5}	.00451
Cs	1.65×10^{-7}	.00667	1.89×10^{-5}	.00451
Te	2.96×10^{-8}	.00667	1.17×10^{-5}	.00404
Xe	1.65×10^{-7}	.00667	1.89×10^{-5}	.00451
Kr	1.65×10^{-7}	.00667	1.89×10^{-5}	.00451

TABLE IV
MATERIALS CONSERVED IN THE FLUID DYNAMICS SOLUTION

Material		Velocity Field	Energy Field
Number	Name		
1	steam	gas	gas
2	hydrogen	gas	gas
3	I	gas	gas
4	Cs	gas	gas
5	Kr	gas	gas
6	Xe	gas	gas
7	Te	gas	gas
8	Water	Water	Water
9	UO_2	Corium	Corium
10	Zr	Corium	Corium
11	ZrO_2	Corium	Corium
12	Steel	Corium	Corium

TABLE V.a
TMI-2 ACCIDENT EVENTS

Time (s)	Event Description
0	loss of main-feedwater to the steam generators (no auxfeed available)
6	pressurizer relief valve opens on high pressure and sticks open
10	reactor scram on a high pressure signal from the pressurizer
41	high pressure injection pump 1A was started manually
121	high pressure injection pump 1C started automatically on low pressure
193	high pressure injection system is set up for manual control
498	auxfeed water now available to the steam generators
563	letdown flow initiated

TABLE V.b
TMI-2 ACCIDENT EVENTS

Time (s)	Event Description
4380	loop B reactor coolant pumps stopped
6037	loop A reactor coolant pumps stopped
8520	pressurizer relief valve block valve closed
9600	high pressure injection terminated
10440	reactor coolant pump 2B operated for 20min
11880	full capacity high pressure injection
12080	reactor building radiation monitor off-scale

TABLE VI.a
VESSEL COMPONENT DESCRIPTION

Component Number	DESCRIPTION	Number of Cells
93	Vessel Cold Leg Connection	2
95	Downcomer	6
97	Lower Plenum, Left	3
98	Lower Plenum, Right	3
99	Core	3
88	Upper Plenum	3
89	Vessel Hot Leg Connection	2
87	Upper Plenum	3
86	Vent Valve	2
92	Top of the Downcomer	2
85	Upper Head	4

TABLE VI.b
LOOP A COMPONENT DESCRIPTION

Component Number	DESCRIPTION	Number of Cells
16	Vessel Hot Leg Connection	3
11	Hot Leg Candy Cane	12
22	Pressurizer	4
25	Pressurizer PORV	2
26	PORV Boundary	1
12	Steam Generator	22
73	Cold Leg Loop Seal	7
13	Primary Pump	2
14	Cold Leg HPI Tee	4
19	HPI Nozzle	1
33	Primary Pump	2
34	Cold Leg HPI Tee	4
39	HPI Nozzle	1
35	Letdown Flow Tee	4
31	Letdown Flow Nozzle	1
94	Vessel Cold Leg Connection	2
70	Main Feedwater Inlet	1
57	Steam Generator Downcomer	8
58	Steam Exit Annulus	7
71	Steam Exit	1
72	Auxillary Feedwater Inlet	1

TABLE VI.c
LOOP B COMPONENT DESCRIPTION

Component Number	DESCRIPTION	Number of Cells
6	Vessel Hot Leg Connection	3
1	Hot Leg Candy Cane	8
2	Steam Generator	22
63	Cold Leg Loop Seal	3
3	Primary Pump	2
4	Cold Leg HPI Tee	4
9	HPI Nozzle	1
60	Main Feedwater Inlet	1
47	Steam Generator Downcomer	8
48	Steam Exit Annulus	7
61	Steam Exit	1
62	Auxillary Feedwater Inlet	1

TABLE VII
CALCULATED STEADY STATE PARAMETERS
FOR NORMAL REACTOR OPERATION

PARAMETER	TRAC PREDICTION	PLANT DATA
VESSEL TEMPERATURE RISE (K)	27.3	27.8 +
HOT LEG TEMPERATURE (K)	590.8	590.8 +
COLD LEG TEMPERATURE (K)	563.5	563. +
MAXIMUM CLADDING TEMPERATURE (K)	611.6	
PUMP PRESSURE RISE (bar)	8.2	8.4 *
VESSEL PRESSURE DROP (bar)	4.2	4.06 +
CORE PRESSURE DROP (bar)	1.06	1.1 +
CORE FLOW RATE (kg/s)	1.76×10^4	1.74×10^4 *
LOOP A FLOW RATE (kg/s)	8.85×10^3	8.69×10^3 *
LOOP B FLOW RATE (kg/s)	8.80×10^3	8.69×10^3 *
PRESSURIZER PRESSURE (bar)	150.2	151. *
PRESSURIZER LEVEL (m)	6.44	
STEAM GEN EXIT FLOW (kg/s)	725.	
MAIN FEED WATER FLOW (kg/s)	725.	

* FROM B & W for TMI

+ FROM DUKE POWER for OCONEE

TABLE VIII
SIGNIFICANT TMI-2 CORE INITIAL CONDITIONS

RING 1

AXIAL LEVEL	POWER FACTOR *	BURNUP (MWd/MT)	NEUTRON FLUENCE (cm^{-2})
1	0.598	1592	8.97×10^{21}
2	1.514	4030	2.27×10^{22}
3	1.682	4479	2.52×10^{22}
4	1.582	4211	2.37×10^{22}
5	1.289	3430	1.93×10^{22}

* Power Factor x Avg. Core Power = Avg. Power in Core Cell

TABLE VIII (Cont.)

RING 2

AXIAL LEVEL	POWER LEVEL *	BURNUP (MWd/MT)	NEUTRON FLUENCE (cm^{-2})
1	0.514	1367	7.70×10^{21}
2	1.288	3455	1.95×10^{22}
3	1.442	3839	2.16×10^{22}
4	1.355	3608	2.03×10^{22}
5	1.104	2940	1.66×10^{22}

* Power Factor x Avg. Core Power = Avg. Power in Core Cell

TABLE VIII (Cont.)

RING 3

AXIAL LEVEL	POWER FACTOR *	BURNUP (MWd/MT)	NEUTRON FLUENCE (cm^{-2})
1	0.382	1017	5.73×10^{21}
2	0.968	2576	1.45×10^{22}
3	1.076	2683	1.61×10^{22}
4	1.011	2692	1.52×10^{22}
5	0.082	2193	1.24×10^{22}

* Power Factor x Avg. Core Power = Avg. Power in Core Cell

TABLE VIII (Cont.)

RING 1

Fission Product Inventory (Kg)

I	CS	XE	KR	TE
0.051	0.251	0.360	0.170	0.026
0.129	0.634	0.911	0.429	0.066
0.144	0.705	1.012	0.477	0.073
0.135	0.662	0.952	0.448	0.069
0.110	0.540	0.775	0.365	0.056

TABLE VIII (Cont.)

RING 2

Fission Product Inventory (KG)

I	CS	XE	KR	TE
0.044	0.022	0.309	0.146	0.022
0.111	0.544	0.781	0.368	0.057
0.123	0.604	0.867	0.409	0.063
0.116	0.568	0.815	0.384	0.059
0.094	0.463	0.664	0.313	0.048

TABLE VIII (Cont.)

RING 3

Fission Product Inventory (KG)

I	CS	XE	KR	TE
0.032	0.160	0.230	0.108	0.017
0.083	0.405	0.582	0.274	0.042
0.092	0.451	0.647	0.305	0.047
0.086	0.424	0.608	0.287	0.044
0.074	0.345	0.496	0.233	0.036

TABLE IX
CORE DECAY POWER FOR TMI-2

Cooling Time	Total Decay Power, MW
1.00+0 s	1.68+2
4.00+0 s	1.48+2
1.00+1 s	1.30+2
4.00+1 s	1.03+2
1.00+2 s	8.60+1
4.00+2 s	6.52+1
1.00+3 s	5.28+1
1.00+0 h	3.56+1
2.00+0 h	2.84+1
5.00+0 h	2.14+1
1.00+1 h	1.74+1
2.00+1 h	1.39+1
5.00+1 h	8.93+0
1.00+2 h	6.59+0
2.00+2 h	4.55+0
5.00+2 h	2.59+0
1.00+3 h	1.56+0
2.00+3 h	8.83−1
5.00+3 h	3.23−1
1.00+0 y	1.40−1
1.00+4 h	1.15−1
2.00+4 h	4.35−2
5.00+4 h	1.13−2

TABLE X
CLADDING BALLOONING FLOW BLOCKAGE PARAMETERS FOR TMI-2

Core Ring (Fig.1)	Burst Time (s)	Burst Temp. (K)	Single Rod Burst Strain (pct.)	Max. Assembly Blockage (pct.)
1	9605	1105	79	73
2	9685	1110	90	82
3	9970	1190	89	81

TABLE XI
FISSION PRODUCT RELEASE FROM TMI-2 FUEL

Species	Beginning Inventory (kg)	Inventory At Reflood (kg)
Xe	5.518	4.359
Kr	2.600	2.054
I	.784	.619
Cs	3.842	3.035
Te	.400	.378

TABLE XII
TIMES FOR CONTROL ROD DISINTEGRATION IN EACH CORE SECTION

All Rings					
Axial Level	1	2	3	4	5
Time (s)	–	115905	111245	108885	110645

TABLE XIII
TIMES FOR FUEL ROD DISINTEGRATION IN EACH CORE SECTION

Ring 1					
Axial Section	1	2	3	4	5
Disintegration Time after Reflood (s)	–	7.58	10.25	5.38	0.03
Ring 2					
Axial Section	1	2	3	4	5
Disintegration Time after Reflood (s)	–	22.80	10.25	36.15	0.03
Ring 3					
Axial Section	1	2	3	4	5
Disintegration Time after Reflood (s)	–	4.06	10.25	9.91	32.66

TABLE XIV
CLADDING BALLOONING SENSITIVITY STUDY

VARIABLE	BASE CASE	2% MAX. FLOW AREA REDUCTION
H_2 Production up to Reflood (Kg)	109	104
Total Fission Products Release up to Reflood (Kg)	1.720	1.656
Number of Core Cells in which Fuel Embrittled	12	12
Time Period over which Embrittlement Occurred (s)	10709–11610	10684–11604

TABLE XV
STEAM STARVATION SENSITIVITY STUDY

VARIABLE	BASE CASE	LOW STEAM STARVATION
H_2 Production up to Reflood (Kg)	109	130
Total Fission Products Release up to Reflood (Kg)	1.720	3.029
Number of Core Cells in which Fuel Embrittled	12	12
Time Period over which Embrittlement Occurred (s)	10709–11610	10693–11543

TABLE XVI
SENSITIVITY STUDY RESULTS FOR CLADDING
OXIDATION BEYOND FORMATION LIQUEFIED FUEL

VARIABLE	BASE CASE	OXIDATION WITH LIQUIFIED FUEL
H_2 Production up to Reflood (Kg)	109	119
Total Fission Products Release up to Reflood (Kg)	1.720	1.910
Number of Core Cells in which Fuel Embrittled	12	12
Time Period over which Embrittlement Occurred (s)	10709–11610	10709–11595

TABLE XVII
STRUCTURAL MODEL PARAMETERS

Component	Material	Melting Point (K)	Thickness (cm)	Radii r_i (m)	Radii r_o (m)	Number of Computing Nodes	Initial Temp. at all nodes (K)	Base Case Boundary Conditions: Convection	Base Case Boundary Conditions: Black Body Temp. that boundary radiates to
Wall*	304ss	1700	12	1.6	1.72	11	560	Approximate downcomer properties (see text)	Radiation not considered
Lower Core Support Plate	304ss	1700	12.2	0	1.6	11	560	Adiabatic	core inlet fluid temp.
Upper Core Support Plate	304ss	1700	8.4	0	1.6	11	560	Adiabatic	core outlet fluid temp.

* composite of baffle plates, core barrel, and thermal shield

TABLE XVIII
VIEWFACTORS (F_{ij}) FOR CELLS WITH FUEL PINS

Receiving Surface (J) / Radiating Surface (i)	Pins	Bottom	Top	Inside	Outside	
Pins	.96735	.00484	.00484	.00000	.02296	
Bottom	.85180	.00000	.00000	.00000	.14820	
Top	.85180	.00000	.00000	.00000	.14820	Ring 1
Inside	.93164	.03418	.03418	.00000	.00000	
Outside	.93164	.03418	.03418	.00000	.00000	
Pins	.96606	.00509	.00509	.00792	.01584	
Bottom	.82362	.00000	.00000	.05879	.11759	
Top	.82362	.00000	.00000	.05879	.11759	Ring 2
Inside	.91597	.04202	.04202	.00000	.00000	
Outside	.91597	.04202	.04202	.00000	.00000	
Pins	.96827	.00409	.00409	.00969	.01387	
Bottom	.97882	.00000	.00000	.02066	.00052	
Top	.97882	.00000	.00000	.02066	.00052	Ring 3
Inside	.98250	.00875	.00875	.00000	.00000	
Outside	.98250	.00016	.00016	.00000	.01719	

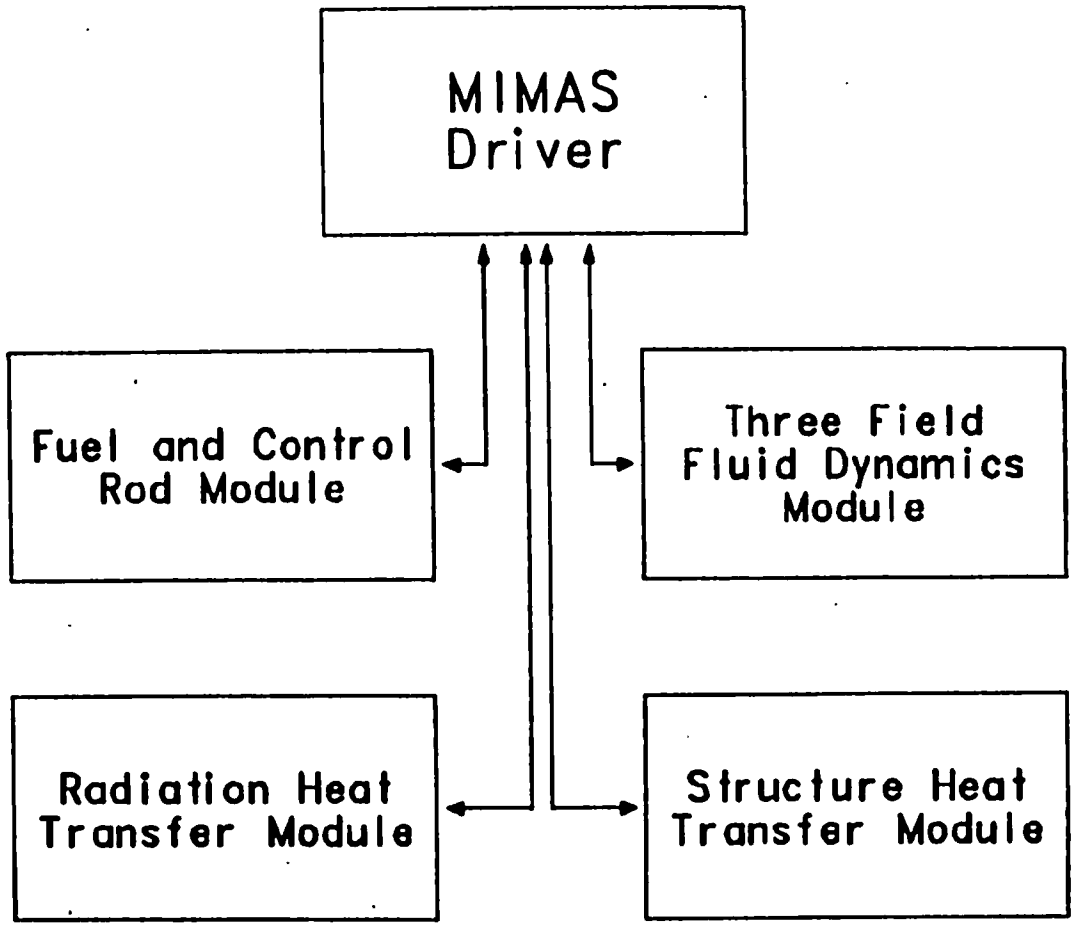

Fig. 1.
General program structure of MIMAS.

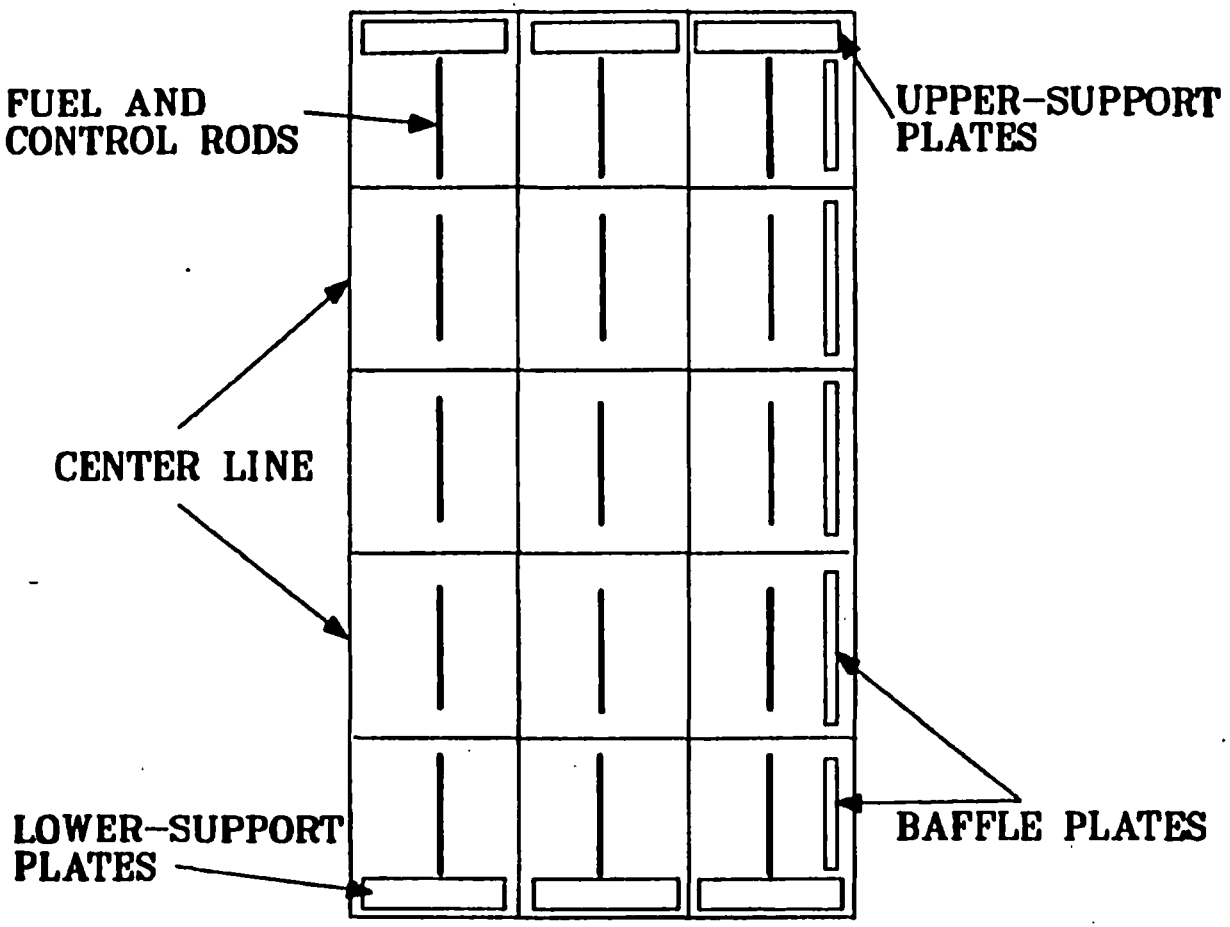

Fig. 2.
MIMAS modeling schematic of the core region: five axial levels, 3 radial rings, heat slabs for the support plates and baffle walls, and fuel and control rod sections in each cell. Cell level numbers increase from bottom to top and ring numbers increase from left to right.

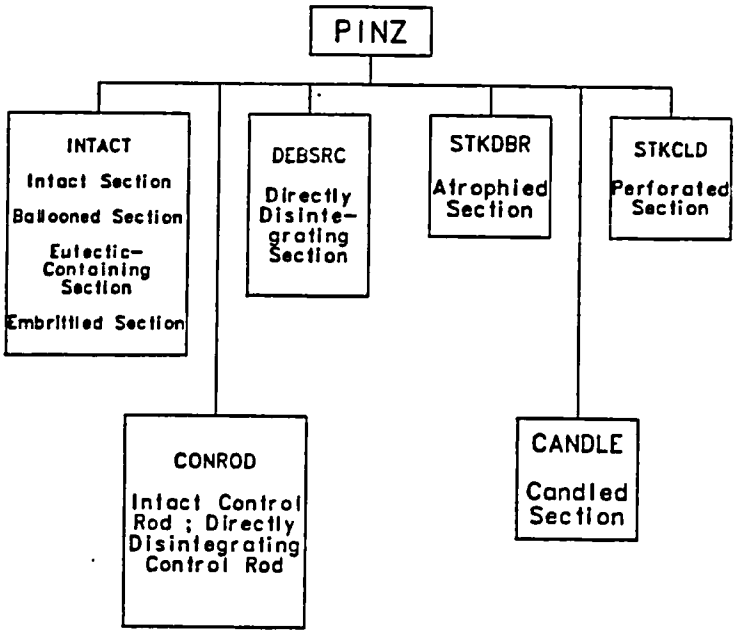

Fig. 3.
MIMAS fuel rod model subroutines called by PINZ.

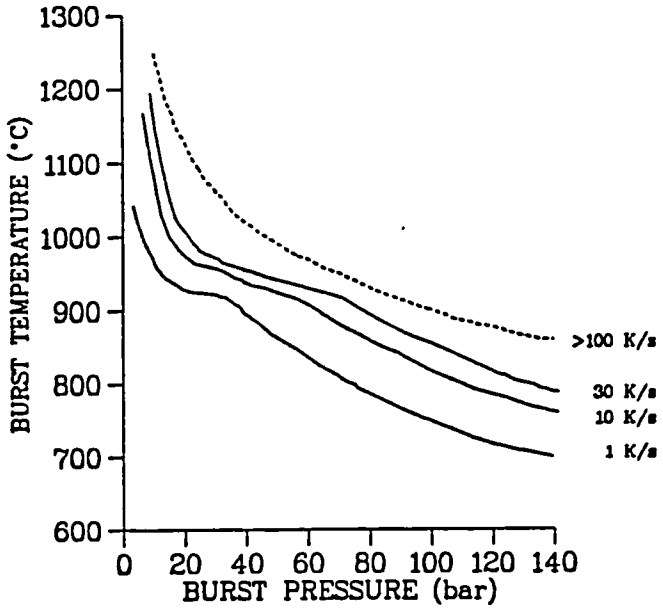

Fig. 4.
REBEKA burst temperature/pressure correlation.

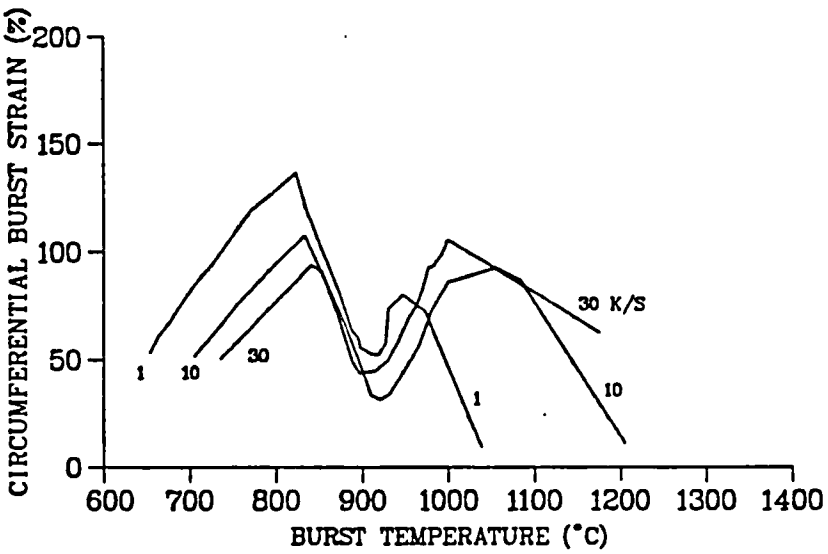

Fig. 5.
REBEKA burst temperature/strain correlation.

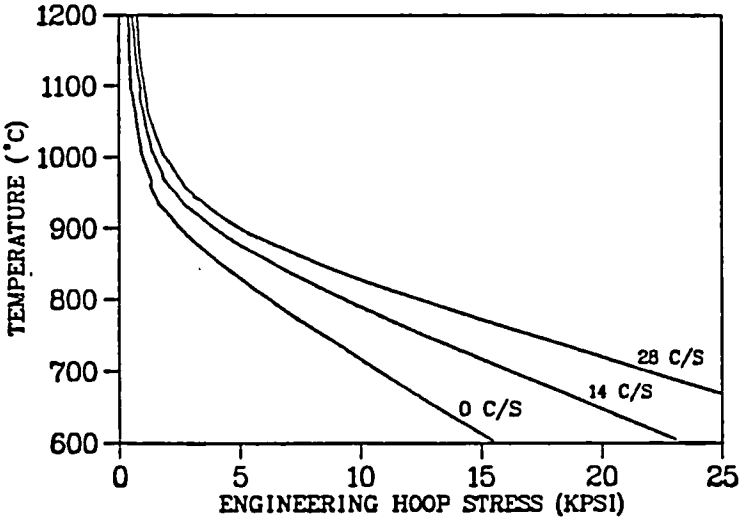

Fig. 6.
NUREG-0630 burst temperature/stress correlation.

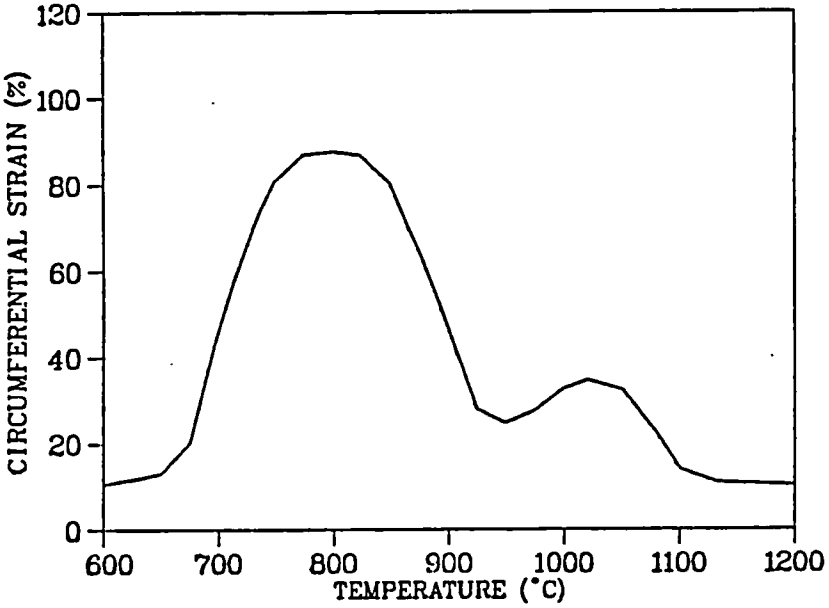

Fig. 7.
NUREG-0630 burst temperature/strain correlation (low temperature ramp rates).

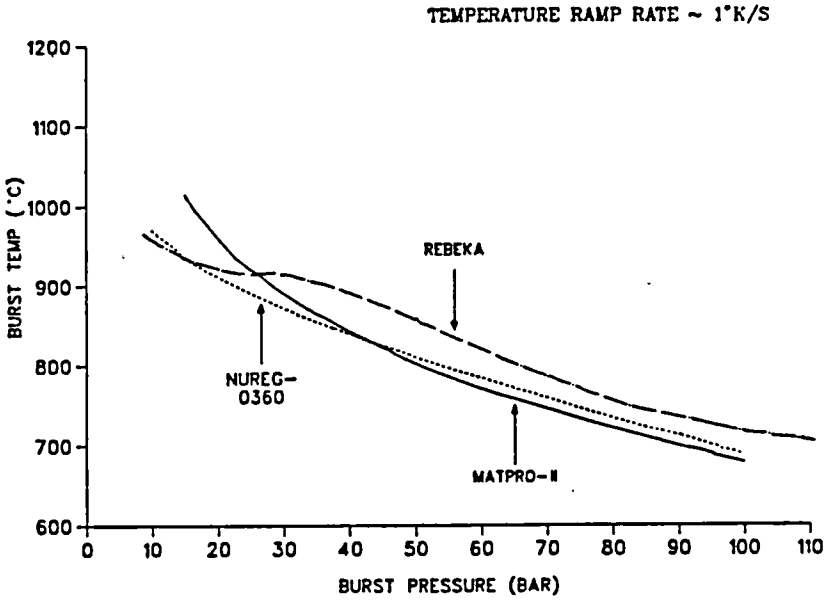

Fig. 8.
Comparison of burst temperature/pressure correlations at low temperature ramp rates.

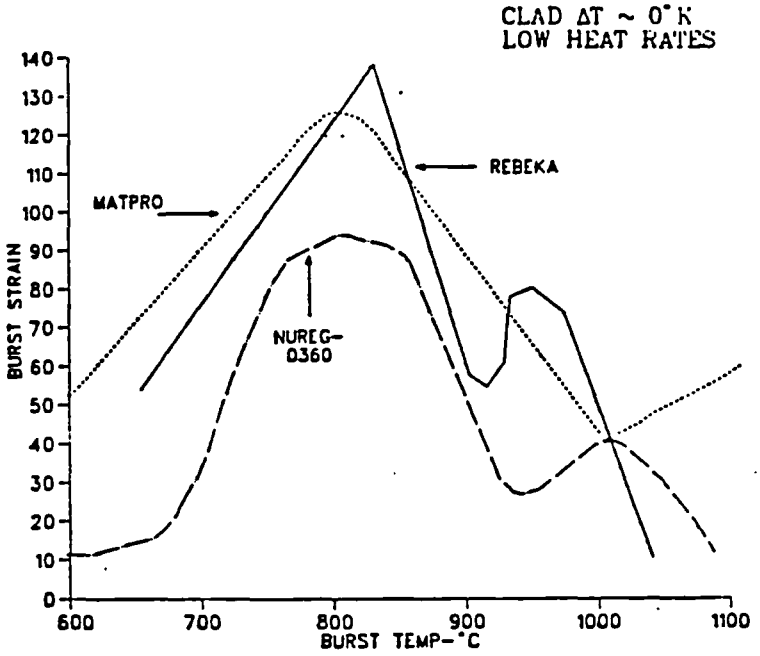

Fig. 9.
Comparison of burst temperature/strain correlations at low temperature ramp rates.

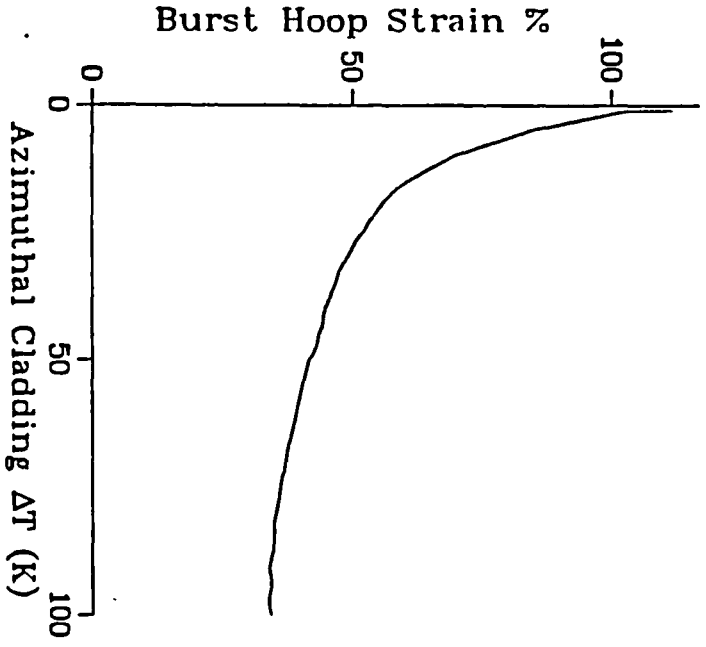

Fig. 10.
Cladding burst strain versus circumferential temperature gradient (from Ref. 9).

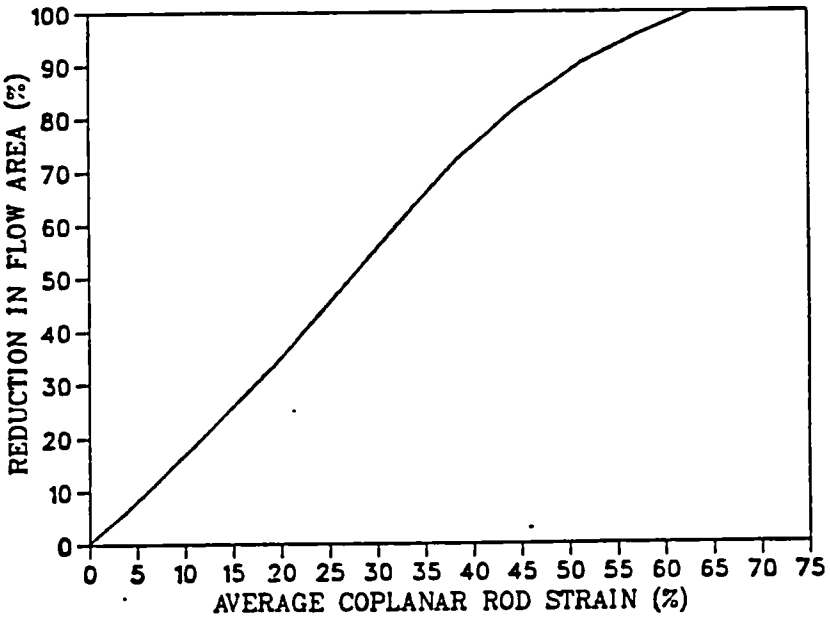

Fig. 11.
rod bundle flow area versus coplannar rod circumferential strain (from Ref. 10).

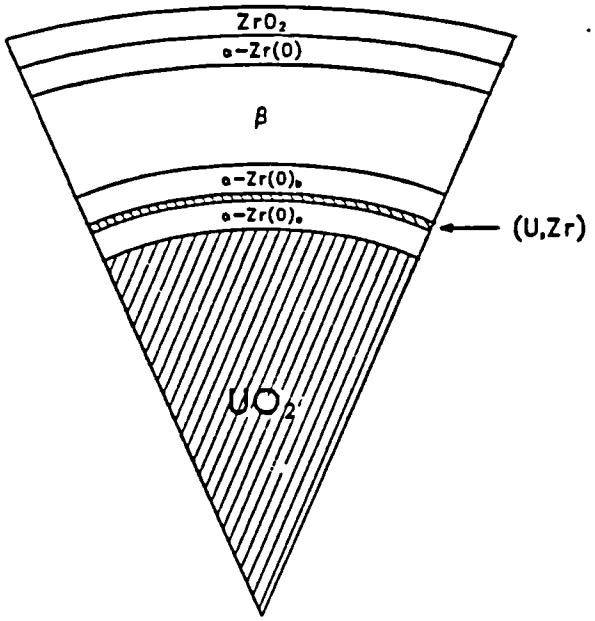

Fig. 12.
Cross section of fuel rod with oxidized cladding (Ref. 7).

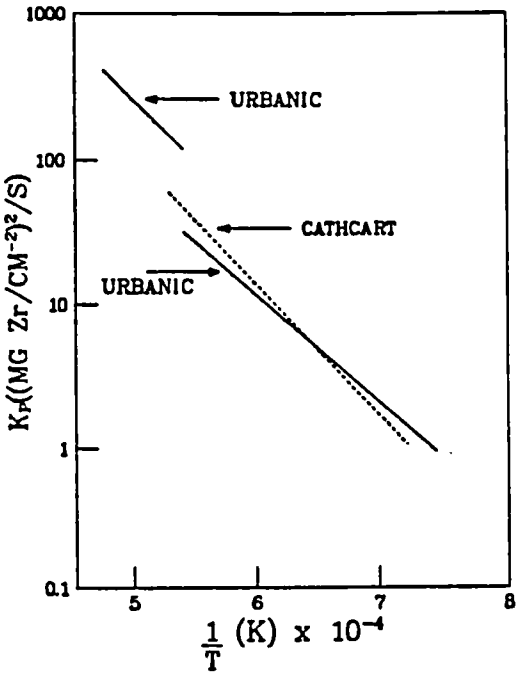

Fig. 13.
Comparison of Urbanic and MATPRO-11 (Cathcart) Zr-O reaction rates.

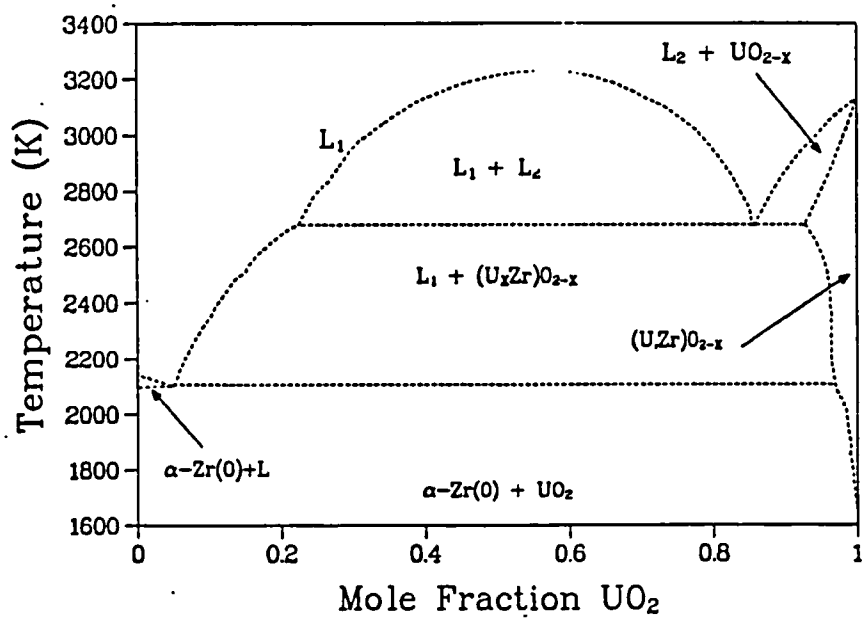

Fig. 14.
Zr-UO_2 binary phase diagram.

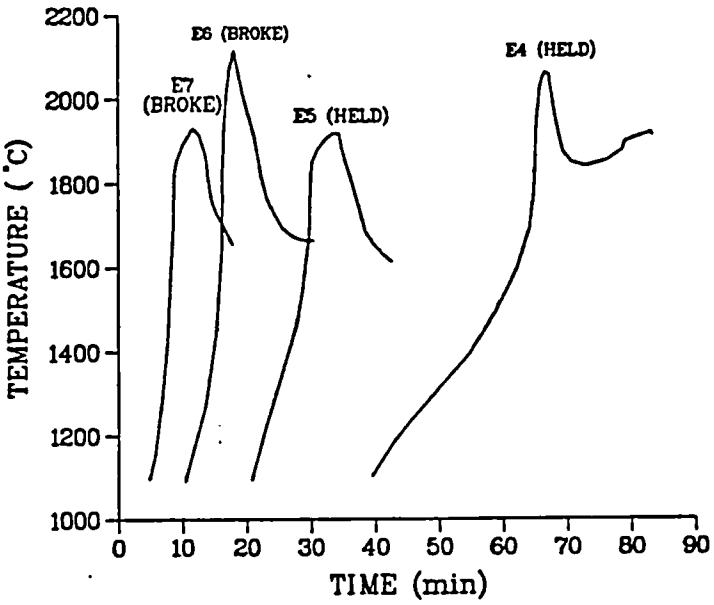

Fig. 15.
Cladding temperature histories in electrically heated ESSI fuel rod tests (Ref. 23).

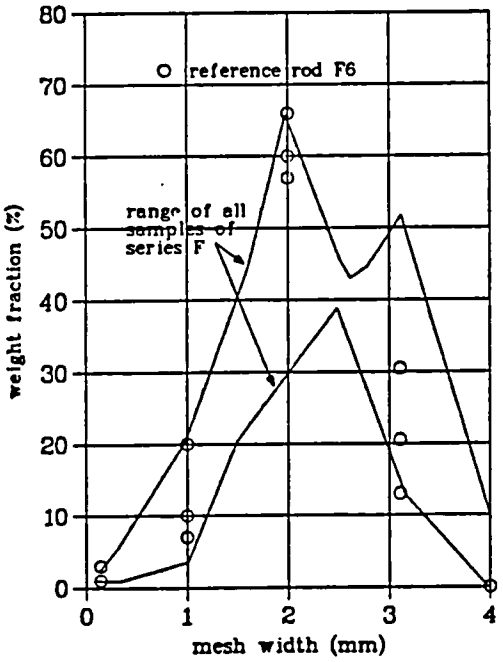

Fig. 16.
Debris particle size distributions from KfK series F tests (Ref. 27).

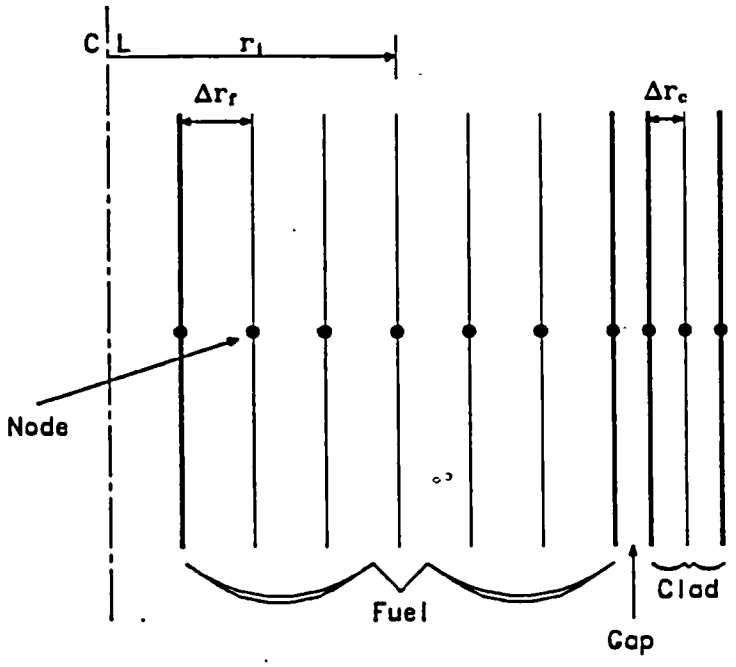

Fig. 17.
Finite-difference noding scheme for MIMAS fuel rod thermal model.

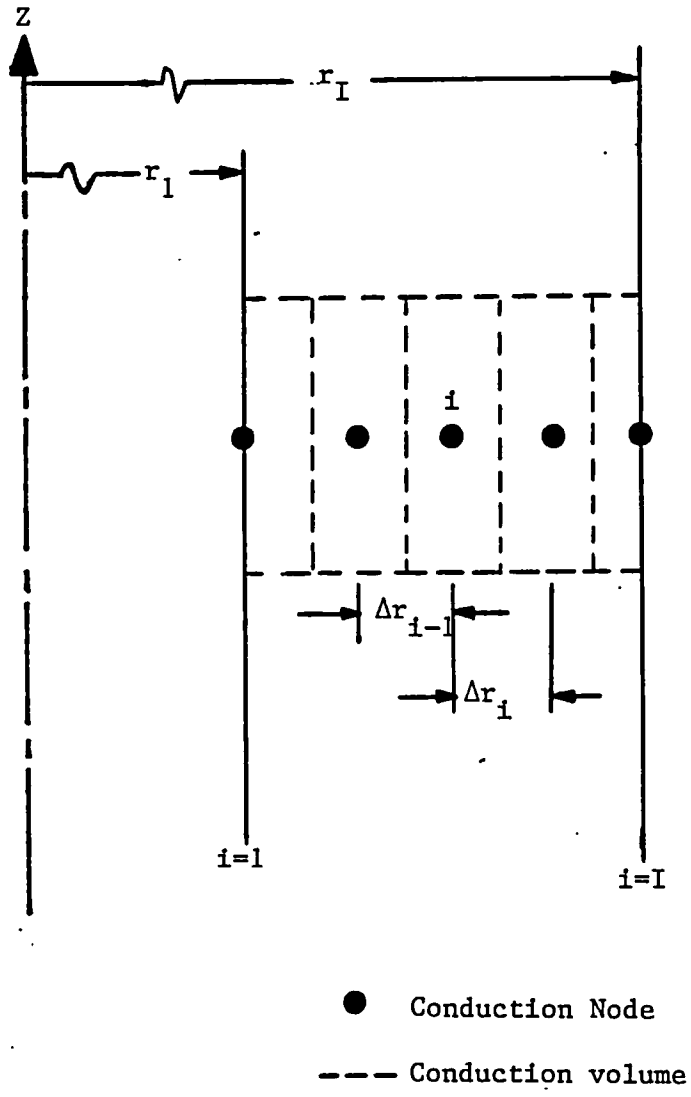

Fig. 18.
Cylindrical Wall Geometry

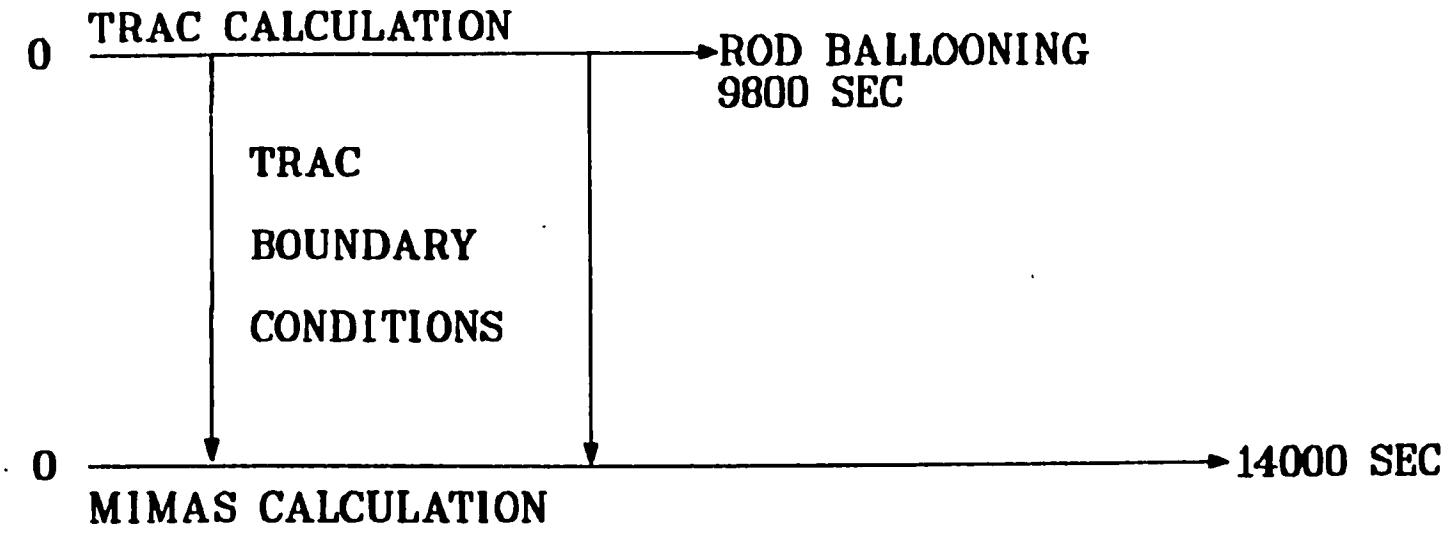

Fig. 19.
Schematic of the calculational scheme using the TRAC and MIMAS codes in a tandem operation.

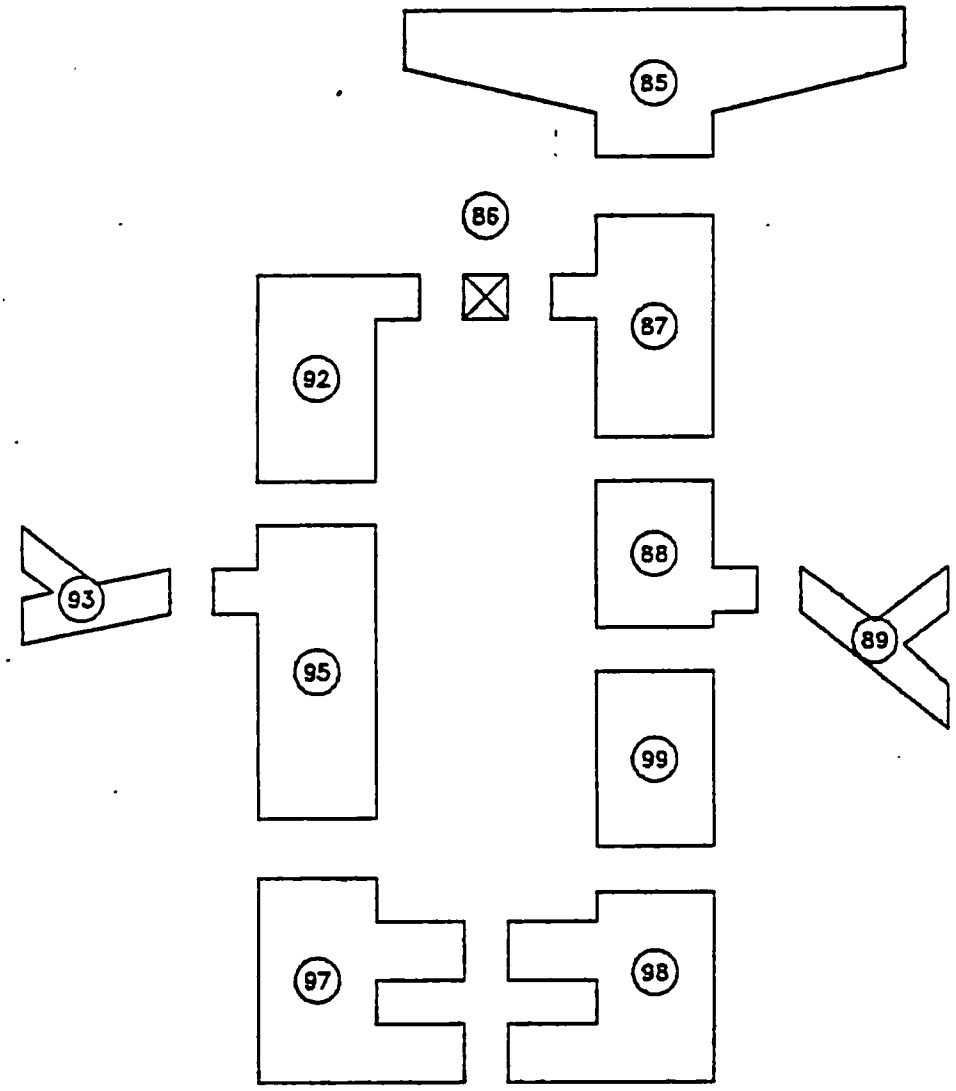

Fig. 20a.
TRAC modeling schematic of the reactor vessel.

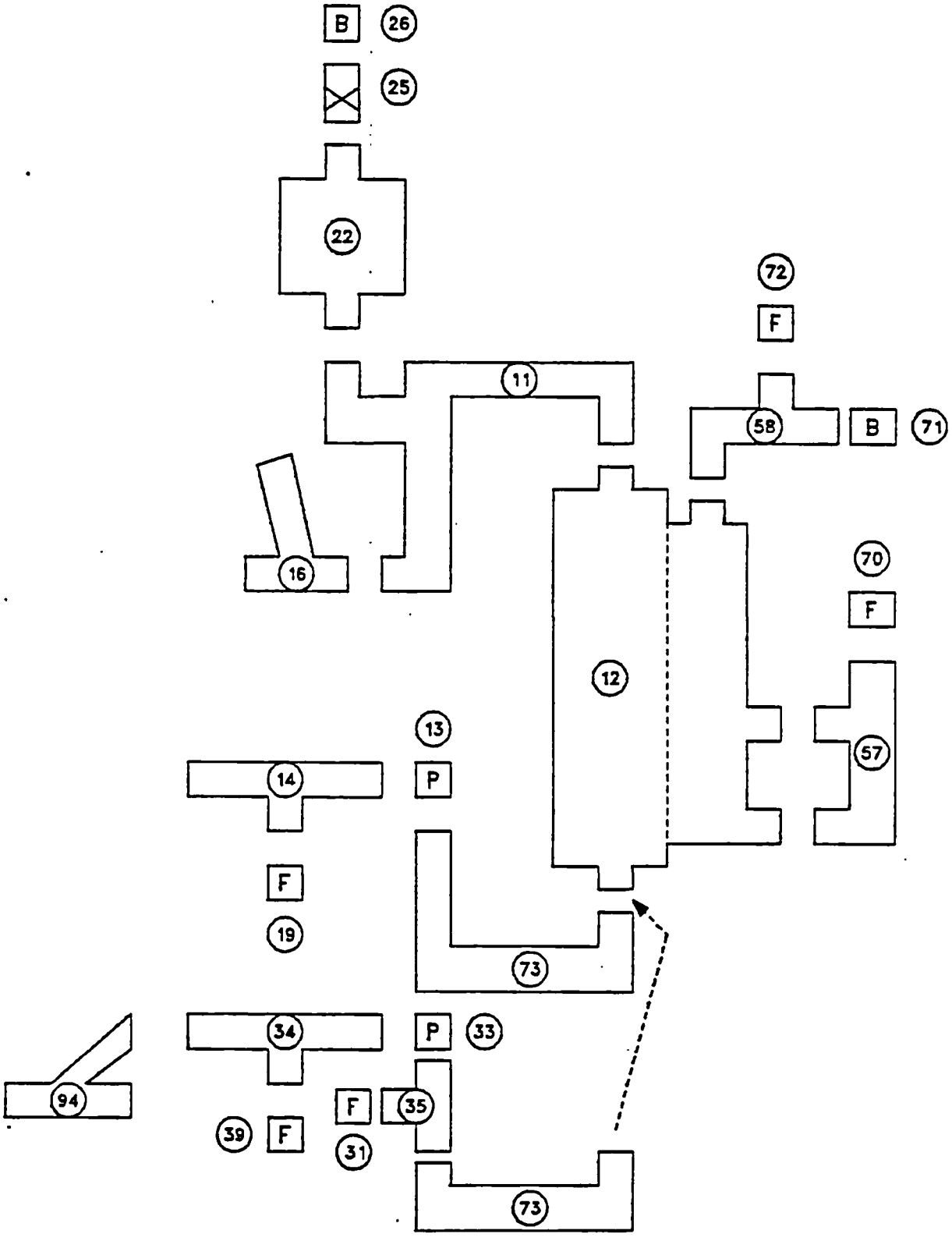

Fig. 20b.
TRAC modeling schematic of the loop-A components.

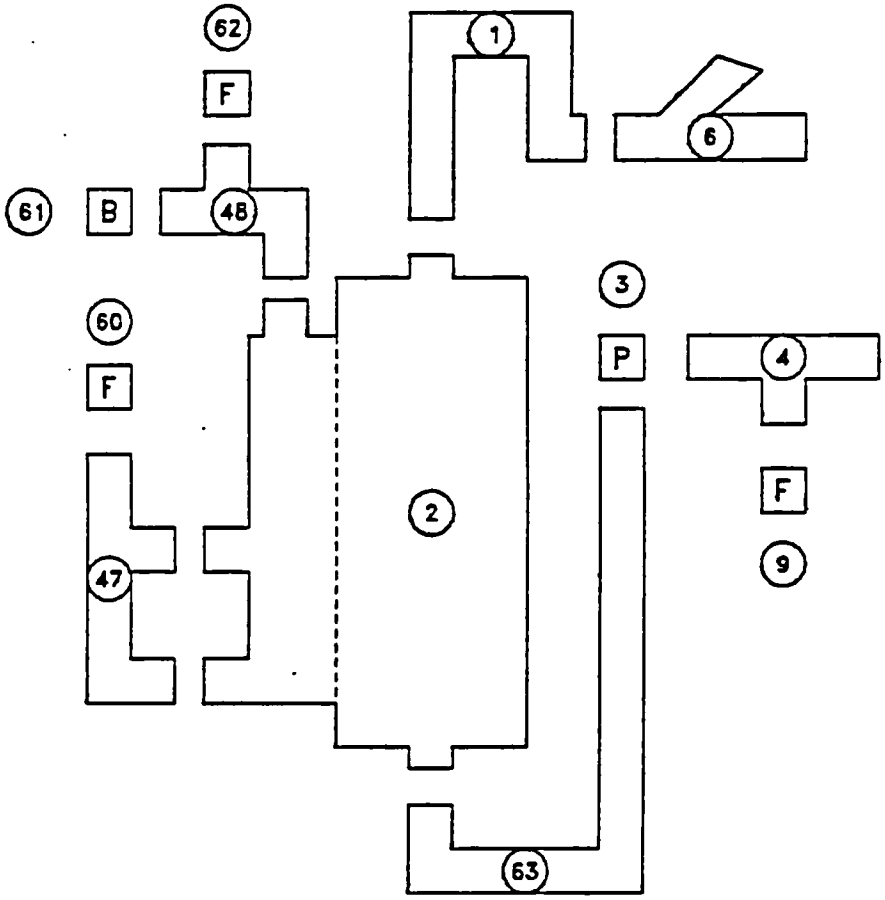

Fig. 20c.
TRAC modeling schematic of the loop-B components.

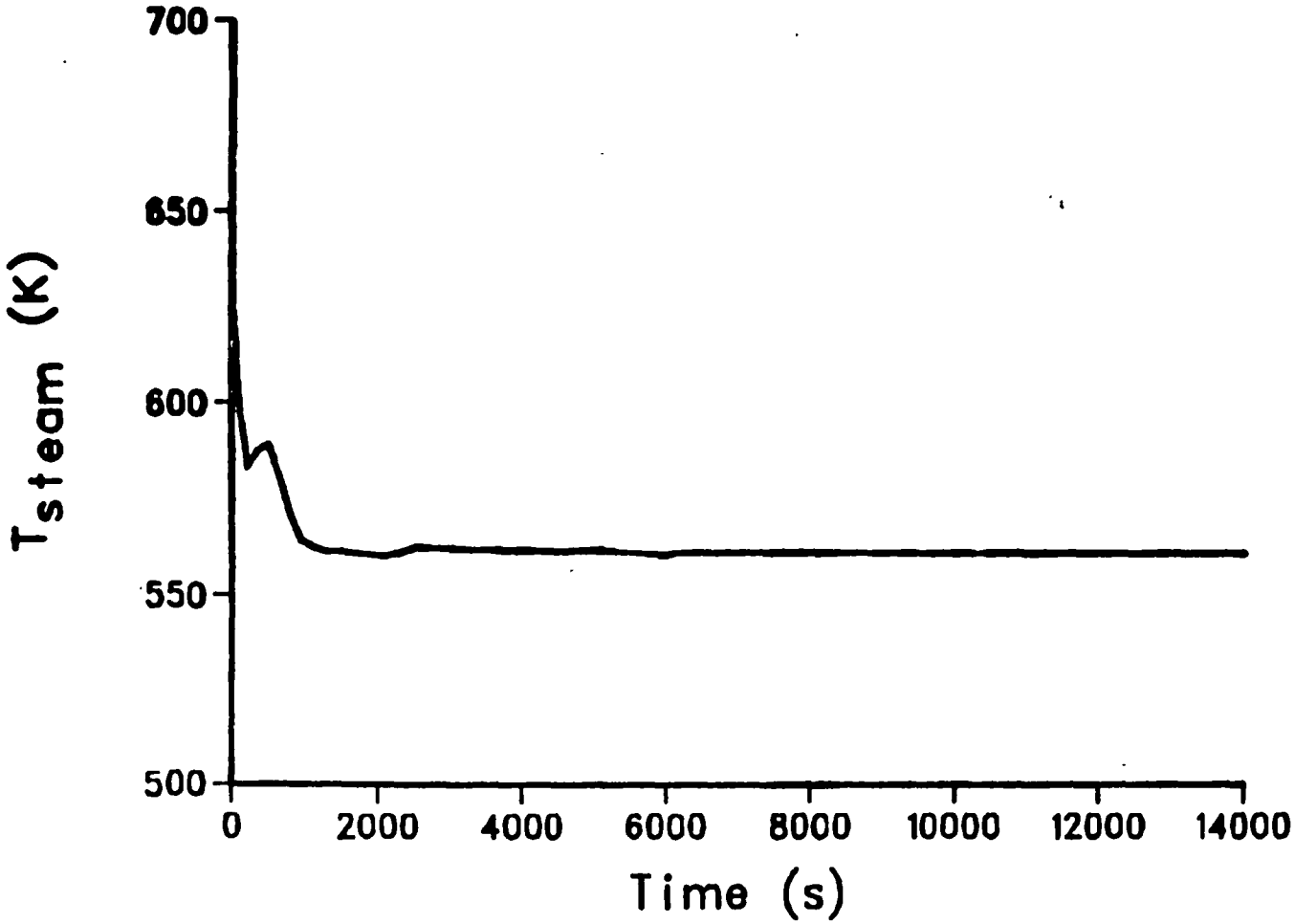

Fig. 21a.
MIMAS steam temperature boundary condition at the core lower-support plate.

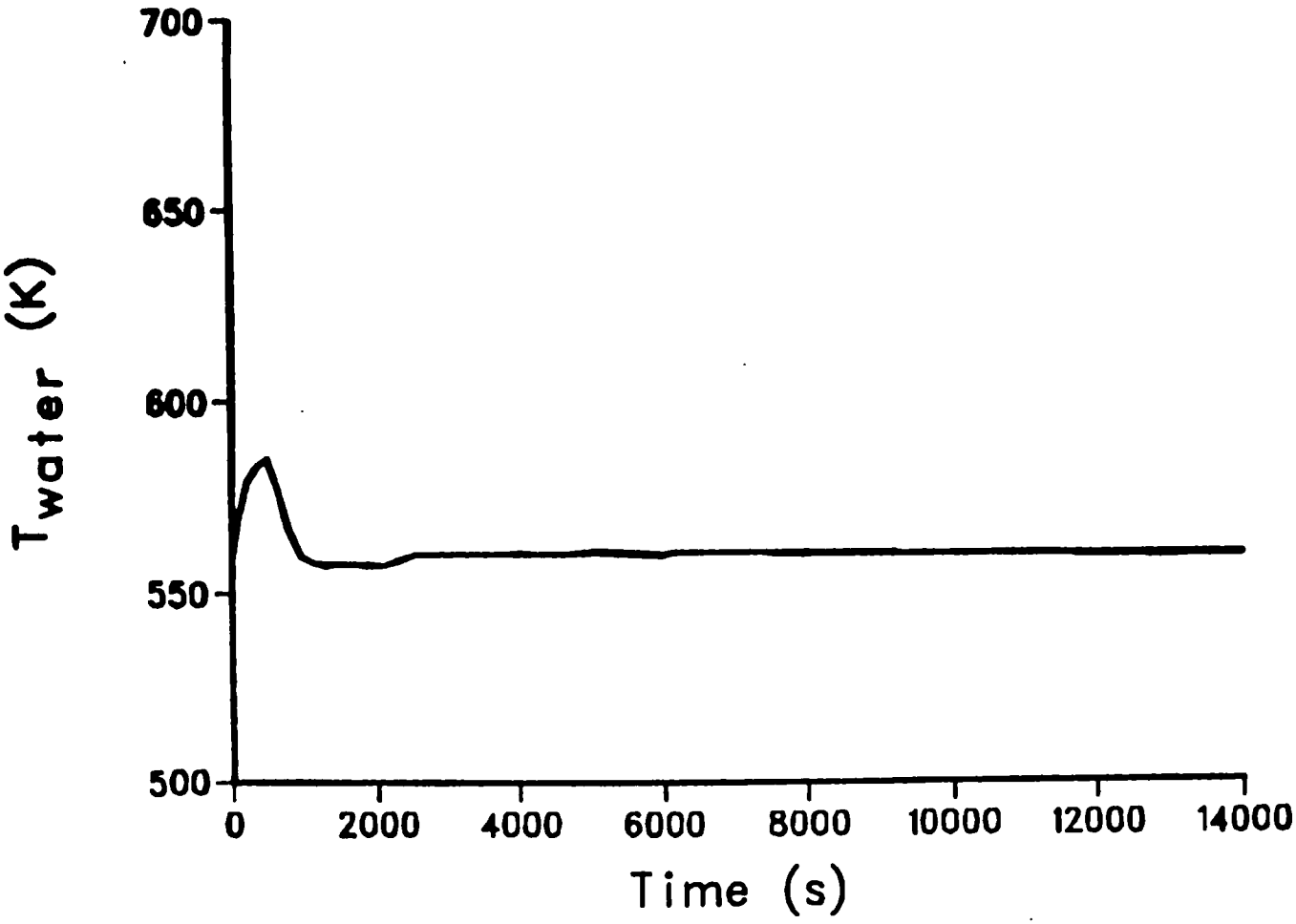

Fig. 21b.
MIMAS water temperature boundary condition at the core lower-support plate.

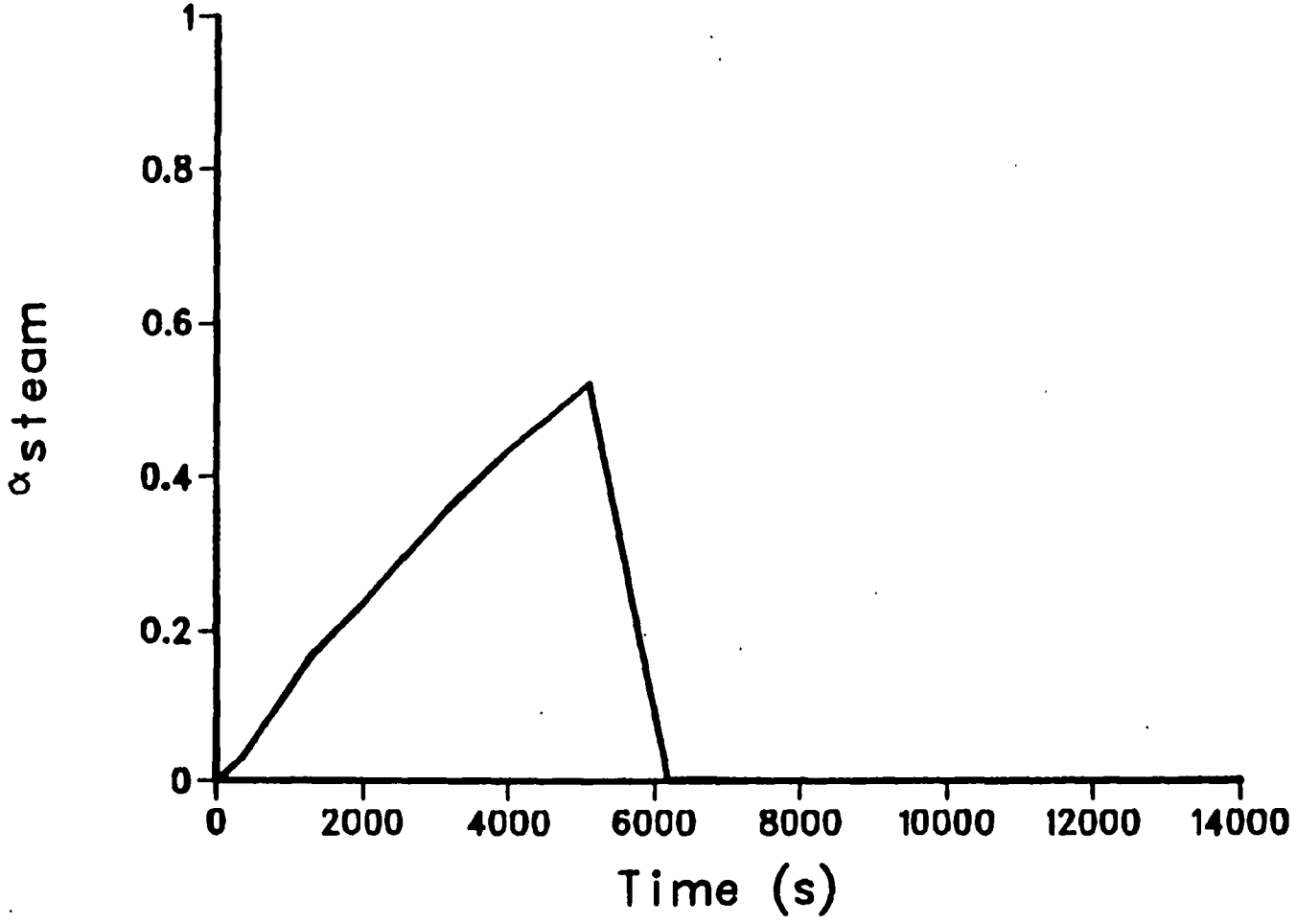

Fig. 22a.
MIMAS steam volume fraction boundary condition at the core lower-support plate.

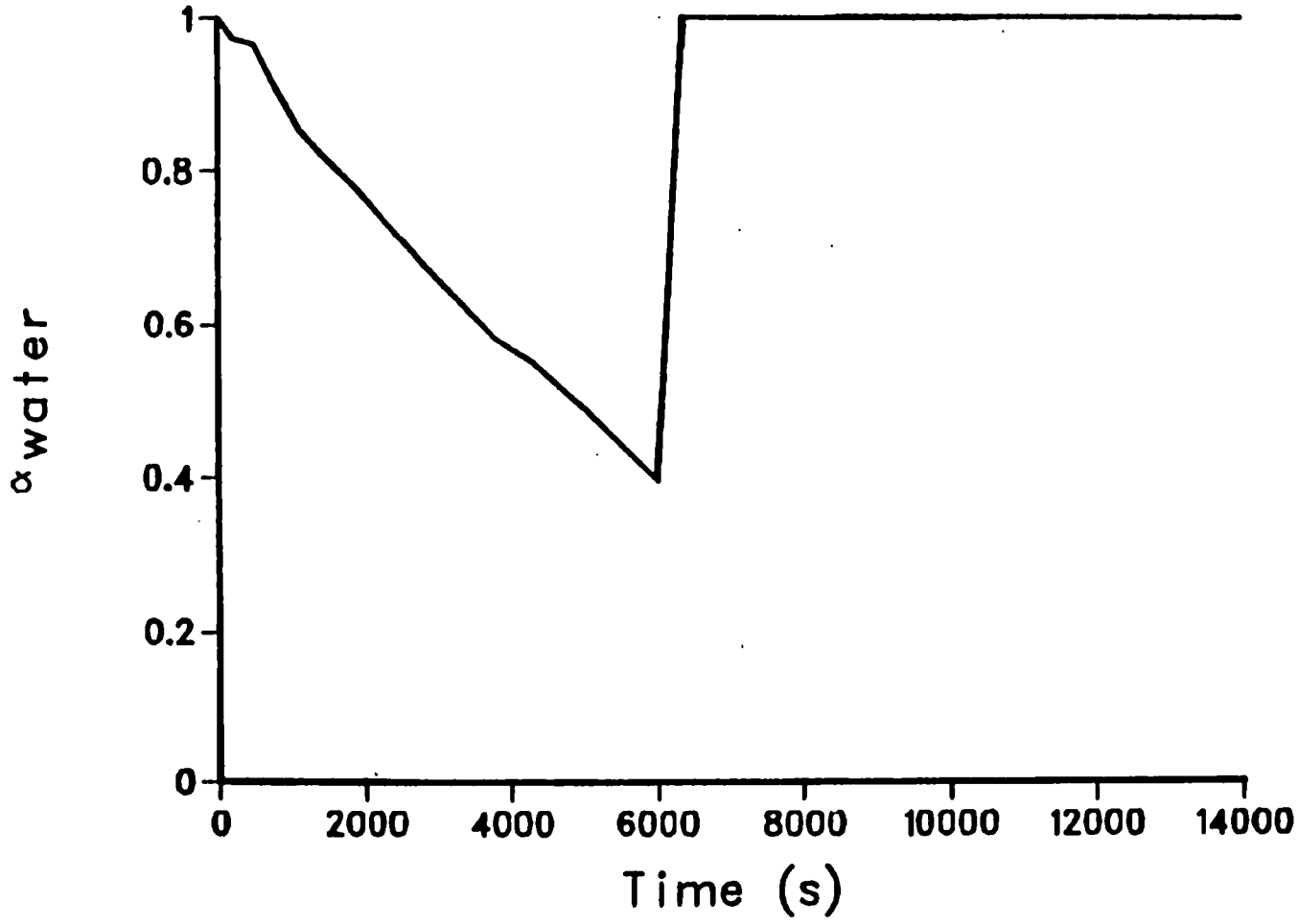

Fig. 22b.
MIMAS water volume fraction boundary condition at the core lower-support plate.

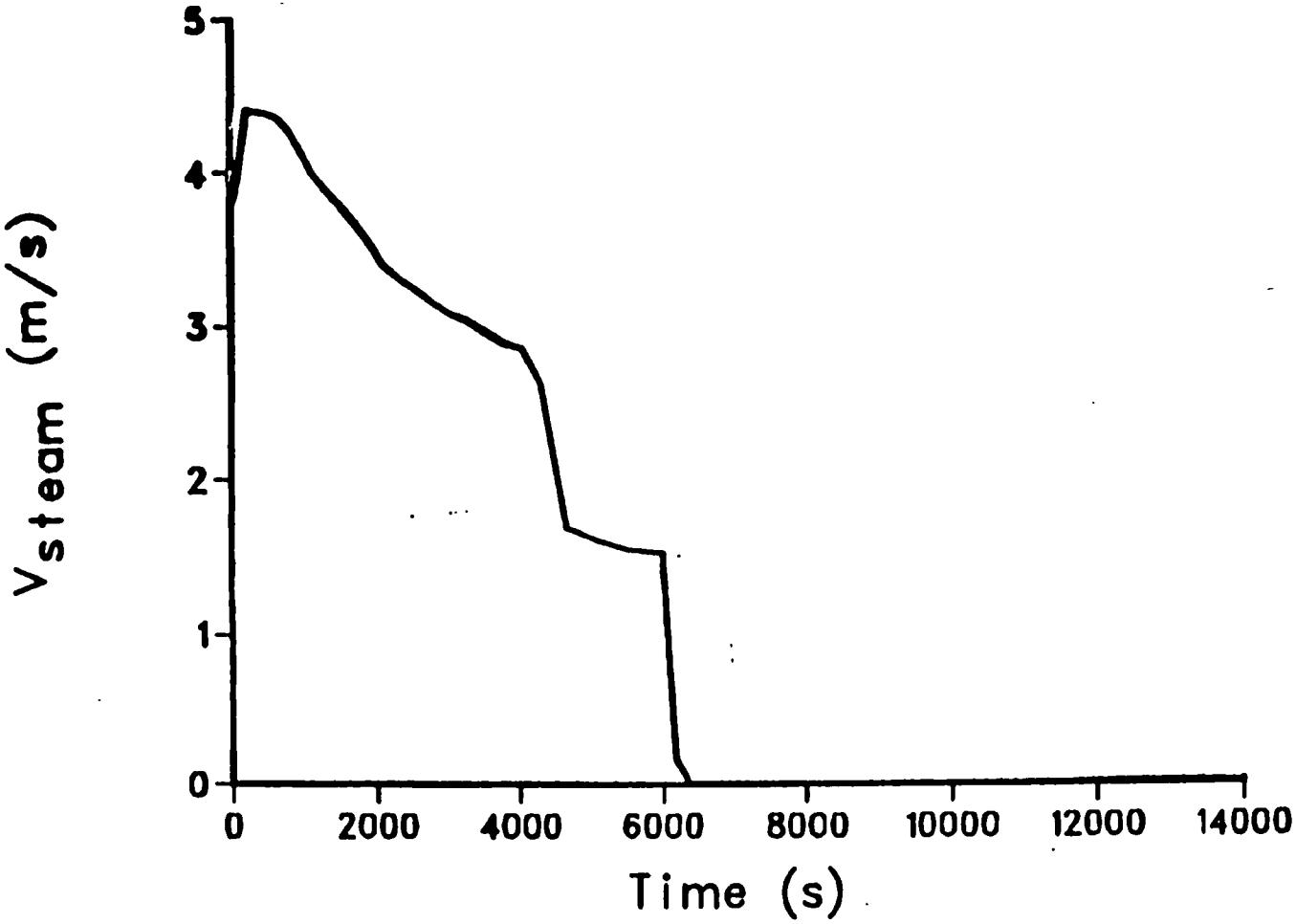

Fig. 23a.
MIMAS steam velocity boundary condition at the core lower-support plate.

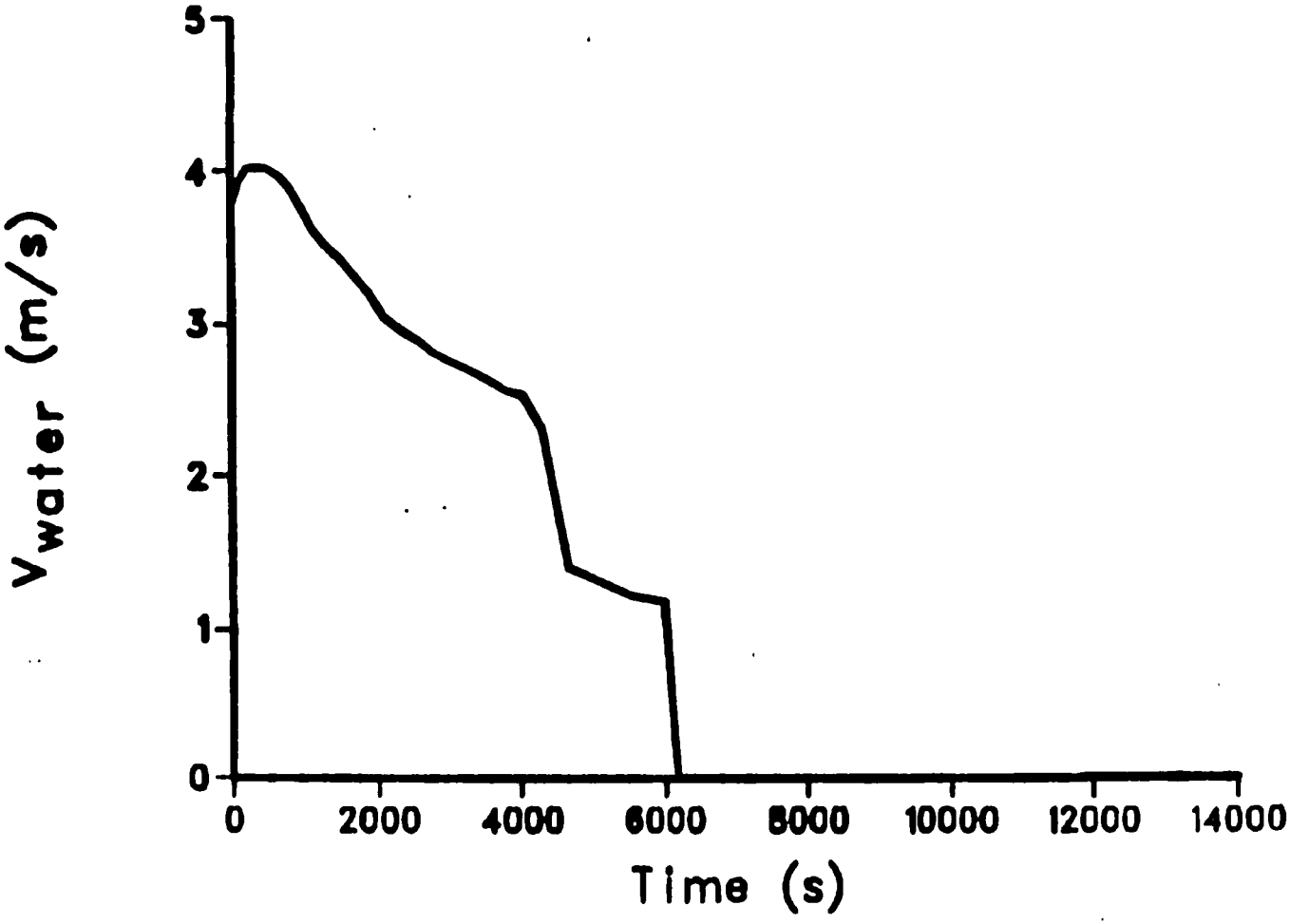

Fig. 23b.
MIMAS water velocity boundary condition at the core lower-support plate.

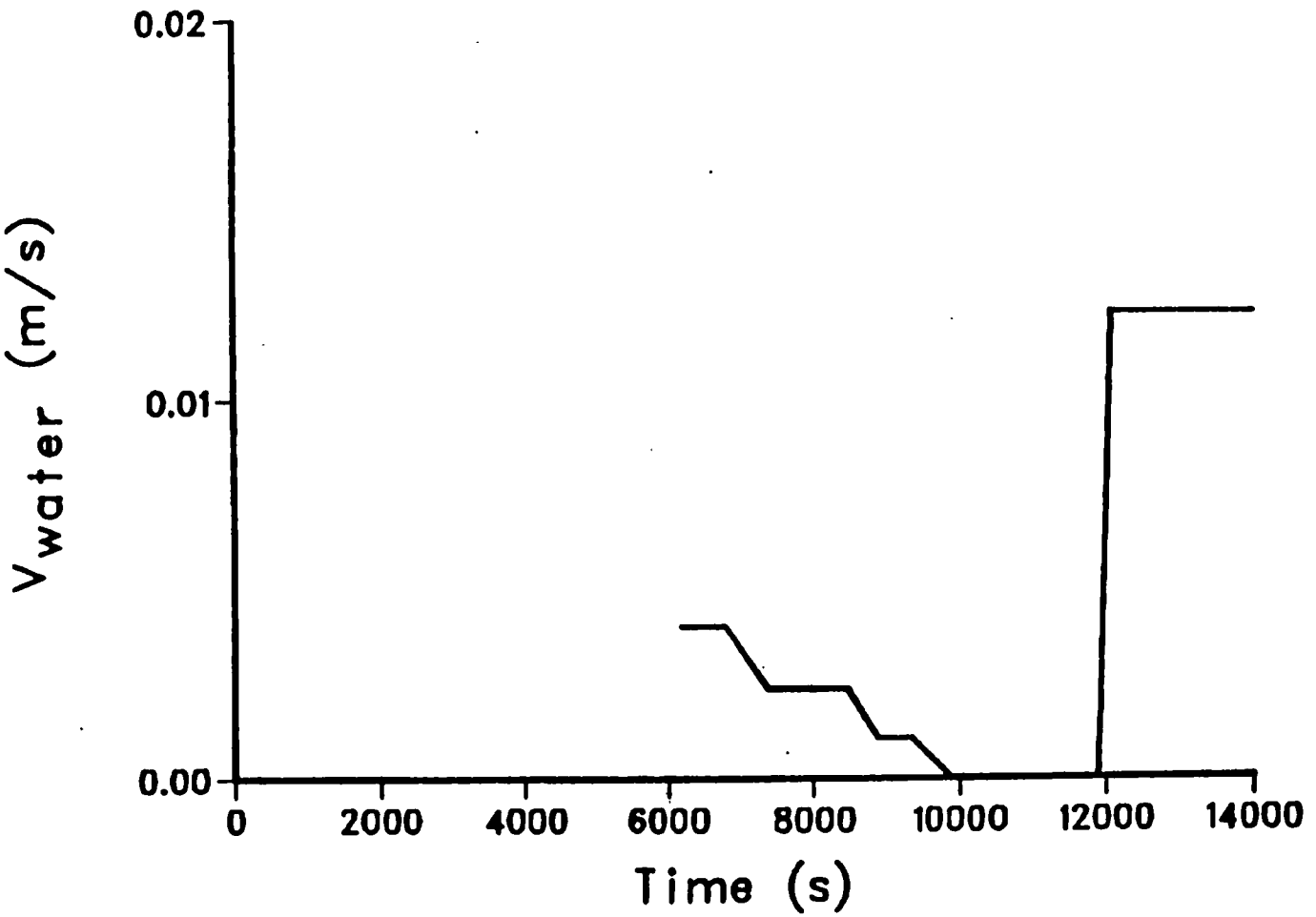

Fig. 23c.
MIMAS water velocity boundary condition at the core lower-support plate.

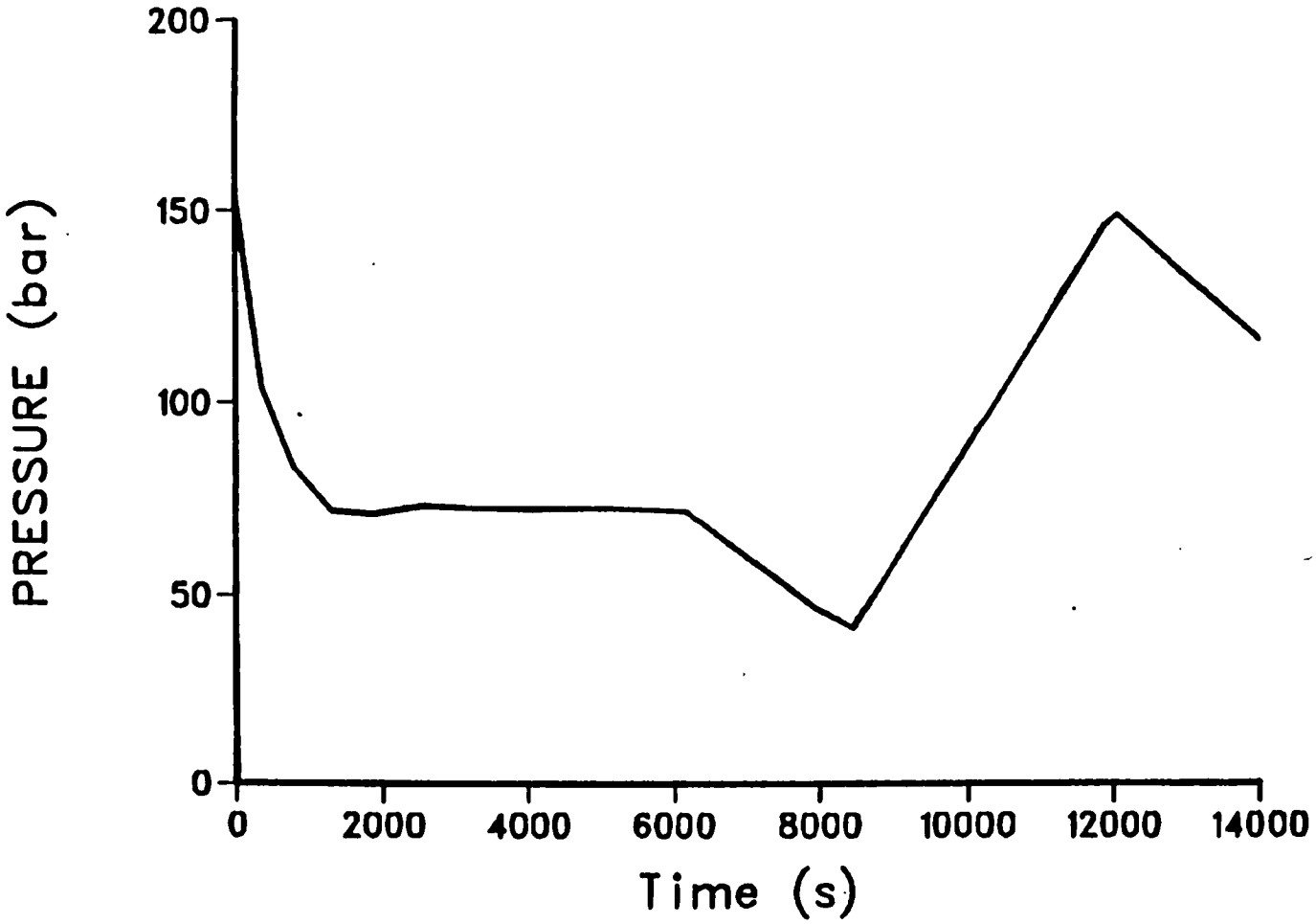

Fig. 24.
MIMAS total pressure boundary condition at the core upper-support plate.

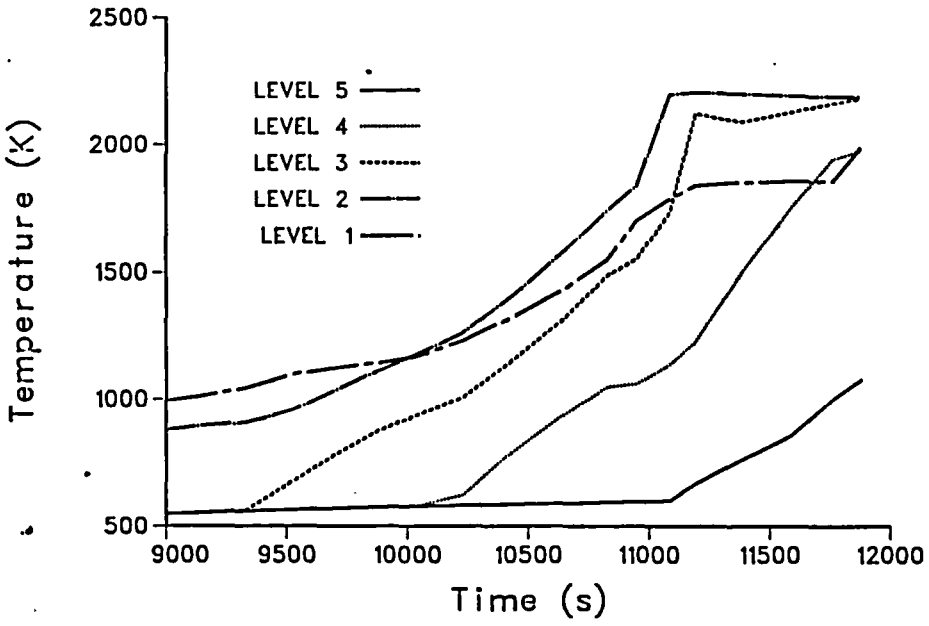

Fig. 25.
Cladding temperature vs time and axial position for core ring 1.

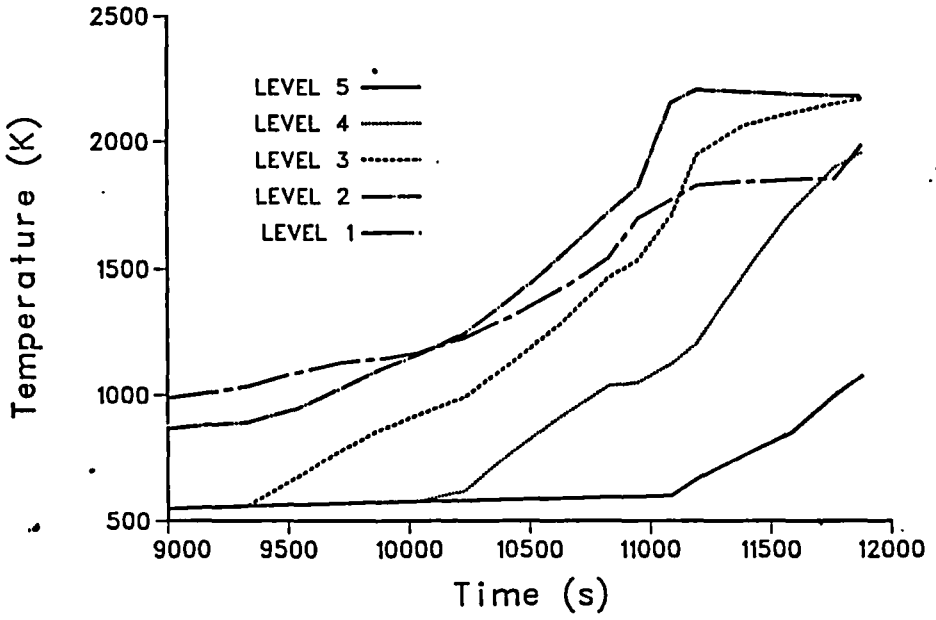

Fig. 26.
Cladding temperature vs time and axial position for core ring 2.

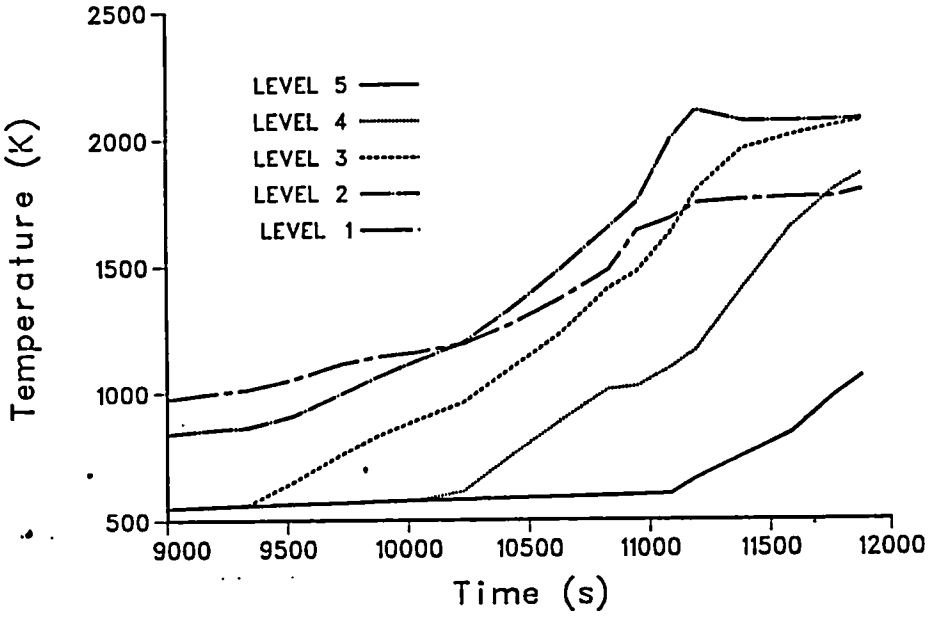

Fig. 27.
Cladding temperature vs time and axial position for core ring 3.

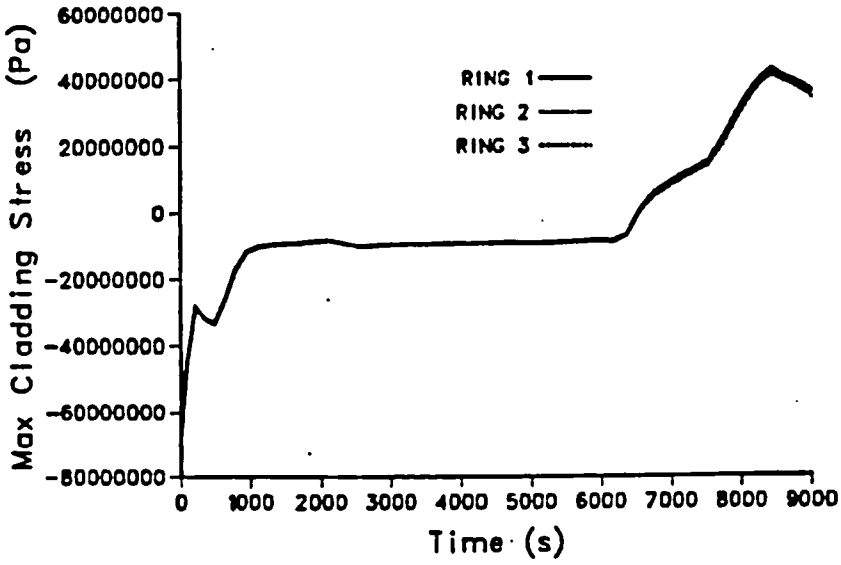

Fig. 28.
Maximum cladding stress vs time for 0-9000 s into TMI-2 accident.

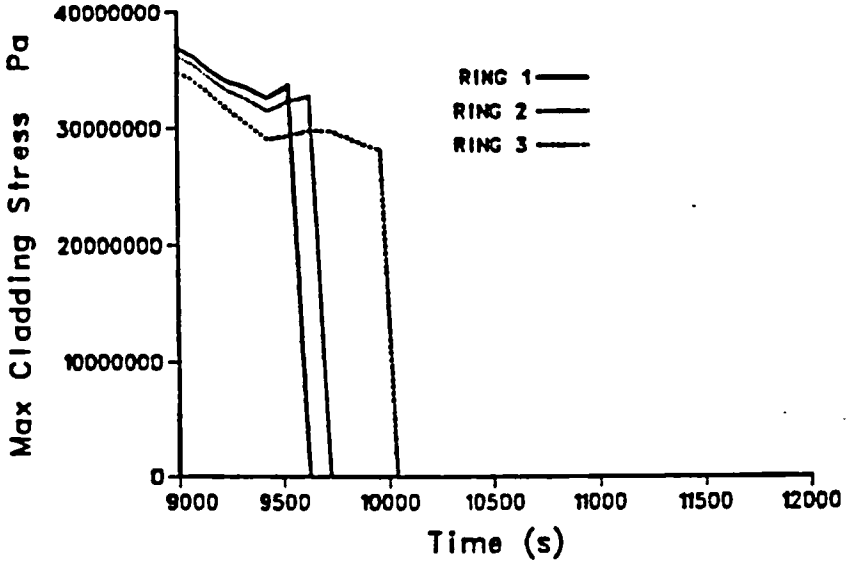

Fig. 29.
Maximum cladding stress vs time for 9000-12000 s into TMI-2 accident.

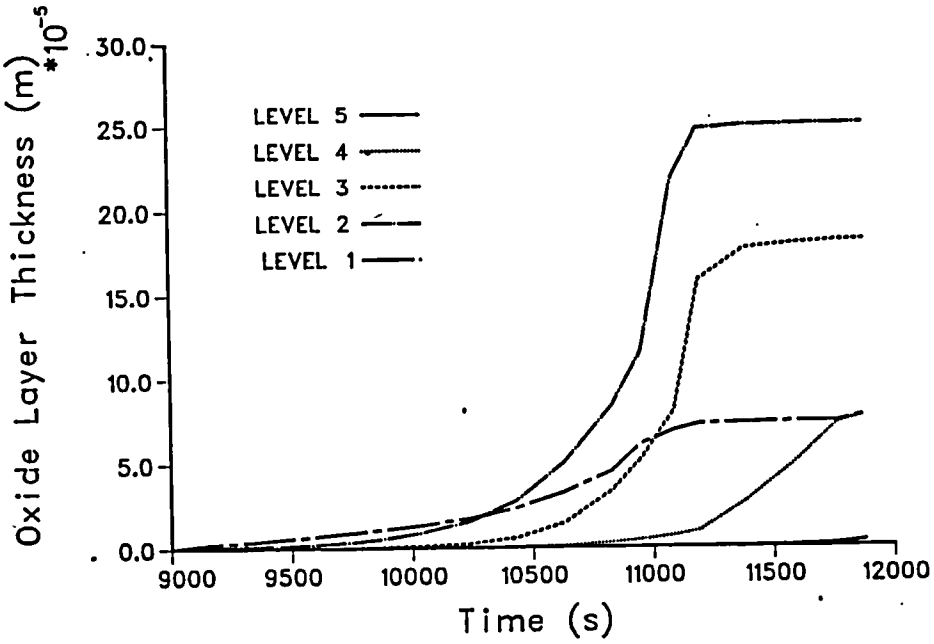

Fig. 30.
Cladding oxide layer thickness vs time and axial position for core ring 1.

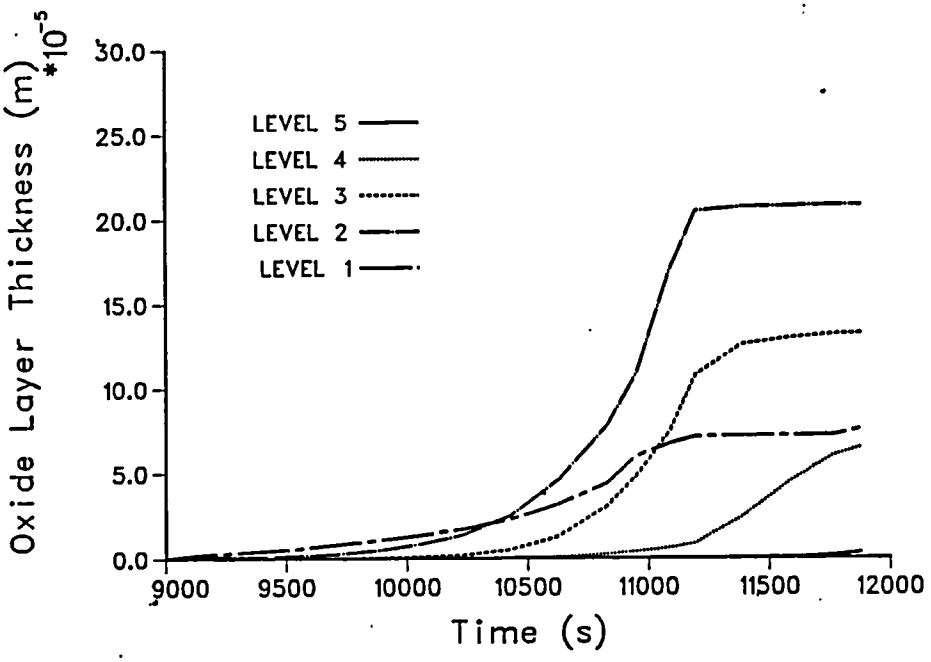

Fig. 31.
Cladding oxide layer thickness vs time and axial position for core ring 2.

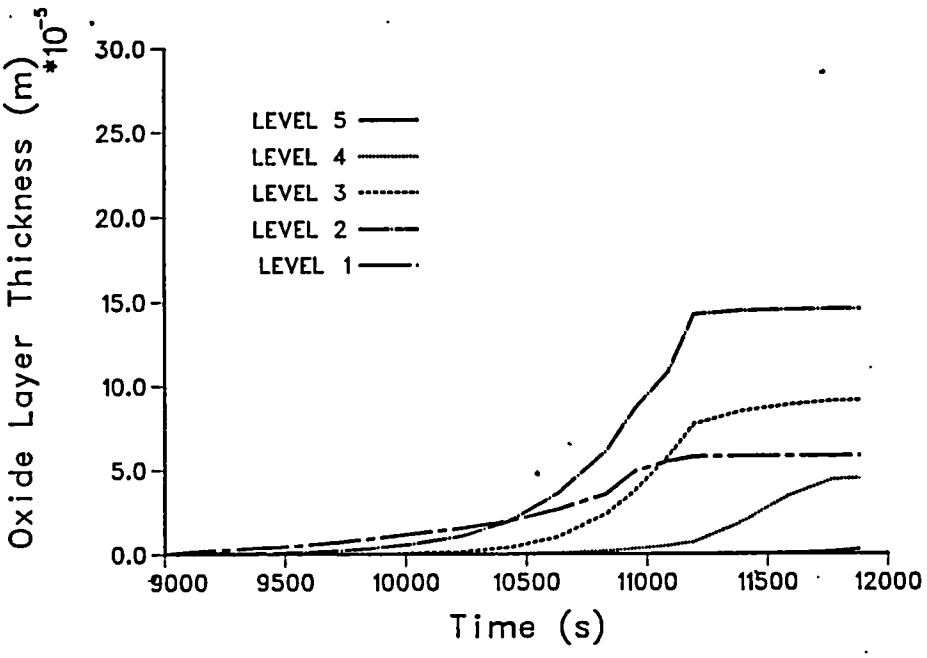

Fig. 32.
Cladding oxide layer thickness vs time and axial position for core ring 3.

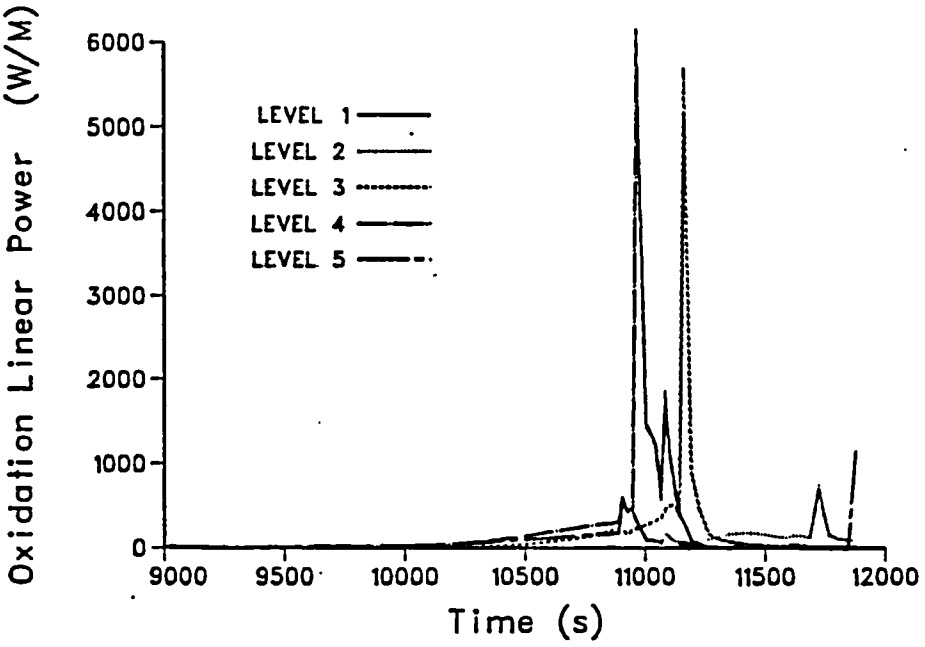

Fig. 33.
Cladding oxidation power vs. time and axial position for core ring 1.

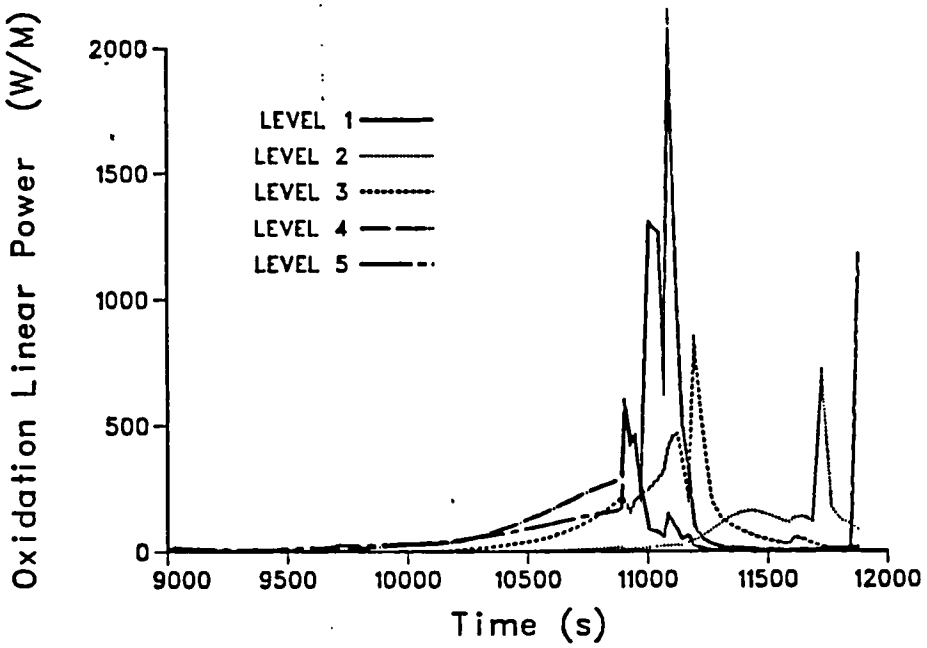

Fig. 34.
Cladding oxidation power vs. time and axial position for core ring 2.

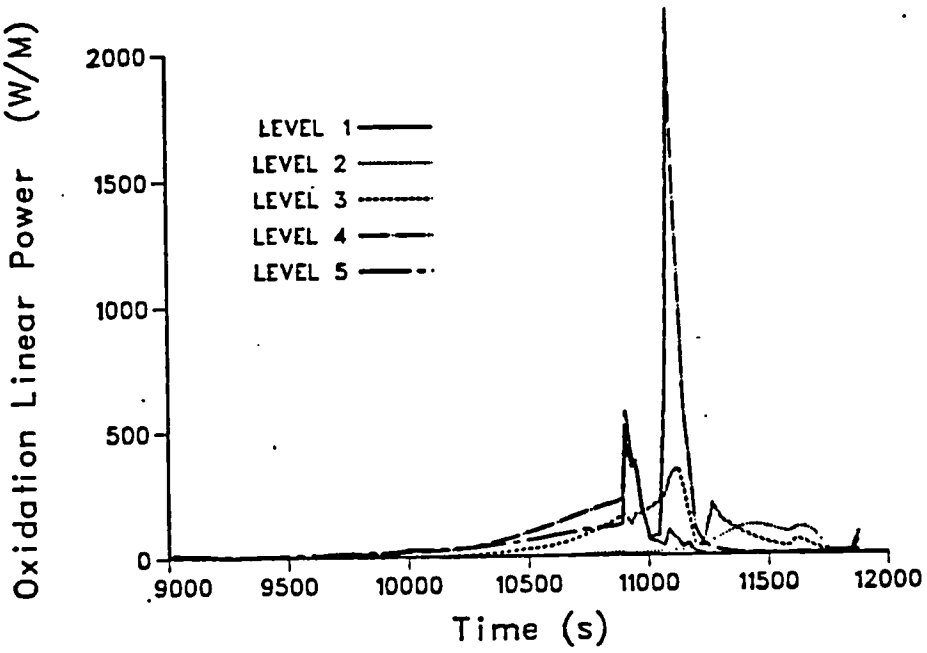

Fig. 35.
Cladding oxidation power vs time and axial position for core ring 3.

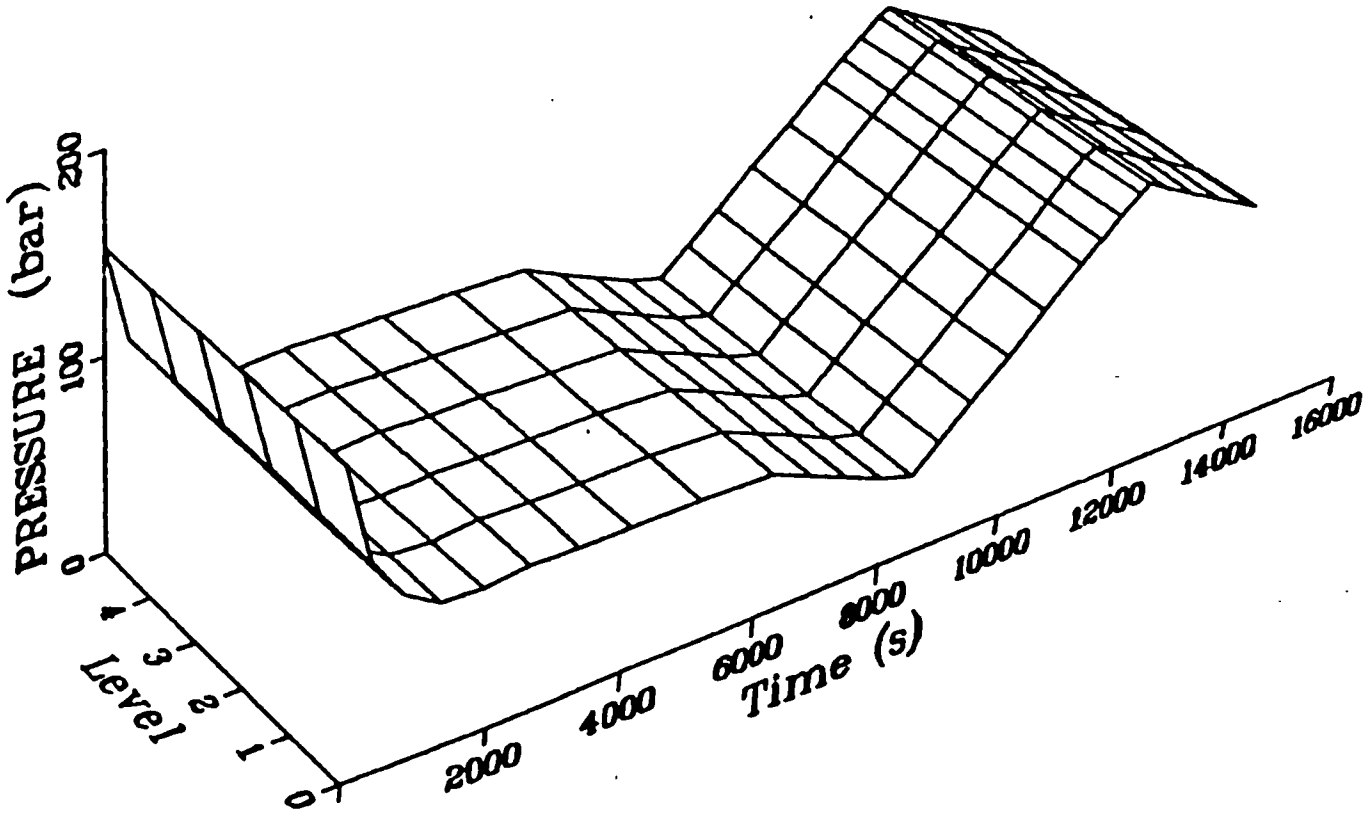

Fig. 36.
Total pressure surface shown as a function of core level and time (0 to 14000 s).

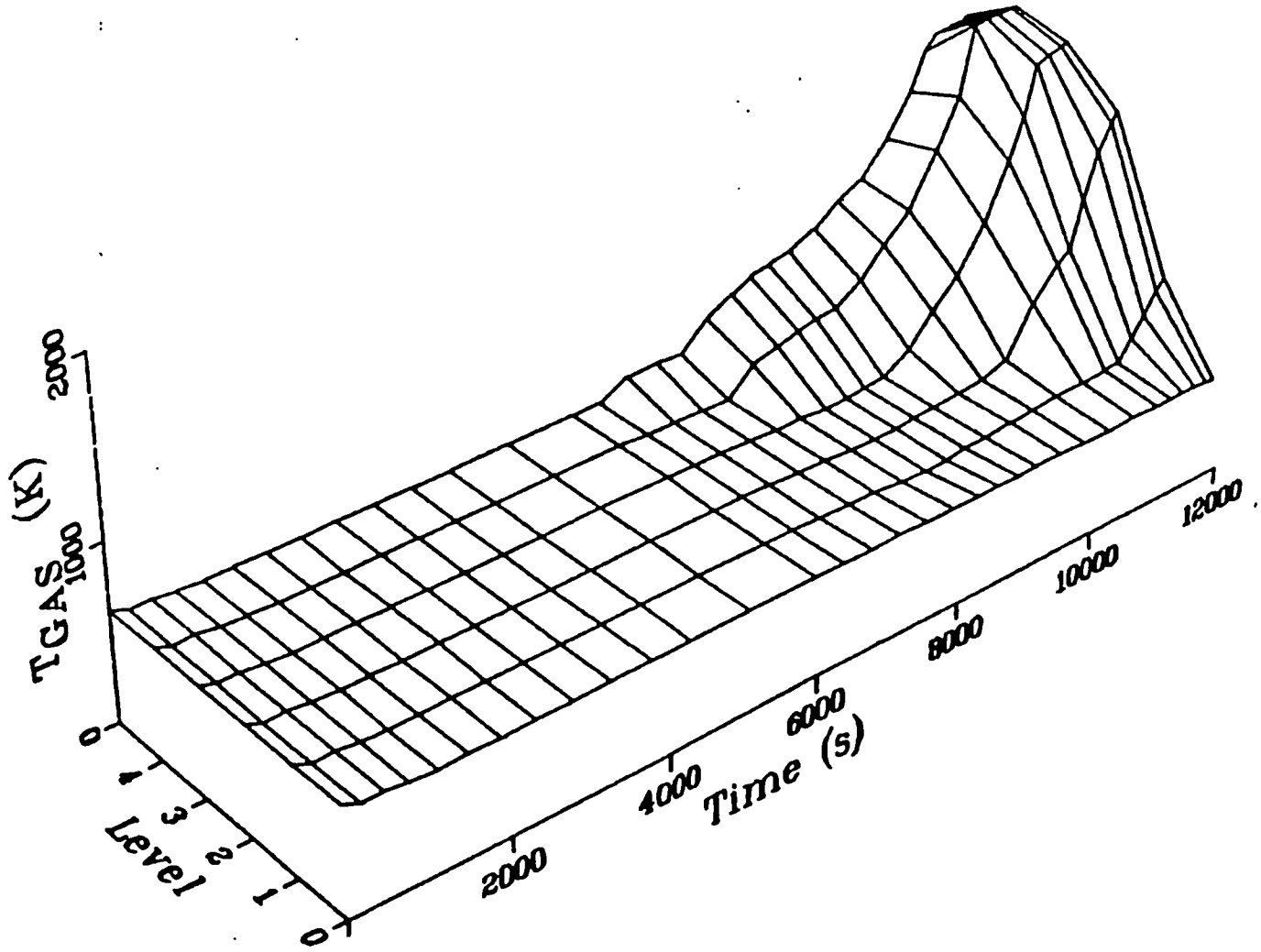

Fig. 37.
Gas temperature surface shown as a function of core level and time (0 to 11880 s).

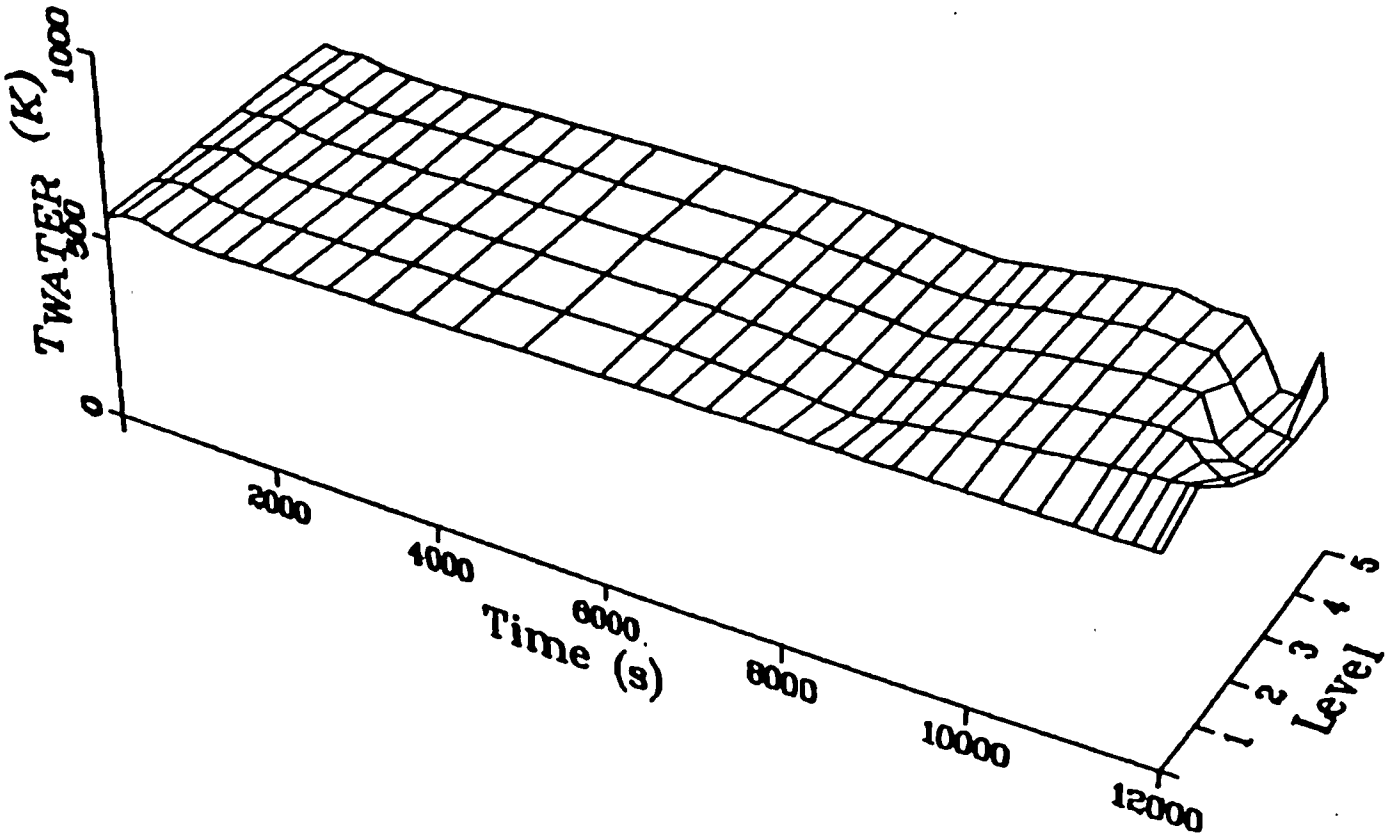

Fig. 38.
Water temperature surface shown as a function of core level and time (0 to 11880 s).

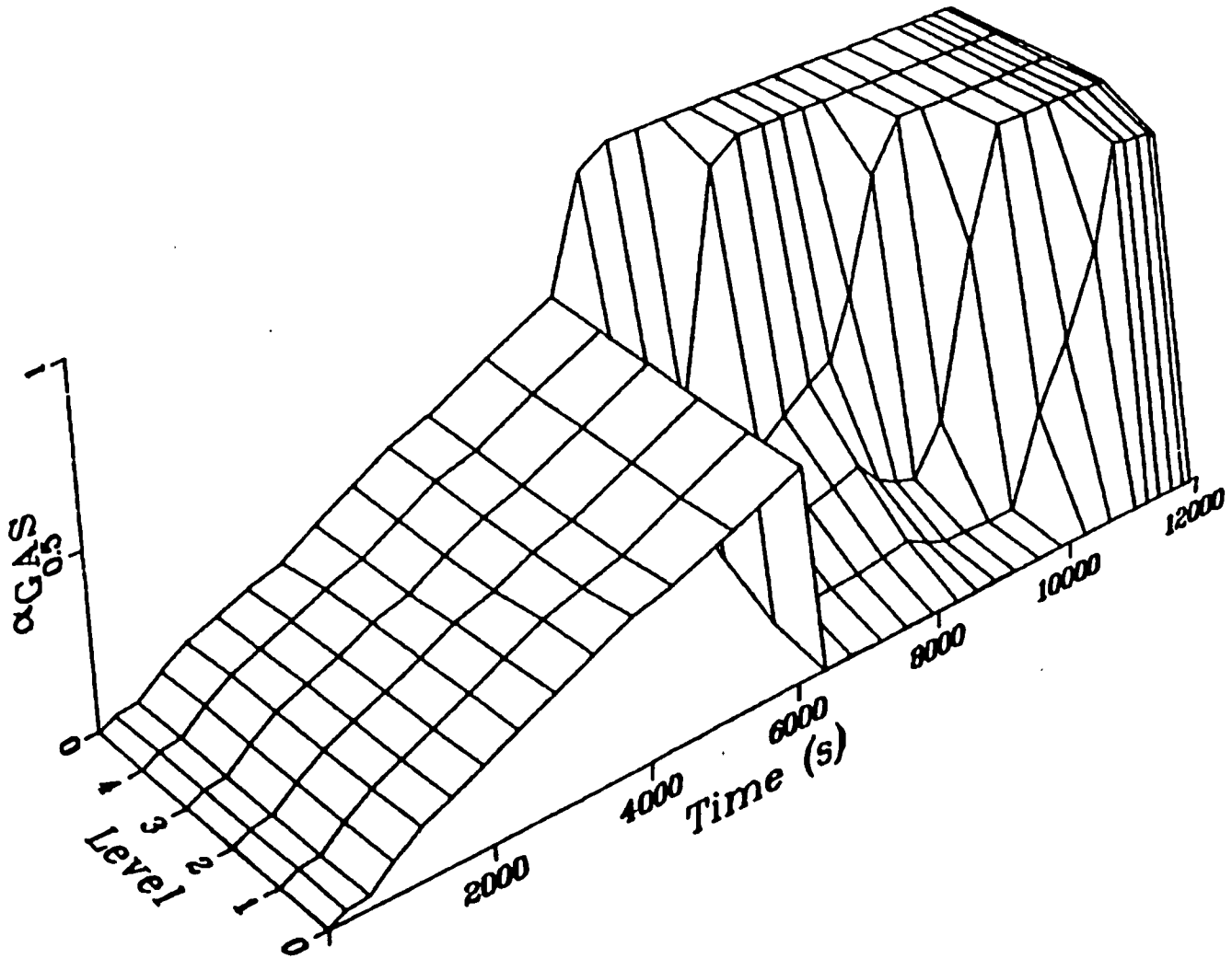

Fig. 39.
Gas volume fraction surface shown as a function of core level and time (0 to 11880 s).

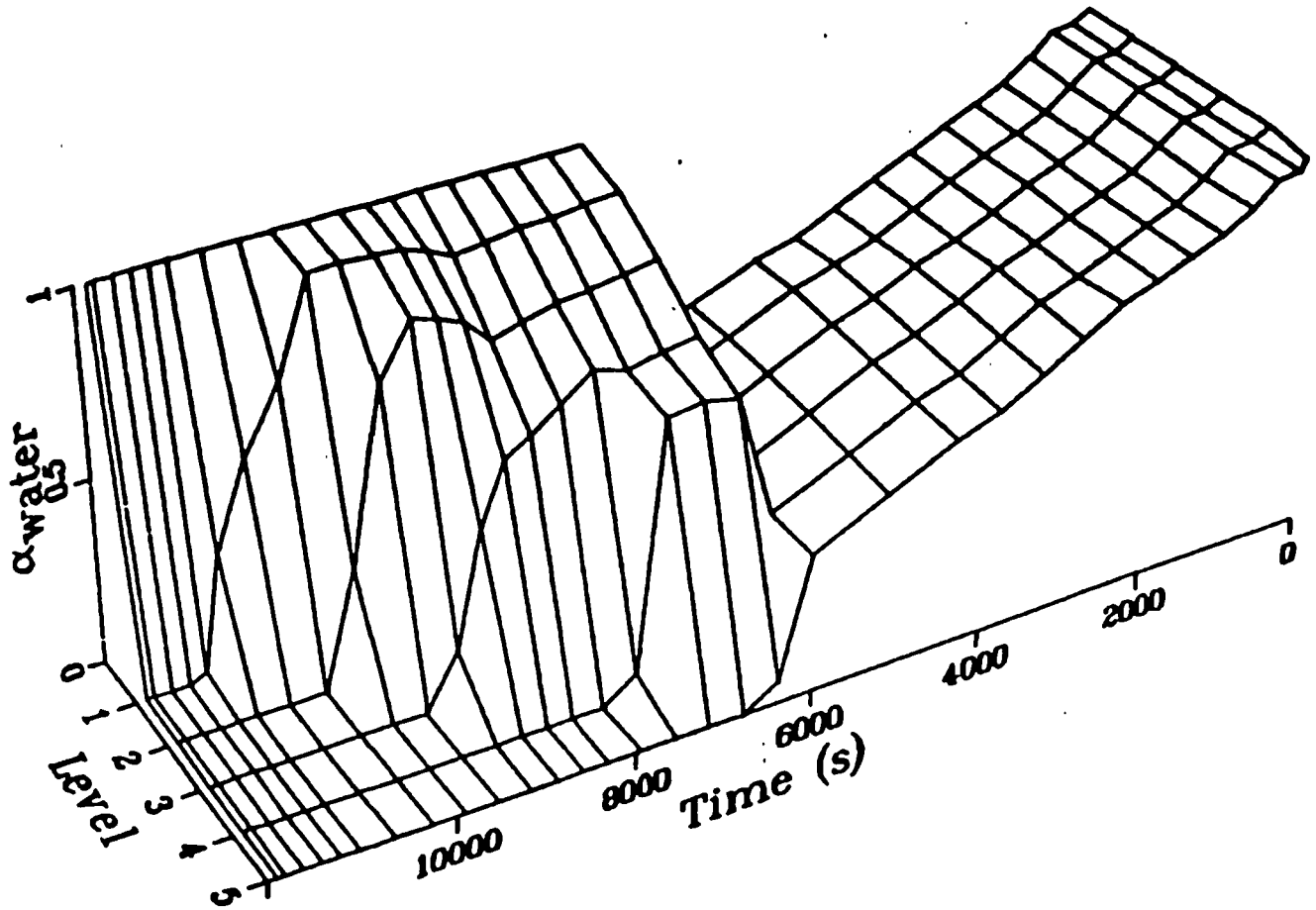

Fig. 40.
Water volume fraction surface shown as a function of core level and time (0 to 11880 s).

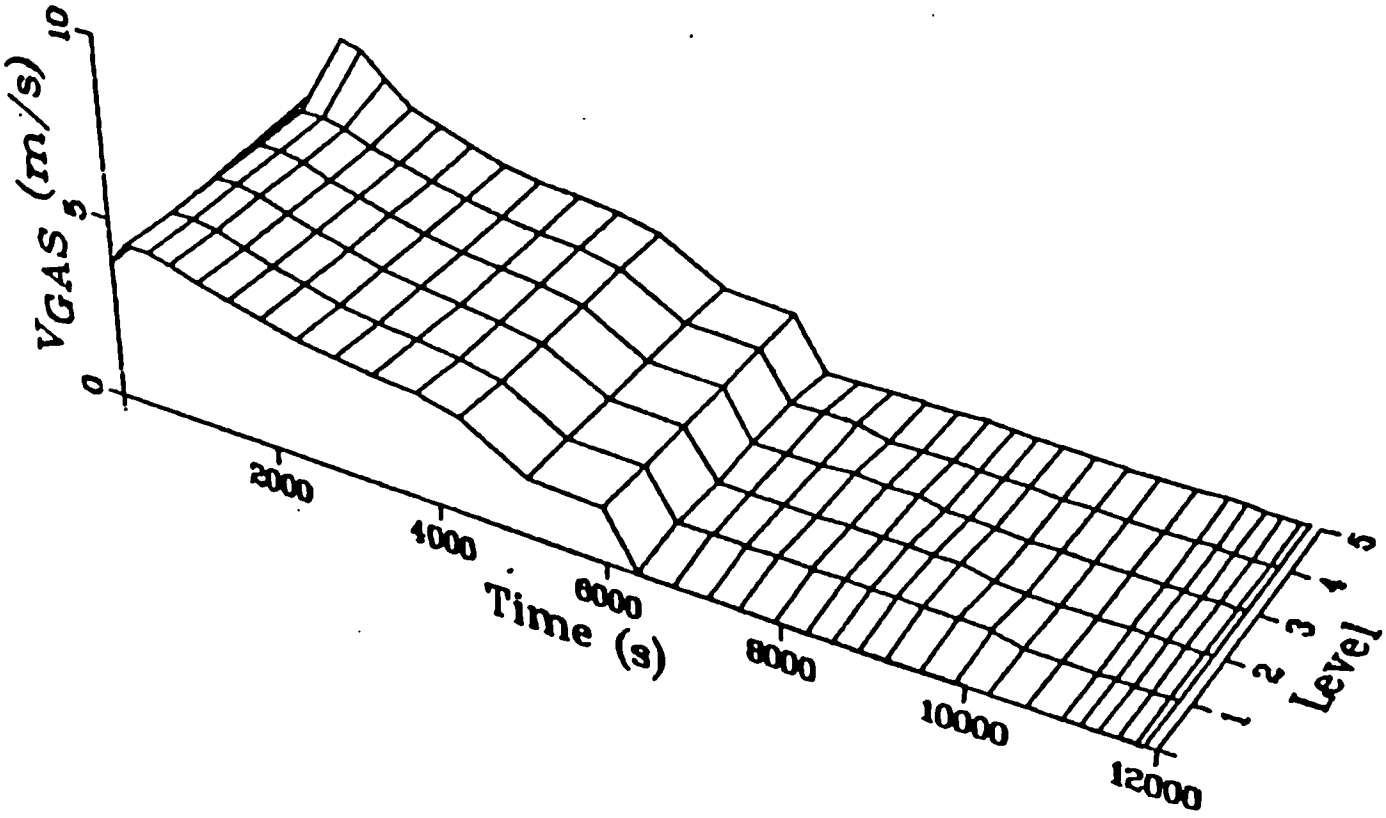

Fig. 41.
Gas velocity surface shown as a function of core level and time (0 to 11880 s).

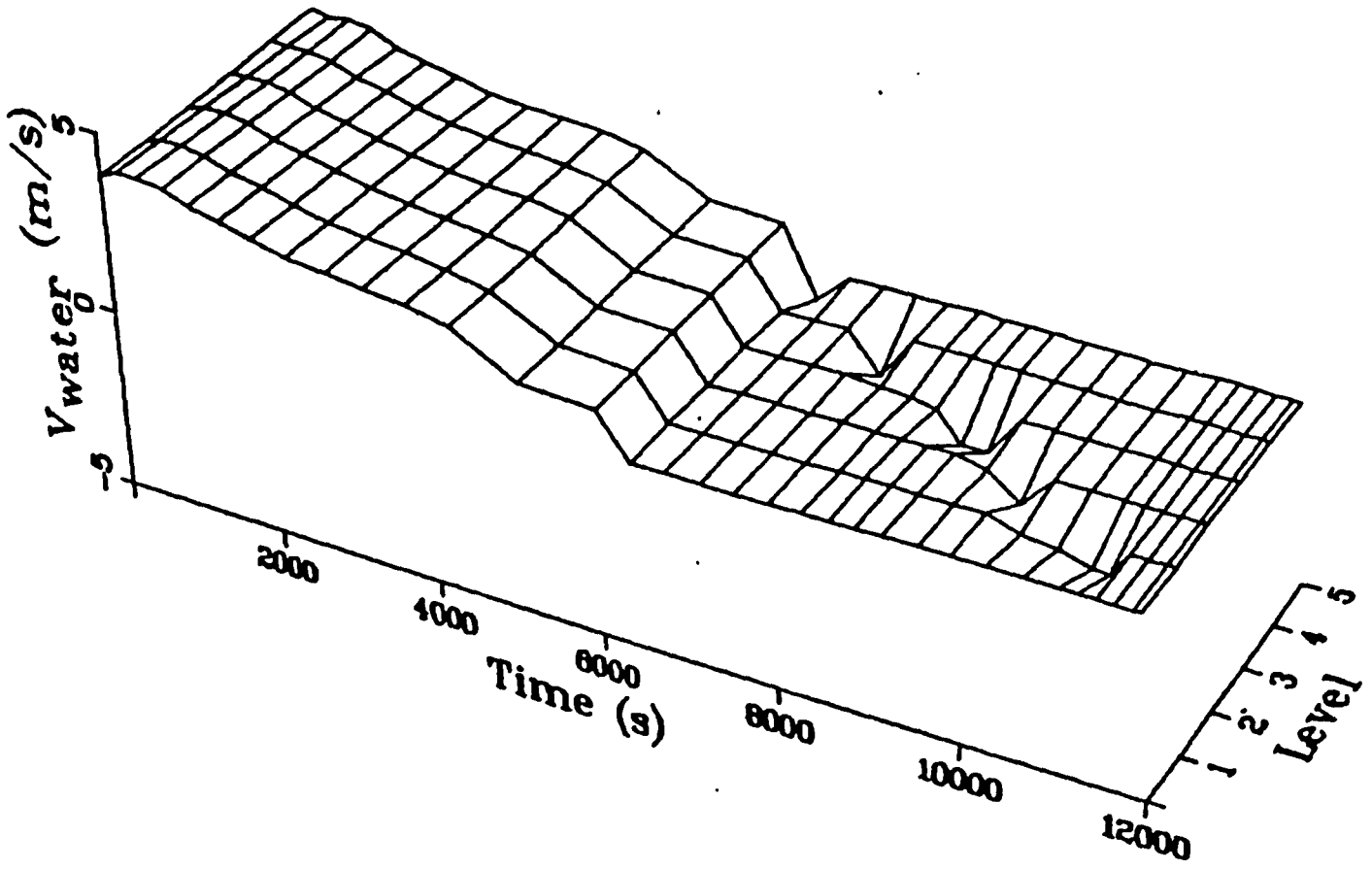

Fig. 42.
Water velocity surface shown as a function of core level and time (0 to 11880 s).

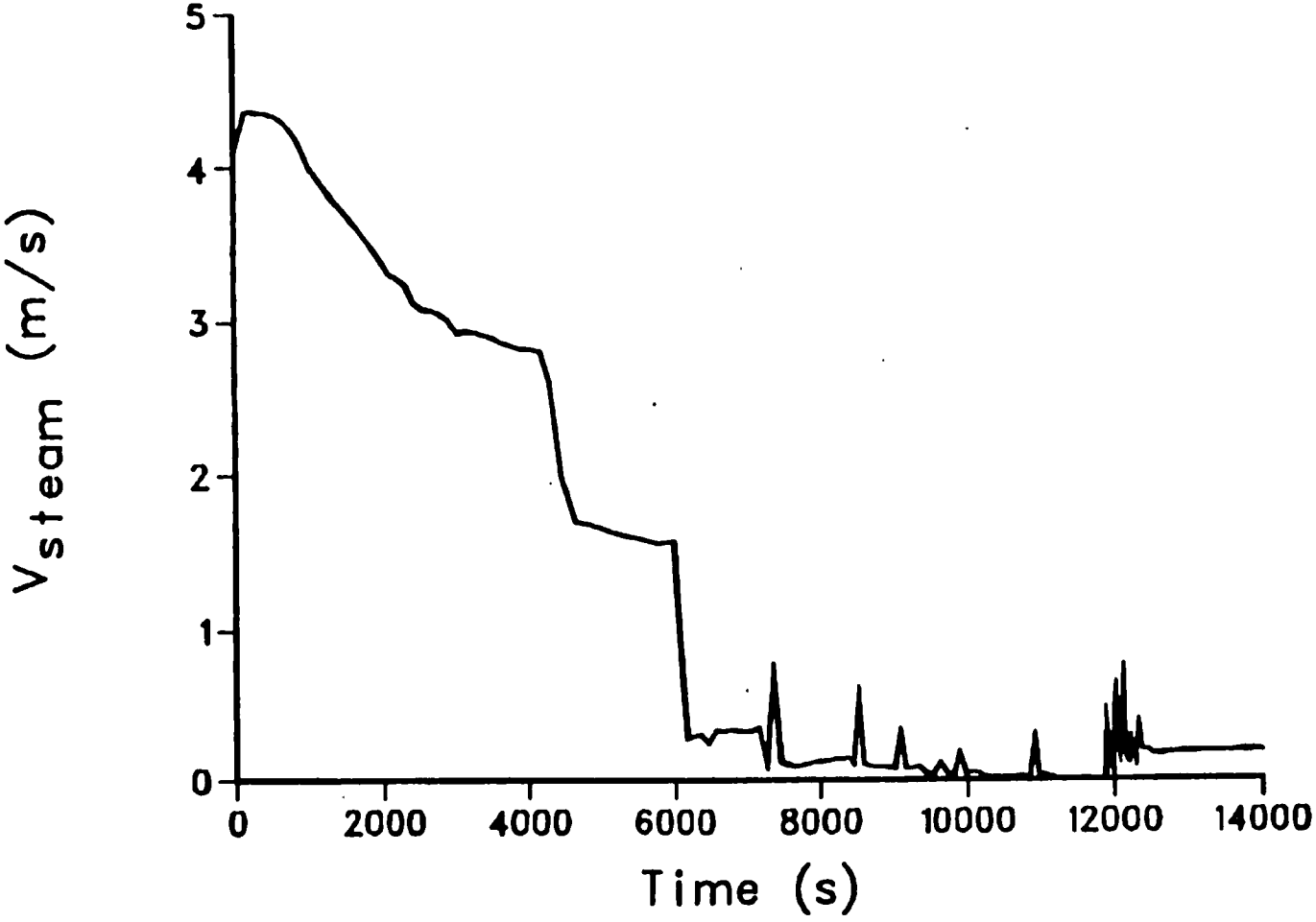

Fig. 43.
Gas velocity at core level 4 shown as a function of time (0 to 14000 s).

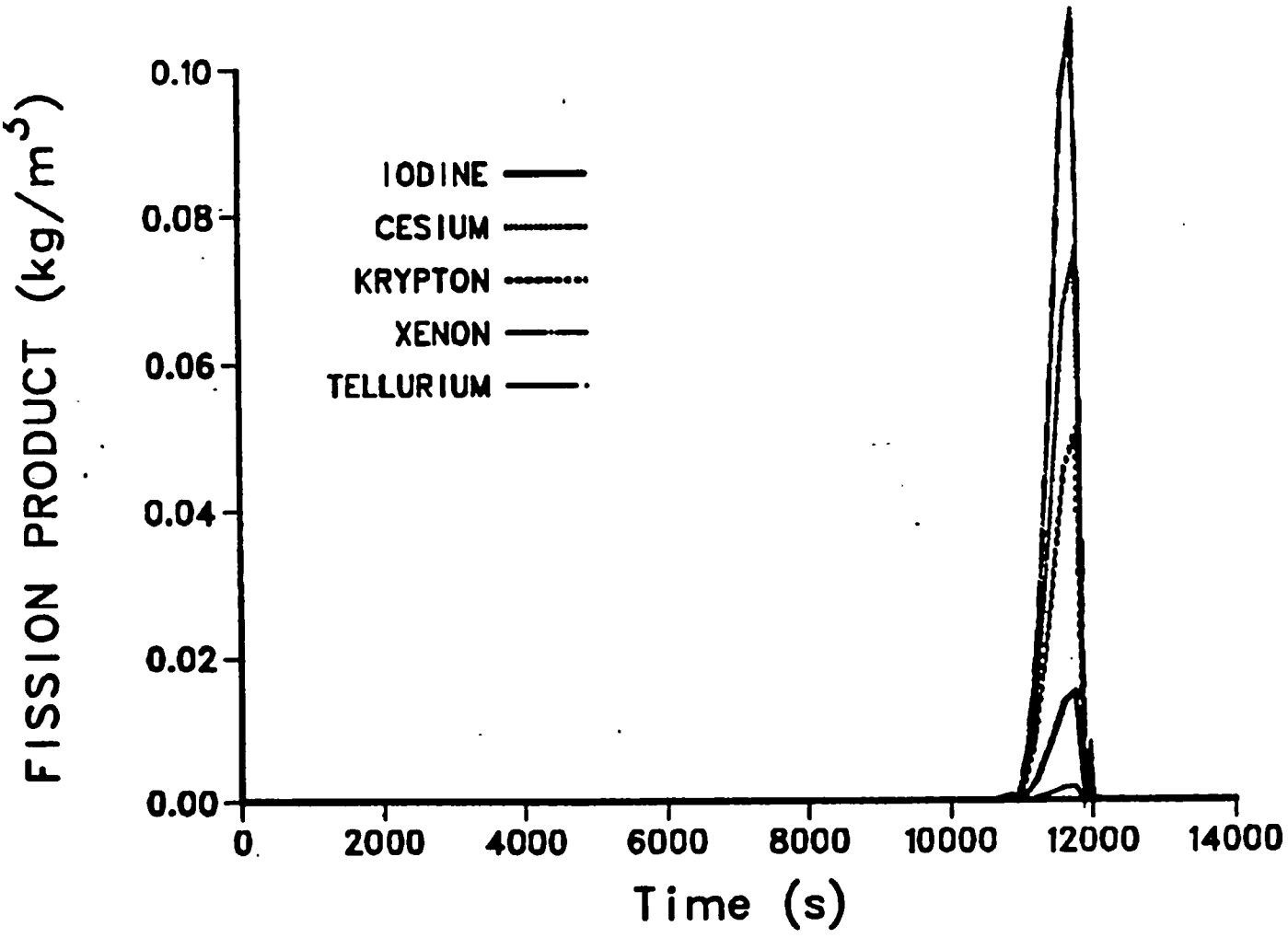

Fig. 44.
Fission product densities at core level 5 (core top) shown as a function of time (0 to 14000 s).

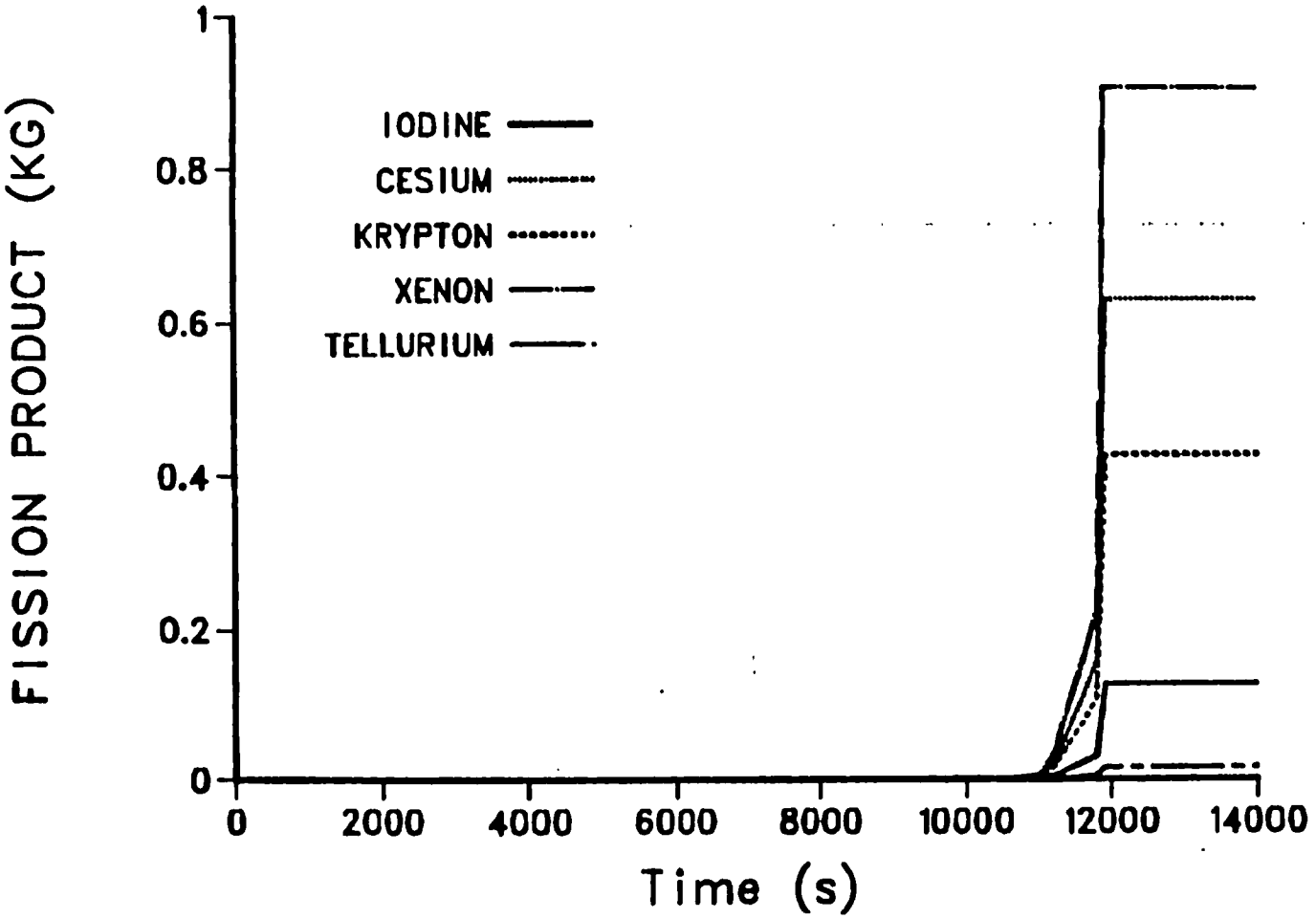

Fig. 45.
Fission product masses exiting the core region shown as a function of time (0 to 14000 s).

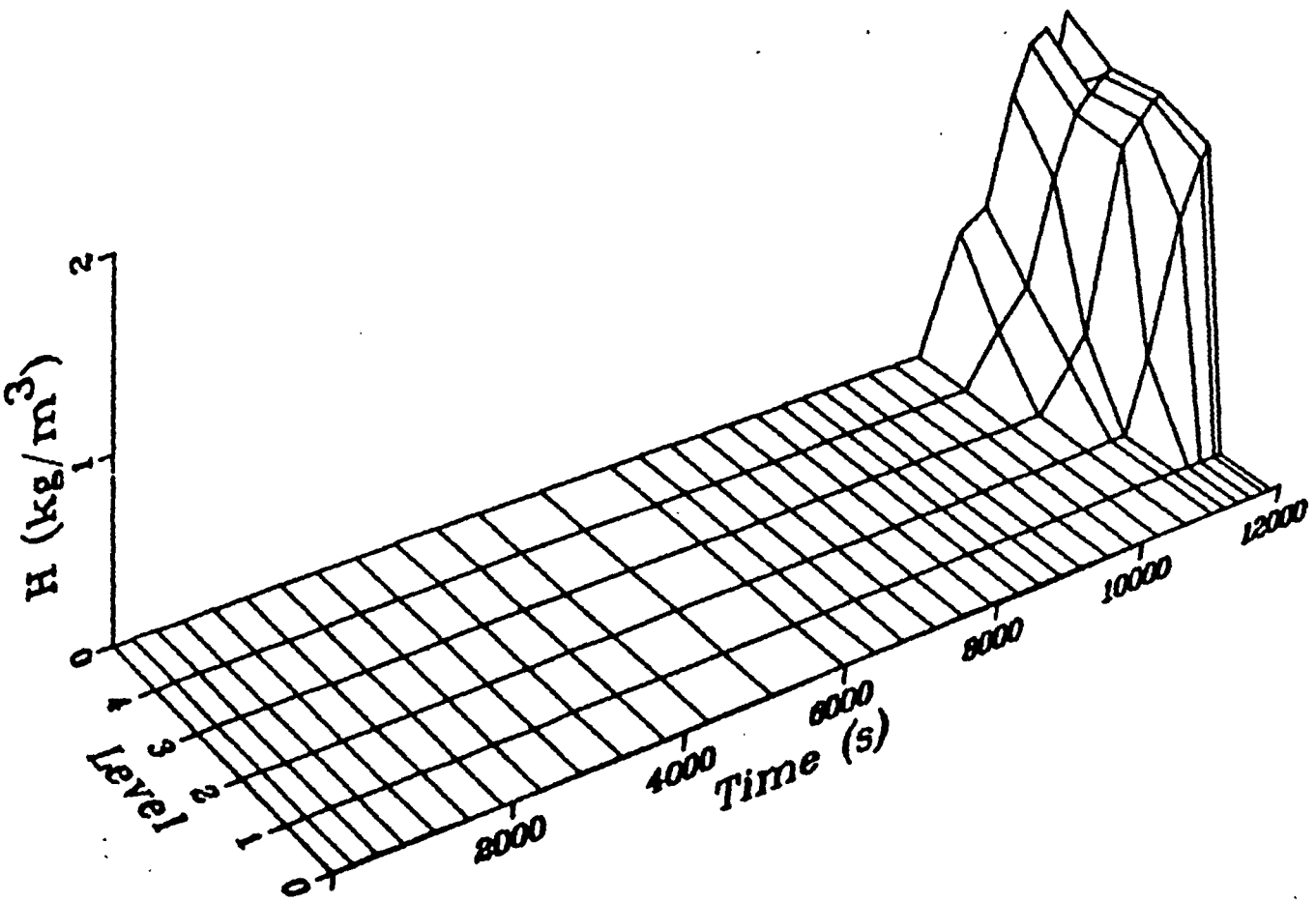

Fig. 46.
Hydrogen density surface shown as a function of core level and time (0 to 11880 s).

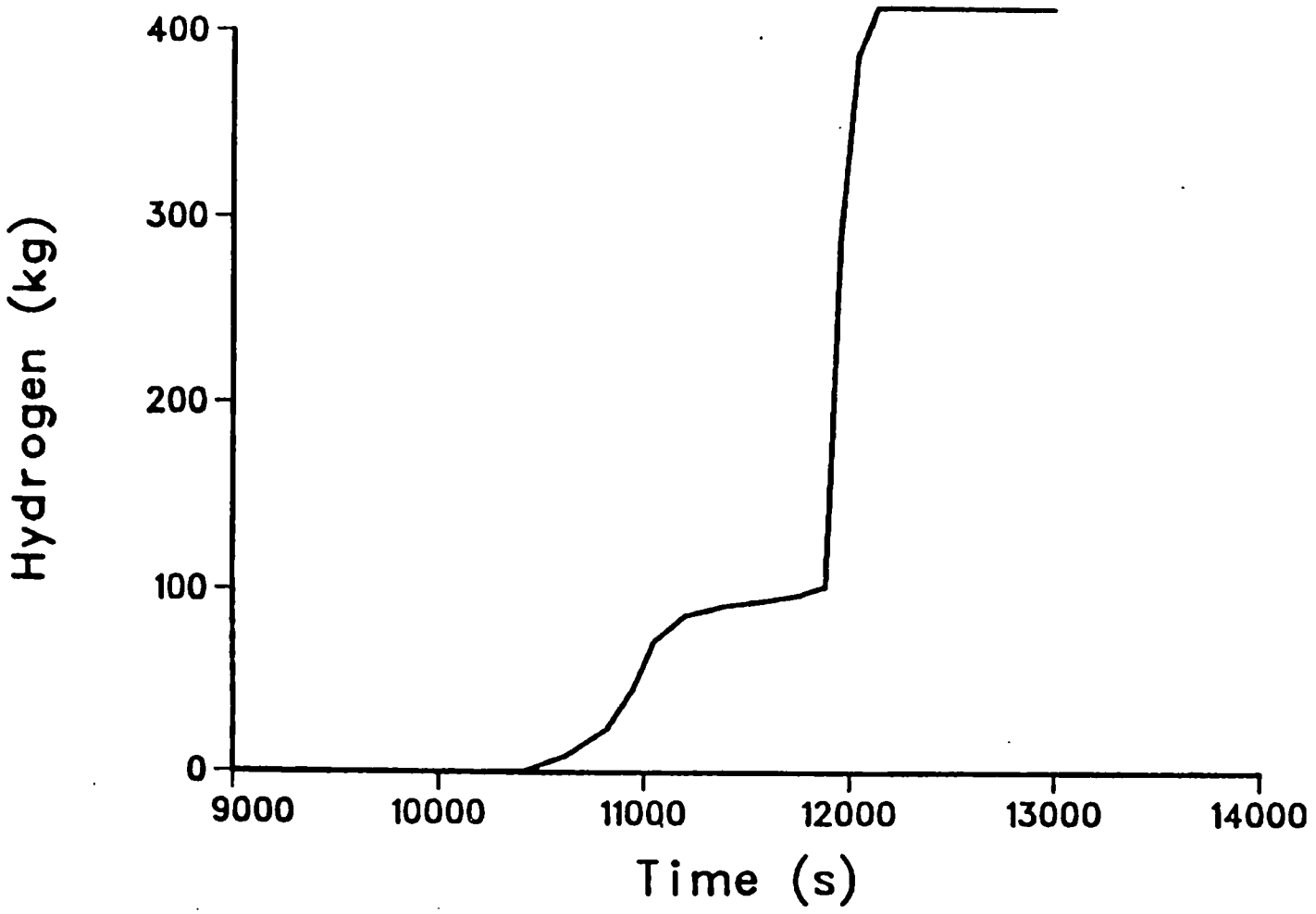

Fig. 47.
Hydrogen mass exiting the core region shown as a function of time (0 to 14000 s).

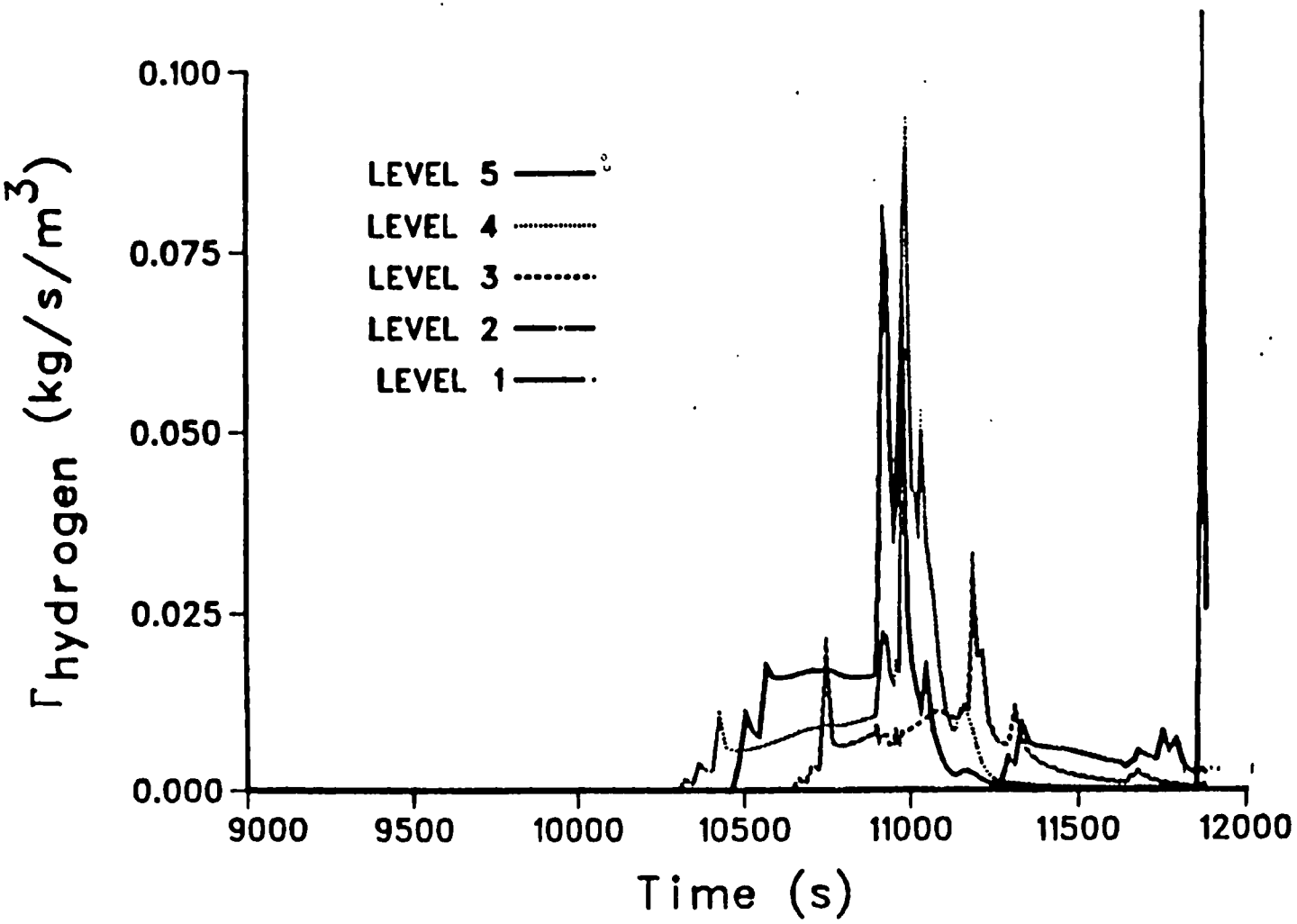

Fig. 48.
Hydrogen generation functions for core levels 1 through 5 shown as a function of time (0 to 11880 s).

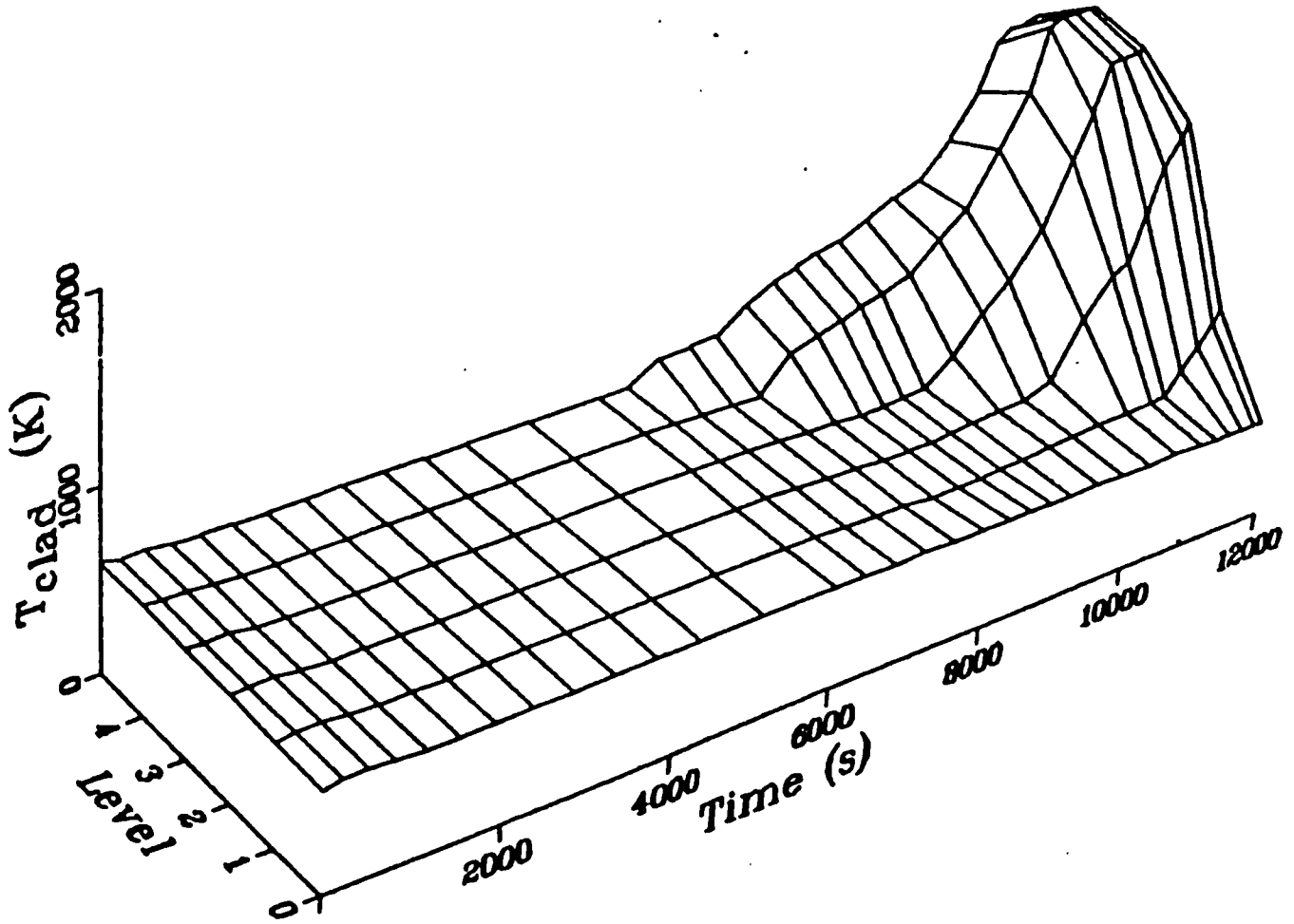

Fig. 49.
Cladding surface temperature shown as a function of core level and time (0 to 11880 s).

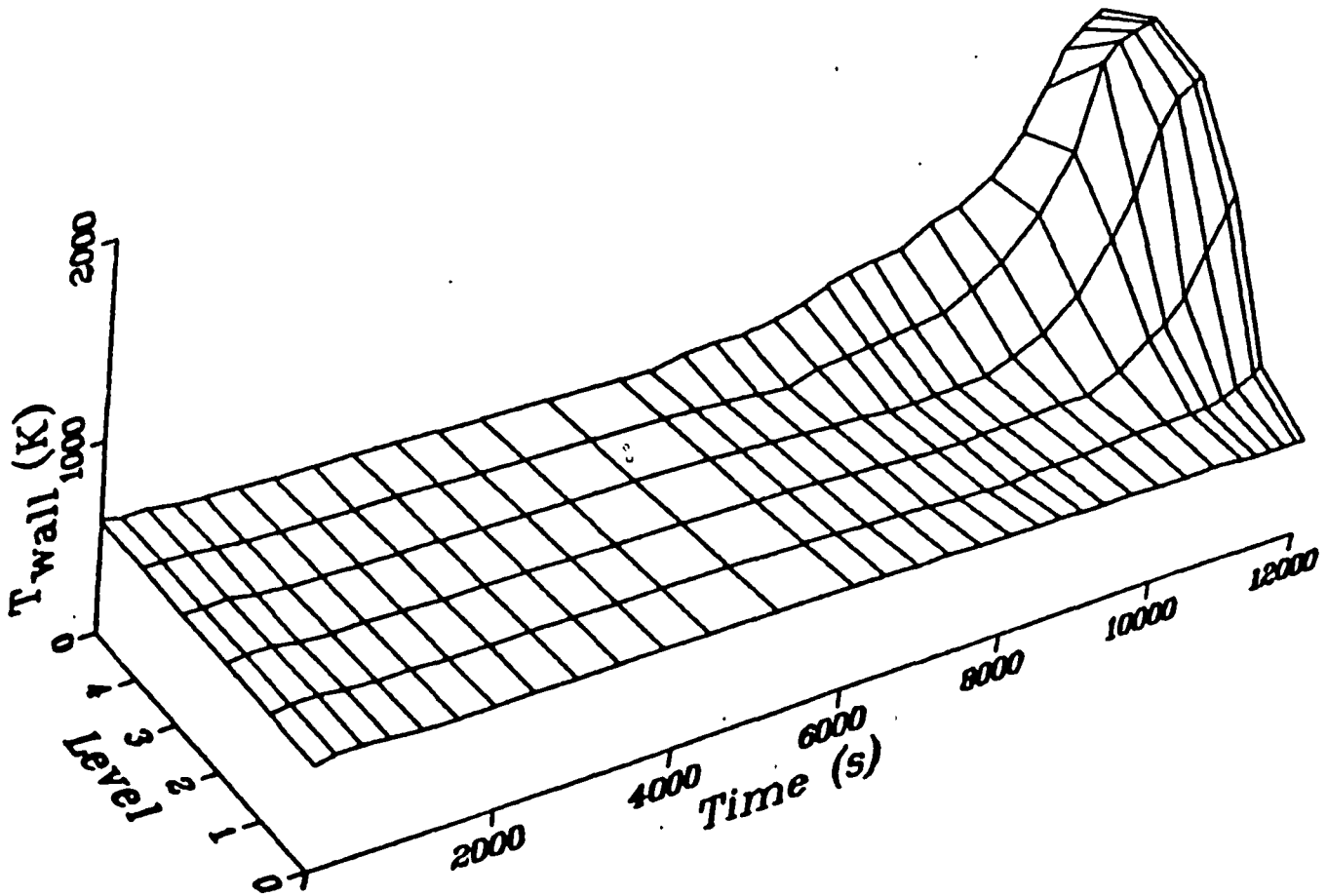

Fig. 50.
Baffle wall surface temperature shown as a function of core level and time (0 to 11880 s).

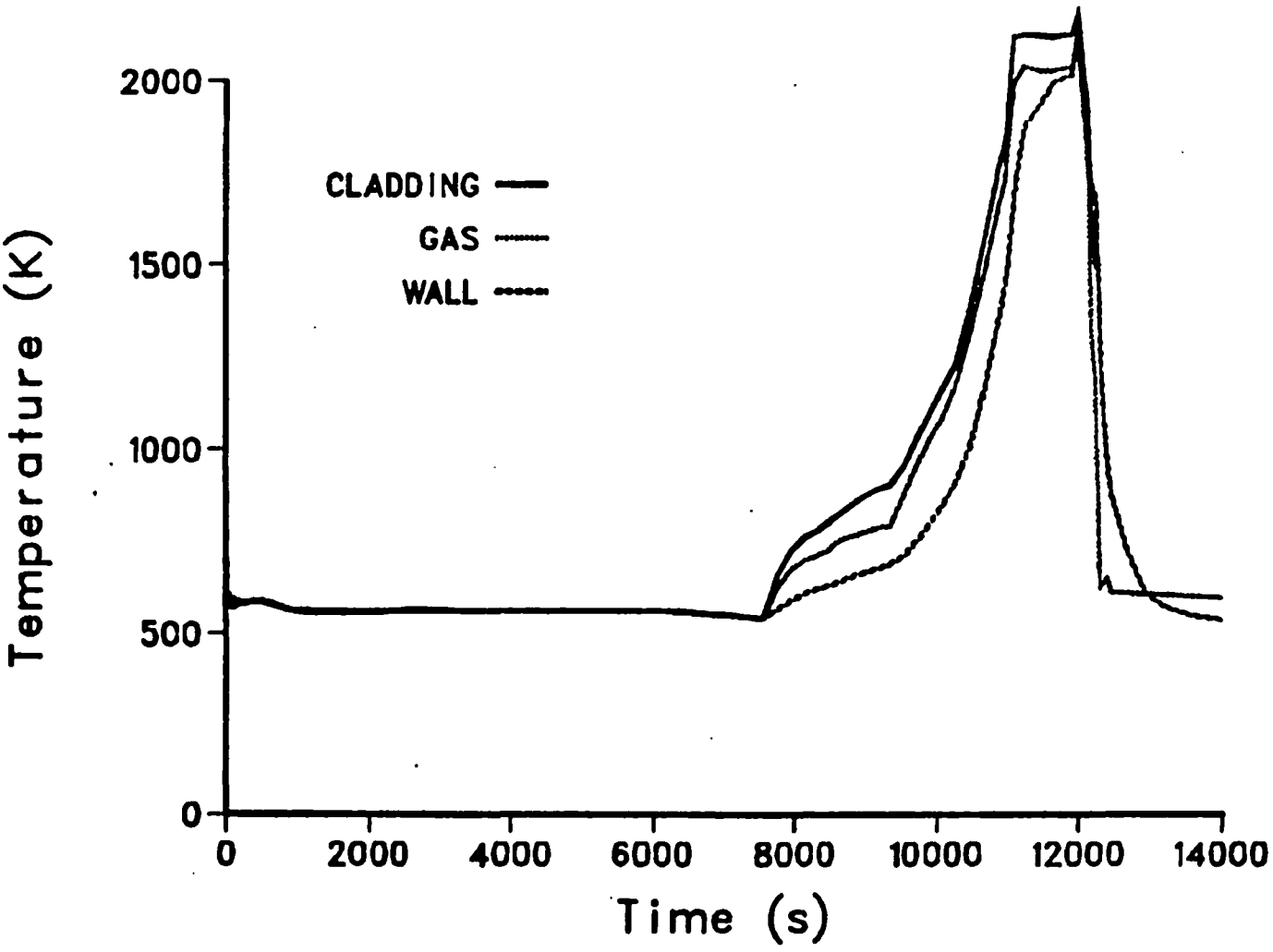

Fig. 51.
Cladding, gas, and Baffle wall temperatures at core level 4 (hottest level) shown as a function of time (0 to 14000 s).

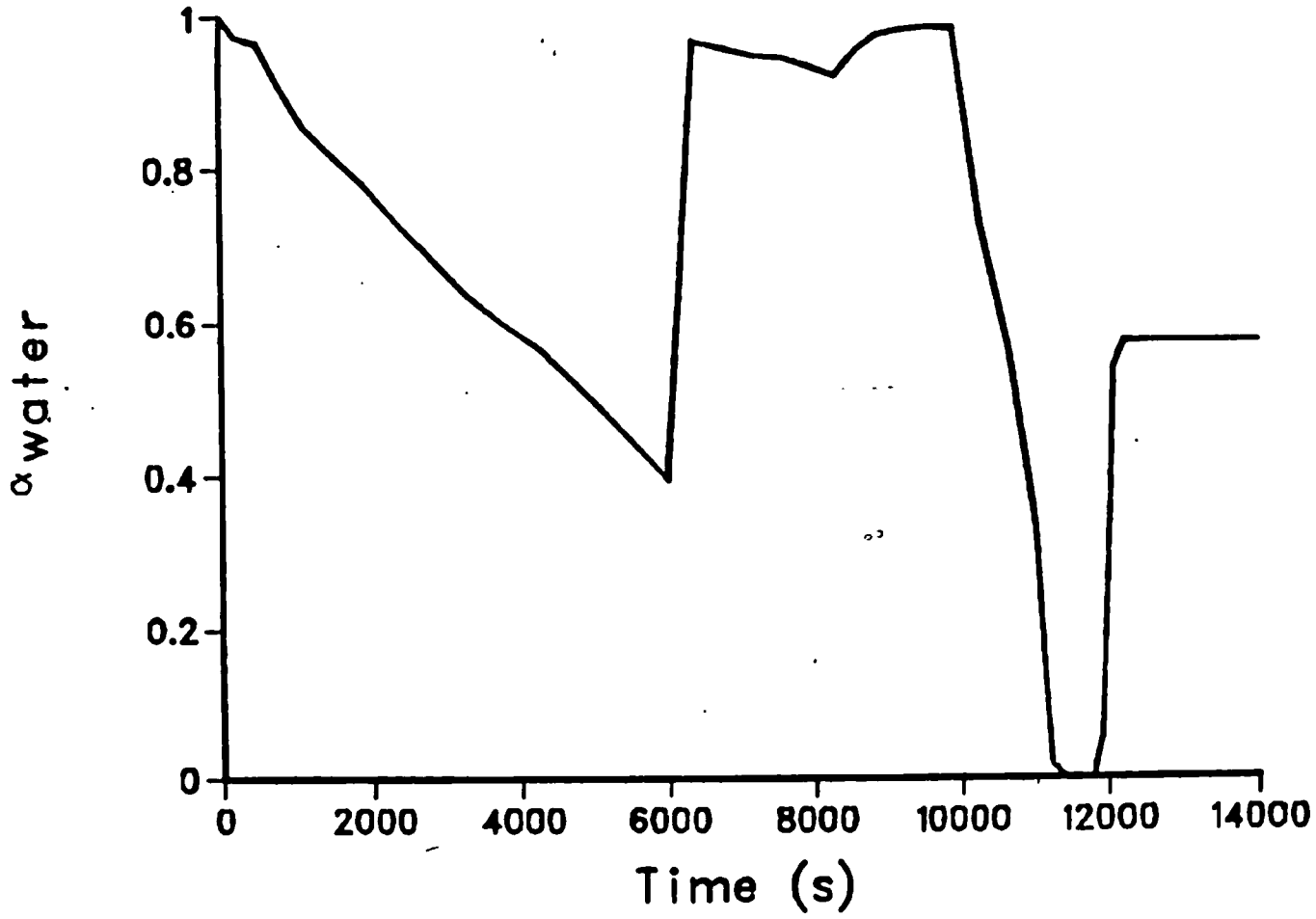

Fig. 52.
Water volume fraction at core level 1 (core bottom) shown as a function of time (0 to 14000 s).

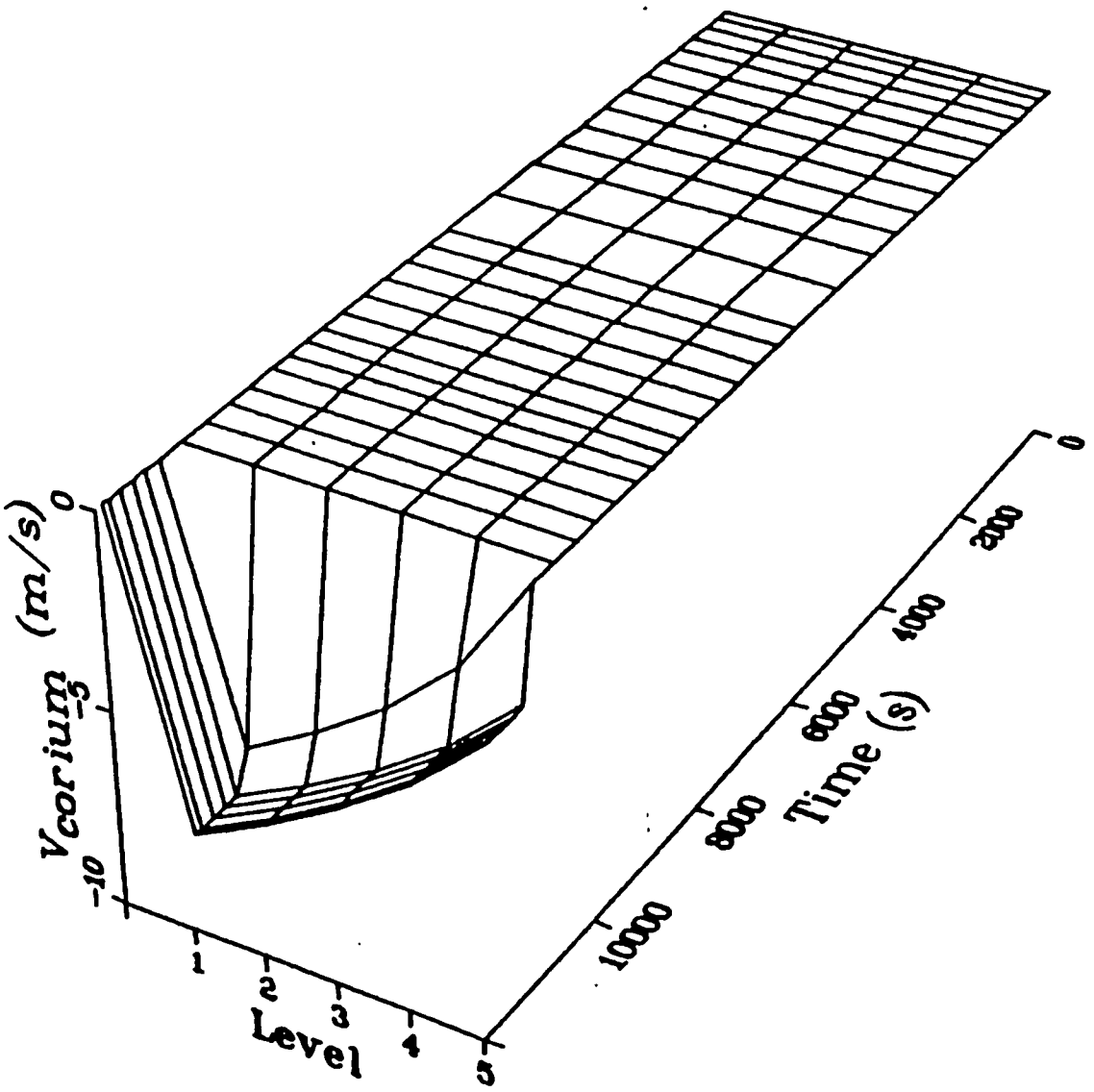

Fig. 53.
Corium velocity surface shown as a function of core level and time (0 to 11880 s).

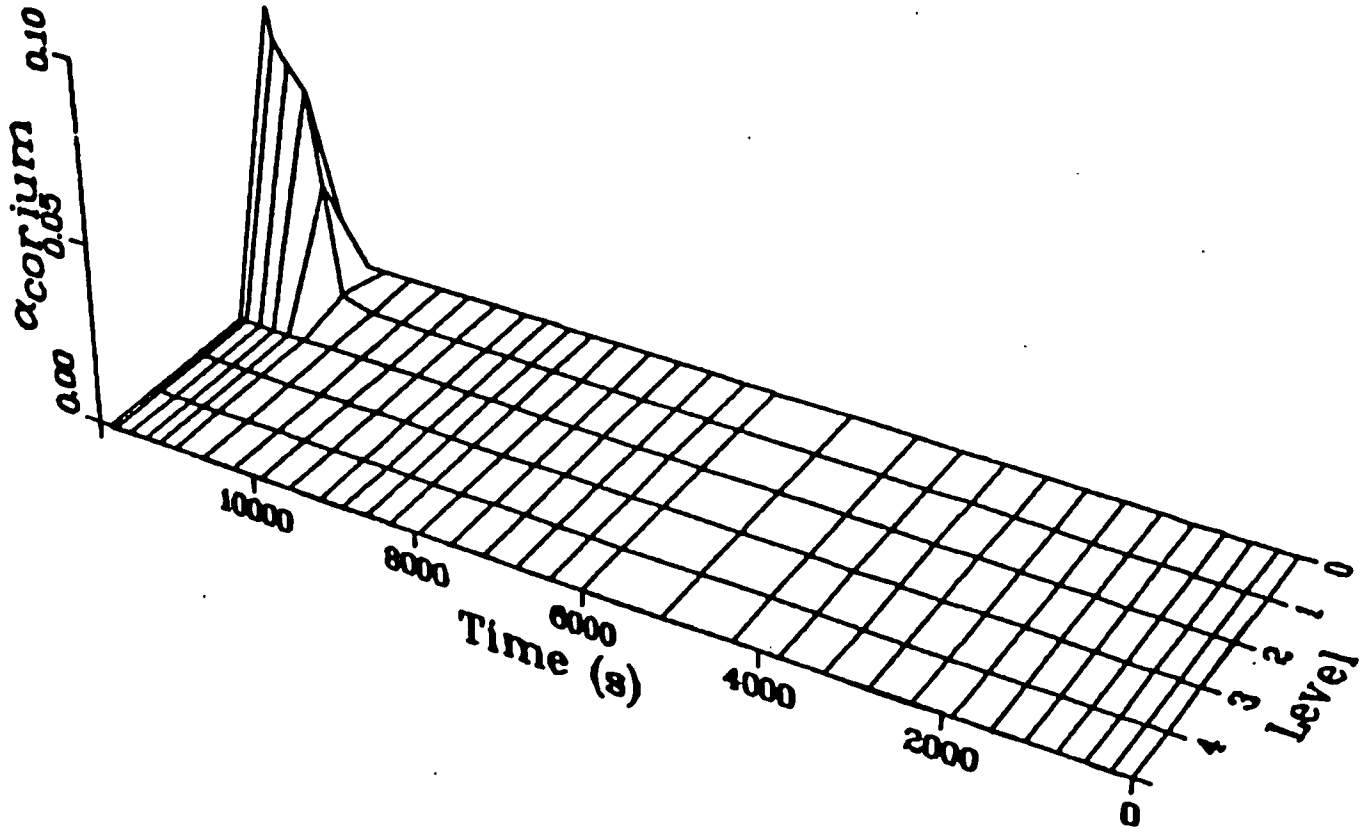

Fig. 54.
Corium volume fraction surface shown as a function of core level and time (0 to 11880 s).

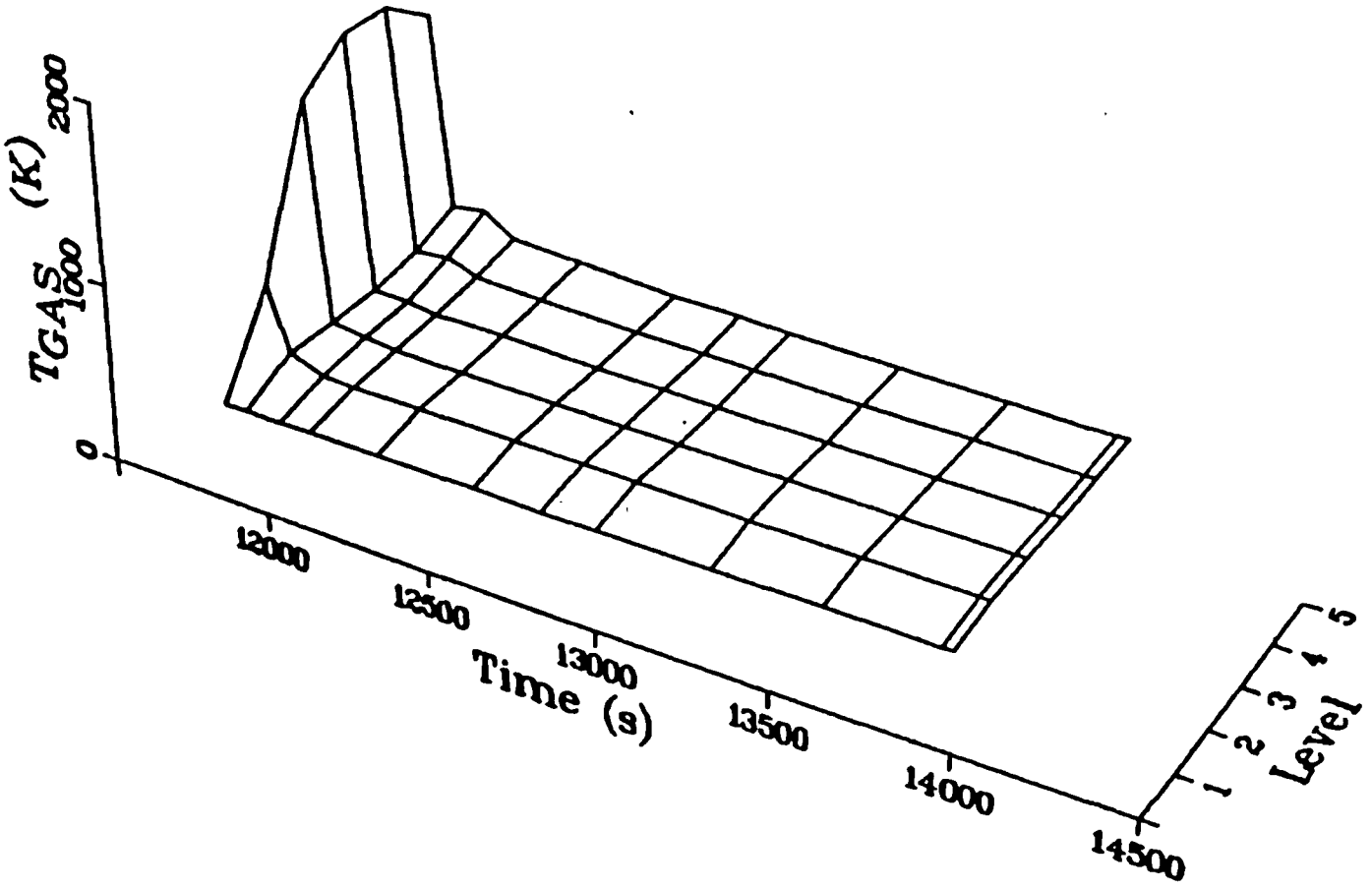

Fig. 55.
Gas temperature surface shown as a function of core level and time (11880 to 14000 s).

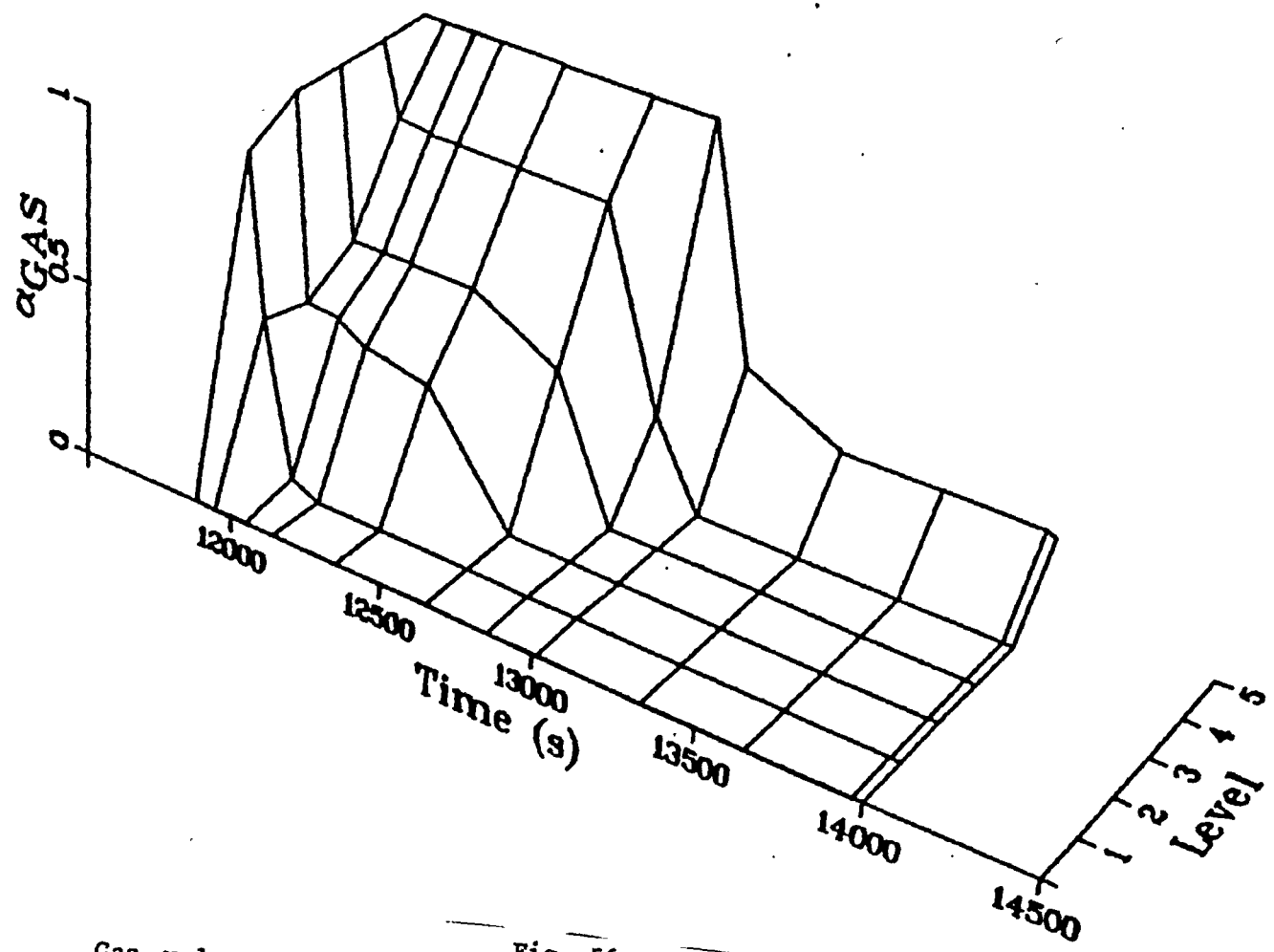

Fig. 56.
Gas volume fraction surface shown as a function of core level and time (11880 to 14000 s).

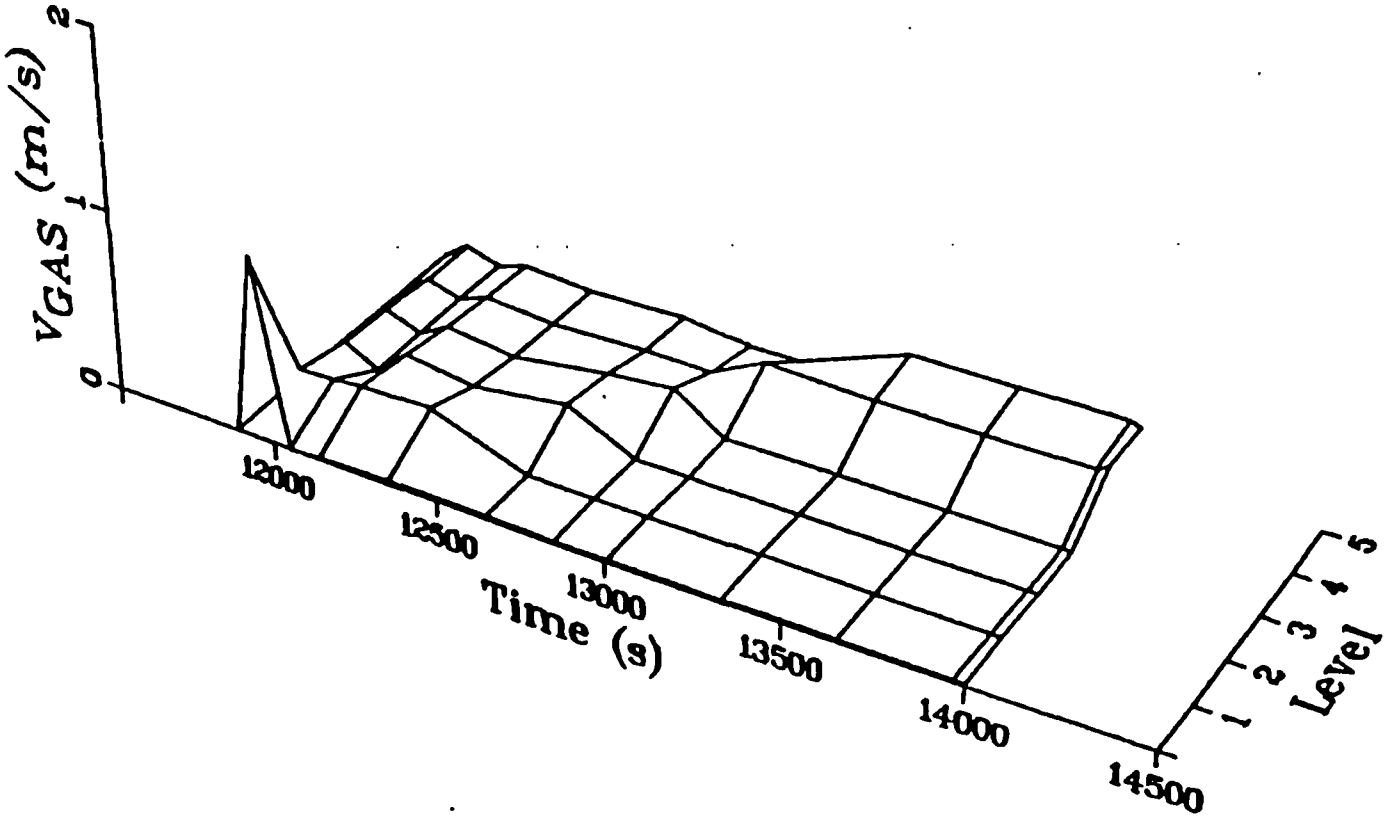

Fig. 57.
Gas velocity surface shown as a function of core level and time (11880 to 14000 s).

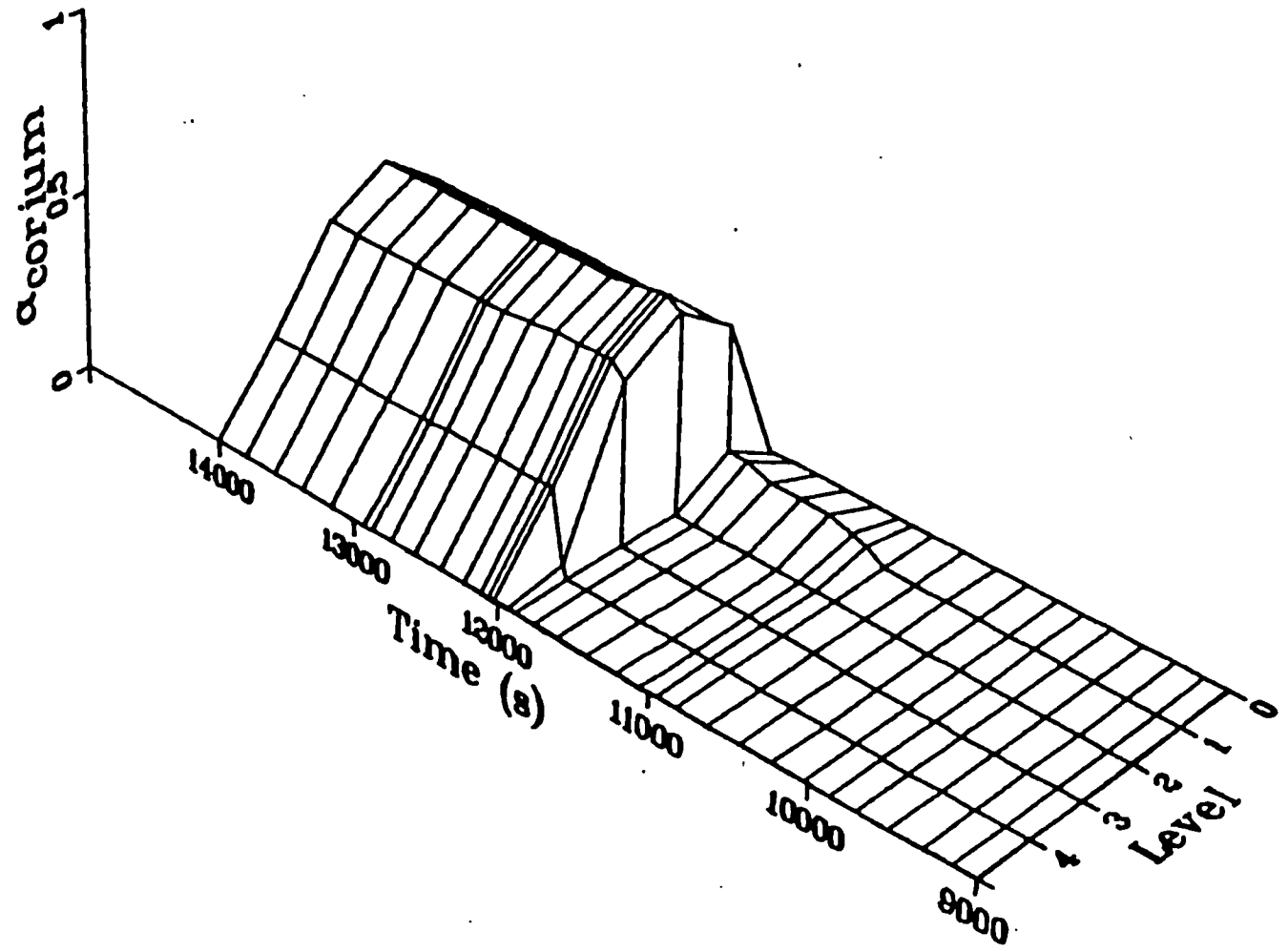

Fig. 58.
Corium volume fraction surface shown as a function of core level and time (9000 to 14000 s).

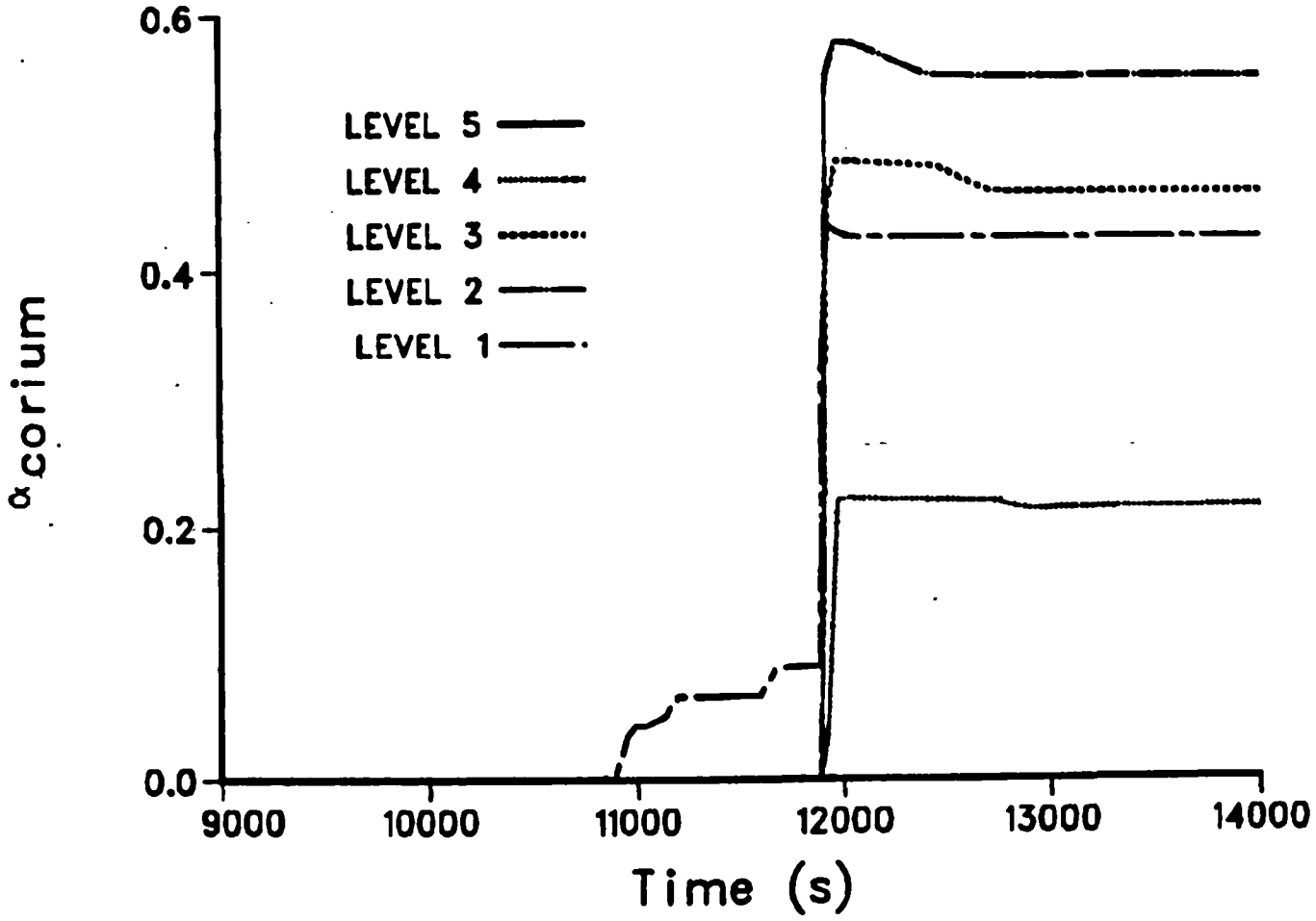

Fig. 59.
Corium volume fraction shown as a function of core level and time (0 to 13000 s).

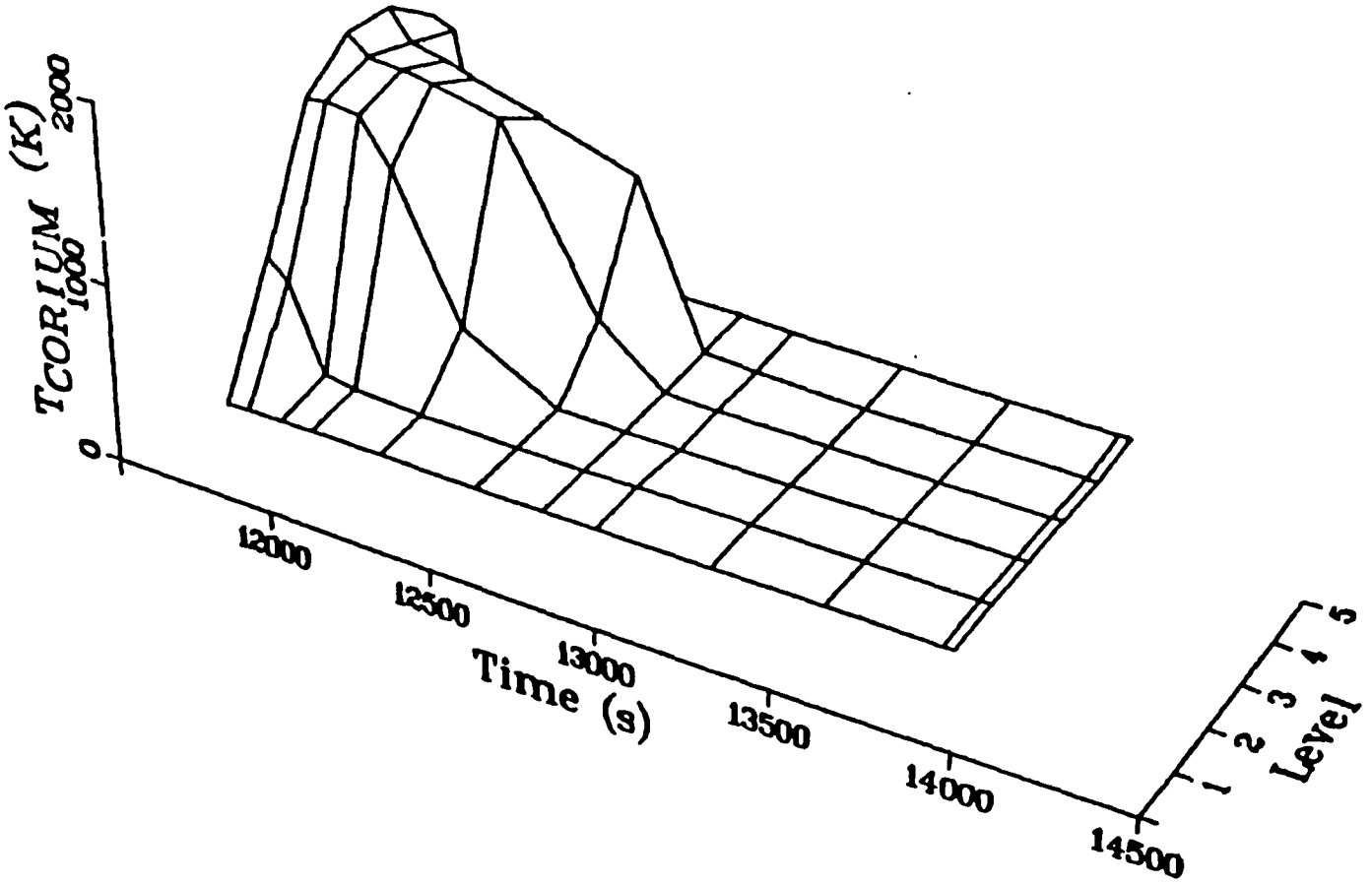

Fig. 60.
Corium temperature surface shown as a function of core level and time (11880 to 14000 s).

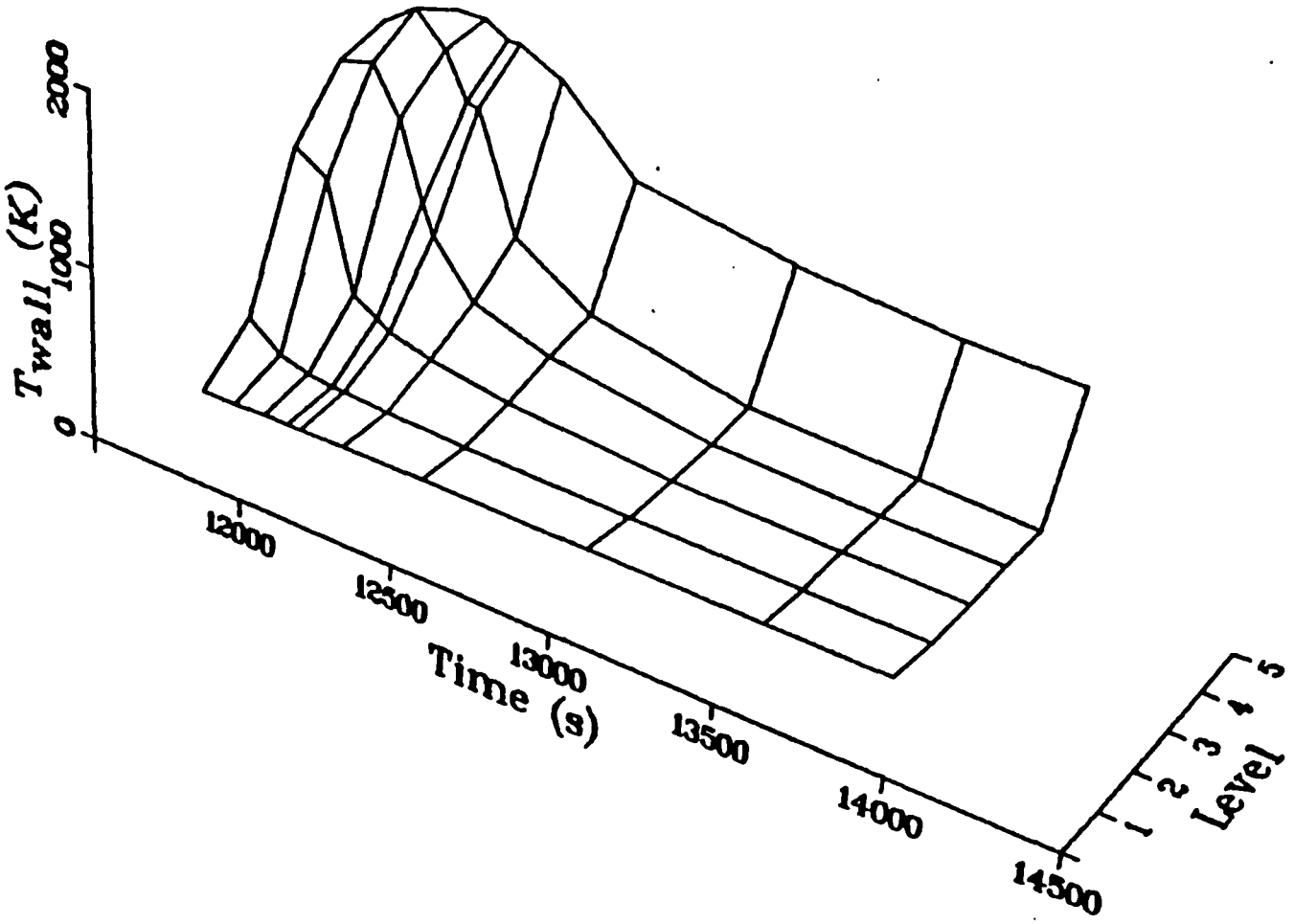

Fig. 61.
Baffle wall surface temperature shown as a function of core level and time (11880 to 14000 s).

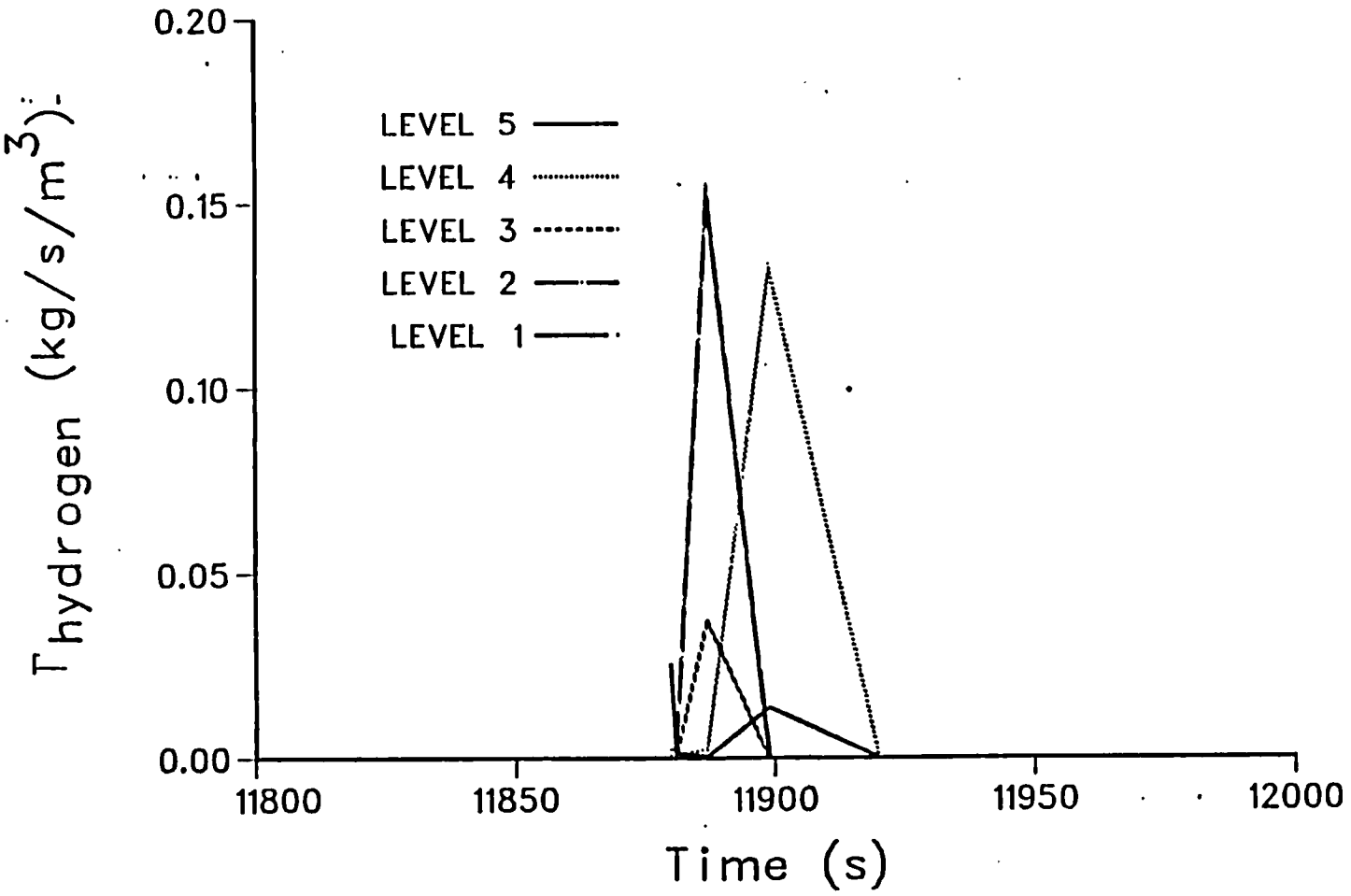

Fig. 62.
Hydrogen generation functions for core levels 1 through 5 shown as a function of time (11880 to 14000 s).

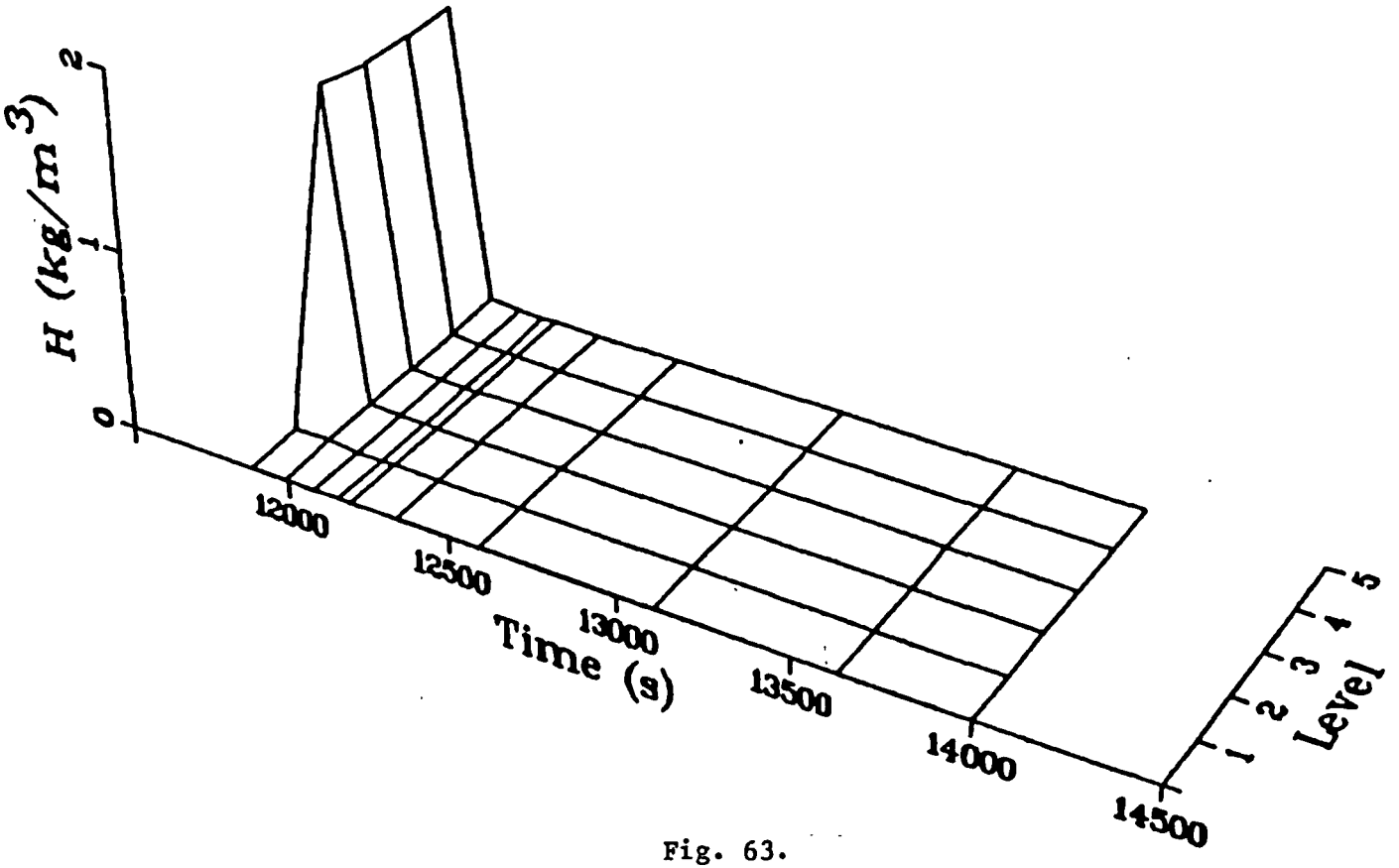

Fig. 63.
Hydrogen density surface shown as a function of core level and time (11880 to 14000 s).

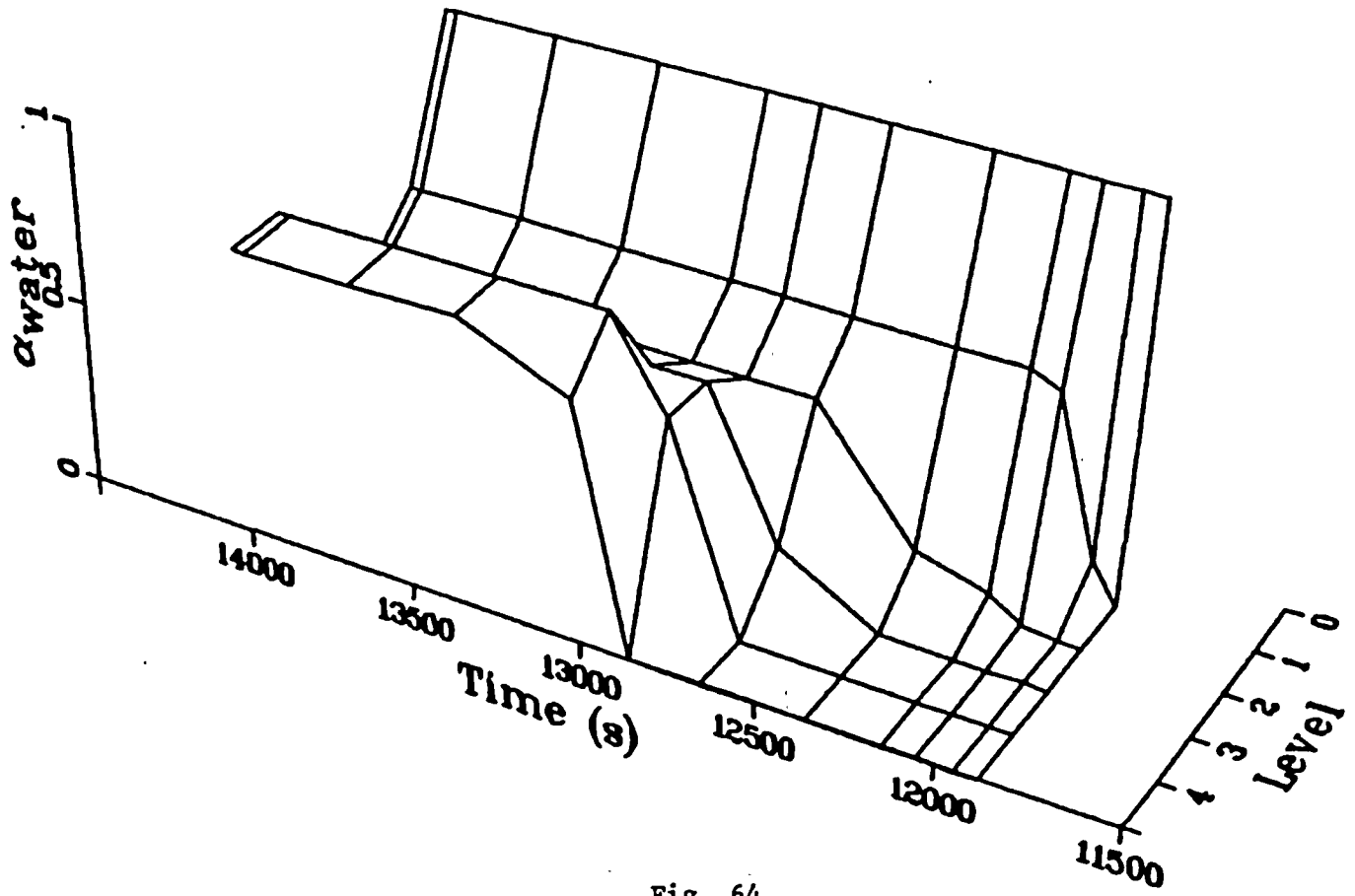

Fig. 64
Water volume fraction surface shown as a function of core level and time (11880 to 14000 s).

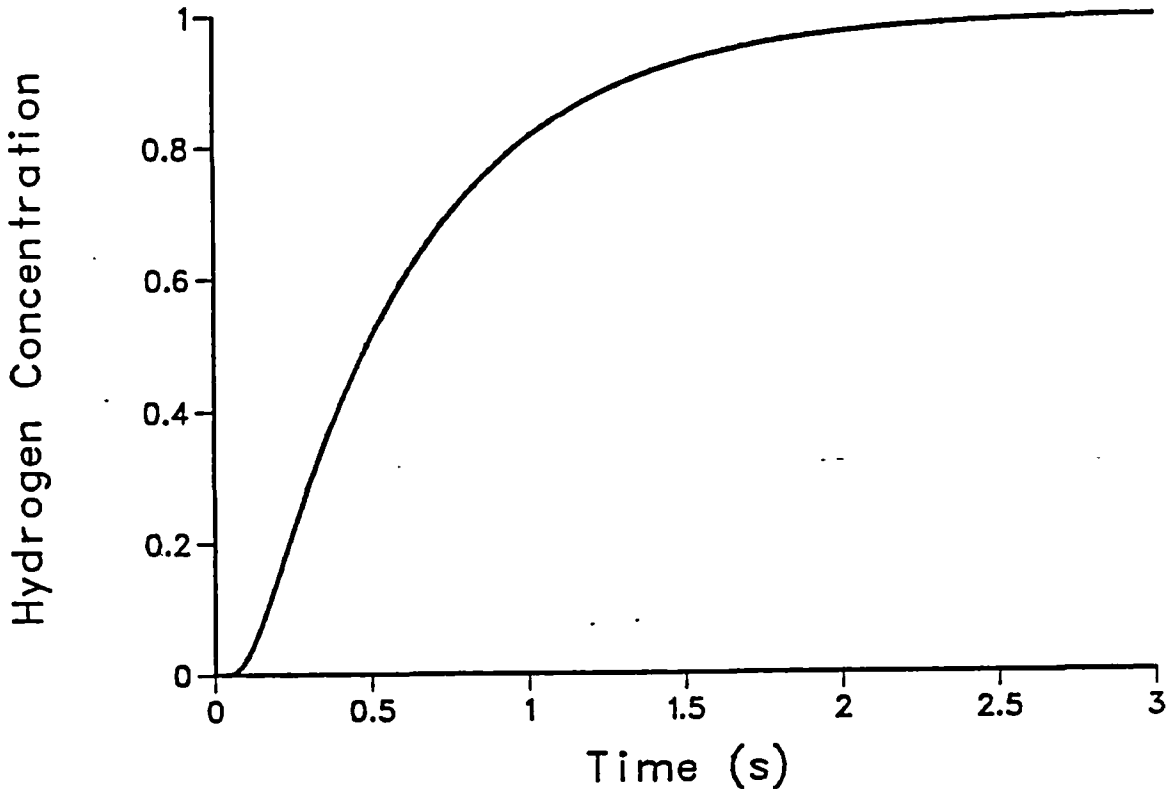

Fig. 65.
H_2 concentration midway between fuel pins.

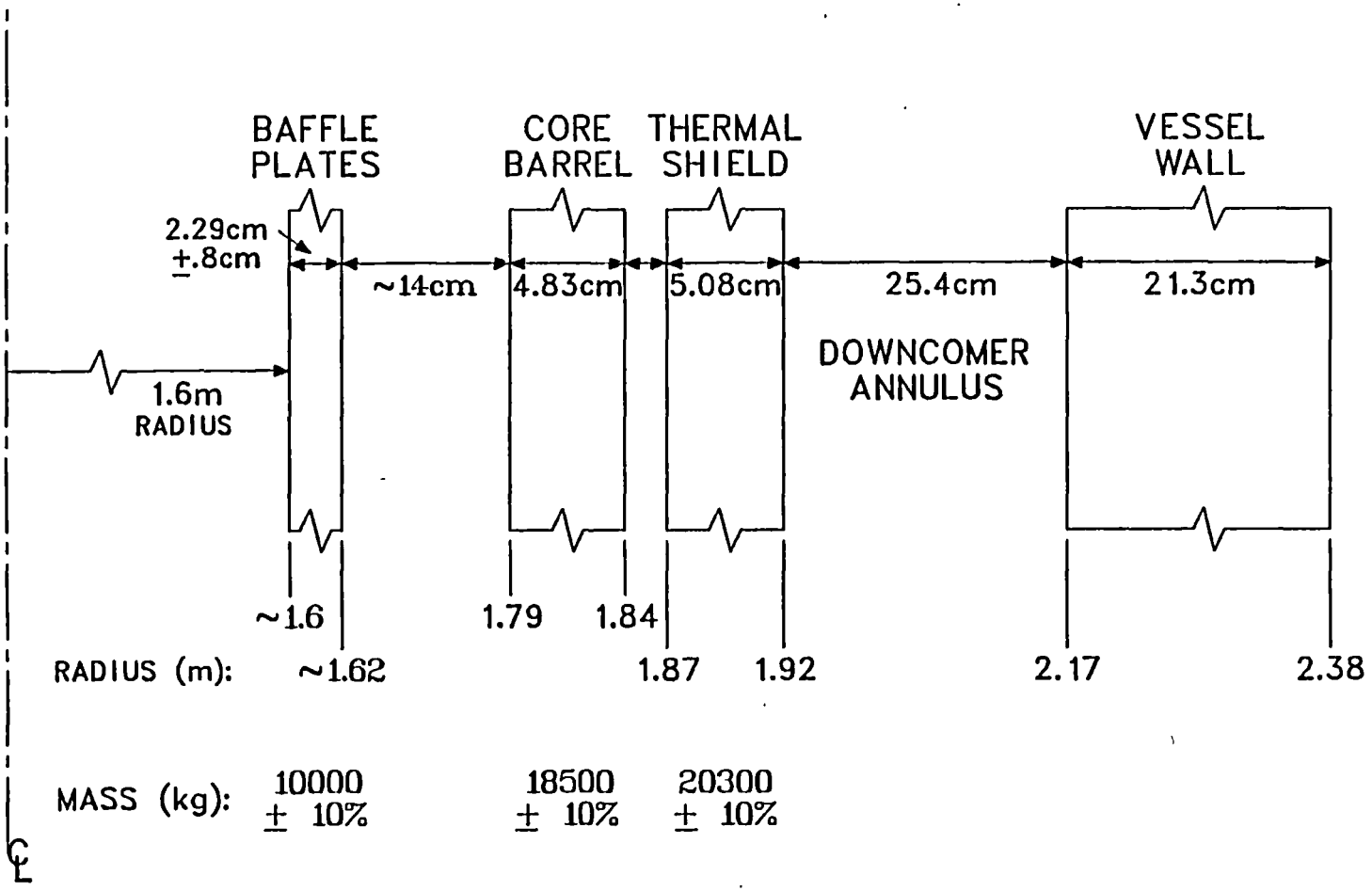

Fig. 66.
TMI radially adjacent core region hardware (data from Ref. 40).

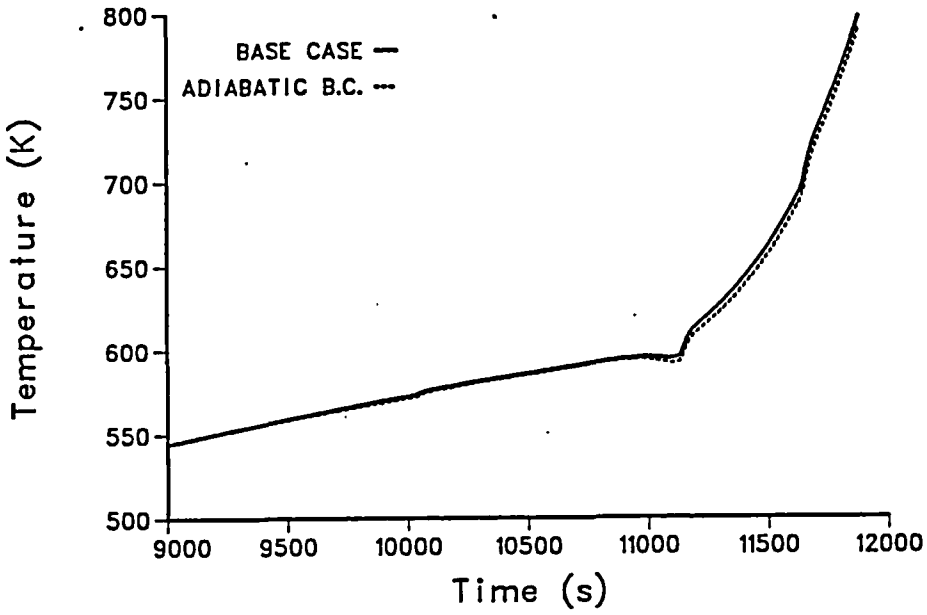

Fig. 67.
Wall surface temperature--level 1.

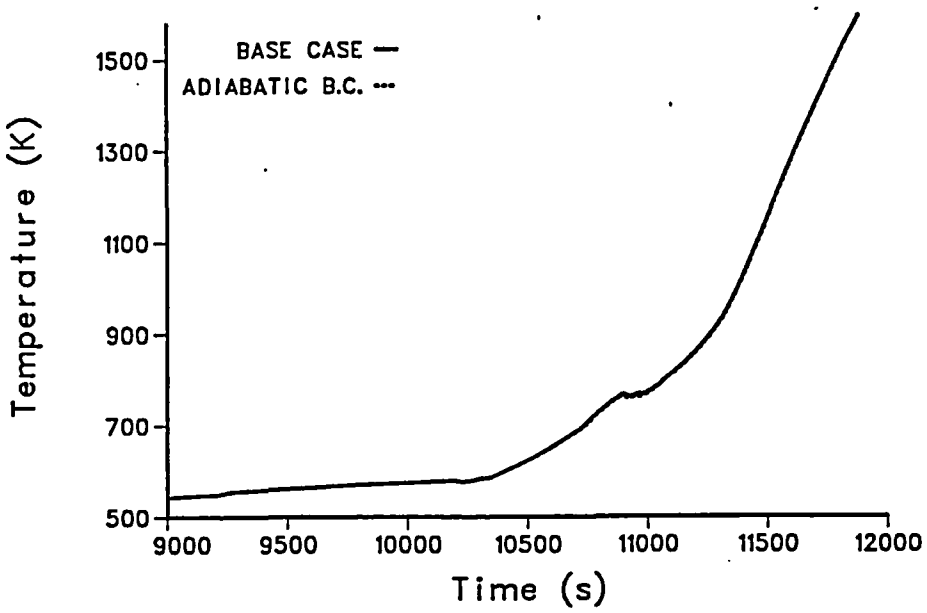

Fig. 68.
Wall surface temperature--level 2.

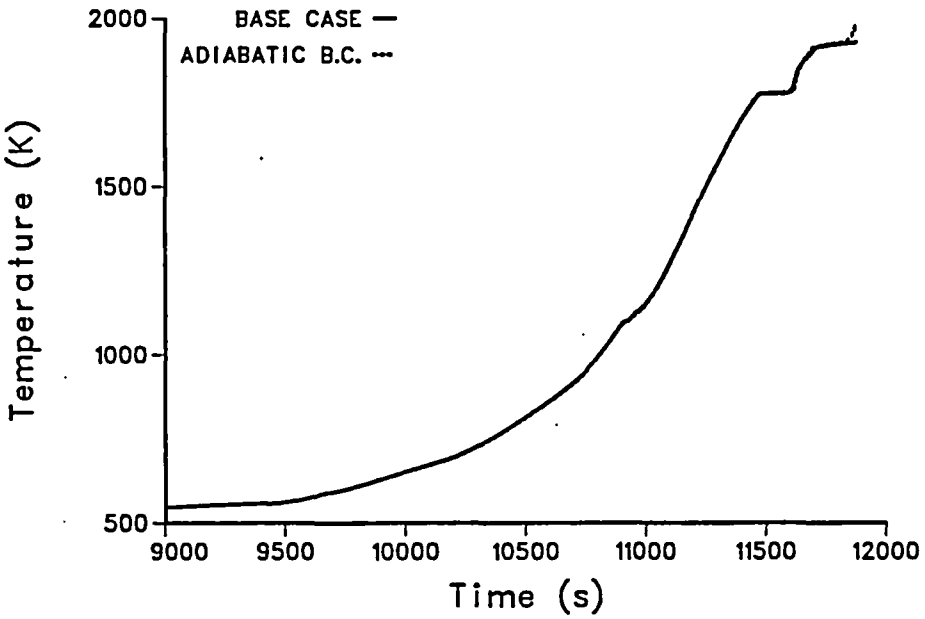

Fig. 69.
Wall surface temperature--level 3.

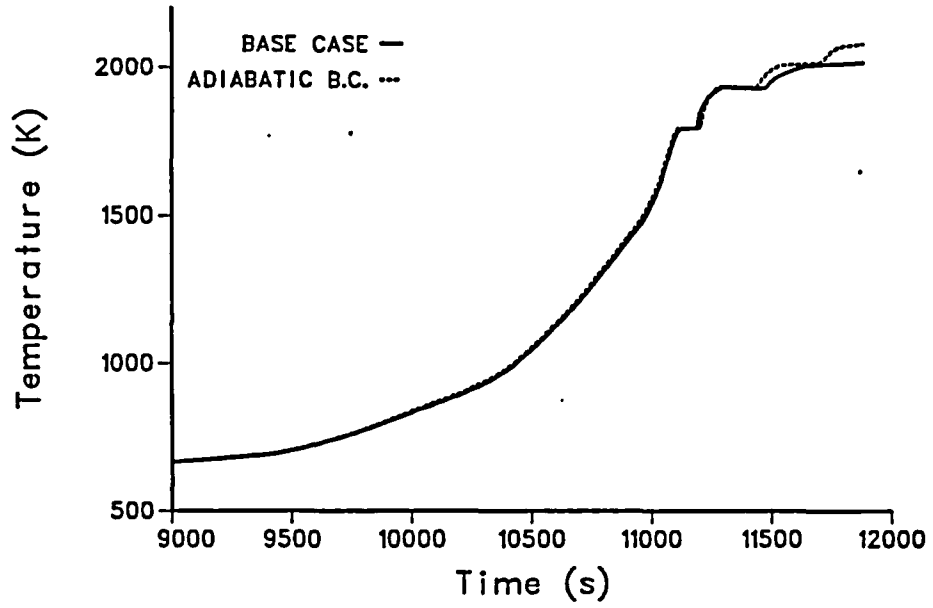

Fig. 70.
Wall surface temperature--level 4.

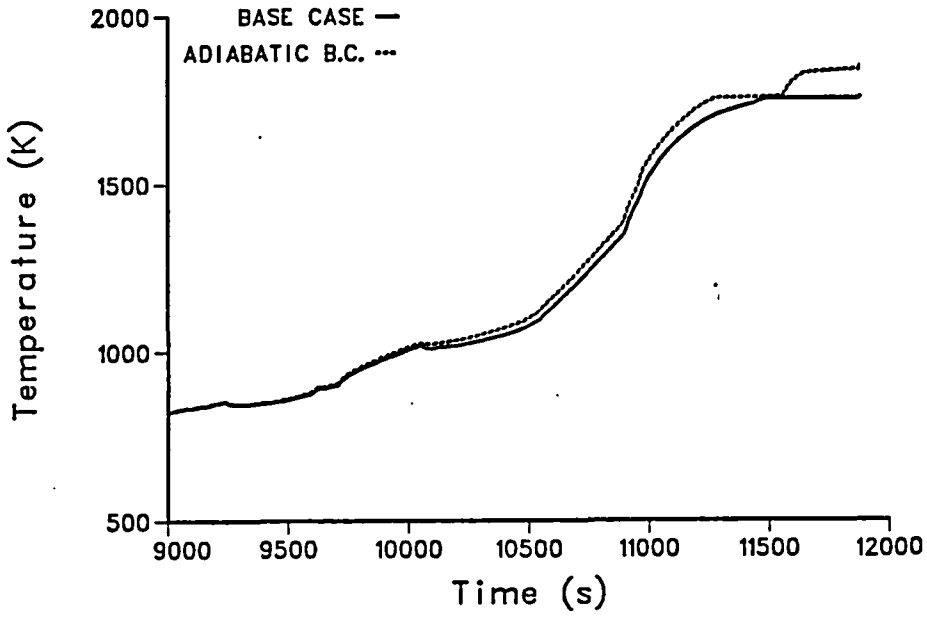

Fig. 71.
Wall surface temperature--level 5.

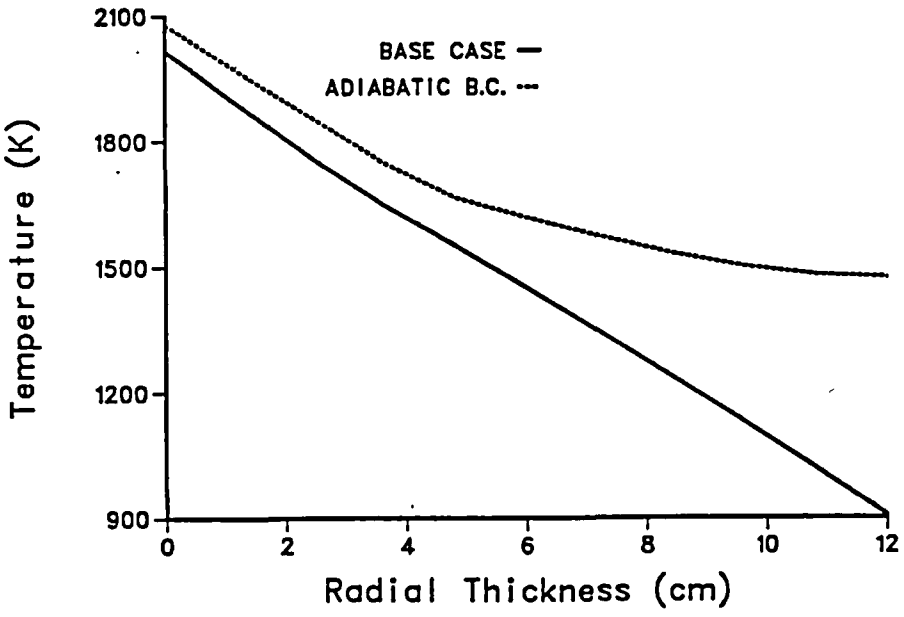

Fig. 72.
Wall temperature profile--level 4 (t = 11880 s).

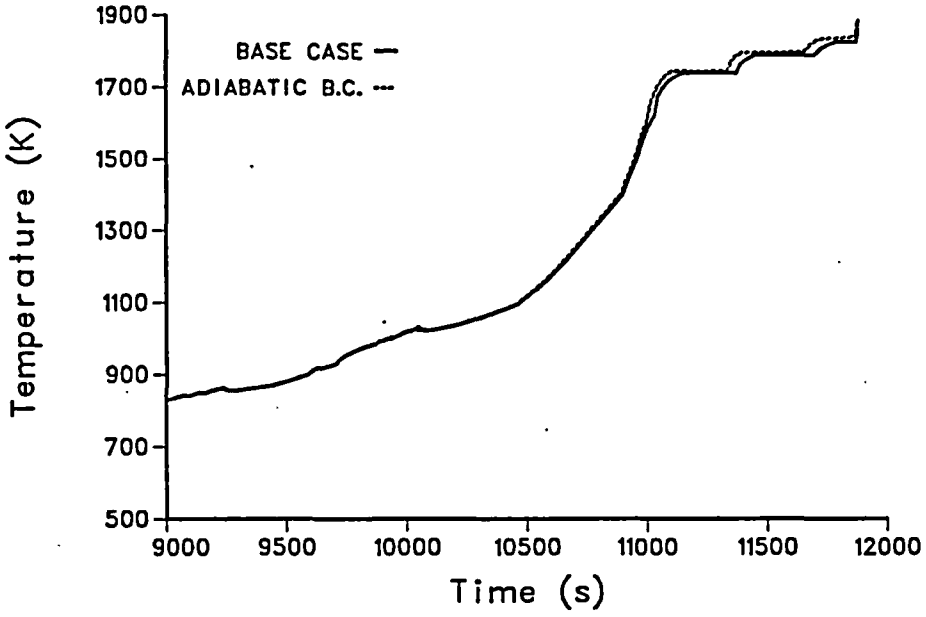

Fig. 73.
Top plate temperature--ring 1.

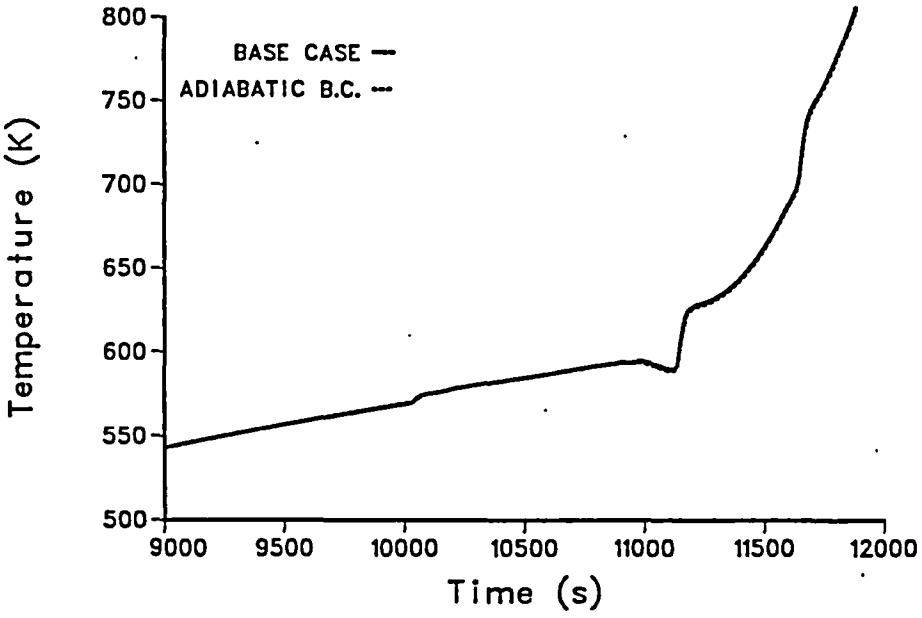

Fig. 74.
Bottom plate temperature--ring 1.

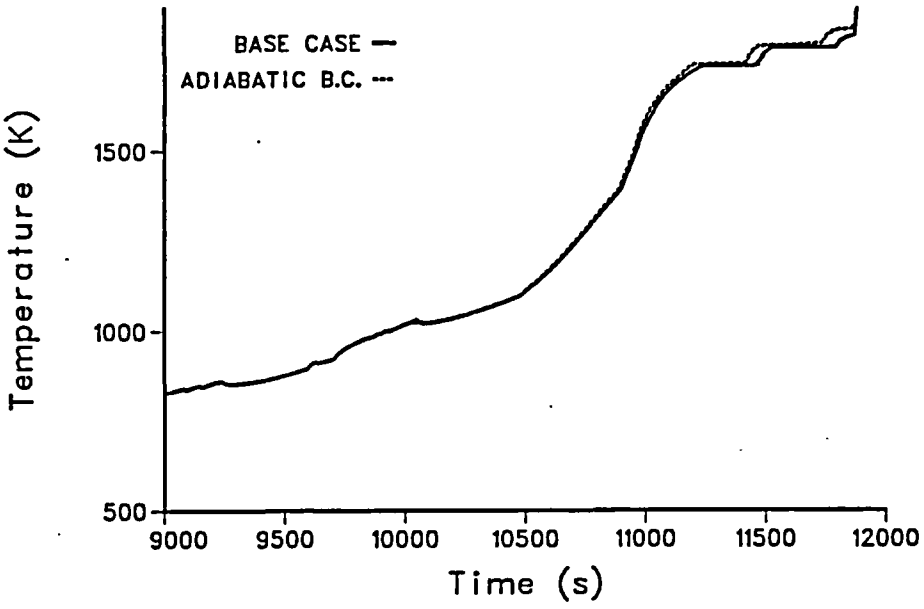

Fig. 75.
Top plate temperature--ring 2.

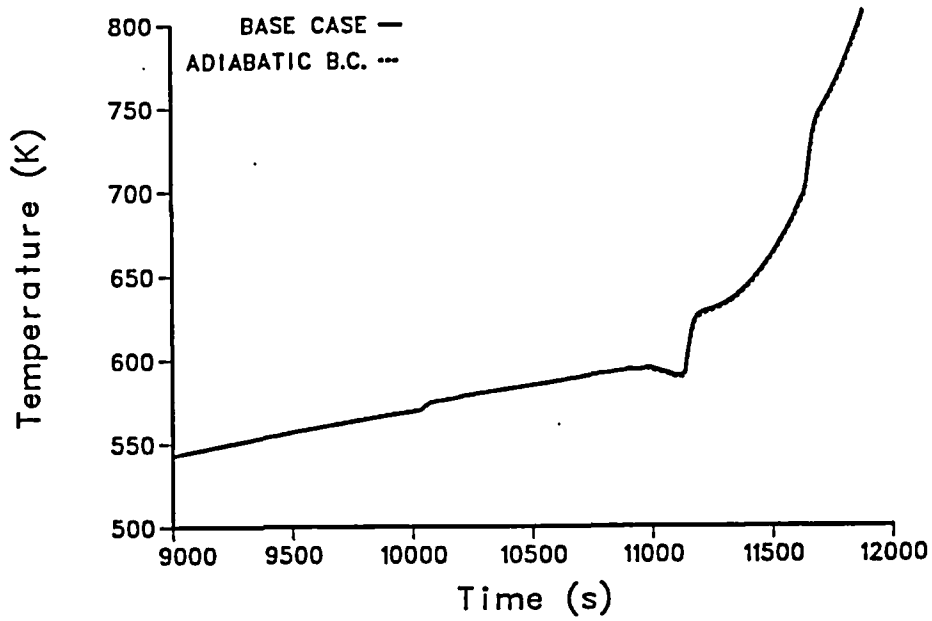

Fig. 76.
Bottom plate temperature--ring 2.

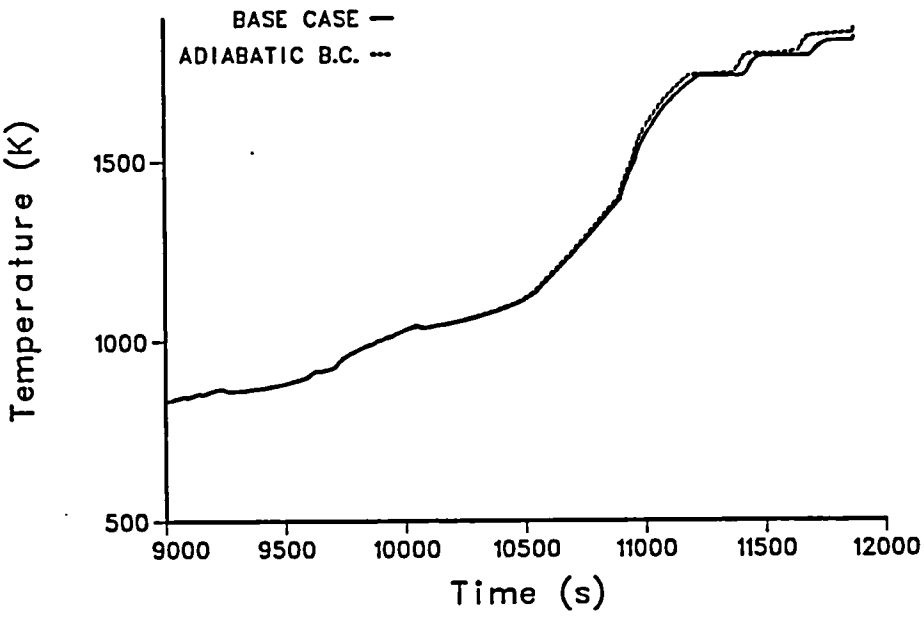

Fig. 77.
Top plate temperature--ring 3.

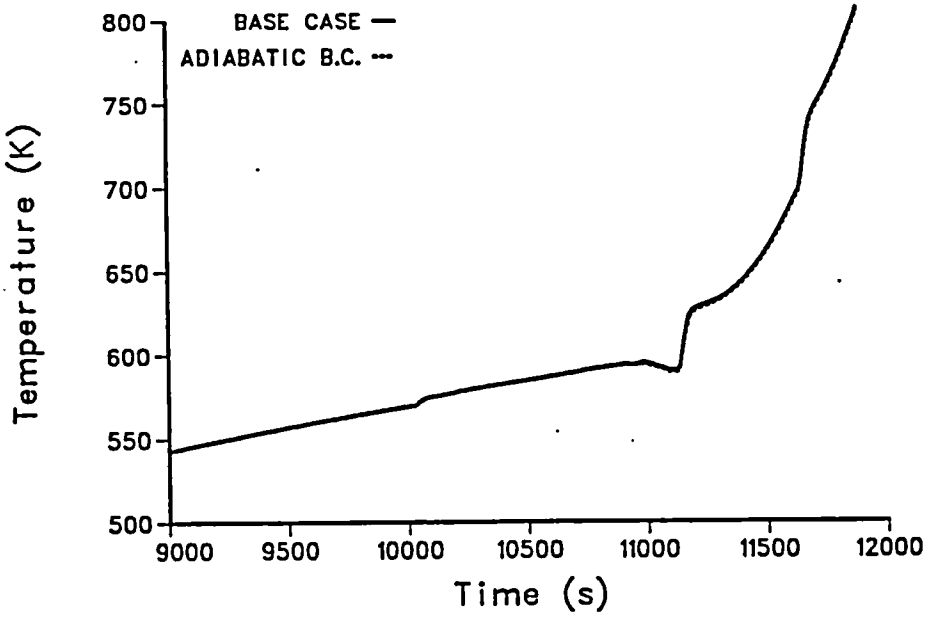

Fig. 78.
Bottom plate temperature--ring 3.

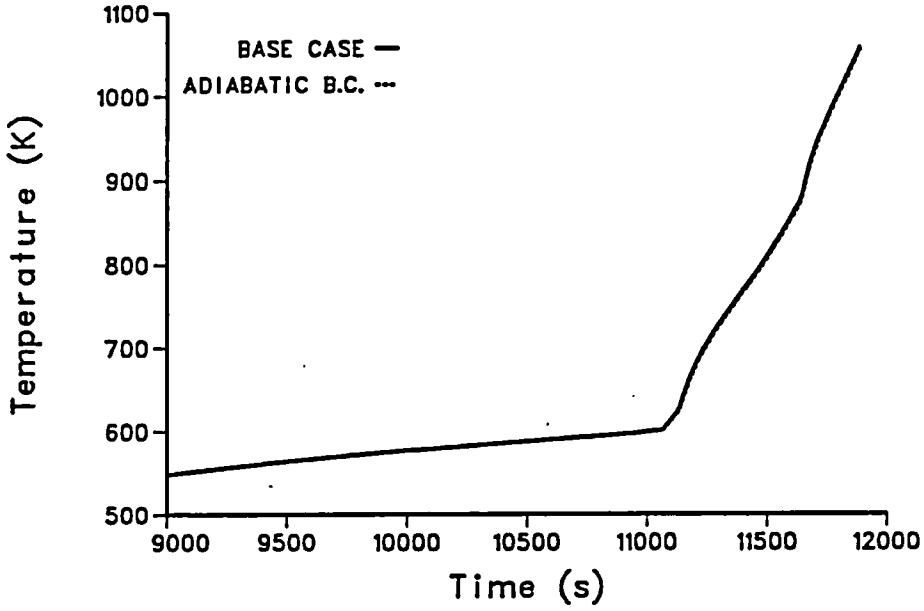

Fig. 79.
Cladding temperature--ring 1, level 1.

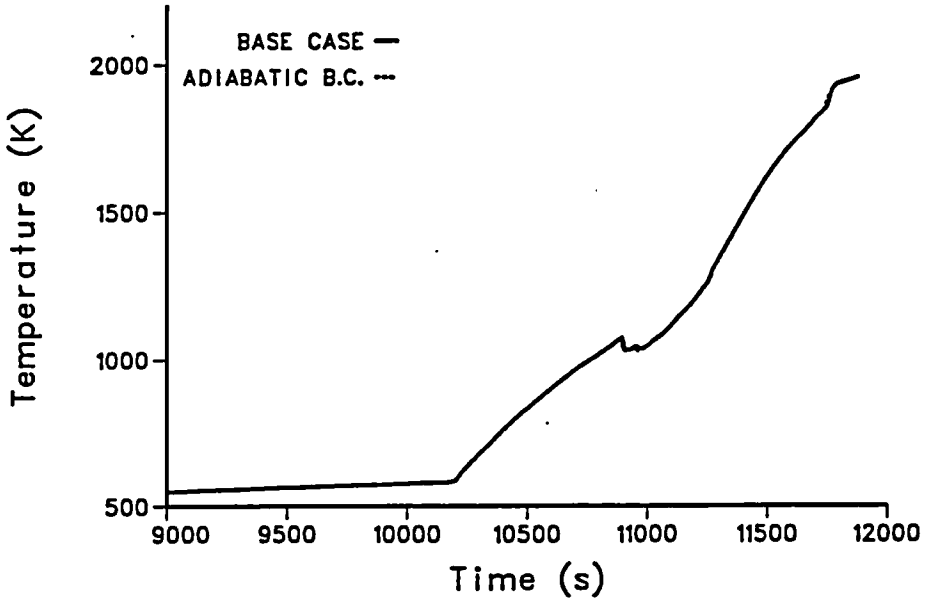

Fig. 80.
Cladding temperature--ring 1, level 2.

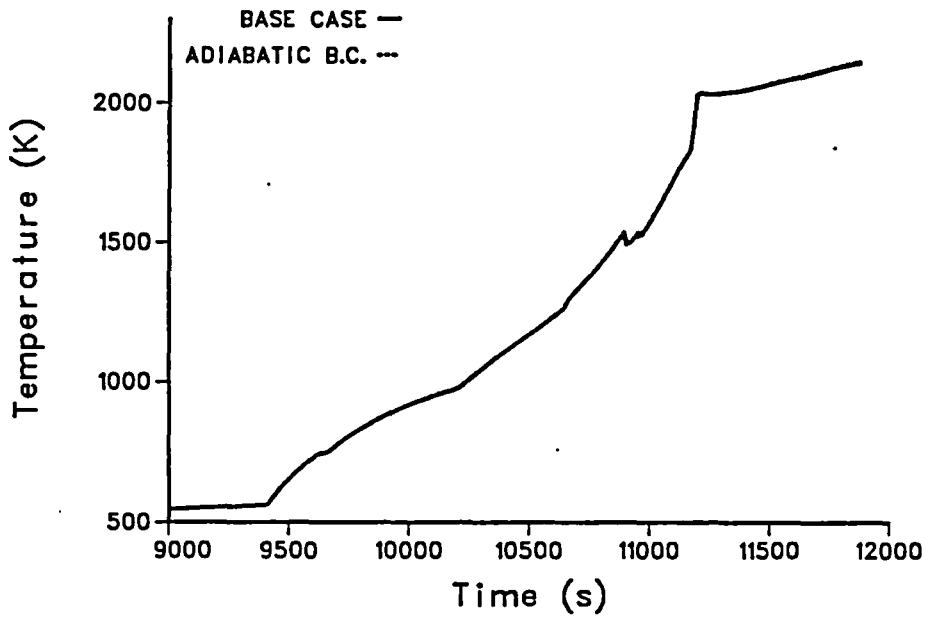

Fig. 81.
Cladding temperature--ring 1, level 3.

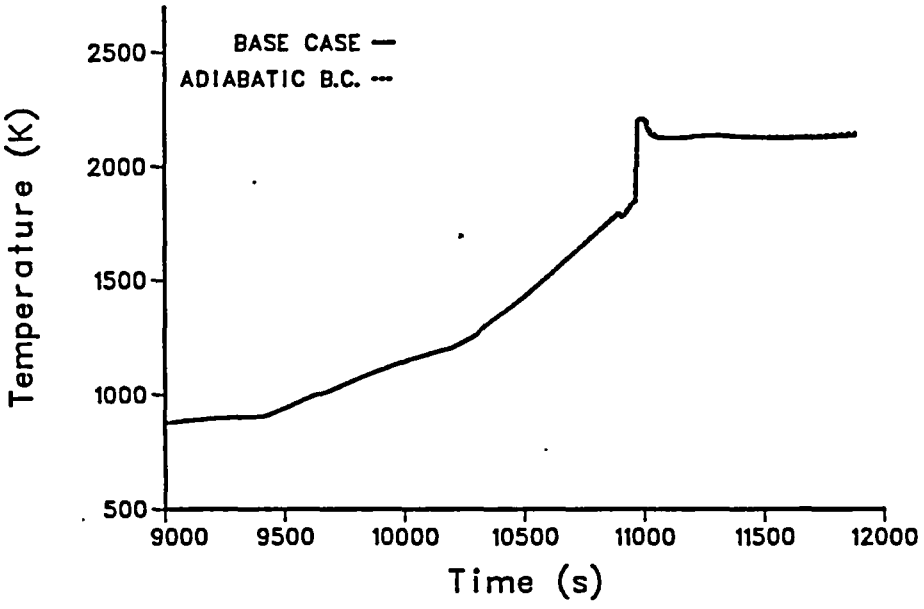

Fig. 82.
Cladding temperature--ring 1, level 4.

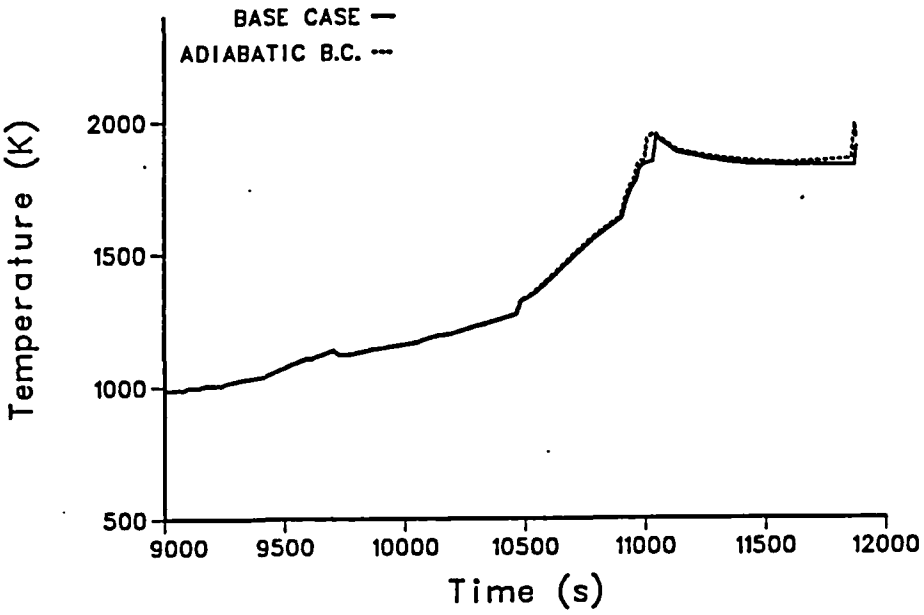

Fig. 83.
Cladding temperature--ring 1, level 5.

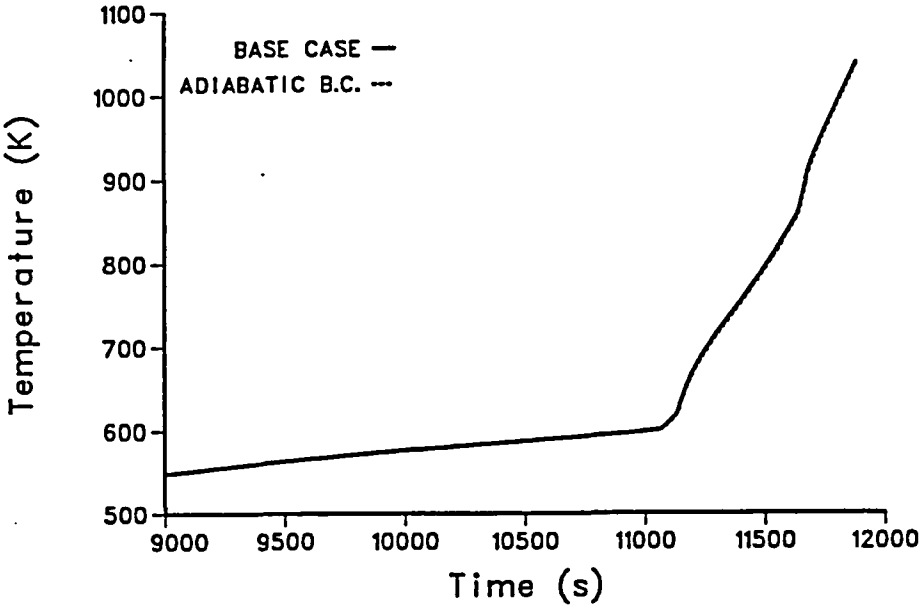

Fig. 84.
Cladding temperature--ring 3, level 1.

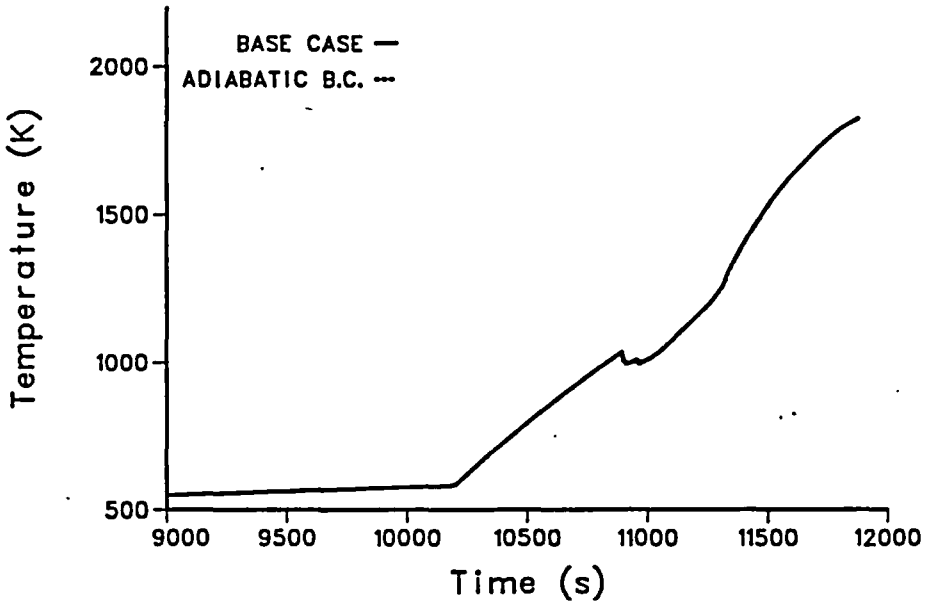

Fig. 85.
Cladding temperature--ring 3, level 2.

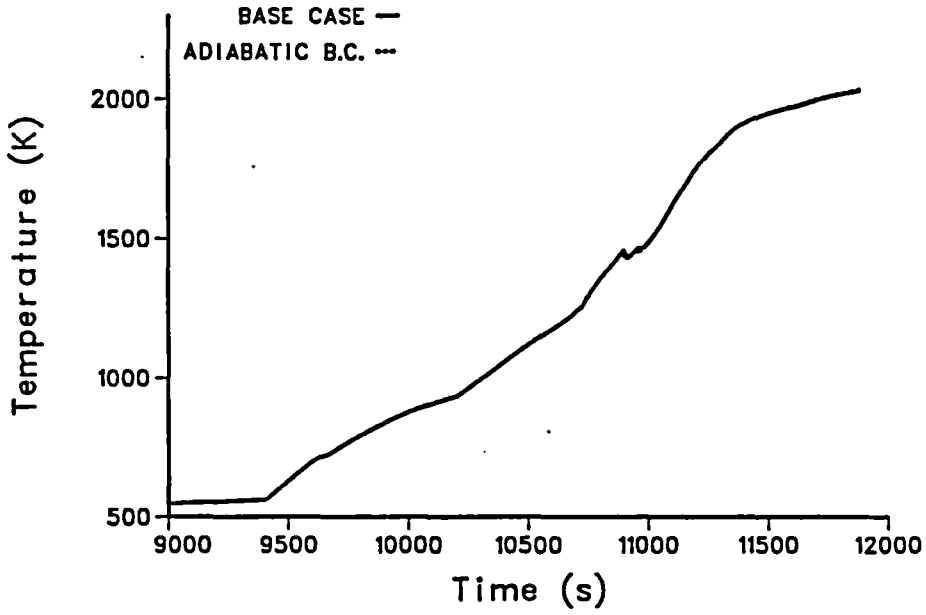

Fig. 86.
Cladding temperature--ring 3, level 3.

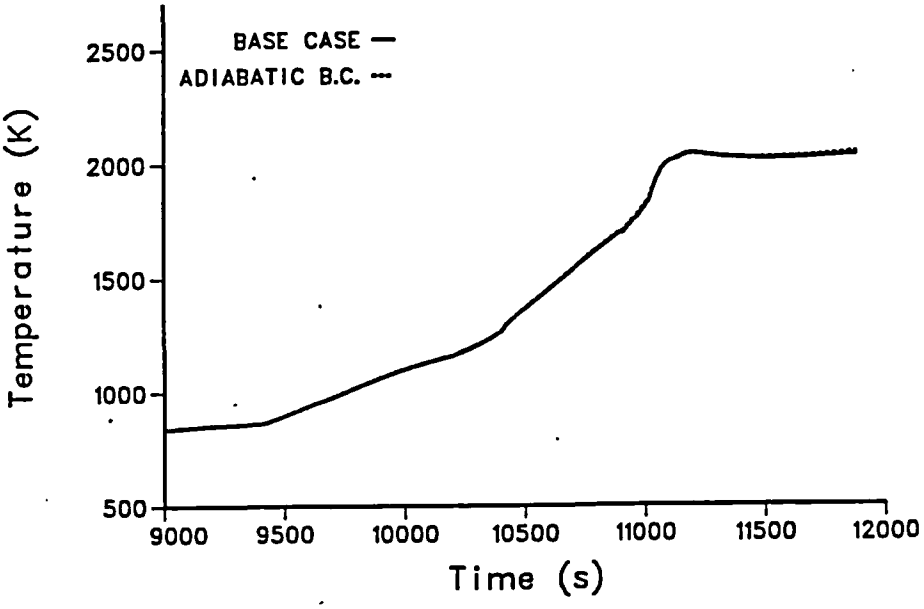

Fig. 87.
Cladding temperatures--ring 3, level 4.

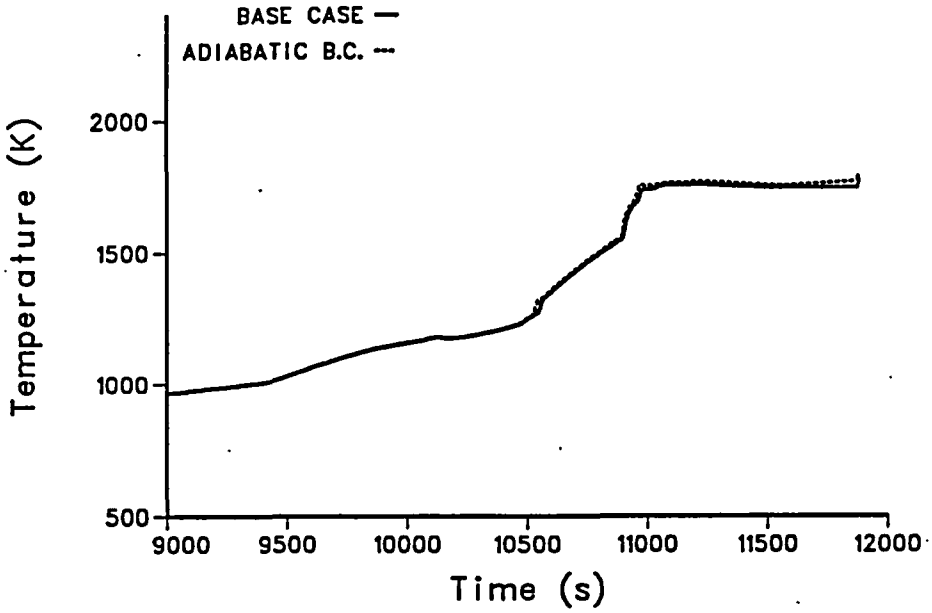

Fig. 88.
Cladding temperature--ring 3, level 5.

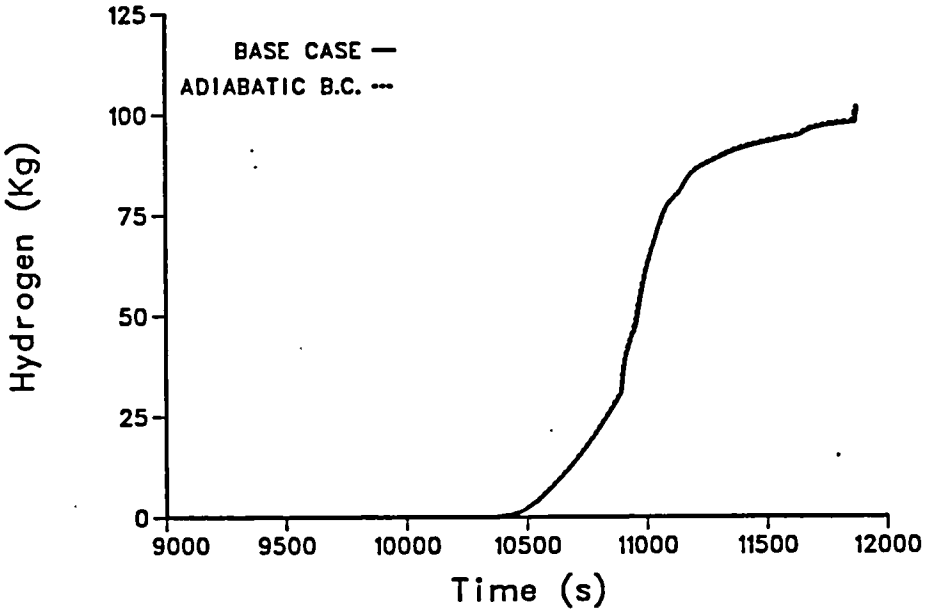

Fig. 89.
Hydrogen exiting core.

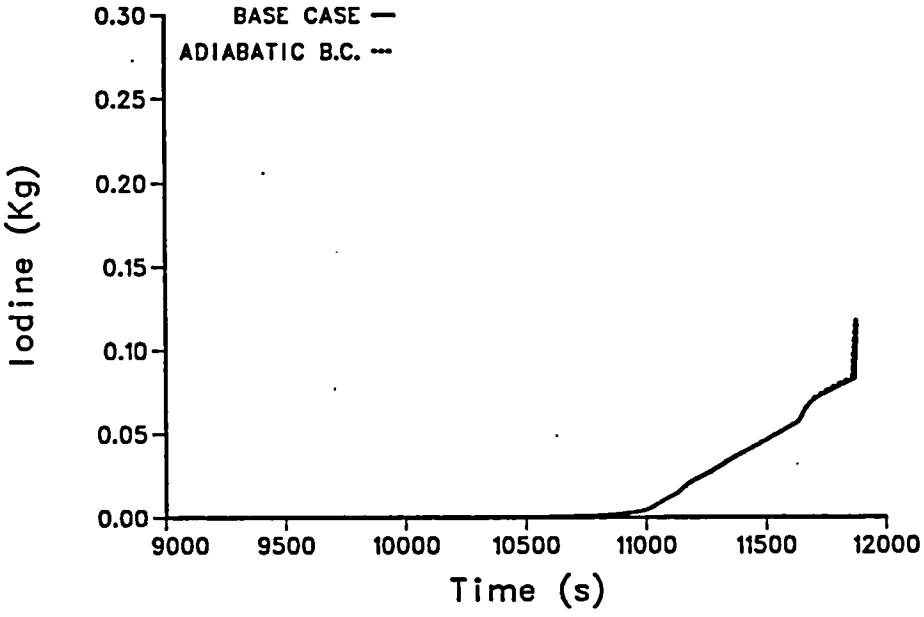

Fig. 90.
Iodine exiting core.

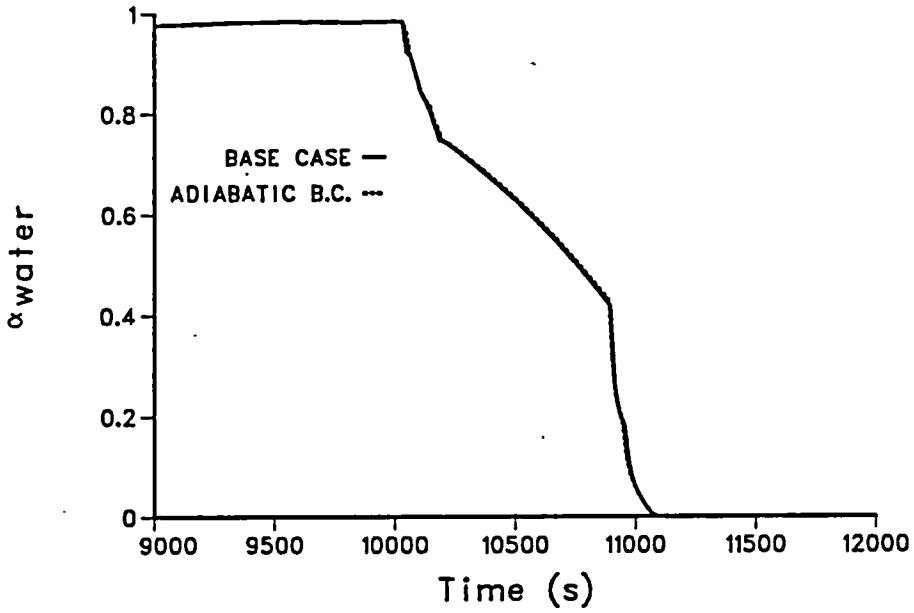

Fig. 91.
Liquid volume fraction--level 1.

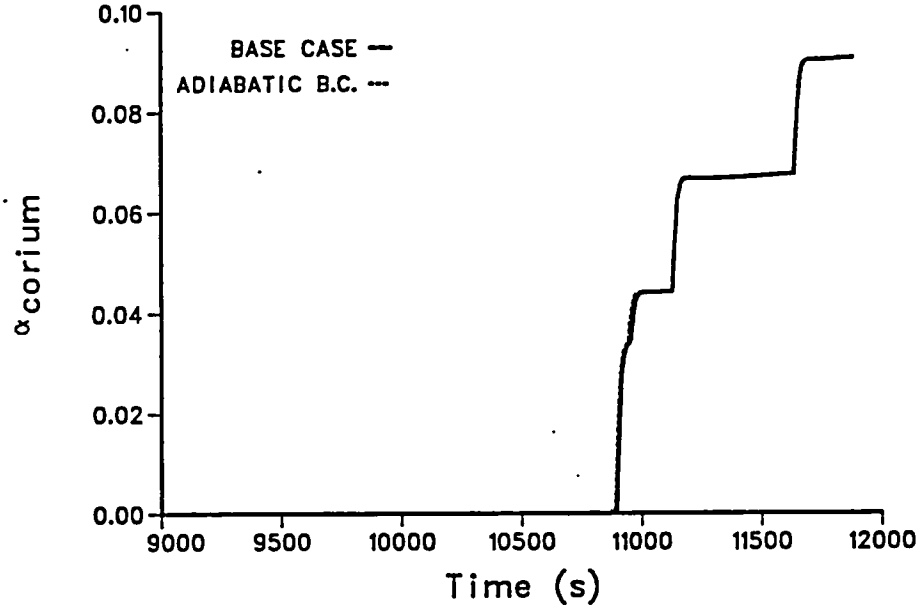

Fig. 92.
Corium volume fraction--level 1.

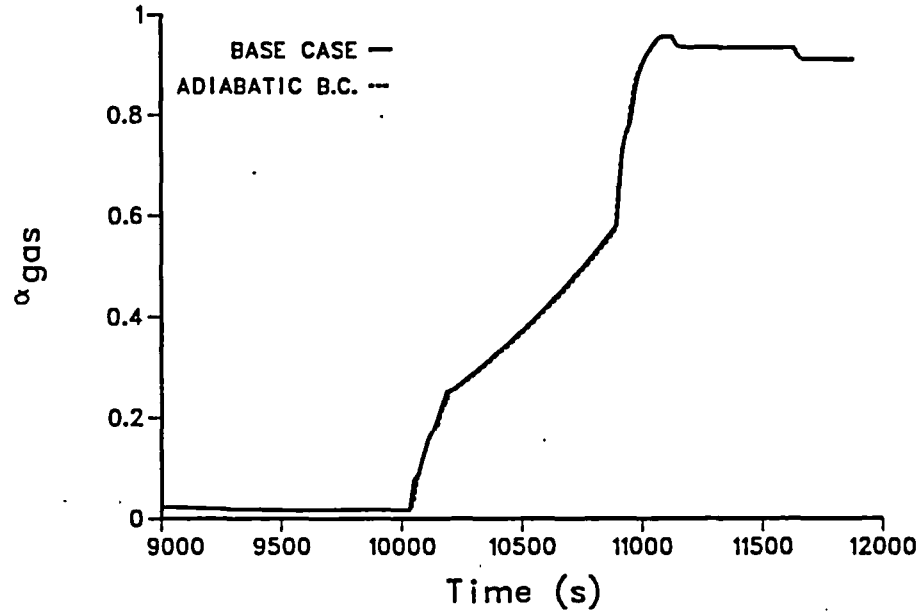

Fig. 93.
Gas volume fraction--level 1.

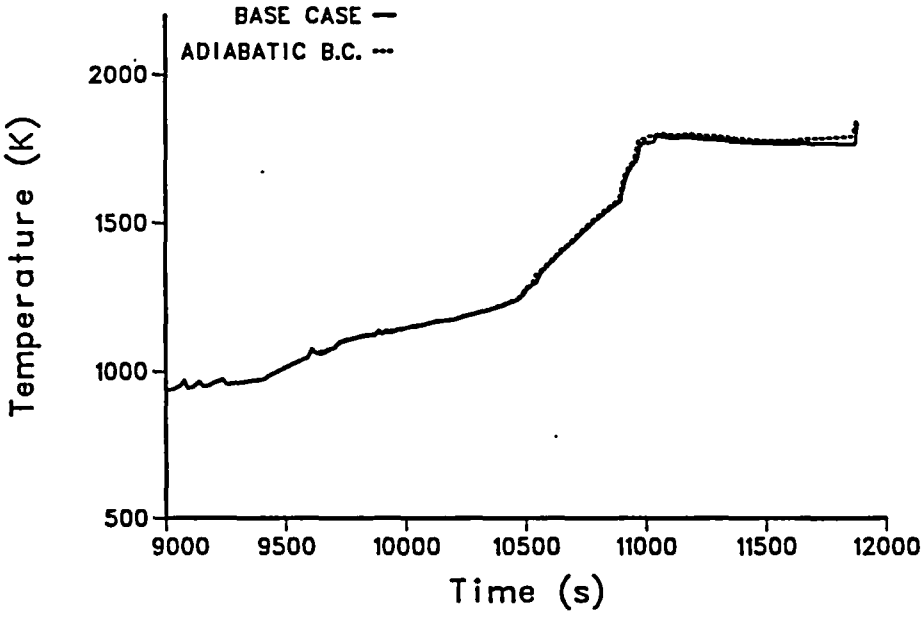

Fig. 94.
Gas temperature--level 5.

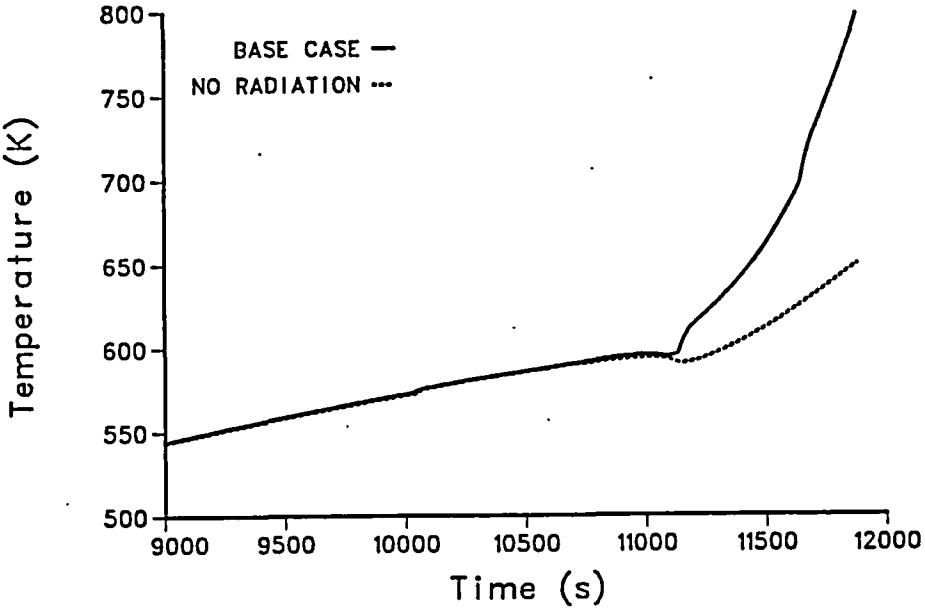

Fig. 95.
Wall surface temperature--level 1.

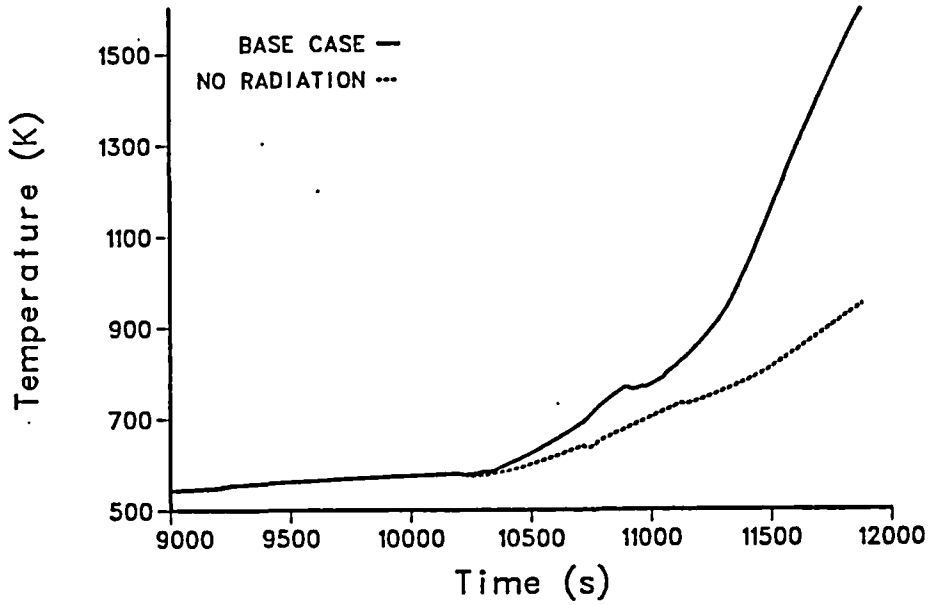

Fig. 96.
Wall surface temperature--level 2.

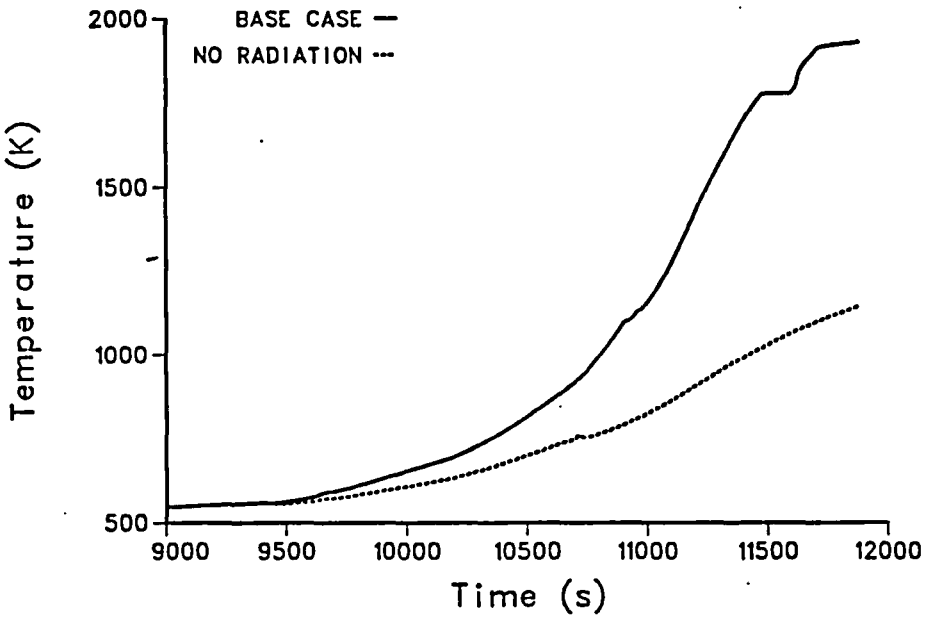

Fig. 97.
Wall surface temperature--level 3.

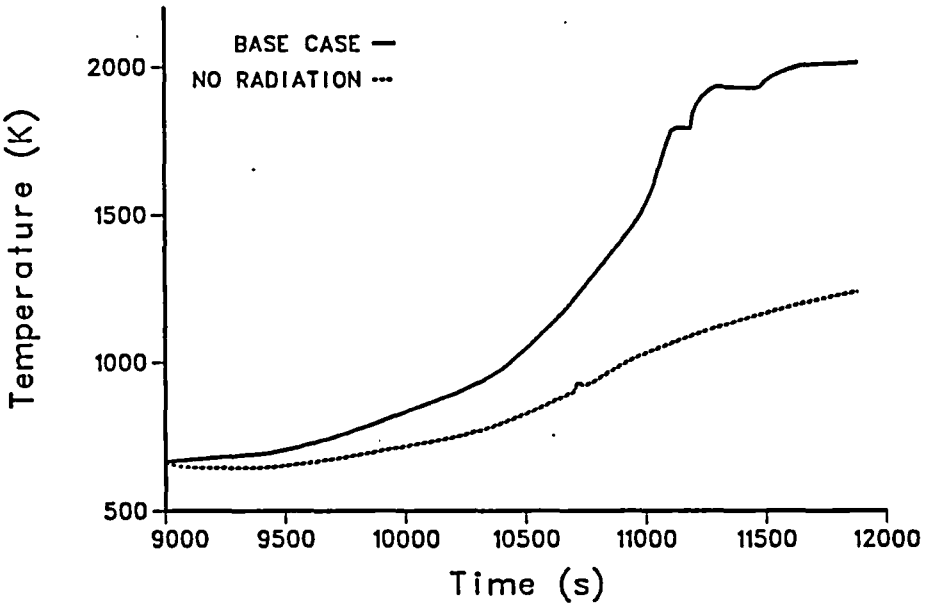

Fig. 98.
Wall surface temperature--level 4.

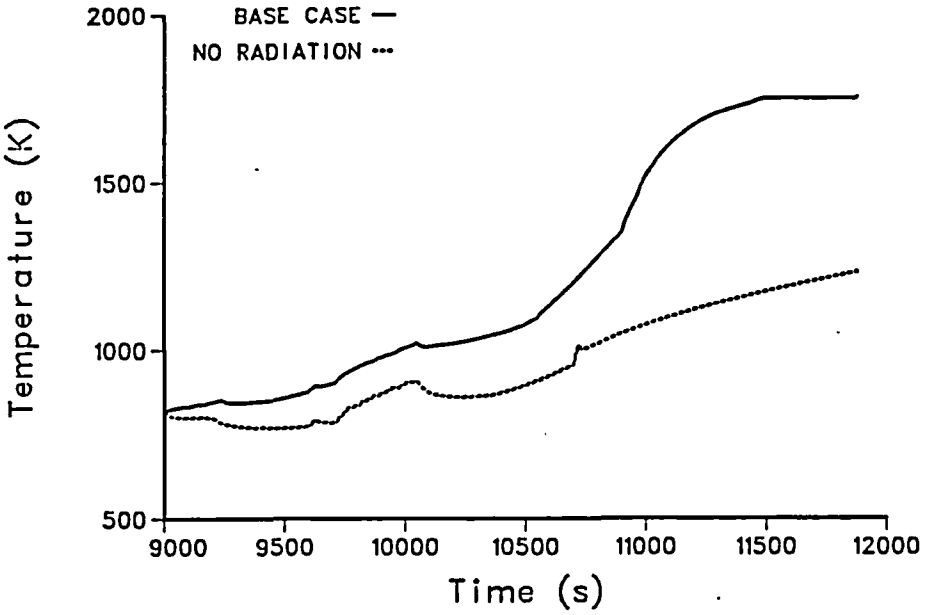

Fig. 99.
Wall surface temperature--level 5.

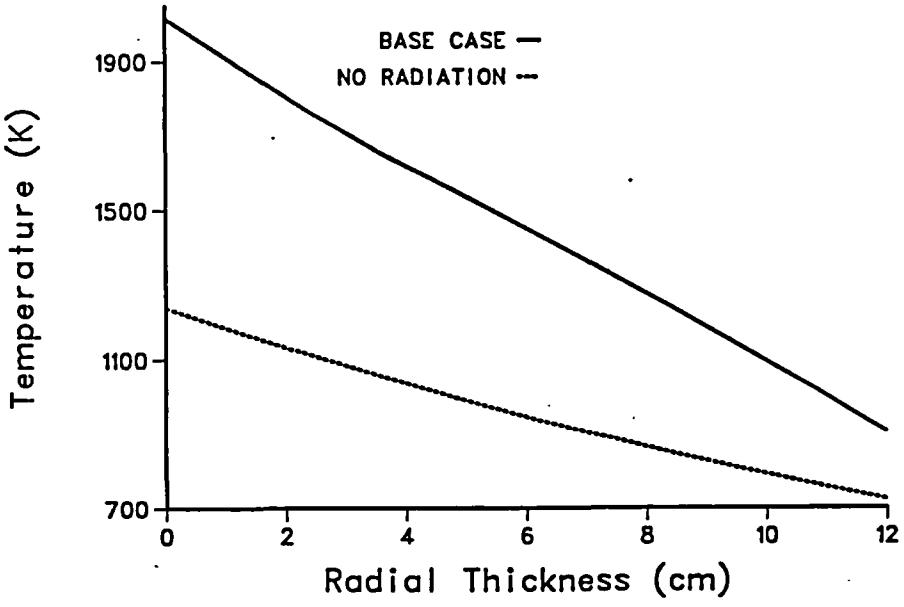

Fig. 100.
Wall temperature profile--level 4 (t = 11880 s).

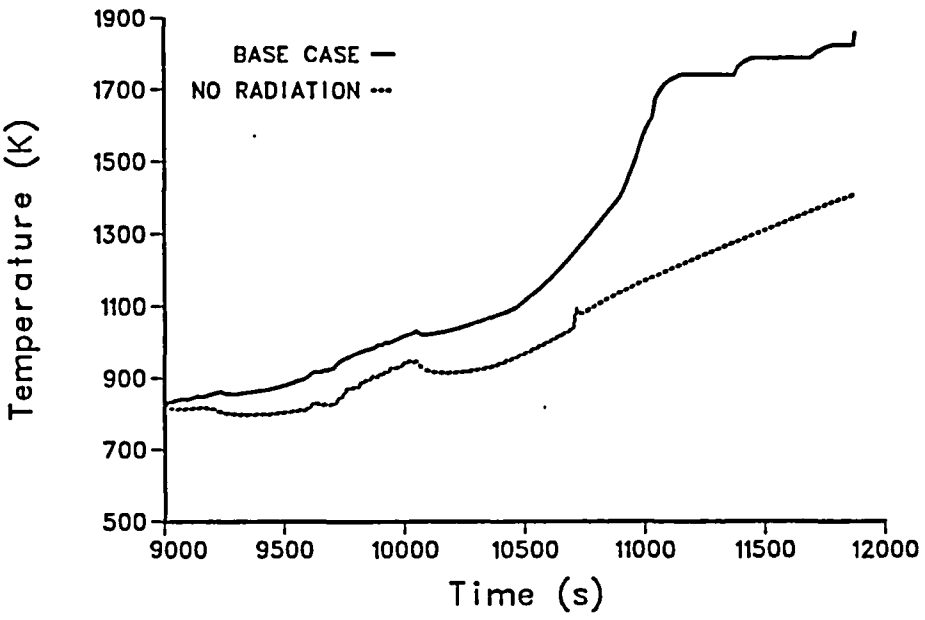

Fig. 101.
Top plate temperature--ring 1.

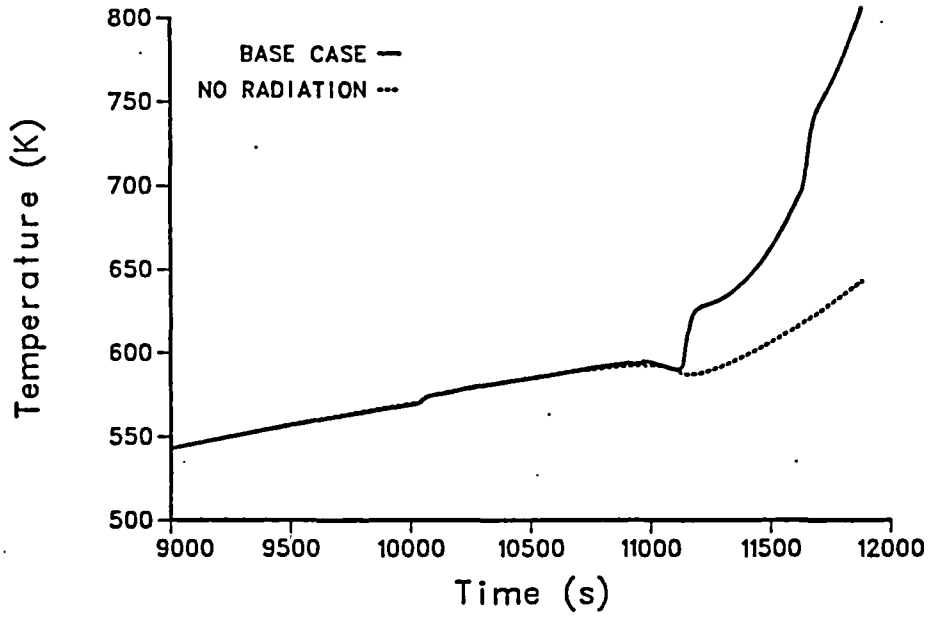

Fig. 102.
Bottom plate temperature--ring 1.

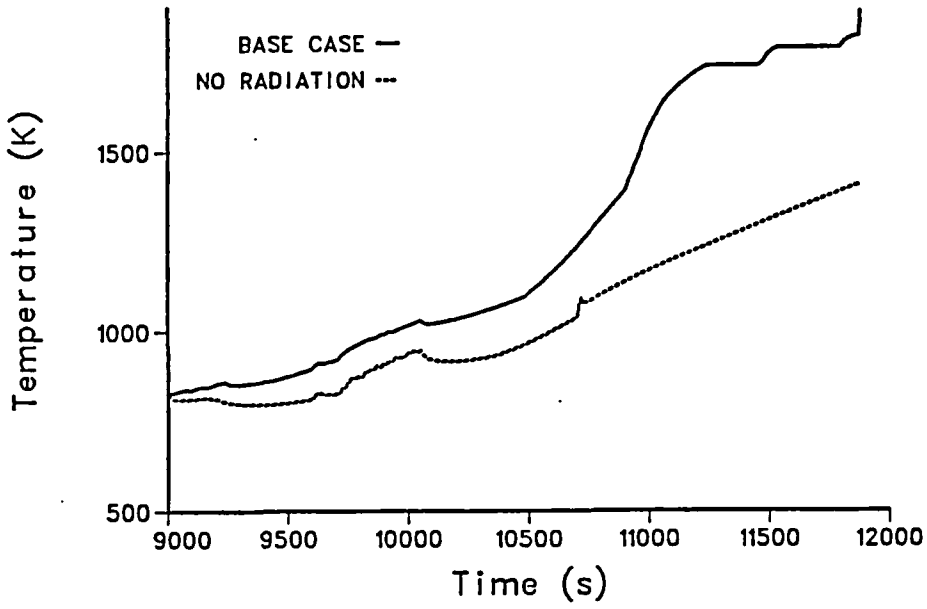

Fig. 103.
Top plate temperature--ring 2.

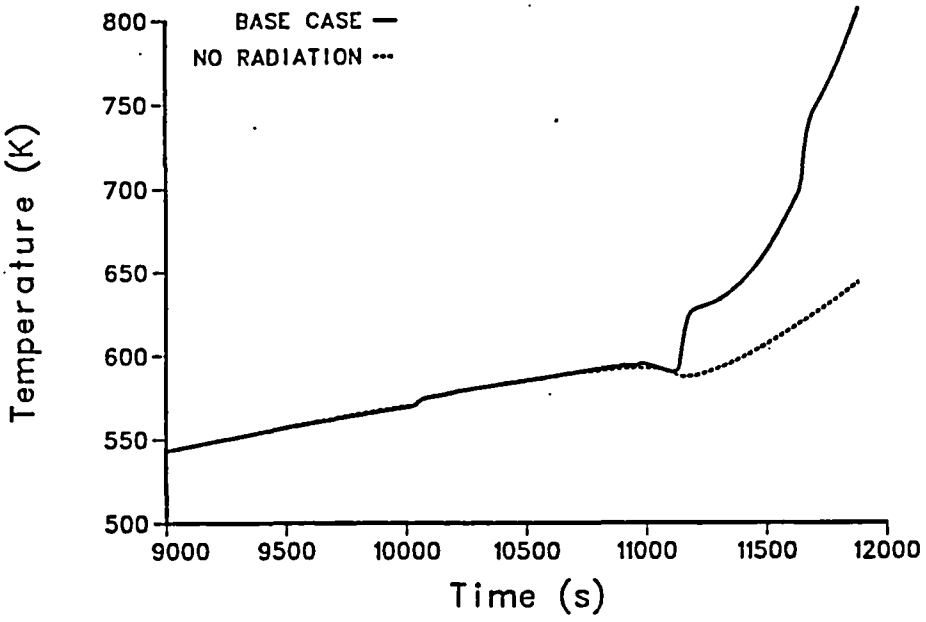

Fig. 104.
Bottom plate temperature--ring 2.

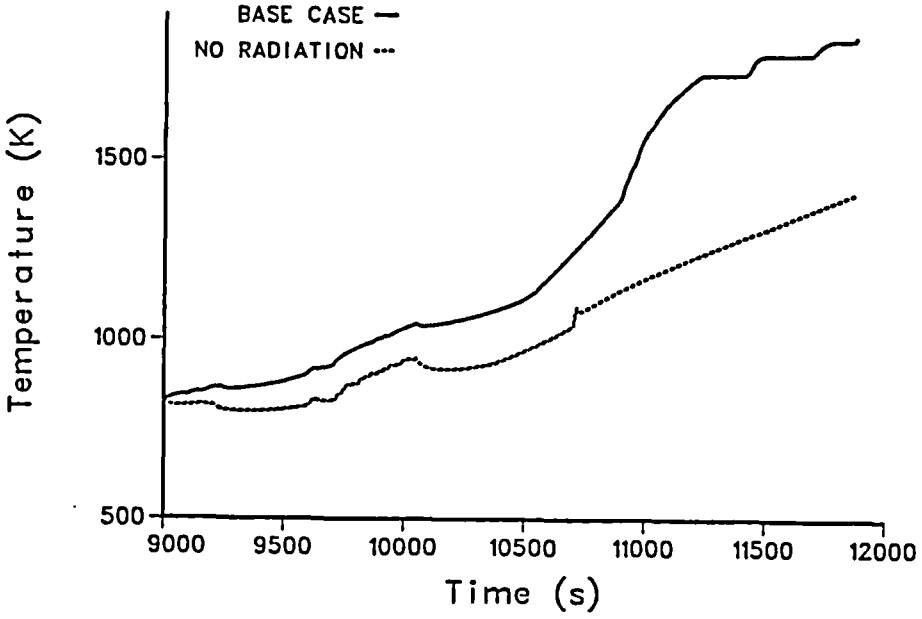

Fig. 105.
Top plate temperature--ring 3.

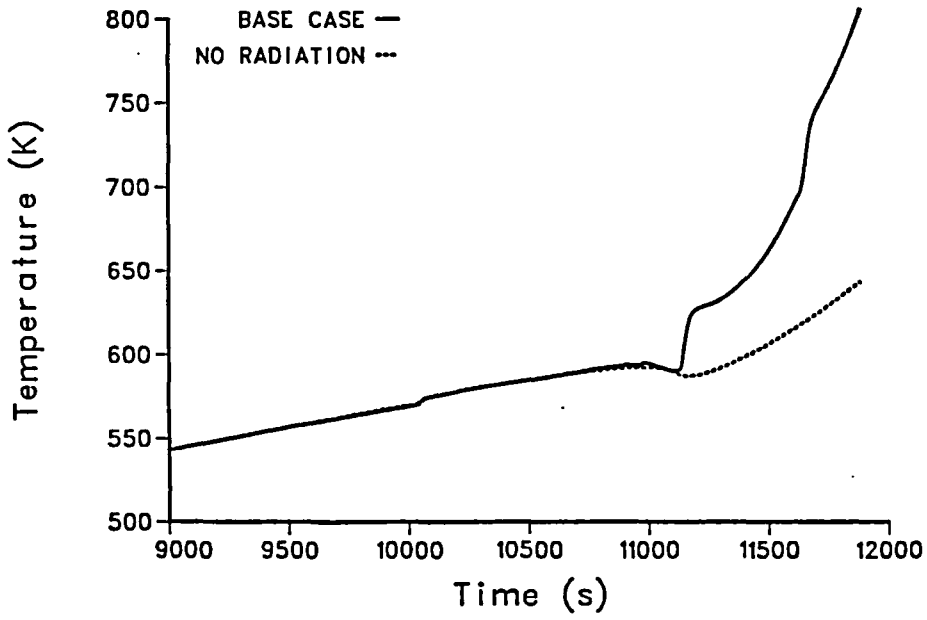

Fig. 106.
Bottom plate temperature--ring 3.

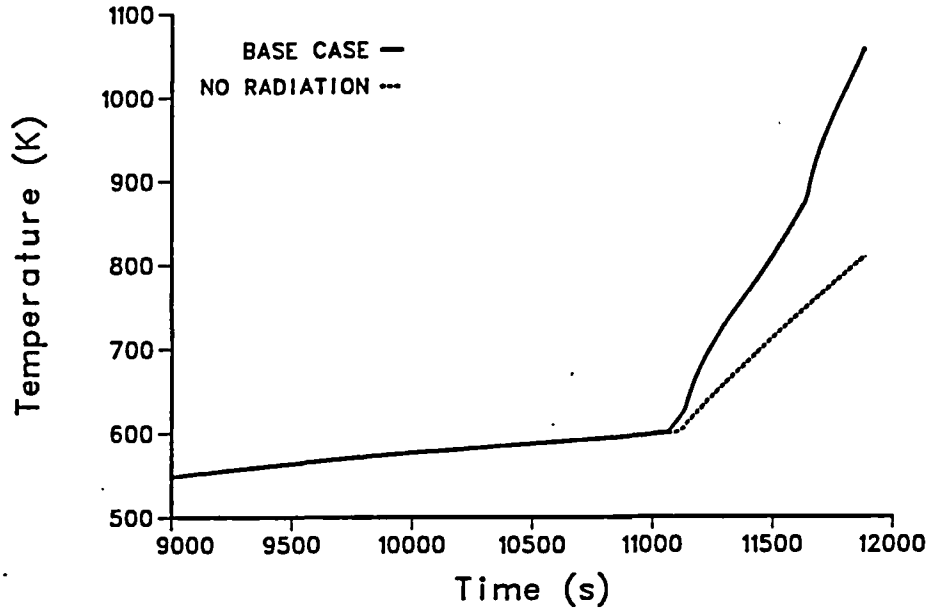

Fig. 107.
Cladding temperature--ring 1, level 1.

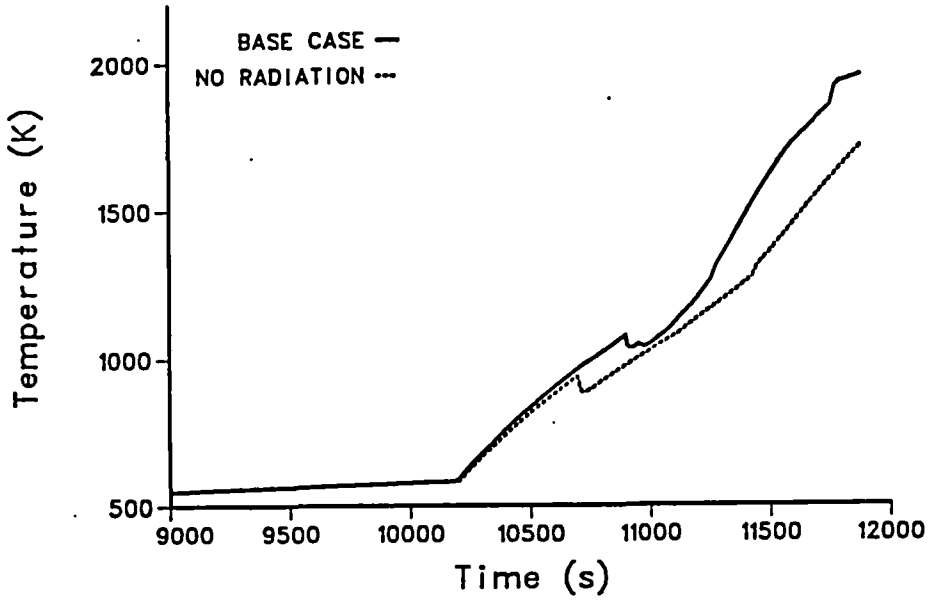

Fig. 108.
Cladding temperature--ring 1, level 2.

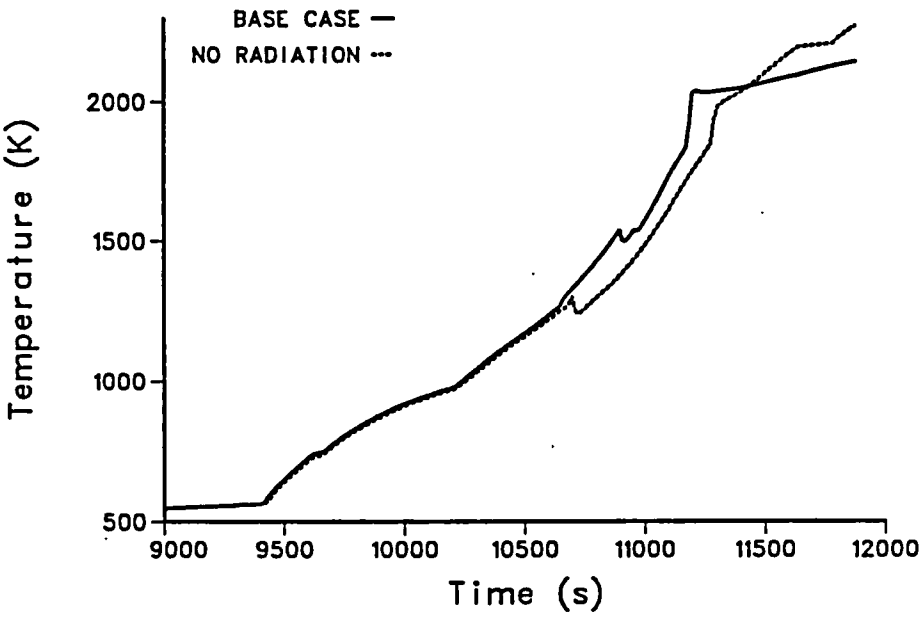

Fig. 109.
Cladding temperature--ring 1, level 3.

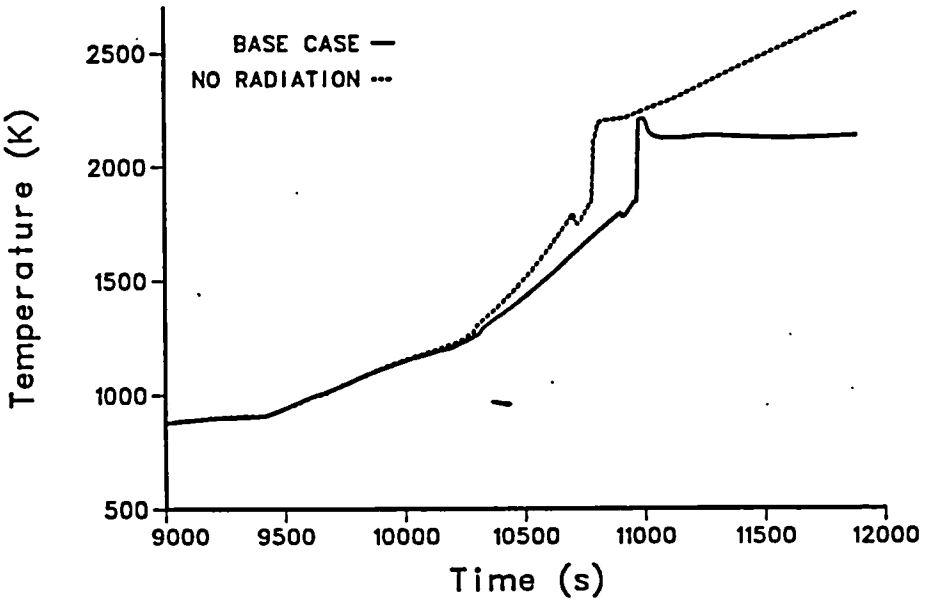

Fig. 110.
Cladding temperature--ring 1, level 4.

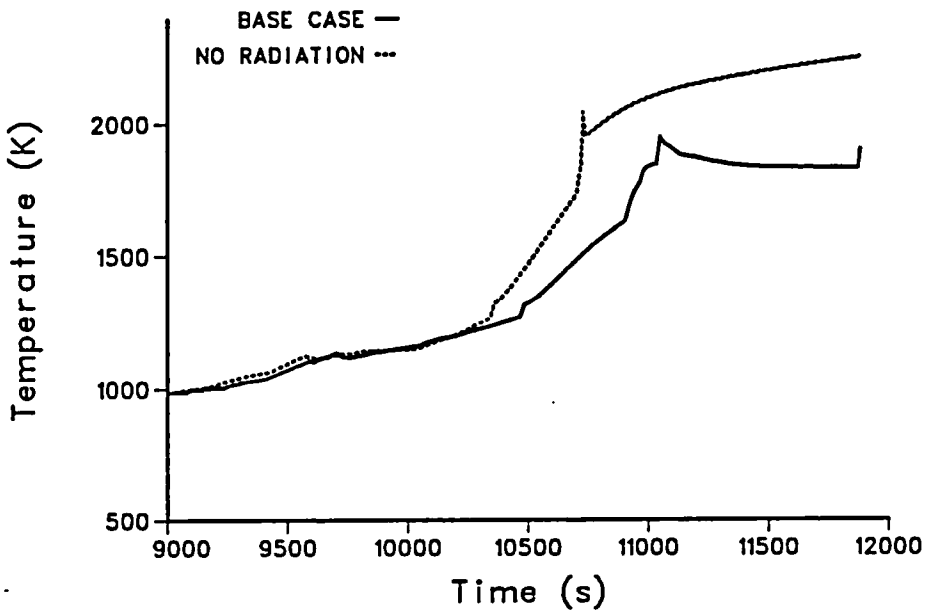

Fig. 111.
Cladding temperature--ring 1, level 5.

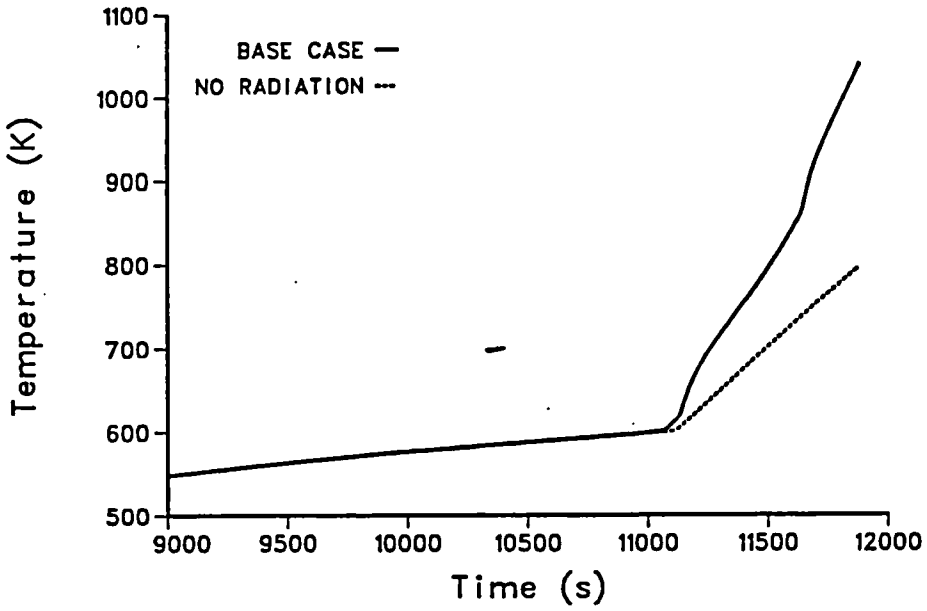

Fig. 112.
Cladding temperature--ring 3, level 1.

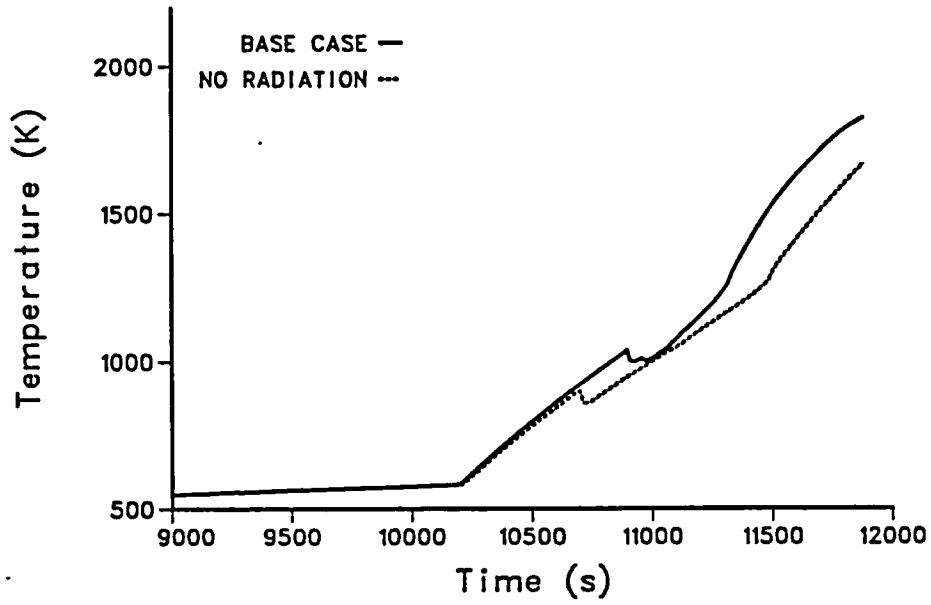

Fig. 113.
Cladding temperature--ring 3, level 2.

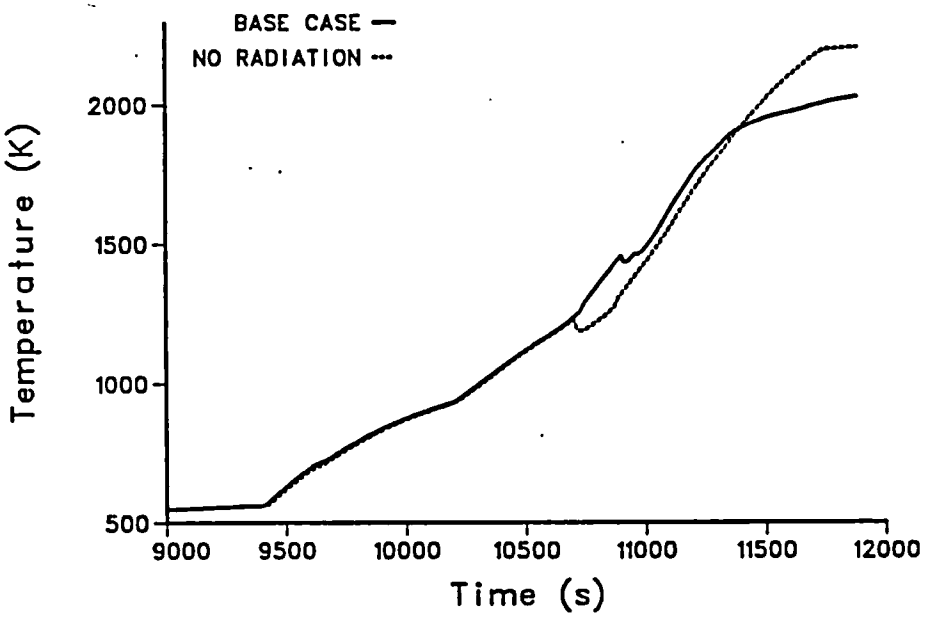

Fig. 114.
Cladding temperature--ring 3, level 3.

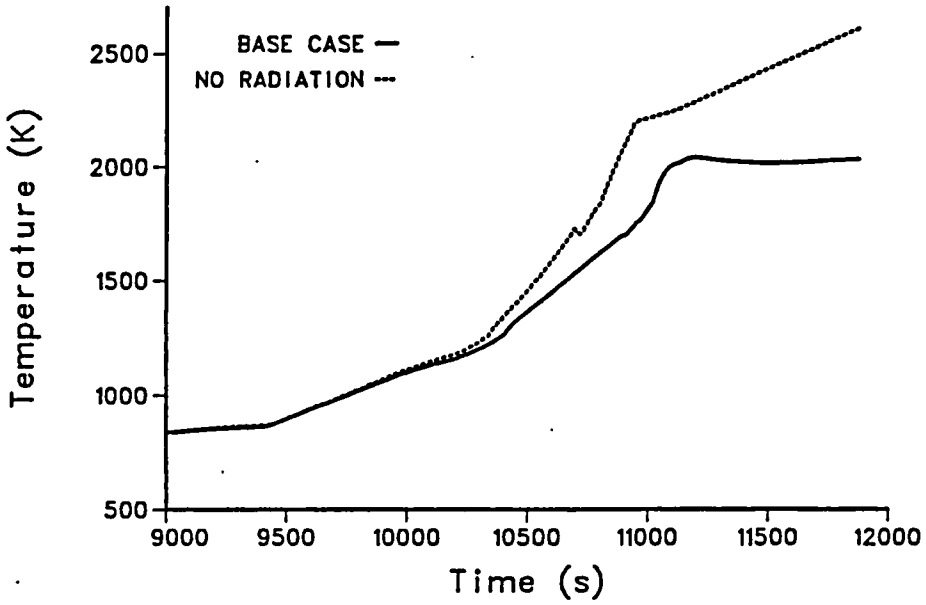

Fig. 115.
Cladding temperature--ring 3, level 4.

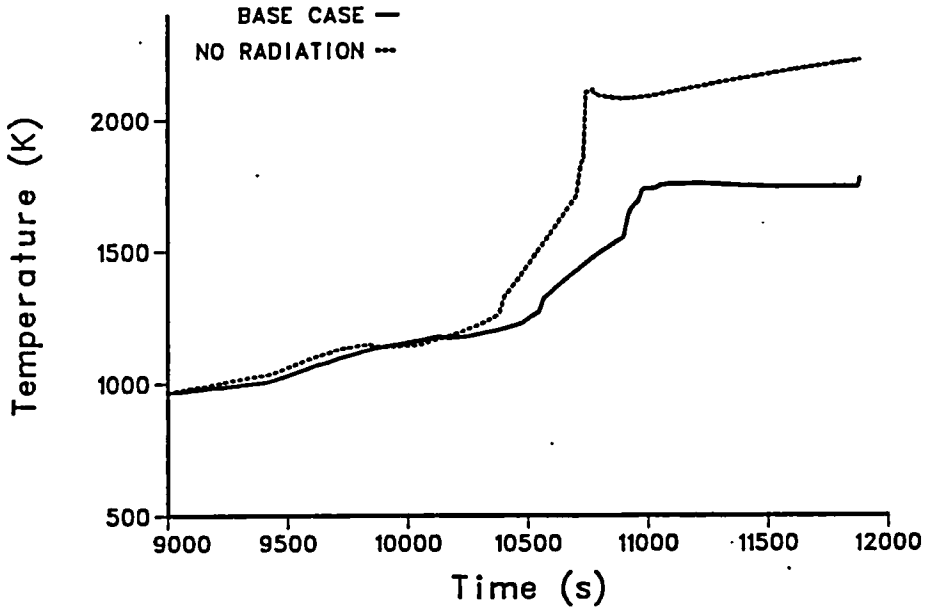

Fig. 116.
Cladding temperature--ring 3, level 5.

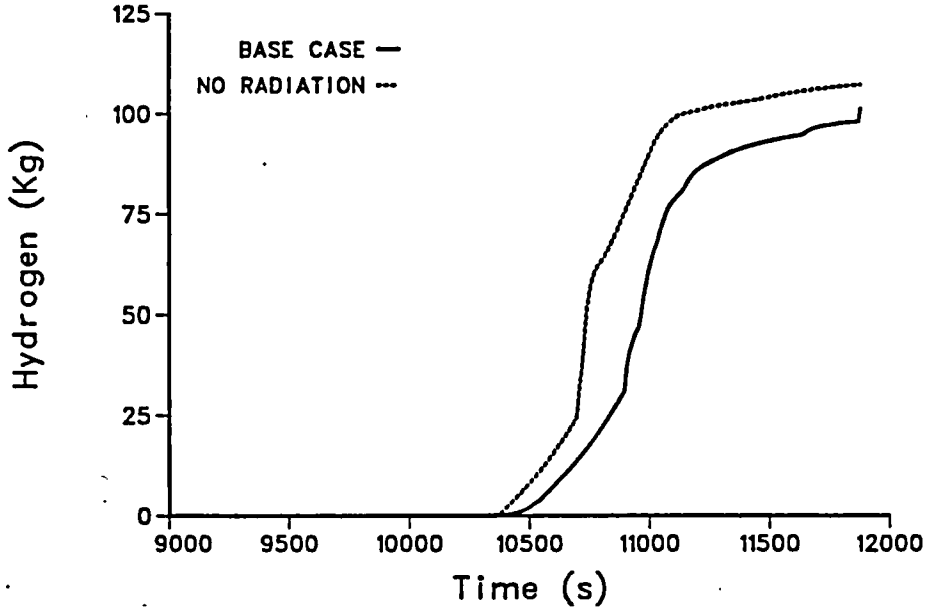

Fig. 117.
Hydrogen exiting core.

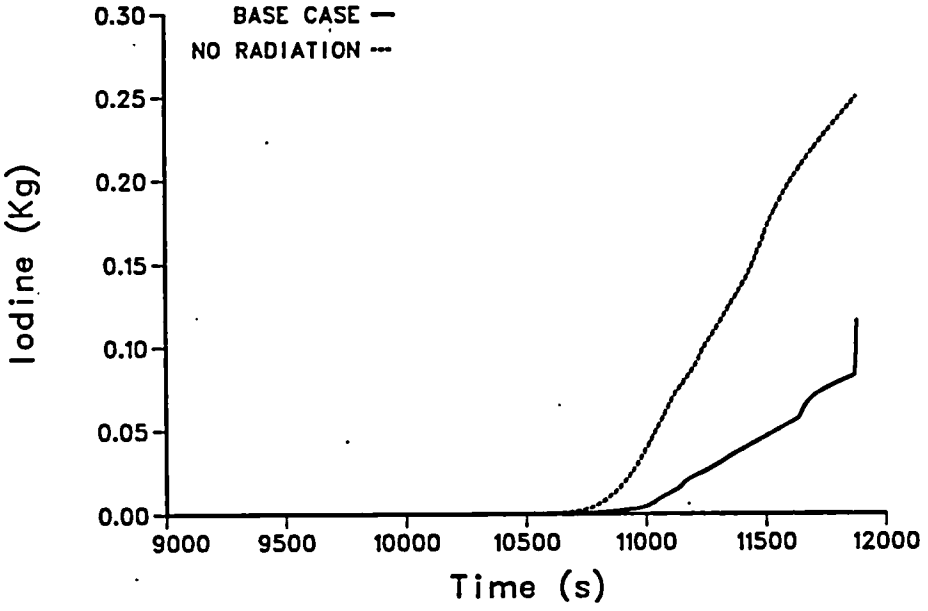

Fig. 118.
Iodine exiting core.

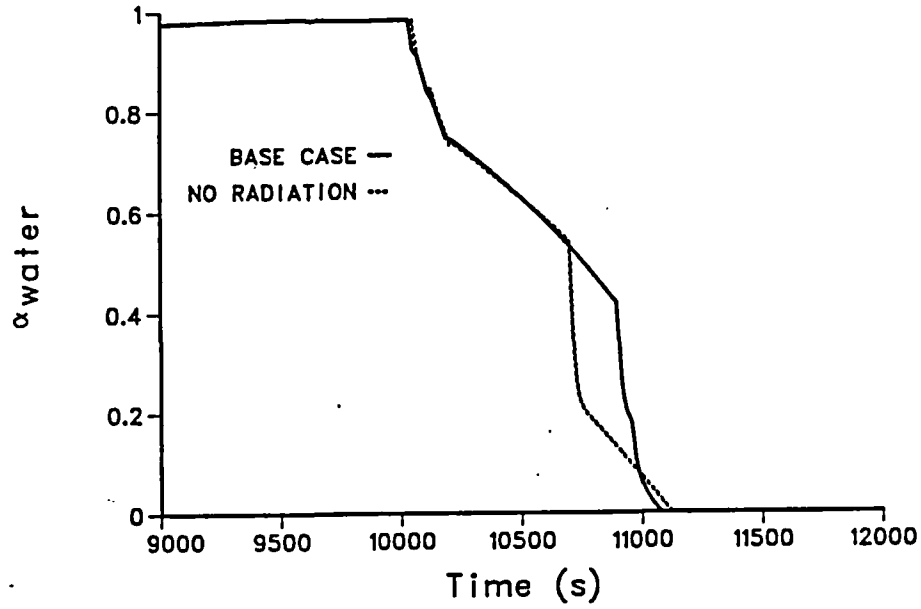

Fig. 119.
Liquid volume fraction--level 1.

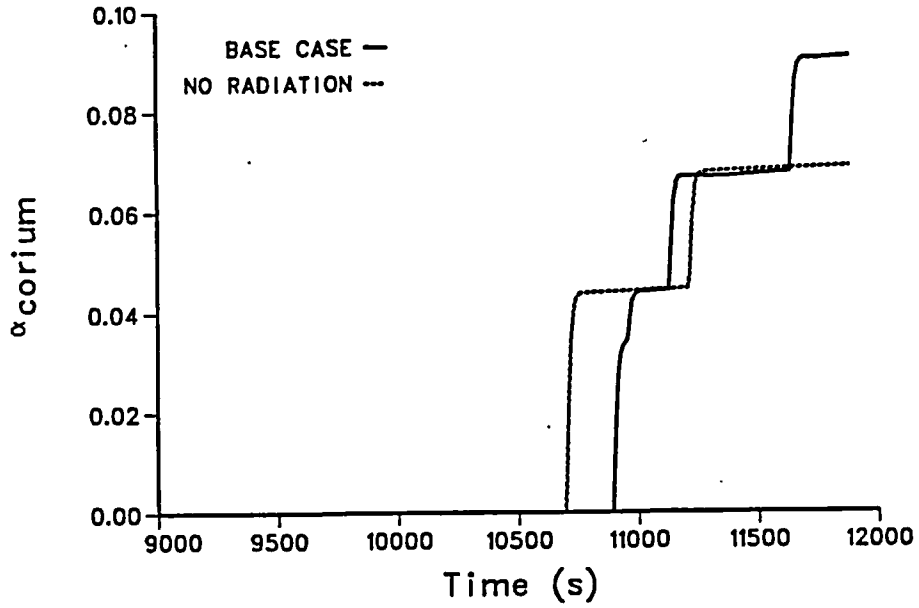

Fig. 120.
Corium volume fraction--level 1.

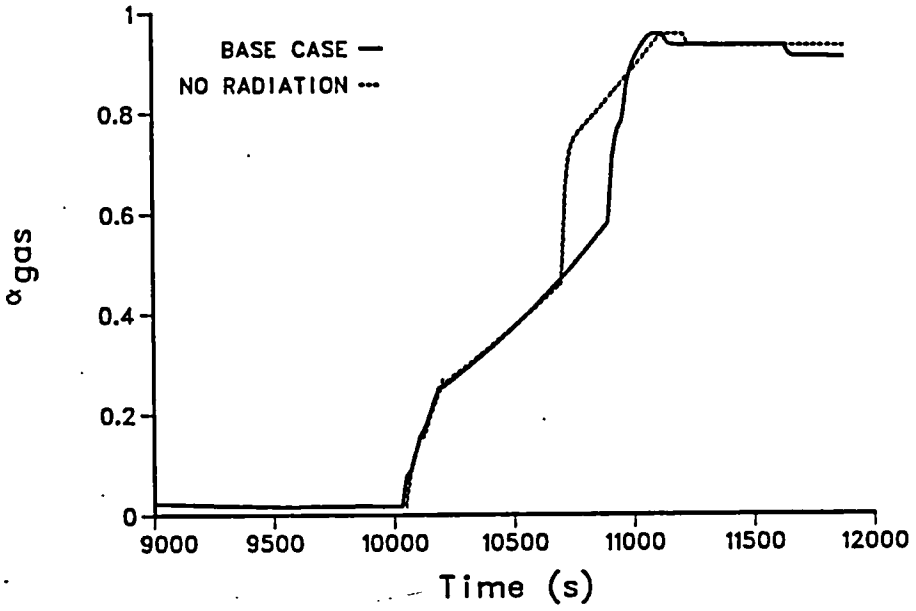

Fig. 121.
Gas volume fraction--level 1.

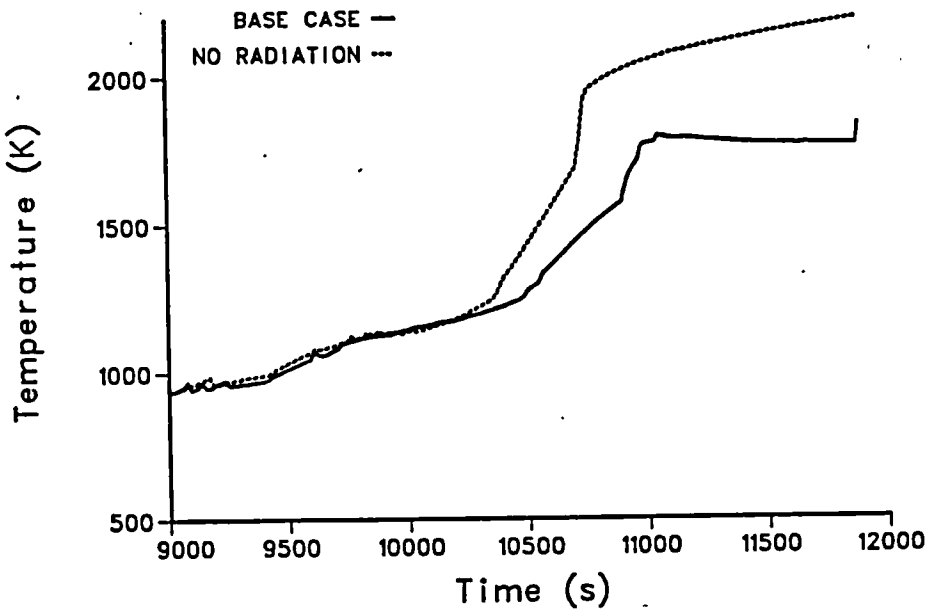

Fig. 122.
Gas temperature--level 5.

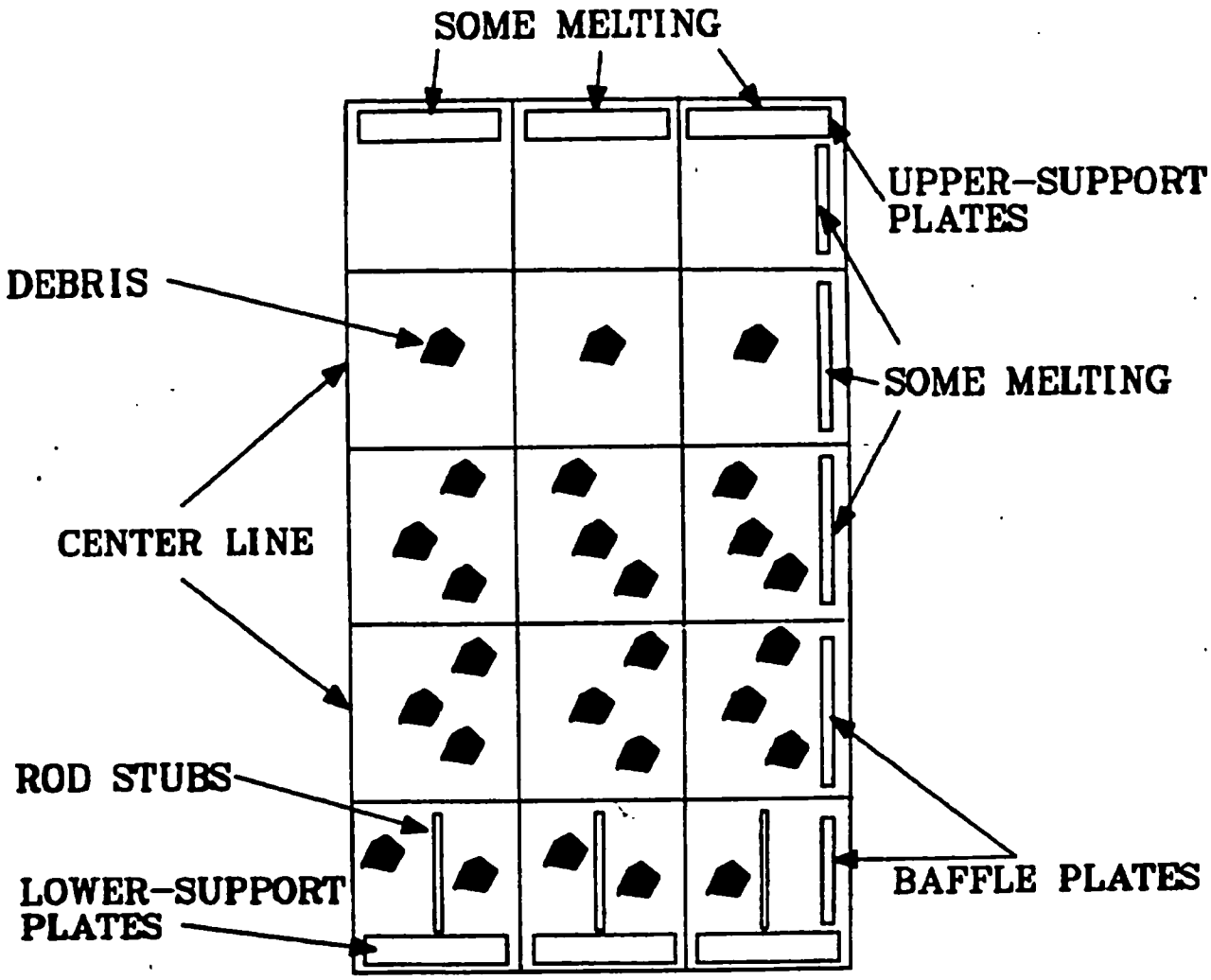

Fig. 123.
MIMAS modeling schematic of the core region showing final damage configuration.